



City Research Online

City, University of London Institutional Repository

Citation: Nadimi Shahraki, S. (2017). Stress Transmission in a Granular System. (Unpublished Doctoral thesis, City, University of London)

This is the accepted version of the paper.

This version of the publication may differ from the final published version.

Permanent repository link: <https://openaccess.city.ac.uk/id/eprint/18579/>

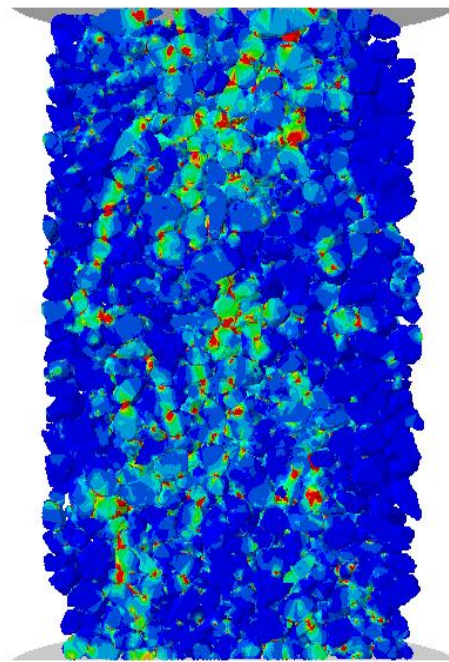
Link to published version:

Copyright: City Research Online aims to make research outputs of City, University of London available to a wider audience. Copyright and Moral Rights remain with the author(s) and/or copyright holders. URLs from City Research Online may be freely distributed and linked to.

Reuse: Copies of full items can be used for personal research or study, educational, or not-for-profit purposes without prior permission or charge. Provided that the authors, title and full bibliographic details are credited, a hyperlink and/or URL is given for the original metadata page and the content is not changed in any way.

STRESS TRANSMISSION IN A GRANULAR SYSTEM

Sadegh NADIMI SHAHRAKI



A thesis submitted to the University of London in fulfilment of the requirements
for the degree of Doctor of Philosophy

City, University of London
Department of Civil Engineering
Research Centre for Multi-scale Geotechnical Engineering

SEPTEMBER 2017

“To see a World in a Grain of Sand

And a Heaven in a Wild Flower

...

by William Blake

ORCID: 0000-0002-0971-7089

TABLE OF CONTENTS

List of Tables	vii
List of Figures	viii
Acknowledgments	xv
Declaration	xvi
Abstract	xvii
Notation	xix
Abbreviations	xxi
Published Contents	xxii
Chapter I: Introduction	
1.1 Overview on Modelling of Granular Materials	1
1.2 Grain-scale Characterisation	2
1.2.1 <i>Granular fabric</i>	2
1.2.2 <i>Stress transmission</i>	3
1.3 Contact Behaviour	4
1.4 Aim and Objectives	4
1.5 Outline of Thesis	5
1.6 Contributions	6
1.7 Tables and Figures	8
Chapter II: Image-based Investigation into the Primary Fabric of Stress-transmitting Particles in Sand	
2.1 Introduction	9
2.2 Material and Methods	11
2.2.1 <i>Reigate sand</i>	11
2.2.2 <i>Experiments</i>	12
2.2.3 <i>3D image process</i>	13
2.3 Statistical Analysis of the Contact Vectors	14
2.3.1 <i>Angular histograms analysis</i>	14
2.3.2 <i>Fabric tensor analysis</i>	16
2.3.3 <i>Contact normal and branch vector relationship</i>	18
2.4 Networks of Stress-transmitting Particles	19
2.4.1 <i>Methodology</i>	19
2.4.2 <i>Load-bearing particles forming the force chains</i>	21
2.4.3 <i>Quantitative description of the load-bearing particles</i>	22
2.4.4 <i>Spatial distribution of the force chains</i>	23
2.5 Conclusions	25
2.6 Tables and Figures	27
Chapter III: A Micro Finite-Element Model for Soil Behaviour	
3.1 Introduction	43
3.2 The μ FE Model	45

3.2.1 <i>Image acquisition and processing</i>	45
3.2.2 <i>Mesh generation</i>	47
3.2.3 <i>Numerical fundamentals</i>	48
3.3 A Case Study	50
3.3.1 <i>The model</i>	51
3.3.2 <i>Assessing energy quantities</i>	52
3.3.3 <i>The effect of the yield stress</i>	53
3.3.4 <i>Grain kinematics and stress distribution inside grains</i>	53
3.4 Conclusions	56
3.5 Postscript	57
3.5.1 <i>Delaunay refined algorithm</i>	57
3.5.2 <i>Inertia tensor</i>	58
3.6 Tables and Figures	59

Chapter IV: A Micro Finite-Element Model for Soil Behaviour: Numerical Validation

4.1 Introduction	69
4.2 Behaviour of a Single Sphere	70
4.2.1 <i>Mesh size effect</i>	70
4.2.2 <i>Normal loading</i>	70
4.2.3 <i>Tangential loading</i>	71
4.2.4 <i>Torsional loading</i>	72
4.2.5 <i>Rotational loading</i>	72
4.3 Behaviour of an Assembly of Spheres	73
4.3.1 <i>Model description</i>	74
4.3.2 <i>Elastic behaviour</i>	74
4.3.3 <i>Elastic-plastic behaviour</i>	74
4.4 Conclusions	76
4.5 Tables and Figures	77

Chapter V: Single-Grain Virtualisation for Contact Behaviour Analysis on Sand

5.1 Introduction	83
5.2 Virtualisation of a Single Grain	85
5.2.1 <i>Image acquisition system</i>	85
5.2.2 <i>Volume reconstruction & mesh generation</i>	85
5.2.3 <i>Sensitivity analysis of the reconstruction method</i>	87
5.3 Single Grain Compression Test	88
5.3.1 <i>Single grain tests on spherical beads</i>	88
5.3.2 <i>Single grain tests on sand</i>	89
5.4 Results and Discussion	90
5.5 Conclusions	91
5.6 Tables and Figures	93

Chapter VI: Contact Behaviour of Particles with Surface Roughness	
6.1 Introduction	104
6.2 Modelling of Surface Roughness	105
6.2.1 <i>Roughness measurement</i>	105
6.2.2 μ FE <i>mesh generation</i>	105
6.2.3 <i>Numerical model description</i>	106
6.2.4 <i>Roughness effect in normal loading</i>	106
6.2.5 <i>Roughness effect in tangential loading</i>	107
6.2.6 <i>The effect of loading history</i>	107
6.3 Contact Area Measurement	108
6.3.1 <i>Theoretical considerations</i>	108
6.3.2 <i>Comparison with numerical measurement of contact area</i>	109
6.4 Conclusions	110
6.5 Tables and Figures	111
Chapter VII: A Micro Finite-Element Model for Soil Behaviour: Experimental Evaluation	
7.1 Introduction	120
7.2 μ FE Model	121
7.3 A Case Study	122
7.3.1 <i>Experiments</i>	122
7.3.2 <i>Numerical modelling</i>	123
7.3.3 <i>Evolution of the active contacts</i>	123
7.3.4 <i>Force balance condition</i>	124
7.3.5 <i>Formation of stress chains</i>	125
7.4 Concluding Remarks	125
7.5 Tables and Figures	127
Chapter VIII: Conclusions and Future Work	
8.1 Summary	134
8.1.1 <i>Image-based investigation</i>	134
8.1.2 <i>Numerical investigation</i>	135
8.1.3 <i>Contact mechanics</i>	136
8.2 Ongoing and Future Work	137
8.2.1 <i>Simulation of grain breakage</i>	137
8.2.2 <i>Tribological characterisation of contact interaction</i>	137
8.2.3 <i>Experimental strain measurement in a granular assembly</i>	138
8.2.4 <i>Blind prediction of stress-strain behaviour</i>	138
References	139
Appendix A: Enhancing Soil Sample Preparation by Thermal Cycling	
A.1 Introduction	152
A.2 Experimental Method	153
A.2.1 <i>Materials</i>	153

A.2.2 <i>Sample preparation and void ratio measurements</i>	154
A.2.3 <i>Experimental set-up</i>	154
A.3 Results and Discussion	155
A.3.1 <i>Effect of container and initial density</i>	155
A.3.2 <i>Effect of grain morphology and packing</i>	156
A.3.3 <i>Thermally induced grain rearrangement</i>	157
A.4 Conclusions	157
A.5 Tables and Figures	159

Appendix B: On the Torsional Loading of Elastoplastic Spheres in Contact

B.1 Background	167
B.2 Elastic Interaction	169
B.3 Elastoplastic Interaction	170
B.4 Closing Remarks	170
B.5 Tables and Figures	172

Appendix C: On the Tensile Strength of Soil Grains in Hertzian Response

C.1 Introduction	176
C.1.1 <i>Single grain breakage</i>	176
C.1.2 <i>Theoretical consideration</i>	177
C.2 Numerical Investigation	178
C.2.1 <i>Constitutive model</i>	178
C.2.2 <i>Numerical model</i>	179
C.2.3 <i>Results</i>	180
C.3 Experimental Investigation	180
C.3.1 <i>Glass bead</i>	180
C.3.2 <i>Silica sand</i>	181
C.3.3 <i>Carbonate sand</i>	181
C.4 Closing Remarks	181
C.5 Tables and Figures	183

LIST OF TABLES

Table 2-1	Specific volume (v) of the intact and reconstituted samples prior to loading
Table 2-2	Summary of the intact and reconstituted samples investigated in the post-peak regime (ϵ_a =axial strain, q/p' =deviator stress/mean stress, u =specific volume)
Table 2-3	Results on the fabric tensor data for the contact normal (CNV) and branch vector (BV)
Table 2-4	Number particles in the different networks with the correspondent percentage of grains satisfying the stability criterion from contact to truss network and the stability plus load transmission criteria from contact network to force chains
Table 3-1	Analysis of four selected grains in terms of displacement arrows, inertia tensor and the associate eigenvalues and eigenvectors and number of active contacts
Table 4-1	Material parameters used in the simulations
Table 5-1	Physical and mechanical properties used in the numerical simulations of silica sand
Table 5-2	Physical and mechanical properties used for the analytical solution of glass beads
Table 6-1	Physical and mechanical properties for glass ballotini
Table A-1	Physical properties of granular materials used
Table A-2	Summary of results obtained from thermal cycling experiments
Table A-3	Coefficient of thermal expansion of materials used in experiments and expected expansion
Table A-4	Change in void ratio at end of five thermal cycles for the three sands using the PMMA container
Table B-1	Physical and mechanical parameters of the spheres
Table B-2	Isotropic hardening parameters
Table C-1	Physical and mechanical parameters
Table C-2	Compressive and tensile strengths for different value of parameter χ and the maximum normal force obtained corresponds to the onset of breakage

LIST OF FIGURES

- Figure 1-1 Relevant scales for granular modelling in this study
- Figure 2-1 Microscope image of a thin section of Reigate sand under polarised light
- Figure 2-2 Mechanical and volumetric response for the intact and reconstituted samples
- Figure 2-3 Schematic diagram illustrating the contact normal (CNV) and branch vector (BV)
- Figure 2-4 Rose diagrams for the intact and reconstituted specimens prior to loading (shading indicates average contact area in voxels); (a) CNV Int0; (b) BV Int0; (c) CNV Rec0; (d) BV Rec0
- Figure 2-5 Rose diagrams for the specimens at load stage 3 (shading indicates average contact area in voxel); (a) CNV Int3; (b) BV Int3; (c) CNV Rec3S; (d) BV Rec3S
- Figure 2-6 Rose diagrams for the specimens at load stage 4 (shading indicates average contact area in voxel); (a) CNV Int4S; (b) BV Int4S; (c) CNV Rec4S; (d) BV Rec4S
- Figure 2-7 Evolution of the major principal fabric orientation for contact normal for load stages (LSt) 3 and 4, the data for the samples containing the shear band are marked with circles
- Figure 2-8 Distribution of angle α for the specimens: (a) Int3 shaded by EI; (b) Int3 shaded by S; (c) Int3 shaded by CA; (d) Int3S shaded by EI; (e) Int3S shaded by S (f) Int3S shaded by CA; (g) Rec3 shaded by EI; (h) Rec3 shaded by S; (i) Rec3 shaded by CA
- Figure 2-9 a) Schematic of the truss network in a granular assembly, b) detail of a truss network for sample lant3 for a section of 60 voxels thickness
- Figure 2-10 Truss-like elements in a sub-volume (size in voxels: 600x600x60) for sample, a) Int3 outside the shear band, b) Int3S, containing the shear band
- Figure 2-11 Methodology flowchart: (a) μ CT image (600x600x600 voxels), (b) contact network, (c) truss network, (d) network of the stress transmitting grains or force chains (represented by segments connecting the centroids of the load-bearing grains)
- Figure 2-12 Rose diagrams showing the distribution of the particle orientation, given by the orientation of the particle's major axis, for the sample Int3 -shading indicates average elongation ratios of the particles within each angular bean: a) for the particles forming the contact network, (b) for the particles forming the force chains
- Figure 2-13 Rose diagrams showing the distribution of the particle orientation for the sample Int3S -shading indicates average elongation ratios of the

- particles within each angular bean: a) for the particles forming the contact network, (b) for the particles forming the force chains
- Figure 2-14 Comparison of the particle size distribution for the grains composing each of the three networks, respectively: a) for sample Int3 outside the shear band and b) for the sample Int3S containing the shear band
- Figure 2-15 Coordination number distribution for the grains composing each of the three networks, respectively: a) for sample Int3 and b) for the sample Int3S
- Figure 2-16 Coordination number versus number of trusses for both the truss network and the force chain for sample Int3
- Figure 2-17 Contact surface area distribution using all grains in the sample, using the grains that passed the stability criterion and the one that satisfy the load transmission criterion, a) for the intact sample outside the shear band and b) for the intact sample containing the shear band
- Figure 2-18 Force chains obtained for sample Int3 for a section of: a) 60 voxels thickness and b) 300 voxels thickness
- Figure 2-19 Illustration of the steps to obtain the network of the stress transmitting grains for the sample Int3: a) 3D vectors, represented by the segments connecting the centroids of the grains forming quasi-vertical contact normals, the vectors associated with larger contact surfaces have brighter colours (only a projection is presented), b) 3D vectors following the low pass filter (c) final network
- Figure 2-20 Illustration of the steps to obtain the network of the stress transmitting grains for the sample Int3S: a) 3D vectors, represented by the segments connecting the centroids of the grains forming quasi-vertical contact normals, the vectors associated with larger contact surfaces have brighter colours (only a projection is presented), b) 3D vectors following the low pass filter (c) final network
- Figure 3-1 Flowchart illustrating the various processes/tools and outcomes involved in the development of this FE model
- Figure 3-2 Three examples of meshed grains to illustrate: a) the finer mesh used to describe angular features of the grain, b) the large elements used in flat regions, c) the mesh of a concave grain
- Figure 3-3 Summary of contact constitutive behaviour for elastic spheres by means of non-dimensional quantities: a) normal force displacement, b) tangential force displacement, c) rolling moment, d) twisting moment
- Figure 3-4 Particle size distribution of Reigate sand obtained from sieving (after Fonseca *et al.*, 2012)
- Figure 3-5 Intact Reigate sand: a) illustration of the block sample and b) micrograph of a thin section under cross-polarised light showing the extended flat contacts between the grains (after Fonseca, 2011)
- Figure 3-6 Boundary conditions used for the simulation of the Oedometer compression

- Figure 3-7 Evolution of the measured kinetic and internal energies for the simulations reported in this study, the near zero values measured for the kinetic energy demonstrates the quasi-static nature of the simulations
- Figure 3-8 Hertzian response of an elastic-plastic sphere measured for four different yield stresses and the general stress field inside the grain
- Figure 3-9 Stress-strain response of the Oedometer compression simulations
- Figure 3-10 Force-displacement measurements from the Oedometer compression simulations
- Figure 3-11 Frictional dissipation measured for the four Oedometer test with different yield stresses
- Figure 3-12 Plastic dissipation measured for the four Oedometer tests with different yield stresses
- Figure 3-13 Granular stress field obtained from the Oedometer compression test for the stages: a) initial ($t=0$), b) intermediate ($t=500$), c) final ($t=1000$)
- Figure 3-14 Detailed views of the contact areas (a,d,g,j), the internal stress distribution (b,e,h,k) and displacement field (c,f,i,l) for single grains selected from the assembly, measured at $t=1000$
- Figure 3-15 Evolution of point stress and displacement values measured at two selected grains throughout deformation from $t=0$ to $t=1000$
- Figure 3-16 Example of a 2D triangulation problem, the input data is represented by the solid vertices and edges and the obtained triangulation is given by the hollow vertices and dashed edges
- Figure 4-1 Transmitting forces and moments between two spheres in contact: normal force (F_N), two tangential forces (F_{sx} and F_{sy}), twisting (M_T) and rolling moments (M_{RY} and M_{RX})
- Figure 4-2 (a) Seeding along three perimetrical edges of a sphere and three examples of different meshing ratios: (b) $MR=0.014$; (c) $MR=0.045$; (d) $MR=0.364$
- Figure 4-3 (a) Layout of model for normal loading, (b) effect of the meshing ratio on normal loading of an elastic sphere
- Figure 4-4 The effect of meshing ratio on the tangential response of a sphere, $F_N=5$ N
- Figure 4-5 The effect of meshing ratio on the relationship torque versus twisting angle, for an elastic sphere under $F_N=40$ N
- Figure 4-6 Rolling moment versus rotational angle under constant normal force $F_N=70$ N
- Figure 4-7 μFE results for a triaxial test on FCC packed elastic spheres: (a) stress ratio versus axial strain response; (b) comparison with Thornton's theory in terms of stress ratio versus friction coefficient

- Figure 4-8 Applied external work versus time for elastic and elastic-plastic models ($\mu=0.22$)
- Figure 4-9 (a) Comparison of the internal strain energy with recoverable strain energy for both elastic and elastic-plastic models; (b) Comparison of frictional and plastic energy dissipation ($\mu=0.22$)
- Figure 4-10 Energy dissipation by plastic yielding during a Hertzian contact cycle, Ee is the elastic energy and EP is the plastic energy (after Amini *et al.*, 2015)
- Figure 4-11 Dissipated energy index for an elastic-plastic assembly of spheres
- Figure 5-1 (a) Micrograph of contact between grains of quartz sand (reprinted from Terzaghi *et al.* 1996, with permission); (b) example of Archard 1957 model of multiple roughness scales (Meccanica, "Surface Roughness and Contact: An Apology," 36, 2001, J.A. Greenwood, © Kluwer Academic Publishers 2001, with permission of Springer)
- Figure 5-2 Schematic of setup used for image acquisition
- Figure 5-3 Flowchart of algorithms used for volume reconstruction and meshing
- Figure 5-4 Schematic of the incremental projection method used to reconstruct the 3D volume
- Figure 5-5 Reconstruction of a sphere with 500 μm diameter (a) planar projection; (b) reconstructed volume (RV) using 2 projections; (c) RV using 6 projections; (d) RV using 30 projections; (e) zoomed view of (a); (f) coarse meshed volume (CMV) of (b); (g) CMV of (c); (h) CMV of (d)
- Figure 5-6 Reconstruction of a sphere with 1000 μm diameter (a) planar projection, (b) reconstructed volume (RV) using 2 projections; (c) RV using 6 projections; (d) RV using 30 projections; (e) zoomed view of (a); (f) coarse meshed volume (CMV) of (b); (g) CMV of (c); (h) CMV of (d)
- Figure 5-7 Evolution of the ratio between real volume (V_R) and measured volume (V_M) for a sphere with (a) 500 μm diameter (b) 1000 μm diameter
- Figure 5-8 Setup for the single grain experiments
- Figure 5-9 Geometry and mesh of a sphere in contact with two rigid plates
- Figure 5-10 (a) Comparison between numerical modelling and Hertz theory for a single grain under compression; (b) internal stress distribution in a sphere
- Figure 5-11 Single grain response of glass beads from Hertz theory and experimental tests
- Figure 5-12 Four grains tested and corresponding measured diameter (d): (a) LBS1, $d=815\mu\text{m}\approx200\text{ voxel}$; (b) LBS2, $d=1064\mu\text{m}\approx226\text{ voxel}$; (c) LBS3, $d=1073\mu\text{m}\approx253\text{ voxel}$; (d) LBS4, $d=1042\mu\text{m}\approx254\text{ voxel}$

- Figure 5-13 Normal force displacement response from elastic numerical simulations and experimental tests: (a) LBS1; (b) LBS2; (c) LBS3; (d) LBS4
- Figure 5-14 Stress distribution in Grain LBS3 at different loading stages, through a vertical section: (a) displacement = 0 μm , $F_N = 0 \text{ N}$; (b) displacement = 25 μm , $F_N = 0.82 \text{ N}$; (c) displacement = 50 μm , $F_N = 0.12 \text{ N}$; (d) displacement = 75 μm , $F_N = 0.19 \text{ N}$; (e) displacement = 100 μm , $F_N = 4.07 \text{ N}$; (f) displacement = 125 μm , $F_N = 10.47 \text{ N}$
- Figure 5-15 Normal force displacement response from plastic numerical simulations and experimental tests for (a) LBS1; (b) LBS2; (c) LBS3; (d) LBS4
- Figure 5-16 Stress distribution obtained at the end of the elastic-plastic simulation for (a) LBS1; (b) LBS2; (c) LBS3; (d) LBS4
- Figure 6-1 Schematic of a sphere in contact with a plate under normal loading showing the region of interest (correct scale)
- Figure 6-2 3D views of the measured regions of interest for (a) rough surface, (b) semi-smooth surface
- Figure 6-3 Work flow used to convert the measured roughness map to a numerical mesh
- Figure 6-4 Cross section through a sphere showing the Volume of Interest (Vol)
- Figure 6-5 Comparison between theory and numerical simulations for smooth and rough contacts in terms of normal force-displacement
- Figure 6-6 Cross section of stress distribution inside the Vol for (a) rough surface at $X=30 \mu\text{m}$, (b) rough surface at $X=70 \mu\text{m}$ (c) semi-smooth surface at $X=70 \mu\text{m}$
- Figure 6-7 Tangential force-displacement obtained from (a) simulation of rough surface, (b) M&D theory
- Figure 6-8 Tangential force-displacement for a rough surface with unloading history
- Figure 6-9 Comparison between M&D theory, rough-elastic numerical simulation, and rough-elastoplastic simulation with unloading history
- Figure 6-10 Schematic representation of the root mean square slope (g) within a sampling profile
- Figure 6-11 Numerical results of a semi-smooth surface, a) contact force and contact area versus normal displacement; and contact regions (shown in grey) for values of normal displacement of b) $\delta_n=0.6 \mu\text{m}$, c) $\delta_n=1.2 \mu\text{m}$, d) $\delta_n=1.8 \mu\text{m}$, e) $\delta_n=2.4 \mu\text{m}$
- Figure 6-12 Numerical results of a rough surface, a) contact force and contact area versus normal displacement; and contact regions (shown in grey) for values of normal displacement of b) $\delta_n=0.6 \mu\text{m}$, c) $\delta_n=1.2 \mu\text{m}$, d) $\delta_n=1.8 \mu\text{m}$, e) $\delta_n=2.4 \mu\text{m}$

- Figure 6-13 Effect of g on contact area versus normal force
- Figure 7-1 Schematic illustration of the μ FE model (a) image acquisition and processing, (b) the discretization of a grain Ω_n into a collection of elements and nodes, (c) element deformation and stress field computation in finite element context, (d) interaction of grains based on Newton's second law using explicit integration
- Figure 7-2 Numerical full specimen a) at the beginning of the test and b) at 10% axial strain
- Figure 7-3 Comparison between the μ FE model and experiments, (a) stress-strain response and (b) volume-axial strains relations
- Figure 7-4 Two local views of deformation in the membrane
- Figure 7-5 Schematic showing the criterion used to identify a node belonging to an active contact
- Figure 7-6 Evolution of contact normal in: a) XY plane, b) XZ plane, c) YZ plane, for the four stages with an axial strain level of 2.5%, 5.5%, 7.5% and 9.5% and the associated number of vectors of 105744, 129431, 93160, and 69078, respectively
- Figure 7-7 The nodal force-displacement distribution at three strain increments shown in (a); (b, d, f) distribution of normal force-displacement and (c, e, g) distribution of tangential force-displacement for i1, i2 and i3, respectively
- Figure 7-8 Formation of stress chains at 9.5% strain for the 200 most stressed grains
- Figure A-1 Schematic diagram illustrating the evolution of the internal fabric of a natural sand under thermal cycling; initial fabric taken from a tomography image (μ CT)
- Figure A-2 Particle size distributions for the four materials: glass ballotini (GB), fine carbonate sand (FCS), coarse carbonate sand (CCS) and silica sand (SS)
- Figure A-3 Schematic diagram of set-up used in experiments, including details of sample and container sizes (H being the initial height of the sample and D the internal diameter of the container): (a) PMMA container; (b) aluminium container
- Figure A-4 Void ratio evolution for 20 thermal cycles for: (a) silica sand (SS); (b) fine carbonate sand (FCS), for a PMMA container (P32) and an aluminium container (A140)
- Figure A-5 Void ratio evolution for 20 cycles of a sample of glass ballotini (GB) for a PMMA container (P32) and an aluminium container (A140): (a) using the global void ratio; (b) using the global void ratio normalised by the initial void ratio

- Figure A-6 Void ratio evolution for five thermal cycles using a PMMA container (P32) for: (a) coarse carbonate sand (CCS); (b) silica sand (SS); (c) fine carbonate sand (FCS)
- Figure A-7 Schematic diagram illustrating the grain arrangement due to thermal cycling leading to a more compacted fabric (filling of large void) and formation of a new contact network: (a) contact network before thermal cycling; (b) contact network after thermal cycling
- Figure A-8 Tomographic image of coarse carbonate sand, taken before thermal cycling, showing the presence of large voids within the material
- Figure B-1 Contact area including stick and slip regions for two identical spheres subjected to torsional moment and normal loading
- Figure B-2 Non-dimensional relationship between torque and twisting angle for spherical grains
- Figure B-3 Schematic showing the inner core and cut section of the deformable sphere
- Figure B-4 Meshed sphere in contact with the rigid plate; mesh defined by smaller elements in the contact area
- Figure B-5 Comparison between theory and numerical modelling for elastic interaction of two identical elastic spheres
- Figure B-6 Stress-strain for isotropic hardening material used in the simulation
- Figure B-7 Comparison between the numerical modelling of elastic and plastic interaction of two identical spheres under torsion and constant normal loading
- Figure B-8 Comparison between the normalised twisting moments derived from numerical modelling of elastic and plastic interaction of two identical spheres under torsion and constant normal loading
- Figure B-9 Comparison between the numerical modelling of elastic and plastic interaction and Deresiewicz's solution of two identical spheres under torsion and constant normal loading
- Figure C-1 Response of the material under uniaxial loading (a) in tension and (b) in compression
- Figure C-2 Response of a spherical grain under compression for different tensile strengths
- Figure C-3 Schematic of the single grain test under normal load
- Figure C-4 Distribution of the maximum normal load applied on the glass beads of a) 1.1-1.4 mm (SD=123, Med=459), b) 2.0-2.4 mm (SD=136, Med=979), c) 3.6-4.0 mm diameter (SD=357, Med=1290); d) comparison between the typical normal force-displacement response of glass beads and Hertzian theory
- Figure C-5 Typical normal force-displacement response of silica sand
- Figure C-6 Distribution of maximum normal load applied on the grains of, a) silica sand, b) carbonate sand

ACKNOWLEDGMENTS

I would like to express my sincerest gratitude to my first supervisor Dr Joana Fonseca for her endless support throughout this research. This dissertation is the product of her encouragement, excitement and guidance.

I am deeply grateful to my second supervisor Prof Neil Taylor for his constructive criticism of this work, and for his kind advices.

I wish to thank Prof Sarah Stallebrass for her support and constructive comments along with Dr Richard Goodey for his practical knowledge.

I am very privileged to have been part of Research Centre for Multi-scale Geotechnical Engineering and thankful for the special time I had at City. I am particularly grateful to Prof John Atkinson, Dr Andrew McNamara, Dr Brett McKinley, Dr Sam Divall, Dr Neil Phillips, Dr Hitesh Halai, Dr Binh Le, Jignasha Panchal, and Greta Tangetti for discussions about the research as well as all life matters. My acknowledgments also go to the laboratory technicians, Mr Jim Hookers and Mr Melvyn Hayes, for their assistance.

I would not have been able to come to London and this thesis would not has been possible, without financial support of City, University of London through university doctoral scholarship. Once again, I would like to express my deepest gratitude to Dr Joana Fonseca who have made it possible for me to achieve my dream.

Finally, I want to thank the most deserving people in my life. My wife, Farnoosh, has been my dearest friend, partner and advisor. It is to Farnoosh that I dedicate this dissertation. I would also like to thank my parents and my sister for the support they have given me throughout my entire life and teaching me to be calm and open minded.

Sadegh Nadimi
London, 2017

DECLARATIONS

I grant powers of discretion to the University Librarian to allow this dissertation be copied in whole or in part without further reference to me. This permission covers only single copies made for study purposes, subject to normal conditions of acknowledgement.

ABSTRACT

A sample of soil under external loads shows nonlinear behaviour. These external loads are propagated through grain-to-grain contacts. Consequently, the grains are being subjected to both tensile and compressive stresses according to their shape, position, and number of contacts. Thus, the nonlinear mechanical behaviour of soil may be described by investigating inter-particle stress transmission.

The direct measurement of stress is a challenging task, both experimentally and numerically. In this study, stress-transmitting grains in a sand specimen are identified using an image-based approach. The methodology consists of measuring the geometrical data of the individual grains and following their evolution. On the numerical side, a more realistic description of soil behaviour is provided by developing a computational approach that quantifies internal stresses in each individual grain, termed micro Finite Element (μ FE) model. The fabric of a natural sand obtained from the micro computed tomography (μ CT) is virtualised to simulate the mechanical response of the material. The grain-to-grain interactions under loading are modelled in a framework of combined discrete-finite element method. Each individual grain is represented by a collection of nodes and elements and modelled as a continuum body that can deform according to a prescribed constitutive properties with appropriate friction contact conditions.

The insights that can be gained into the stress transmission mechanisms and yield initiation within the grains are shown in a case study of an intact sand subjected to 1D compression. This includes stress and displacement field, inertia tensor, and active contact area. The contact behaviour used in the model is validated against existing theories for a single sphere and an assembly of spheres under triaxial loading. Then, single grain tests are conducted experimentally and numerically in order to better understand the influence of grain morphology on stress transmission. This study shows the strong dependency of contact behaviour on grain morphology. In addition, the effect of surface roughness is investigated showing the role of asperity abrasion under low normal loading.

The evaluation of the μ FE model has yielded results that compare well to experimental data obtained from a triaxial test in a μ CT scanner. The stress field within each grain in the granular media is studied, contributing new insights beyond the commonly reported force chains. The ‘stress chain’ concept is considered as an alternative way to reflect grain breakage that may initiate on the weak force network and compromise the stability of the assembly. It is thus suggested that the ‘stress chain’ concept can be richer than ‘force chain’ and contains information about grain shape, mechanical properties and local fabric.

NOTATION

a	radius of contact area
A_{PR}	radius of contact area proposed by Pastewka & Robbins (2016)
D	depth
D_e	watershed depth
D_{max}	maximum depth of all catchment basins
d_{50}	median grain diameter
E	elastic modulus
E^*	effective contact stiffness
E_e	elastic energy
E_K	kinetic energy
E_P	plastic energy
E_t	Hardening modulus
E_u	internal energy
E_{WF}	external work
F	applied load vector
F_c	contact forces vector
F_{ext}	applied external loads vector
F_I	internal force vector
F_{int}	internal resisting forces vector
$F_{M\&D}$	tangential contact force
F_N	normal contact force
F_N^*	normal contact force with history
G	shear modulus
h	overclosure
I_{xx}	moments of inertia around x axis
I_{xy}, I_{yx}	products of inertia on xy plane
I_{xz}, I_{zx}	products of inertia on xz plane
I_{yy}	moments of inertia around y axis
I_{yz}, I_{zy}	products of inertia on yz plane
I_{zz}	moments of inertia around z axis
K	bulk modulus

l	level parameter
M	mass matrix
M_R	rolling moment
M_T	twisting moment
M	mass
N_{CA}	number of active contacts
p	pressure
Q_x	traction force in x-direction
Q_y	traction force in y-direction
R	radius of sphere
S	contact interface/area
s	seeding distance
U	internal energy per unit mass
g	root mean square slope of the surface
R	radius of sphere
T	threshold parameter
t	time
U	internal energy per unit mass
u	displacement
\dot{u}	velocity
\ddot{u}	acceleration
V	volume
V_R	volume of the object
V_M	measured volume
v	velocity field vector
x	nodal displacement vector
β	twisting angle
ΔF_N	Change in nodal normal contact forces
ΔF_T	Change in nodal tangential contact forces
ΔU	Change in displacement magnitude
δ_n	normal displacement
δ_t	tangential deflection
$\delta_{t\max}$	maximum tangential deflection

ε_x	Johnson's creep model
ε_a	Axial strain
ε_v	Volumetric strain
ν	Poisson ratio
κ	A constant for surface roughness
μ	friction coefficient
Π	virtual work
ρ	density
σ_{xy}	shear stress in xy plane along the y-axis
σ_y	yield stress
σ_{zz}	normal stress along the z-axis

ABBREVIATIONS

1D	one-dimensional
2D	two-dimensional
3D	three-dimensional
4D	four- dimensional
BV	branch vector
CCS	coarse carbonate sand
CGAL	computational geometry algorithms library
CNV	contact normal vector
DEM	discrete-element method
EI	elongation index
FCC	face-centred cubic
FCS	fine carbonate sand
FE	finite-element
GB	glass ballotini
IDM	inverse distance map
Int	intact sample
LBS	Leighton Buzzard sand
M&D	Mindlin & Deresiewicz
MR	meshing ratio
PMMA	poly (methyl methacrylate)
Rec	reconstituted sample
RMS	root mean square
S	sphericity
SS	silica sand
VV	vectorial volume
Vol	volume of interest
μ CT	micro computed tomography
μ FE	micro finite-element

PUBLISHED CONTENTS

Fonseca, J., Nadimi, S., Reyes-Aldasoro, C.C, O'Sullivan, C. & Coop, M.R. (2016). Image-based investigation into the primary fabric of stress transmitting particles in sand. *Soils & Foundations* **56**, No. 5, 818-834.

DOI: <http://dx.doi.org/10.1016/j.sandf.2016.08.007>.

Nadimi, S. & Fonseca, J. (2016). Enhancing soil sample preparation by thermal cycling. *Géotechnique* **66**, No. 11, 953-958.

DOI: <http://dx.doi.org/10.1680/jgeot.15.T.033>.

Nadimi, S. & Fonseca, J. (2017a). A micro finite element model for soil behaviour. *Géotechnique* (Published Online).

DOI: <https://doi.org/10.1680/jgeot.16.P.147>.

Nadimi, S. & Fonseca, J. (2017b). A micro finite element model for soil behaviour: numerical validation. *Géotechnique* (Published Online).

DOI: <https://doi.org/10.1680/jgeot.16.P.163>.

Nadimi, S. & Fonseca, J. (2017c). Single grain virtualisation for contact behaviour analysis on sand. *Journal of Geotechnical and Geoenvironmental Engineering* **143**, No. 9, 06017010.

DOI: [https://doi.org/10.1061/\(ASCE\)GT.1943-5606.0001740](https://doi.org/10.1061/(ASCE)GT.1943-5606.0001740).

Nadimi, S. & Fonseca, J. (2017d). On the torsional loading of elastic-plastic spheres in contact. *EPJ Web of Conferences* **140**, 05001.

DOI: <https://doi.org/10.1051/epjconf/201714005001>.

Nadimi, S. & Fonseca, J. (2017e). On the tensile strength of soil grains in Hertzian response. *EPJ Web of Conferences* **140**, 07001.

DOI: <https://doi.org/10.1051/epjconf/201714007001>.

Nadimi, S., Otsubo, M., Fonseca, J. & O'Sullivan C. (201X). Contact behaviour of particles with surface roughness. *Computers and Geotechnics* (In Preparation).

Nadimi, S., Fonseca, J. Andò, E. & Viggiani, G. (201X). A micro finite element model for soil behaviour: experimental evaluation. *Géotechnique* (In Preparation).

INTRODUCTION

1.1 Overview on Modelling of Granular Materials

During the twentieth century, modelling of granular materials gained significant attention in two scientific communities: soil mechanics and powder technology. Geotechnical engineers have been mainly concerned with predicting failure and deformation of soils, whereas interest lies in continuous flow of granular materials in powder technology (Radjai, et al., 2017).

In 1970, Prof Kenneth Roscoe indicated a route for soil mechanics research in his Rankine Lecture. He emphasised the need to better understand fundamental soil mechanics by working with “*soils in their simplest possible states*” and “*soil samples in initially uniform states*”. He stressed on the need to employ “*non-destructive (e.g. X- and γ-ray) methods of checking the uniformity of the behaviour of the soils at all stages*” and “*scanning electron microscopy methods of studying the change of soil fabric during mechanical deformation*”. Subsequently, the outcomes of these fundamental studies might be applied at different level, by developing a) “*stress-strain theories for these soils in terms of the fundamental soil parameters*”, b) “*model tests on mixed boundary value problems*”, c) “*centrifugal model test methods so that prototype problems can be studied at reduced scale*” and d) “*controlled field tests to check the theories at full-scale*”.

It can be said that he has drawn a road map which starts with studying fabric evolution and stress transmission to develop soil constitutive models. Then, the models can be used to predict boundary value problems, from small-scale to field-scale. Finally, he suggested that the opportunities and challenges in soil mechanics can be applied to any particulate materials (Roscoe, 1970). This road map was followed during subsequent decades by geo-technologists.

As computational technology and non-destructive methods advanced, the fundamental studies of soil fabric have posed plenty of challenges and attracted a great deal of attention. Our understanding of fabric evolution has significantly improved by studying the behaviour of individual particles by means of photo-

elastic experiments, micro computed tomography (μ CT) and discrete element modelling (DEM).

Despite major improvements in particulate soil mechanics, there are still fundamental challenges which need to be addressed through experimental and computational models to better understand the force-displacement relationship of particles and to use the micromechanical observations to predict soil behaviour. In particular, most of our current understanding of stress-transmission phenomena comes from DEM simulations and photo-elastic experiments using idealised grains. There is an essential need for innovative methods to assess and enhance understanding and theories based upon idealised grains for real soil across scales. This study is an attempt to meet this research gap by considering four scales: contact, grain, assembly, and representative volume element (RVE), as sketched in Fig. 1-1. In the next section of this chapter, the current knowledge on grain-scale characterisation and contact interaction are explained.

1.2 Grain-scale Characterisation

During his practical investigations, Terzaghi (1920) noted that a “*fundamental error was introduced by Coulomb, who purposely ignored the fact that sand consists of individual grains, and who dealt with the sand as if it were a homogeneous mass with certain mechanical properties*”. However, time and technology were required to start “*again from the elementary fact that the sand consists of individual grains*”. In this section, the main parameters for grain-scale characterisation are briefly described in terms of granular fabric and stress transmission.

1.2.1 Granular fabric

Been & Jefferies (1985) suggested that sand behaviour can be characterised by means of two variables: “*a state parameter which combines the influence of void ratio and stress*” and “*a fabric parameter which characterises the arrangement of the grains*”. The fabric descriptor is of geometrical nature and can be defined at different scales. An important parameter to describe fabric anisotropy is the average connectivity per grain, called coordination number (O’Sullivan, 2011).

The fabric can be defined by different descriptors such as branch vector, which join the centre of two contacting grains; contact index, the average area of contact per grains; and voids size and shape (Satake, 1982; Kuhn, 1999; Fonseca, *et al.*, 2013a).

The fabric is well defined at a mesoscopic scale, whereas grain-scale fabric is a dynamic variable in space and time (Radjai, *et al.*, 2017). An advantage of grain-scale fabric is the incorporation of force balance and kinematic compatibility (Troadec *et al.*, 2002). Granular kinematic refers to the translation and rotation of grains in an assembly of grains. The formation of micro-bands, even at early stage of deformation, can be identified by DEM simulations which show the way that a shear band will form (Kuhn, 1999). Intense rotation of grains can also mark the shear zone (Oda, *et al.*, 1982). Grain rotation and torsion play a significant role in the local kinematics. New contacts are formed as the grain move, which have short life.

1.2.2 Stress transmission

In a granular assembly, the stress is transmitted through contact forces from a grain to another grain. The nonlinear mechanical behaviour of a soil can be described by inter-particle stress transmission (Santamarina, 2001). A highly inhomogeneous distribution of stress in granular materials has been shown in photo elastic experiments and DEM simulations (Dantu, 1957; Radjai *et al.*, 1997; Thornton, 1997; Majmudar & Behringer, 2005). In a photo elastic experiment, the stress pattern can be observed due to strong contact forces between a set of particles. These particles form columnar-like structures which named force chains. In DEM simulation, the fabric evolves based on incremental propagation of contact forces, and the stress is a secondary parameter that can be calculated from contact forces. The studies of force distribution have shown that the value and distribution of strong force chains, grains carrying higher than average contact force, are not sensitive to the packing state, while weak force chains show different distribution from deformation to failure and appear to only balance system equilibrium (Antony, 2001).

1.3 Contact Behaviour

The force-displacement relationships of two contacting grains are called contact laws. A fundamental requirement of grain-scale modelling is to ensure that contact constitutive laws are representative of grain-to-grain contact in the material under investigation. A full contact interaction between two grains involves normal loading in combination with tangential, torsional and rotational loading. Experimental research has been concentrated on contact behaviour of sand to fill this gap in soil mechanics (e.g. Cole *et al.*, 2010; Cavarretta *et al.*, 2010; Senetakis *et al.*, 2013; Nardelli *et al.*, 2017). Normal force-displacement and tangential force-displacement relationships have been considered to advance current constitutive laws. Recently, the effect of surface roughness has also been taken to account (Otsubo *et al.*, 2017). It is believed that abrasion of asperities has large influence on the force-displacement relationship, in particular under low normal loading. A quantitative evaluation of contact topology and its effect on frictional properties is still an important gap in the literature concerning contact mechanics. As mentioned in the previous section, despite the role of grain rotation and torsion in local granular kinematics (e.g. Oda *et al.*, 1982), rolling and twisting moments have only been considered in few studies (e.g. Jiang *et al.*, 2005).

1.4 Aim and Objectives

Obtaining direct measurement of stress transmission in RVE of soil grains and linking them with local kinematics are challenging tasks. This study employs different methodologies with the aim of analysing stress-transmitting grains in a soil specimen. The objectives of the work are:

- To identify stress-transmitting grains in an assembly of sand using existing theoretical principles
- To develop a numerical model capable of estimating stress concentration in individual grains by coupling contact dynamics and contact topology
- To validate the proposed model based on theoretical formulation for full contact interaction including normal loading in combination with tangential, torsional and rotational loading

- To investigate the role of grain morphology and surface roughness on stress transmission
- To evaluate the proposed model by comparison with a laboratory element test and analyse stress-transmitting grains

1.5 Outline of Thesis

The thesis comprises eight chapters and three appendices.

Chapter 1 (this chapter) provides an overview on modelling of granular materials and demonstrated the need and relevance of the present work. Aim and objectives of the study are also presented.

Chapter 2 describes an algorithm for stability and load transmission of granular materials, which was developed by considering recent findings in literature, to provide new insight into the characterisation of the stress-transmitting sand grains. It investigates how grain rearrangements influence the stability of the material using geometrical data extracted from μ CT images.

Chapter 3 introduces the μ FE model in detail, including image processing, image based meshing and numerical formulations. It presents a case study of a sand assembly subjected to Oedometer compression to reveal the insights that can be gained into the stress transmission mechanisms and yield initiation within the grains.

Chapter 4 reports the numerical validation for the μ FE model. It focuses on constitutive contact behaviour in the μ FE model against existent theories, for a single sphere and an assembly of spheres. The ability of the model to simulate elastic-plastic behaviour is demonstrated.

Chapter 5 investigates the influence of grain morphology on contact behaviour of sand grains using laboratory testing and numerical modelling. It also describes a simple methodology for virtualising irregular shaped grains.

Chapter 6 explores in more detail the effect of surface roughness on grain-to-grain contact behaviour. The map of surface roughness obtained by optical interferometry is imported into the μ FE framework. The contribution of grain abrasion on normal force-displacement and tangential force-displacement is quantified numerically.

Chapter 7 evaluates the μ FE model against a triaxial compression test performed inside a μ CT scanner. After comparing the macroscopic response of the virtualised specimen with the experiment, the grain-to-grain contacts are identified and analysed based on normal contact forces. The stress field within each grain is studied, contributing new results beyond the commonly reported force chains.

Chapter 8 critically assesses the strengths and weaknesses of the work and describes the implications for future research.

Appendix A presents a technique to enhance laboratory sample preparation, by systematically increasing the density of soil sample using thermal cycling. This was motivated from differences in the nature of contacts for the intact and reconstituted soil samples observed in chapter 2. The methodology enhances the grain-to-boundary contact which is believed to affect the soil behaviour in element testing.

Appendix B focuses on a lack in literature regarding the torsional loading of elastoplastic spheres. The application of a theoretical formulations for elastoplastic spheres is verified using μ FE framework.

Appendix C describes a preliminary attempt to demonstrate the capability of μ FE framework in considering grain breakage. The role of empirical parameter introduced in literature on tensile strength of a sphere is investigated; followed by some single-grain experiments.

1.6 Contributions

It is important to note that chapters 2, 3, 4, 5 and appendices have been published in peer-reviewed journals. Chapters 6 and 7 have also been prepared in the format of a technical paper for publication. This section describes the contribution of Ph.D. candidate (SN) and co-authors on the contents.

Chapter 2 published in *Soils & Foundations*. This study used the geometrical measurements from the doctoral research of Dr Joana Fonseca (JF) with the contributions of Prof Catherine O'Sullivan and Prof Matthew Coop. SN developed the algorithm for identification of force chains and conducted the network analysis (section 4). Dr Carlos Reyes-Aldasoro contributed with the visualisation of the

spatial distribution of the force chains. JF and SN drafted the manuscript. All authors discussed the results and commented on the paper.

Chapter 3 published in *Géotechnique*. This study used the tomography data from doctoral research of JF. SN developed the contact detection algorithm, image-based meshing technique, and the numerical model. SN carried out the simulations and analysis. SN drafted the manuscript. JF reviewed and commented on the paper.

Chapter 4 published in *Géotechnique*. SN conducted the simulations and analysis, and drafted the manuscript. JF reviewed and commented on the paper.

Chapter 5 published in *J. Geotech. Geoenviron. Eng.* SN carried out the experiments and developed the virtualisation code. SN conducted the simulations and analysis, and drafted the manuscript. JF reviewed and commented on the paper.

Chapter 6 was prepared for publication in *Computers & Geotechnics*. Dr Masahide Otsubo and Prof Catherine O'Sullivan provided the interferometry data. SN developed a meshing technique based on interferometry data. SN conducted the simulations and analysis, and drafted the manuscript. The future publication may be subject to change based on co-authors' and reviewers' comments.

Chapter 7 was prepared for publication in *Géotechnique*. Dr Edward Andò and Prof Gioacchino Viggiani contributed with experimental data of *in situ* triaxial test on sand. SN segmented and meshed the tomographic data. SN conducted the simulations and analysis, and drafted the manuscript. The future publication may be subject to change based on co-authors' and reviewer's comments.

Appendix A published in *Géotechnique*. SN conducted the experiments and analysis. SN and JF drafted the manuscript.

Appendix B published in *EPJ Web of Conferences*. SN conducted the simulations and analysis, and drafted the paper. JF reviewed and commented on the paper.

Appendix C published in *EPJ Web of Conferences*. SN conducted the experiments, simulations and analysis, and drafted the paper. JF reviewed and commented on the paper.

1.7 Tables and Figures

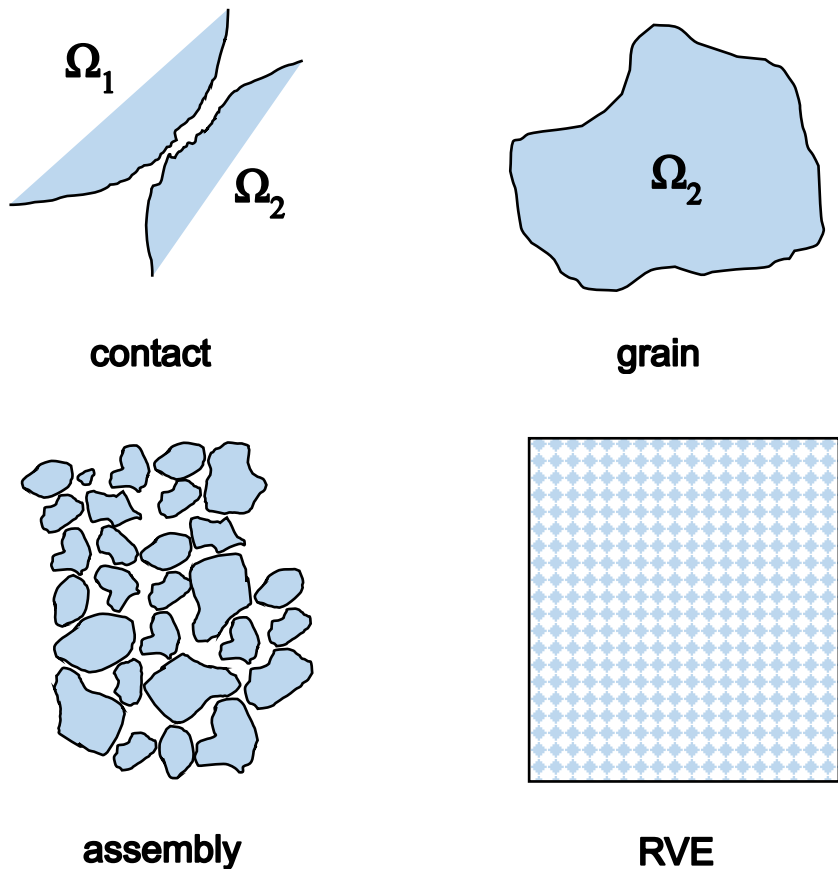


Fig. 1-1. Relevant scales for granular modelling in this study

IMAGE-BASED INVESTIGATION INTO THE PRIMARY FABRIC OF STRESS-TRANSMITTING PARTICLES IN SAND

Published in: *Soils and Foundations* 2016; 56 (5): 818–834.

2.1 Introduction

Inter-particle stress transmission is a key factor that determines the mechanical behaviour of granular materials, including soil. Recent decades have witnessed significant advances on our understanding of the physical principles that underpin stress transmission phenomena. Photo-elastic experiments and discrete element method simulations have provided evidence that stress transmission in granular materials takes place through well-defined paths termed force chains (Ostojic *et al.*, 2006; Silbert *et al.*, 2002; Tordesillas *et al.*, 2010; Zuriguel *et al.*, 2007; Radjai *et al.*, 1998). Force chains are columnar-like structures formed by the particles that carry the majority of the load in the system (Majmudar & Behringer, 2005; Lin & Tordesillas, 2014). This subset of particles often defined as those carrying above average contact forces is referred to as the strong network. Surrounding the force chains are the particles in the complementary weak network, the subset of contacts not in the strong network, which serve to provide the chains the necessary support (Tordesillas & Muthuswamy, 2009; Barreto & O'Sullivan, 2012). Under continued loading and loss of lateral support due to dilatation, these axially compressed particle columns that are the strong network become unstable and prone to buckling; this has been related to the formation of shear bands (Oda & Kazama, 1998; Rechenmacher *et al.*, 2010; Tordesillas *et al.*, 2012). Clear experimental evidence of the formation of force chains in sandstone is provided by Fonseca *et al.* (2013c); the rupture of the cement between grains during triaxial compression leads to the formation of vertical columns of horizontally unbonded grains, which tend to collapse in localised regions during the shearing progress.

Forces are transmitted only through the interparticle contacts; the non-uniformity of the size and orientation of these contacts, as well as the variation in the properties of the particles forming the contacts, lead to strong inhomogeneities in the force chains (Radjai *et al.*, 1998). Under shear, an anisotropic contact

network develops because some new contacts are formed along the major principal stress, while others are lost perpendicular to it. This was observed in experiments with sands (Oda, 1972; Fonseca *et al.*, 2013b) and DEM simulations (Rothenburg & Bathurst 1989; Thornton, 2000). Radjai *et al.* (1998) showed that since the strong network continually aligns in the direction of the most compressive principal stress, it is more anisotropic than the weak network.

Tordesillas *et al.* (2010) introduced the concept of force cycles to characterise the mutually supportive structures, analogous to structural trusses, that emerge during granular material deformation and which prevent failure (illustrated later). Tordesillas *et al.* observed that force chains tend to stabilise under 3-cycle contact triangle topologies (triangular trusses) with neighbouring grains. These 3-cycle contacts are more effective than other contact topologies in providing resistance to loading by inhibiting relative particle rotations and providing strong lateral support to force chains (e.g. Tordesillas *et al.*, 2011). The three-force cycles act to support the load and secure the stability of the force chain columns. Loss of contacts and rupture of 3-cycles leads to force chain failure due to buckling.

The characterisation of force chains is commonly achieved by discriminating between forces of different magnitudes (Ostojic *et al.*, 2006). Force chains can be visually identified by representing contact forces as lines whose thickness and/or colour indicates magnitude (Voivret *et al.*, 2009; Radjai *et al.*, 1998). The complexity and non-linearity of the force chains in 3D have been shown by identifying the paths of maximum contact force (Makse & Johnson, 2000). Peters *et al.* (2005) characterised force chains in an assembly of disks based on principles of quasi-linearity and stress concentration. Zuriguel *et al.* (2007) used a least squares estimation to fit straight lines to chains identified in photo-elastic experiments; they observed a well-defined correlation between the orientation of the chains and the angular distribution of contacts. Zuriguel *et al.* also reported on different modes of stress transmission for the case of disks when compared with the sample of elliptic cylinders. The splitting and merging of the force chain paths through granular media were investigated by Bouchaud *et al.* (2001). Hanley *et al.* (2015) used a simple link-node model to show that the peak major principle stress these force chains can resist is directly proportional to the confining stress, in line with the Mohr-Coulomb's failure criterion.

The current study makes use of x-ray micro-computed tomography (μ CT) coupled with three dimensional (3D) image analysis tools to investigate the network of stress transmission in specimens of real sand. This comprehensive study follows the preliminary work presented in Fonseca *et al.* (2014). Following the description of the material and the experimental methods, a statistical analysis of the orientation of the contact vectors, comprising both the contact normal vectors and branch vectors, is presented. Then the spatial distribution of these vectors is investigated to provide insight into the networks of stress transmitting particles.

2.2 Material and Methods

This section describes the sand used in the experiments as well as the sampling technique applied to obtain the intact specimens and the sample preparation technique of the reconstituted samples. The methodology employed here consisted of carrying out triaxial tests, impregnating the sample with resin to preserve the fabric at various stages of deformation, extracting small cores for imaging at different locations and finally analysing the 3D images in order to obtain the required information in terms of grain rearrangements and contact evolution under loading. Only the key aspects are described here; further details on the material and the experimental procedures can be found in Fonseca (2011).

2.2.1 Reigate sand

Reigate sand, the material used here, comes from a formation that is part of the Folkestone Beds (Lower Greensand) from Southeast England in the UK. In its intact state, Reigate sand is characterised by very high densities and a locked fabric; it meets the “locked sand” criteria proposed by Dusseault & Morgenstern (1979). This locked fabric enabled the use of block sampling; and thus, effectively undisturbed samples were considered in this experimental study, as discussed in more detail in Fonseca (2011). In its intact state, Reigate sand is a quartz-rich sand with a median grain diameter of approximately 300 μ m (this value decreases for the samples prepared in the laboratory, as discussed in Fonseca *et al.*, 2012). The particle morphology varies from near-spherical grains to highly non-spherical grains with embayments. The microstructural characteristics to note include the

abundance of large flat and concavo-convex contacts, in most cases forming multiple contact regions. These features are evident in the optical microscope image of the intact sand presented in Fig. 2-1. In addition, fissures within the solid grains are also commonly found in this geologically old, once deeply buried, sand. These fissures tend to open up during reconstitution of the soil, which explains the different particle size distribution between the intact and the reconstituted sand (Fonseca *et al.*, 2012).

2.2.2 Experiments

Triaxial compression tests were carried out on both intact and reconstituted samples, 38 mm in diameter and 76 mm in height, of the sand at similar densities in a dry state (Fonseca, 2011). The intact triaxial samples were obtained by carefully trimming an initial block of soil. The samples' long axis orientations corresponded to the vertical *in situ* orientation. The reconstituted samples were created using sand taken from the trimmings of the intact samples. Each sample was isotropically compressed to 300 kPa at a rate of 50 kPa/hour and then subjected to strain controlled compressive shearing at a rate of 1%/hour. The specimens were observed to fail along well-defined shear planes with inclinations of 63° and 57° (from horizontal) for the intact and reconstituted soil, respectively. The reconstituted samples show, together with the more gentle orientation, a thicker shear plane of approximately $11xd_{50}$, compared to the $7xd_{50}$ of the intact soil. Marked differences were observed between the mechanical behaviours of the intact and reconstituted samples, as shown in Fig. 2-2. The intact soil showed a significantly higher peak strength than the reconstituted soil, and a correspondingly greater degree of strain-softening. The greater peak stress ratio, stiffness and rate of dilation exhibited by the intact material, when compared to the reconstituted soil, have been well documented (e.g. Cresswell & Powrie, 2004); the grain-scale phenomena underlying these behaviours, however, remain poorly understood.

In order to investigate the internal fabric of the soil and the mechanism of deformation at the grain-scale, the tests were stopped at different stages of loading and the samples were impregnated with resin while in the cell. A low viscosity resin was used to avoid soil disturbance. Details of the samples considered here are summarised in Table 2-1 for the initial stage prior to loading

(Stage 0) and in Table 2-2 for the two post-peak load stages (Stages 3 and 4). The data in Table 2-1 include intact samples (sample reference ‘Int’) and reconstituted samples (sample reference ‘Rec’). The axial strain (ϵ_a), the stress level (given by the ratio between deviator stress and mean stress, q/p') and the specific volume (v) for the relevant loading stages are provided in Table 2-2. A loss in the initial homogeneity of the samples is seen following the formation of the shear band. The fabric evolution outside and inside the shear band are to be differentiated. The samples are denoted as ‘including shear band’, since the small thickness of the shear plane means that the samples are not likely to be exclusively within the shear band region.

2.2.3 3D image process

Small cores (5 mm diameter) were extracted from regions containing the shear band and from the bulk of the impregnated triaxial samples. The cores were imaged using μ CT in the nanotom (phoenix|x-ray, GE). μ CT is a high resolution imaging technique that enables the internal structure of soil to be investigated (e.g. Oda *et al.*, 2004). The obtained 3D images are maps of x-ray attenuation based on composition and density of the material. Therefore, each voxel (3D pixel) in the image has an intensity value, or colour, associated with the material it represents. The voxel size of the images was 5 μm , *i.e.* approximately $0.016 \times d_{50}$, where d_{50} is the median particle diameter. The images were segmented in order to identify the individual grains, and each particle-phase voxel was assigned an integer identification number (π) to associate it to a specific grain. Contacts between two given particles were identified along the boundaries by considering the voxel π number. For two particles in contact, with intensity values p_1 and p_2 , the particle p_1 voxels were classified as contact voxels if they connected to a voxel of value p_2 , where $p_2 \neq p_1$ and $p_2 \neq 0$ (as the void space has intensity 0). The voxel contact classification used in this study was based on a 6-connectivity voxel neighbourhood relation, and required a total of six orthogonal ‘passes’ through the data along the x, y and z directions (Fonseca, 2011).

2.3 Statistical Analysis of the Contact Vectors

The vectors considered for this analysis were the contact normal vector orientation (CNV) and the branch vector (BV), as illustrated in Fig. 2-3. The vector defining the contact normal was obtained by applying a least squares regression to identify a best-fit plane for each surface defining the contact and this plane defined the contact normal orientation. The branch vector is defined as the vector connecting the centroids of two particles in contact. In spheres BV and CNV are coincident, however, the irregular shape of the grains in real sand imparts significant differences in orientation.

2.3.1 Angular histograms analysis

A convenient way of visualising the orientation distribution of large datasets of vectors is to use planar rose diagrams. These angular histograms show the distribution of the orientations of the 3D vectors projected onto a specific plane. In the cases presented here, the vertical plane was chosen and the angle was measured from the horizontal plane. The contact vectors have an orientation, but not a direction, and the force at each contact will act equally on the two contacting particles, but in opposite directions. In other words, a vector with an angle of 30° has the same orientation as a vector with an angle of 210°; thus, only half of the plane is considered. An extra feature of rose diagrams is the possibility of shading each bin by a scalar parameter whose normal orientations lie within that bin, e.g. average area of the contacts, the particle diameter or the particle aspect ratio.

For the intact samples prior to loading, these vectors show a near isotropic distribution, as illustrated in Fig. 2-4a and 2-4b for the CNV and BV, respectively, with the shading indicating contact area in both cases (contact area presented in voxels which have side length 5 µm). The slight bias along the horizontal and vertical directions is related to the use of a 6-connectivity relation for the contact detection, which favours the normal directions to the voxel faces, in other words, the vertical and horizontal directions. It is likely that using a 16-connectivity in the contact detection phase would avoid this bias and should therefore be considered in future studies. For the reconstituted samples, the distribution is less isotropic with a slight increase in the number of contact normal vectors oriented along the horizontal plane, as shown in Figs 2-4c and 2-4d. It is interesting to note that

contacts with larger areas (darker bins) tend to have more horizontal orientations; this holds true for both CNV and BV for the reconstituted sample and for the CNV of the intact samples. This trend is not observed for the BV of the intact samples.

It is important to emphasise the differences in the nature of the contacts for the intact and reconstituted soil samples. Due to the locked nature of the intact soil, the contacts comprise extended surfaces formed though the geological history of the soil, with measured average areas as high as 450 voxels (values shown in the colour bar); this is further discussed in Fonseca *et al.* (2013a). The contacts of the reconstituted material were formed during the tamping and vibration used to produce dense samples in the laboratory and the associated surface areas are significantly smaller than those observed in the intact samples with measured average values lower than 200 voxels. The number of contacts is also greater for the intact samples as indicated by the number of vectors per bin in the angular histograms, *i.e.* approximately 2800 per bin when compared to the 1500 per bin for the reconstituted sample (note that different scales are used to provide better details of the data). For the same sand, there are more contact normal vectors than branch vectors since two grains in contact can have multiple contact surfaces which results from the irregular shape of the grains. This difference is more pronounced for the intact samples (an investigation to enhance laboratory sample preparation is presented in Appendix A).

As shearing progresses, there is a clear reorientation of the contact normal vectors towards the direction of the major principal stress. This trend was observed for both intact and reconstituted samples at load stages 3 and 4 outside the shear band and it is demonstrated here for sample Int3 in Fig. 2-5a. The reorientation of these vectors along the vertical direction supports previous observations from photoelastic tests and DEM analyses on the formation of columns of grains creating chains of transmitted stress. This realignment is more obvious for the CNV; however, there a subtle realignment of the BV is evident in Fig. 2-5b. Both Figs 2-5a and 2-5b show that vertically oriented vectors are predominantly associated with larger contacts (darker bins), for both CNV and BV. Fig. 2-5c shows that, for the samples including the shear band, the predominant direction of the contact normal, for the reconstituted samples, deviates from the vertical direction. This finding is in agreement with the rotation and bending of the buckling force chains within the shear band (*e.g.* Oda &

Kazama, 1998; Iwashita & Oda (1998), and this bias is predominantly represented by the large area contacts. This deviation is in agreement with previous studies that showed the buckling of force chains inside the shear band. For these samples, the branch vectors with large contact areas are also more vertically oriented; however, these vectors do not represent the most dominant orientation (Fig. 2-5d).

The samples containing the shear band at load stage 4, presented in Fig. 2-6, show similar trends to those observed at load stage 3. The CNV distribution for the intact samples again shows a dominant vertical orientation, and the effect of the buckling of the force chains is reflected in the slight asymmetric distribution shown in Fig. 2-6a. For the reconstituted sample, the distribution of the CNV vectors presented in Fig. 2-6c exhibits a more marked bias. The contacts with larger surface areas tend to be orientated in the direction of the shear band; this is also observed for the intact samples (Fig. 2-6a). The distributions of the branch vectors shown in Figs 2-6b and 2-6d exhibit a less clear bias in the realignment of the vectors, but the influence of the buckling of force chains is reflected in the more asymmetric distribution when compared with the samples from outside the shear band, as shown in Figs 2-4b, 2-4d and 2-5b. An important observation from the rose diagrams in Fig. 2-6 is the marked difference in the orientation of the contact normal and branch vectors. This is because the BV for a given contact depends on the shape and relative position of the particles in contact rather than simply the orientation of the contact itself. These observations provide evidence of the better suitability of contact normal data to describe microscale changes when compared to the branch vector data when non-spherical particles are used.

2.3.2 Fabric tensor analysis

A second order fabric tensor was used to investigate the preferred orientation of the dataset of CNV and BV vectors and their associated intensity. Following Satake (1982), the tensor was calculated as

$$\Phi_{ij} = \frac{1}{N} \sum_{k=1}^N n_i^k n_j^k \quad \text{Eq. 2-1}$$

where N = the total number of vectors in the system and n_i^k = the unit orientation vector along direction i .

Fabric tensors were calculated for the contact normal vectors (Φ_{ij}^{CNV}) and for the branch vectors (Φ_{ij}^{BV}). The dominant orientation of the dataset was quantified by angle β given by the inclination of the major principal eigenvector relative to the horizontal plane. The anisotropy of the specimen at each load stage was quantified by considering the difference between the maximum and minimum eigenvalues of the fabric tensor, *i.e.*, $\Phi_1 - \Phi_3$. An isotropic system will have $\Phi_1 - \Phi_3 = 0$, and an increase in the bias of the vector distribution will cause an increase in the anisotropy.

The results for the contact normal and branch vector data are presented in Table 2-3 together with the number of vectors used. The CNV data show much higher anisotropy values when compared to the BV data; these results are in accordance with the stronger alignment of the vectors observed in the rose diagrams. This trend is slightly more pronounced for the samples outside the shear band. The evolution of the orientation parameter β^{CNV} is compared with the macro response given by the stress-strain curves of both the intact and reconstituted soil, as seen in Fig. 2-7, for the CNV data. The samples outside the shear band, both intact and reconstituted, show β^{CNV} values greater than 80° , *i.e.*, a deviation from the vertical of less than 10° . For the samples containing the shear band (data points marked with circles), β^{CNV} takes slightly lower values, between $60-80^\circ$. This is in agreement with what was observed in the rose diagrams in Fig. 2-4. Similar to the steady state reached by the deviatoric stress at stages 3 and 4, β^{CNV} appears to reach relatively stable values for the regions inside and outside the shear band, although the limited data prevents more conclusive observations. For the branch vector data, the distribution of the vectors is more isotropic with no clear dominant orientation, as shown by the rose diagrams. Therefore, the physical meaning of β^{CNV} is less significant.

2.3.3 Contact normal and branch vector relationship

DEM simulations typically use ideal circular or spherical particle geometries for which the contact vectors and the branch vectors are collinear. For real soils, however, they are unlikely to be collinear as the schematic in Fig. 2-3 shows. In this study, the relationship between the contact normal and the branch vector orientations was investigated by considering the angle between the vectors, *i.e.*, α as defined in Fig. 2-3. To investigate the relationship between α and grain characteristics, in terms of their morphology and the way they form contacts, the distribution of α is presented using rose diagrams shaded by elongation index (EI), the sphericity (S) and the contact area (CA). The elongation index (EI) is defined as

$$EI = b/a \quad \text{Eq. 2-2}$$

where a = the length of the major principal axis and b = the length of the intermediate principal axis, obtained by applying Principal Component analysis to the cloud of voxels defining each individual grain, as described in Fonseca *et al.* (2012). The sphericity (S) was calculated by

$$S = \frac{\sqrt[3]{36\pi V_p^2}}{SA} \quad \text{Eq. 2-3}$$

where V_p = particle volume; SA = surface area of the particle (both obtained from the image data). Both EI and S take values between 0 and 1 and, since each contact is formed by two grains, the indices used here correspond to the grain with the larger volume. The contact area parameter is measured in voxels.

Fig. 2-8 includes the α data obtained at loading stage 3 for the intact sample outside the shear band and the intact and reconstituted samples including the shear band. For all the samples, angle α varied between 0 and 60° with the most frequent value being about 20°. Referring to Figs 2-8a, 2-8d and 2-8g, it can be

observed that as the geometry deviates from a regular shape, and the elongation index takes lower values (darker bins), α increases, *i.e.*, the elongated grains in contact are more likely to lead to a greater difference between the CNV and the BV vectors. Angle α is also sensitive to the sphericity of the contacting grains, as depicted in Figs 2-8b, 2-8e and 2-8h. For sphericity values closer to 1, *i.e.*, grain shapes close to a spheres, α takes values closer to 0 as would be expected. A clear trend is also found for the contact area (CA measured in voxels) with α increasing as the contact area decreases, as seen in Figs 2-8c, 2-8f and 2-8i. These observations suggest that grains with extended contact surfaces are more likely to show a better approximation between the orientation of the BV and CNV vectors.

2.4 Networks of Stress-transmitting Particles

2.4.1 Methodology

Networks of contacts and contact forces have received considerable attention in recent literature (*e.g.* Tordesillas *et al.*, 2015; Hanley *et al.*, 2014; Lin & Tordesillas, 2014; Ardanza-Trevijano *et al.*, 2014; Newman, 2003). In the absence of force measurements, this study makes use of geometrical considerations to generate the strong network of stress-transmitting particles. The information extracted from the tomographic data is used to construct the contact network. Similar to the above studies, this contact network is represented by a collection of nodes and links, with the nodes representing the grains and the connecting links representing the contacts between the grains.

As shown previously, in order to support the increasing axial load, particles tend to organise in columnar structures transmitting the stress along the direction of the major principal stress. This is better captured by the contact normal vectors. Thus, we use the orientation of the contact normal vectors, and the graphical representation of the network is obtained by connecting the centroids of the grains in contact. The potential force chains and the associated grains are identified here using the following conditions:

- i) *the stability criterion:* the grain participates in at least one 3-cycle contact triangle that provides lateral support to the chain and inhibits rotations; this criterion infers stability.

- ii) *the load transmission criterion:* the contact normals forming each 3-cycle are approximately parallel to the major principal stress (near-to-vertical); in other words, the grain participates in a quasi-linear cluster of three or more grains.

Further details on each criterion are given below. This methodology was applied to the intact samples at load stage 3 both from outside and including the shear band, Int3 and Int3S, respectively.

i) Stability criterion

Following Tordesillas *et al.* (2010), 3-cycle clusters are clusters of three grains in mutual contact. These particles were filtered from the initial contact network using a MATLAB (Mathworks, 2013) script that identifies whether or not a given grain is in contact with two other grains, which in turn also form a contact between them. Fig. 2-9a shows a 2D schematic of the truss abstraction overlaid on a particle assembly; the nodes are at the particle centroids. Note that the analysis was done in 3D but for ease of visualisation, a 2D section is presented here. The 3-cycle contact triangle topologies, identified for the entire sample, form the truss network. Fig. 2-9b shows a section through the 3D truss where only the grains forming at least one 3-cycle contact triangle are accounted for. For ease of visualization, the network is presented for a section with a thickness of 60 voxels corresponding to 300 μm (approximately the soil median grain diameter). Fig. 2-10 compares similar sections through the truss network for the sample outside the shear band (Fig. 2-10a) and the sample containing the shear band (Fig. 2-10b). It can be clearly seen that the effect of the shear band contributes to the exclusion of a larger number of grains which do not participate in any 3-cycle contact from the truss network. Table 2-4 summarises the number of grains comprising each network. For sample Int3, outside the shear band, 95% of the grains forming the contact network satisfy the stability criterion. For the sample including the shear band, the stability criterion is satisfied by 87% of the grains in the contact network. This reduction in the number of grains satisfying the criterion is assumed to be associated with the loss of stability of the columnar structures in the shear band.

ii) Load transmission criterion

A second MATLAB script was developed to identify the grains satisfying the load transmission criterion. In a first pass, the code identifies from each of the 3 contacts composing the cycle, those for which the contact normal vector is near vertical. The acceptable deviation angle from the vertical direction was assumed to be 35° (in spherical coordinates) to account for a degree of curvature in the force chains. The identification numbers (pi) of the grains forming the contacts that passed the near-to-vertical selection were stored and used to investigate whether or not they form a quasi-linear cluster of at least three grains. A given grain ' pi ' will satisfy this condition if it forms a contact with a grain ' pj ' and a grain ' pk ' located below and above the grain's centroid, respectively (Fig. 2-9). As shown in Table 2-4, only 54% of the grains mutually satisfy the load transmission and stability criteria for the sample outside the shear band. For the sample including the shear band, this value is lower, *i.e.*, only 39% of the grains originally forming the contact network form the force chains orientated in the direction of the major principal stress. The bending and rotation of the force chains within the shear band, suggested in previous studies, supports the markedly reduction in the number of vertical columns measured here for the sample containing the shear band.

2.4.2 Load-bearing particles forming the force chains

The grains that were identified to satisfy both the stability and the load transmission criteria are assumed to belong to a force chain. The methodology employed to obtain these load bearing grains is summarised in the flowchart presented in Fig. 2-11. Fig. 2-11a shows the 3D tomographic image acquired and post-processed as detailed in the '3D imaging process' Section. The outcomes of the image analysis procedure include the coordinates (x,y,z) of the grains' centroids and contact normal vectors of the grains in contact. This information was used to draw the contact network formed of lines connecting the centroids of the grains in contact, as displayed in Fig. 2-11b for the entire sample. The truss network illustrated in Fig. 2-11c is represented by segments connecting the centroid of only the grains in contact with at least two other grains, *i.e.*, taking part in a 3-cycle triangle contact topology. Finally, the load bearing grains forming force chains are displayed in Fig. 2-11d by lines joining centroids of contacting

grains that are in truss network where the contacts meet the load stability criterion. Note the significant difference between the initial contact network formed by 2,574 grains and the load bearing network formed by 1,392 grains for the sample outside the shear band as shown in Table 2-4. For the sample including the shear band, only 754 grains out of 1912 initially forming the contact network, are found to compose the force chains. This is an expected result since the stable and quasi-vertical columnar structures of grains tend to decrease in number as deformation inside the shear band progresses.

2.4.3 Quantitative description of the load-bearing particles

Particles in the force chains are primary load bearers that take an active role in the transmission of stress. While the particle-scale mechanisms of stress transmission underpin the macro-response of the material, the characteristics of the grains forming the force chains and the nature of their contact topologies remain largely unknown.

The orientation of a particle can be described by the orientation of its major axis (Fonseca *et al.*, 2013b; Paniagua *et al.*, 2015). Fonseca *et al.* (2013b) considered the same triaxial samples investigated here and showed that for the intact material the grains are preferentially orientated in their most stable positions; that is, their minor principal axes are approximately vertical. Triaxial compression causes a readjustment of the orientations; as the load increases, the material dilates and causes grain breakage along the initial existing fissures. Since the newly-detached grains are randomly oriented, the result is an approximately isotropic distribution, as presented in the rose diagram of the particle's major axis depicted in Fig. 2-12a. When only the grains forming the force chains are used, the rose plot exhibits a higher concentration along the horizontal plane which indicates that the bearing grains tend be in stable positions (Fig. 2-12b). The angular histogram of the grains forming the truss network does not show significant differences when compared with the contact network (shown in Fig. 2-12a), and therefore, is not presented. For the sample containing the shear band, the distribution is affected by the appearance of the shear band, and thus, the interpretation is less straightforward, as discussed in Fonseca *et al.* (2013b). However, there is a more pronounced bias towards near-horizontal directions for particles in the force chains (Fig. 2-13b) when compared with the contact network

as a whole (Fig. 2-13a). For both Figs 2-12 and 2-13, no clear correlation can be found between particle orientation and particle elongation ratio (Eq. 2-2), the latter given by the shading of the bins. The particle size distribution for the three networks, given by the length of the intermediate axis of the grains, is presented in Fig. 2-14. These data suggest that force chains tend to be formed by the larger grains and this trend is more pronounced for the sample containing the shear band (Fig. 2-14b) when compared to the data from outside shear band (Fig. 2-14a). Previous numerical studies also reported that strong force chains pass preferentially through larger grains with a significant number of small grains being excluded from the force network (Voivret *et al.*, 2009).

The coordination number (CN) distribution presented in Fig. 2-15 shows that through the selection process to isolate those grains forming the force chains, the CN value tends to increase, which suggests that the load bearing grains have higher number of contacts. The median CN values for each network are provided to guide the comparison. The difference in CN between truss network and the force chains is greater for the sample including the shear band when compared to the grains outside the shear band, as can be observed when comparing Figs 2-15a and 2-15b. The plot of CN against the number of triangular trusses formed in both the truss and the force chain networks presented in Fig. 2-16 suggests that although higher CN values are associated with grains forming large number of trusses, high CN values alone may not be a suitable indicator of stability. There are particles with CNs as high as 8 that do not participate in any truss structure. Particles forming force chains tend to have CN values between 4 and 16.

The evolution of the contact surface area for the three networks is presented in Figs 2-17a and 2-17b for the samples outside the shear band and containing the shear band, respectively. Similarly, with the trend observed for the particle diameter and CN, a shift of the curves towards larger contact areas from the contact network to the force chains, is observed here. Despite the small evolution, the trend is consistent and is in agreement with the realignment of the contacts with larger surfaces observed in Figs 2-5 and 2-6.

2.4.4 Spatial distribution of the force chains

Fig. 2-18a shows the spatial distribution of the chains through a selected section of 60 voxels thickness. Although the force chains were identified for a minimum of 3 particles in a quasi-linear form, these chains are connected to additional force chains as can be seen by expanding in the three dimensional space to a thickness of 300 voxels in Fig. 2-18b. Three-dimensional visualization of the spatial distribution of force chains is not trivial; however it can be observed that there are some gaps in the network. As suggested in Ghedia & O'Sullivan (2012), it is believed that in the gap between two dominant force chains, there is a network of weaker force chains transmitting smaller contact forces, which contribute to stabilising the strong force chains.

A methodology based on image-processing tools, to enable visualisation of the spatial distribution of the force chains, is used following Fonseca *et al.* (2014). Here, this previous work was improved by considering the contact normal vectors in lieu of the branch vectors. As a starting point, the method uses the truss network so that the stability criterion is satisfied. The second condition is to select only the near-to-vertical contact normal vectors, *i.e.*, using an angle of 35° (in spherical coordinates) to satisfy the load transmission criterion, as previously described. The vectors that satisfy both conditions were allocated into a 3D space of the same dimension as the original image of the sample (*i.e.*, cube of 600 voxels) which we call the vectorial volume (VV). While the orientation and the contact surface areas correspond to the contact normal the vectors are displayed by connecting the centroids of the grains in contact. Fig. 2-19a shows the maximum intensity projections of the VV (calculated for a volume of 50 voxels thickness). The colour of the line joining the particle centroids indicates the contact area (larger contacts are represented by a brighter colour). These projections were filtered using a low pass filter (Reyes-Aldasoro, 2015) in order to enhance the selection of the contacts with a greater intensity (brighter colour) that are, therefore, more likely to belong to the main network of contacts, shown in Fig. 2-19b. This was followed by the application of a watershed transform (Reyes-Aldasoro, 2015) to discard shorter and unconnected lines. The resulting network of the stress-transmitting grains is shown in Fig. 2-19c for the sample Int3 (outside the shear band). The same procedure was applied to the data for sample Int3S, including the shear band, is illustrated in Figs 2-20a, 2-20b and 2-

20c. We hypothesise that these quasi-vertical columnar structures are closely correlated to the networks of stress-transmitting particles. The distribution of the force chains was quantified by measuring the density value of the columns. The values measured for a planar section of 60^2 voxels (approximately d_{50} length) were of 1.2 for the sample outside and 0.4 for the sample containing the shear band. The lower value of 0.4 can be seen as an indication of the buckling of the columnar structures caused by the movement of the shear band and the consequent decrease in the number of near vertical force chains.

2.5 Conclusions

μ CT data on specimens of sand enables the investigation of the stress-transmission phenomena that account for the effect of the grain morphology and contact topology. The observed realignment of the contact normals in the direction of the major principal stress is seen to be linked to the formation of contacts with larger surface areas. The effect of the shear band formation and the associated bending or buckling of these columns has been demonstrated by a greater deviation of the predominant direction of the contact normal vectors from the vertical plane. These observations hold true for both intact and reconstituted samples. The two parameters extracted from the fabric tensor of the contact normal vectors, the anisotropy and major eigenvector, were shown to be able to quantitatively describe the subsequent changes in the topology of the stress transmission mechanisms during triaxial compression. However, the near-vertical realignment of the branch vectors in the post-peak regime and the bending in the shear plane were less obvious. The difference between contact normal and branch vectors was found to increase with the deviation from the spherical shape and with the decrease of the contact surface. Using the conditions of quasi-vertical contact normal vectors and 3-cycle contact, have enabled the identification and quantitative characterisation of the load bearing grains. It is suggested here that these grains tend to be oriented in most stable positions, with the major axis along the horizontal plane, and have on average higher number of contacts. The contribution of the larger surface contacts to the stability of columnar structures of grains was taken into account to develop a method able to provide the spatial distribution of the vectors defining the force chains. The kinematics of shear band formation caused a decrease in the number

of near vertical columnar structures when compared to material outside the shear band, which confirms earlier 2D physical and numerical model observations of force chain orientations in shear bands. This study presents a new understanding on the primary fabric of stress transmitting particles and highlights the effect on the kinematical phenomena of the rich topology found in real sand.

2.6 Tables and Figures

Table 2-1. Specific volume (v) of the intact and reconstituted samples prior to loading

Sample ref.	v	Obs.
Int0	1.48	Intact sample prior to loading
Rec0	1.50	Reconstituted sample prior to loading

Table 2-2. Summary of the intact and reconstituted samples investigated in the post-peak regime (ϵ_a =axial strain, q/p' =deviator stress/mean stress, v =specific volume)

Sample ref.	Load stage details			Sample location
	ϵ_a (%)	q/p'	v	
Int3	3.89	1.73	1.63	Outside shear band
Int3S	3.89	1.73	1.63	Including shear band
Int4	7.94	1.38	1.67	Outside shear band
Int4S	7.94	1.38	1.67	Including shear band
Rec3	9.66	1.46	1.87	Outside shear band
Rec3S	9.66	1.46	1.87	Including shear band
Rec4S	12.35	1.46	1.70	Including shear band

Table 2-3. Results on the fabric tensor data for the contact normal (CNV) and branch vector (BV)

Sample ref.	No. vectors	Fabric tensor parameters			
		$(\phi_1 - \phi_3)^{CNV}$	β^{CNV}	$(\phi_1 - \phi_3)^{BV}$	β^{BV}
Int3	20096	0.088	82	0.061	84
Int3S	12906	0.142	72	0.027	64
Int4	12200	0.081	89	0.052	87
Int4S	24192	0.102	75	0.028	14
Rec3	19674	0.125	86	0.034	23
Rec3S	18924	0.143	76	0.022	63
Rec4S	17630	0.095	68	0.030	21

Table 2-4. Number particles in the different networks with the correspondent percentage of grains satisfying the stability criterion from contact to truss network and the stability plus load transission criteria from contact network to force chains

Sample ref.	Contact network	Truss network	Force chains
Int3	2,574	2,439 ($\approx 95\%$ Cont. Net.)	1392 ($\approx 54\%$ Cont. Net.)
Int3S	1,912	1,666 ($\approx 87\%$ Cont. Net.)	754 ($\approx 39\%$ Cont. Net.)

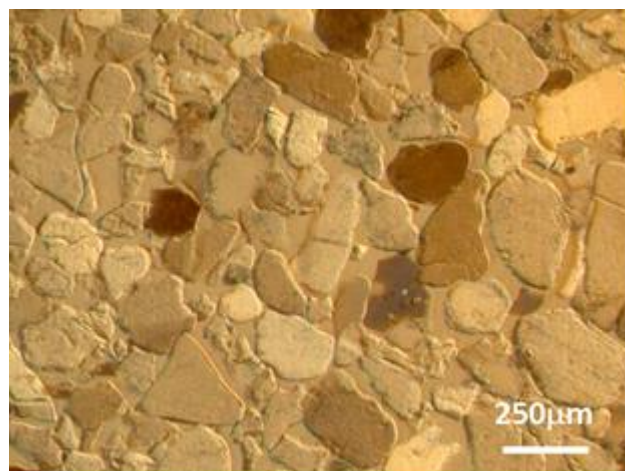


Fig. 2-1. Microscope image of a thin section of Reigate sand under polarised light

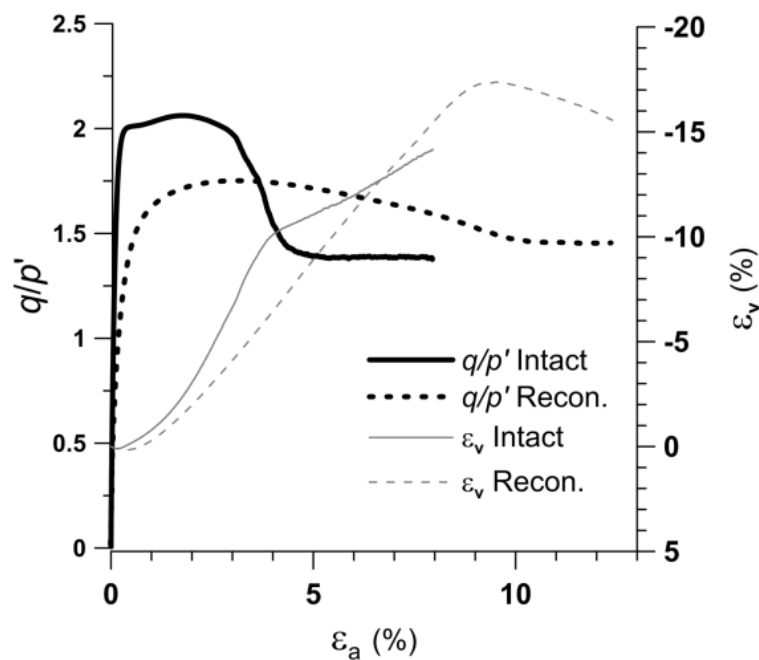


Fig. 2-2. Mechanical and volumetric response for the intact and reconstituted samples

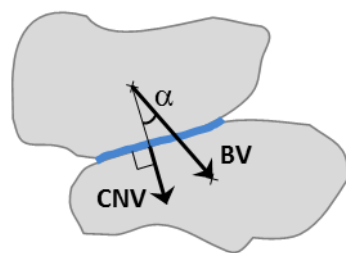


Fig. 2-3. Schematic diagram illustrating the contact normal (CNV) and branch vector (BV)

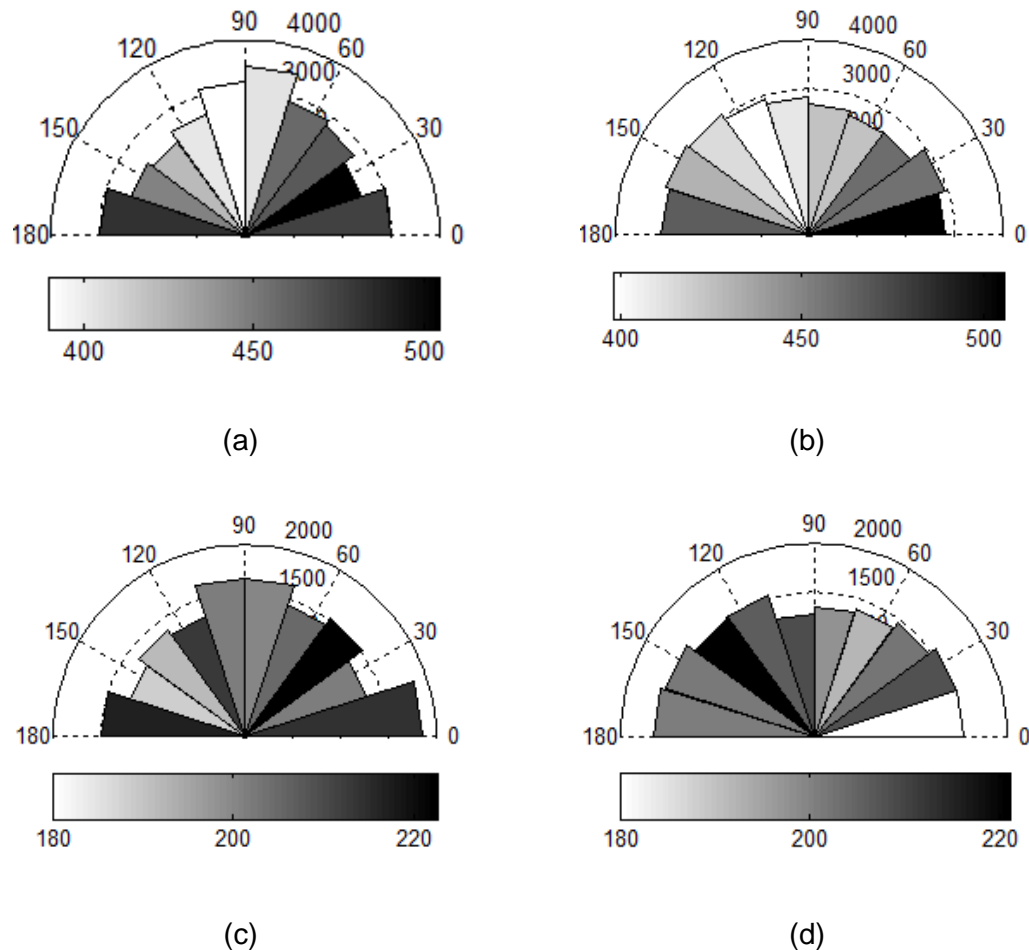


Fig. 2-4. Rose diagrams for the intact and reconstituted specimens prior to loading (shading indicates average contact area in voxels); (a) CNV Int0; (b) BV Int0; (c) CNV Rec0; (d) BV Rec0

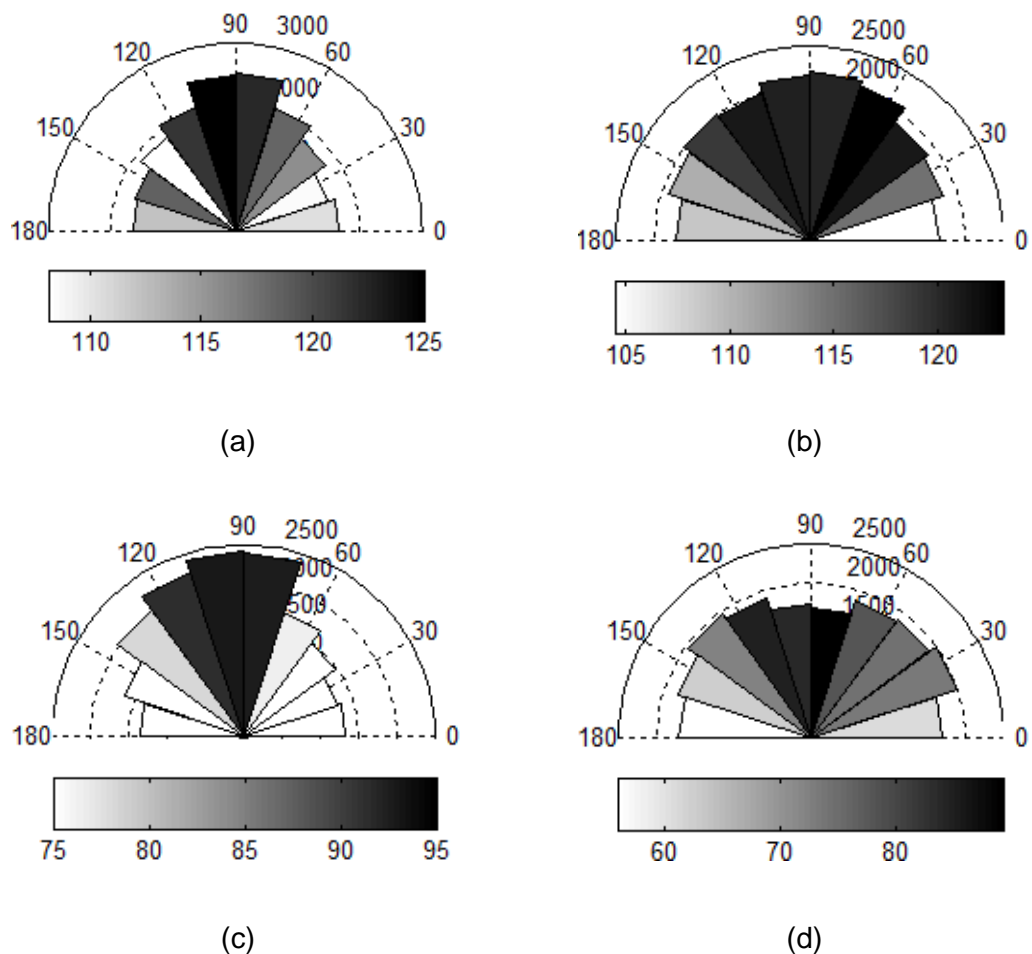


Fig. 2-5. Rose diagrams for the specimens at load stage 3 (shading indicates average contact area in voxel); (a) CNV Int3; (b) BV Int3; (c) CNV Rec3S; (d) BV Rec3S

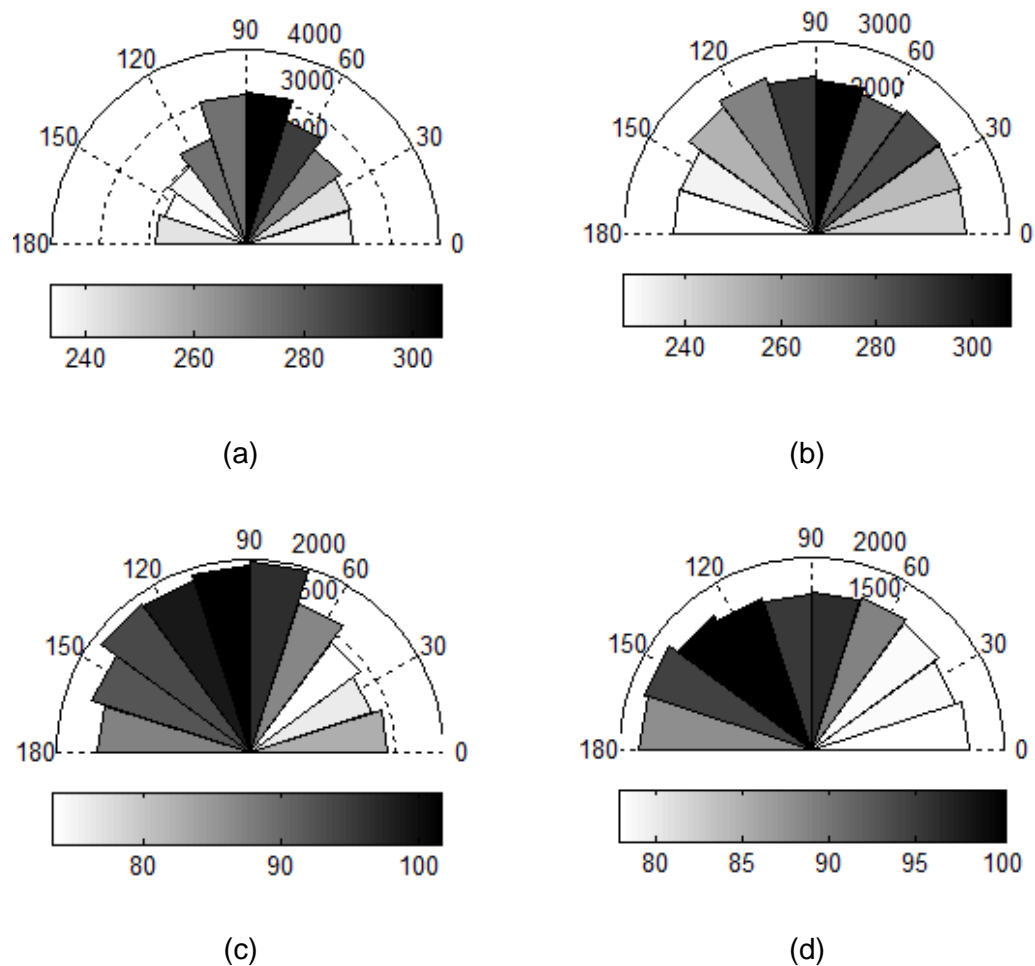


Fig. 2-6. Rose diagrams for the specimens at load stage 4 (shading indicates average contact area in voxel); (a) CNV Int4S; (b) BV Int4S; (c) CNV Rec4S; (d) BV Rec4S

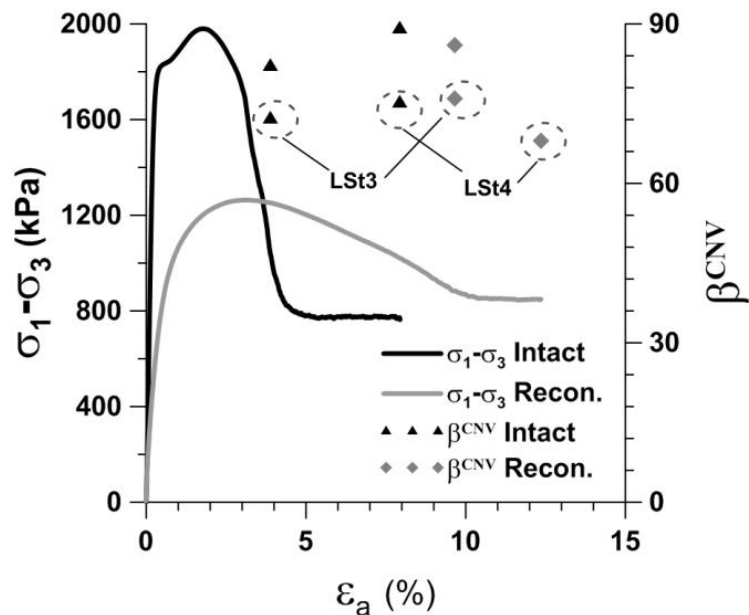


Fig. 2-7. Evolution of the major principal fabric orientation for contact normal for load stages (LSt) 3 and 4, the data for the samples containing the shear band are marked with circles

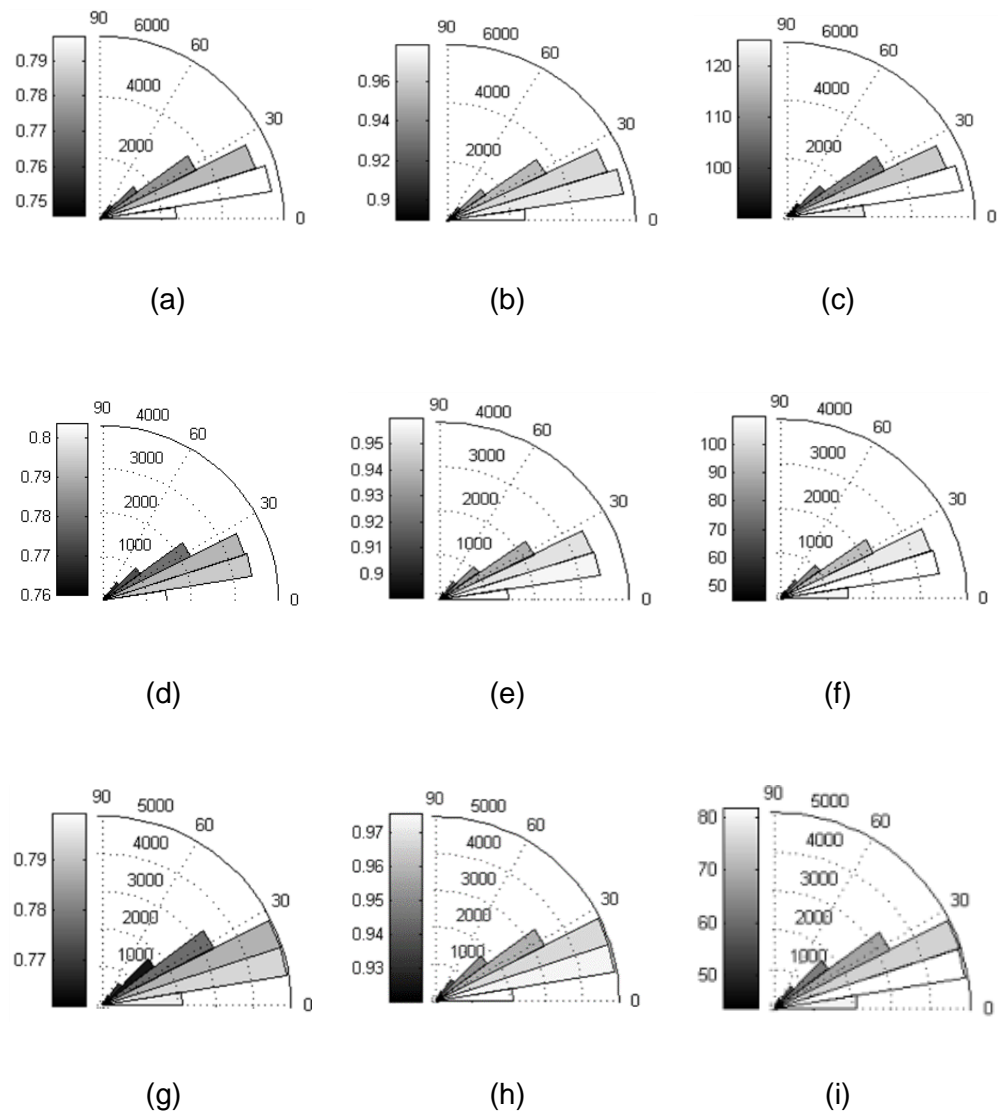


Fig. 2-8. Distribution of angle α for the specimens: (a) Int3 shaded by EI; (b) Int3 shaded by S; (c) Int3 shaded by CA; (d) Int3S shaded by EI; (e) Int3S shaded by S (f) Int3S shaded by CA; (g) Rec3 shaded by EI; (h) Rec3 shaded by S; (i) Rec3 shaded by CA

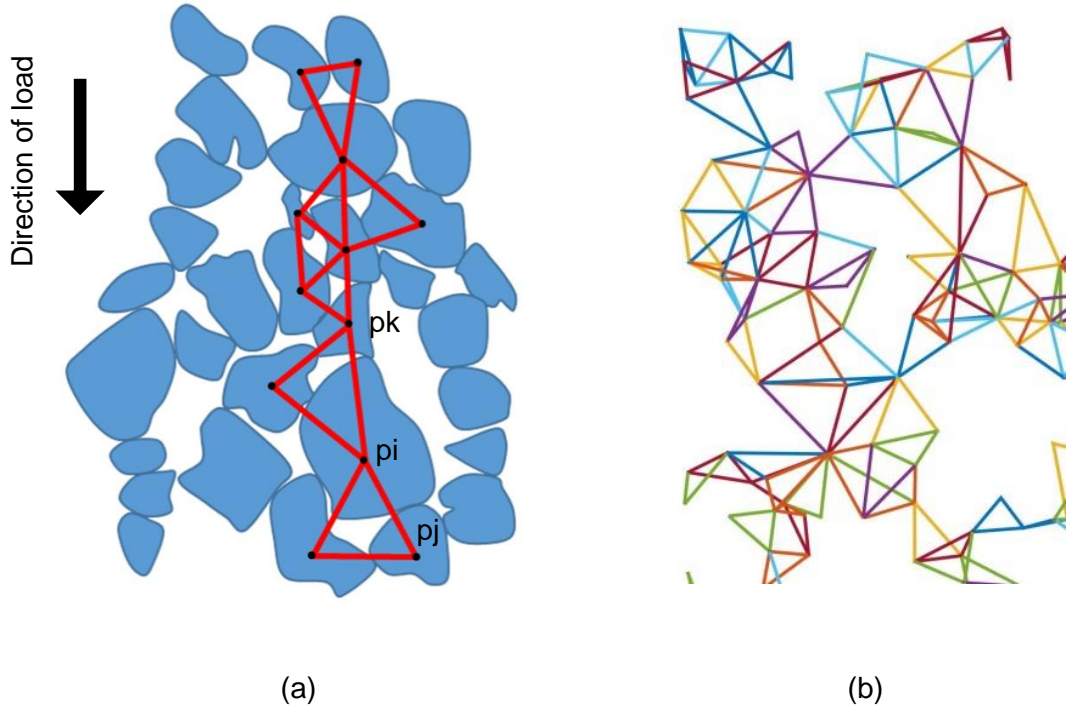


Fig. 2-9. a) Schematic of the truss network in a granular assembly, b) detail of a truss network for sample lant3 for a section of 60 voxels thickness

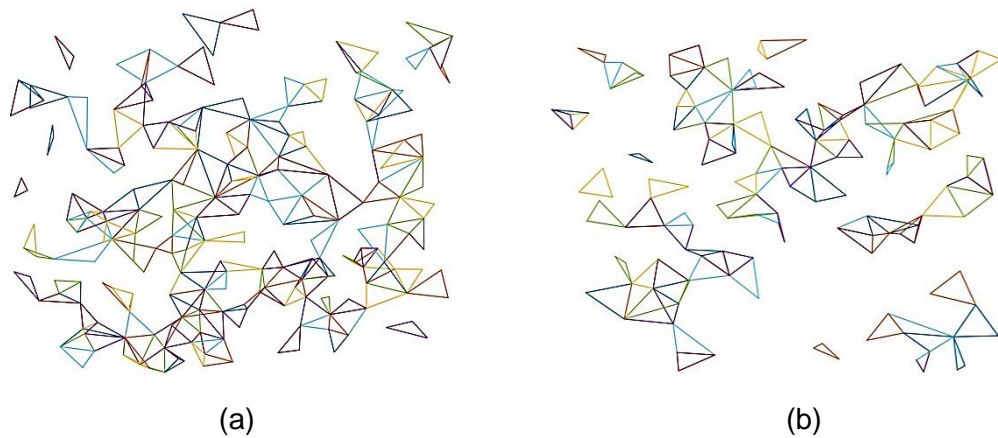


Fig. 2-10. Truss-like elements in a sub-volume (size in voxels: 600x600x60) for sample, a) Int3 outside the shear band, b) Int3S, containing the shear band

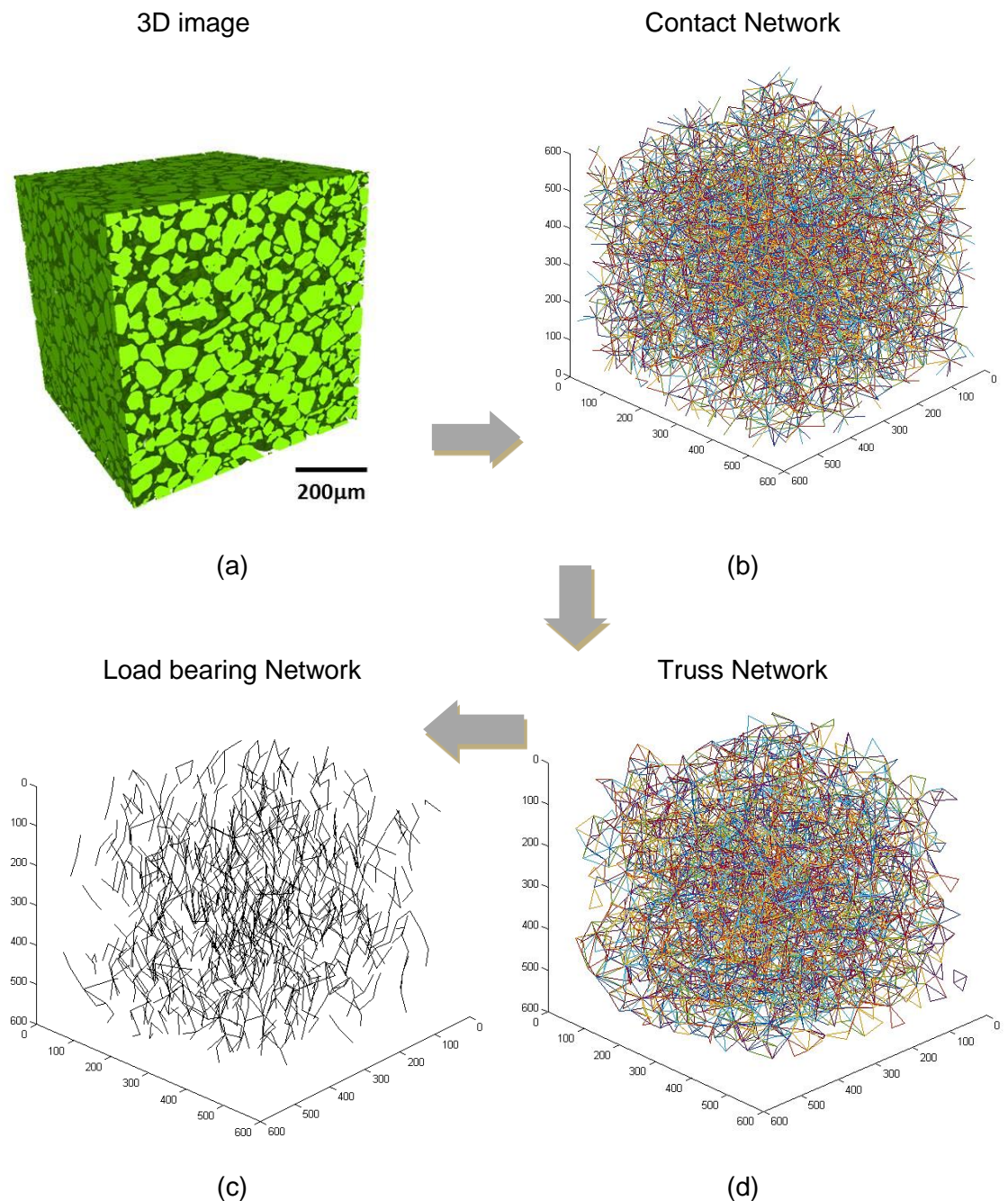


Fig. 2-11. Methodology flowchart: (a) μCT image ($600 \times 600 \times 600$ voxels), (b) contact network, (c) truss network, (d) network of the stress transmitting grains or force chains (represented by segments connecting the centroids of the load-bearing grains)

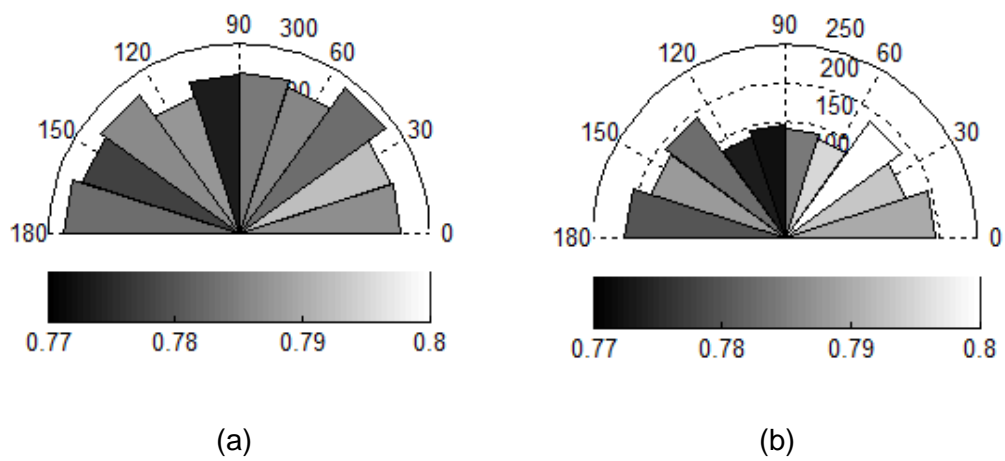


Fig. 2-12. Rose diagrams showing the distribution of the particle orientation, given by the orientation of the particle's major axis, for the sample Int3 -shading indicates average elongation ratios of the particles within each angular bean: a) for the particles forming the contact network, (b) for the particles forming the force chains

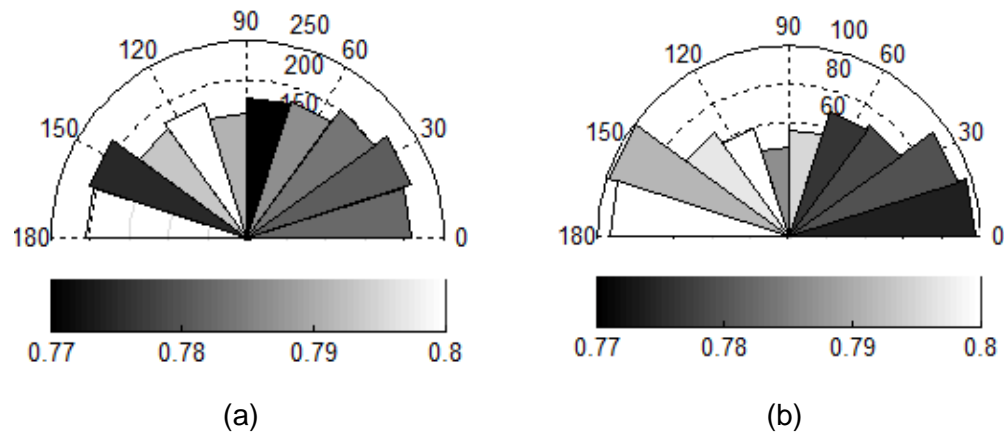
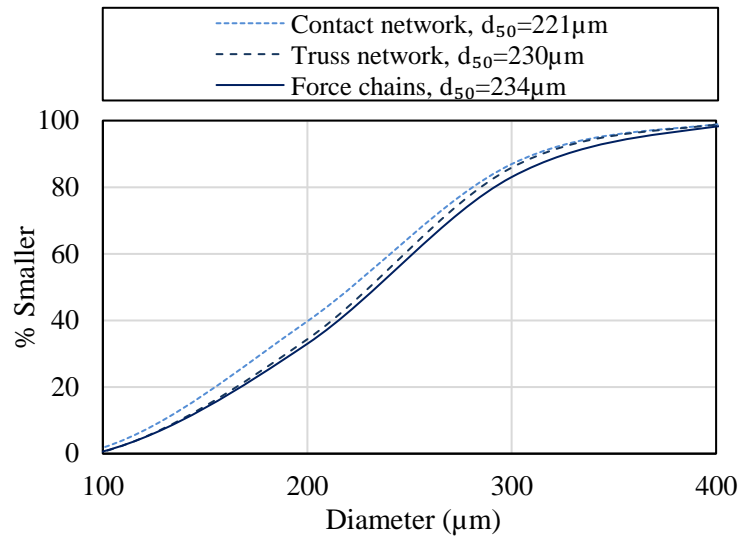
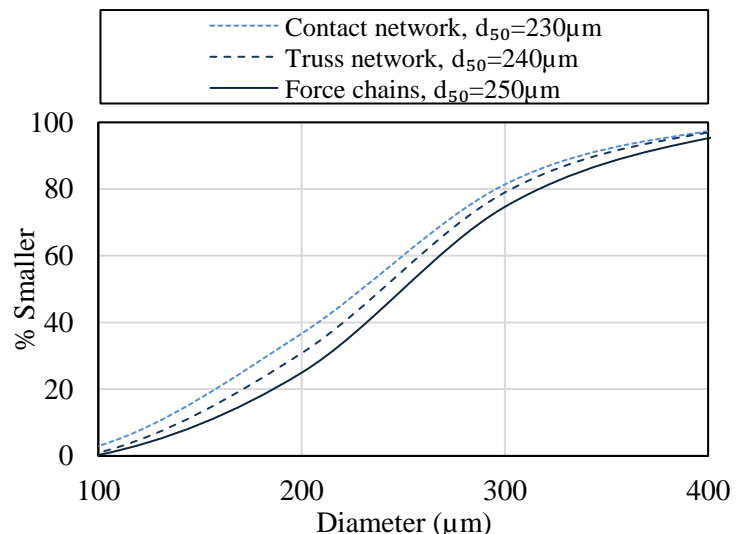


Fig. 2-13. Rose diagrams showing the distribution of the particle orientation for the sample Int3S -shading indicates average elongation ratios of the particles within each angular bean: a) for the particles forming the contact network, (b) for the particles forming the force chains

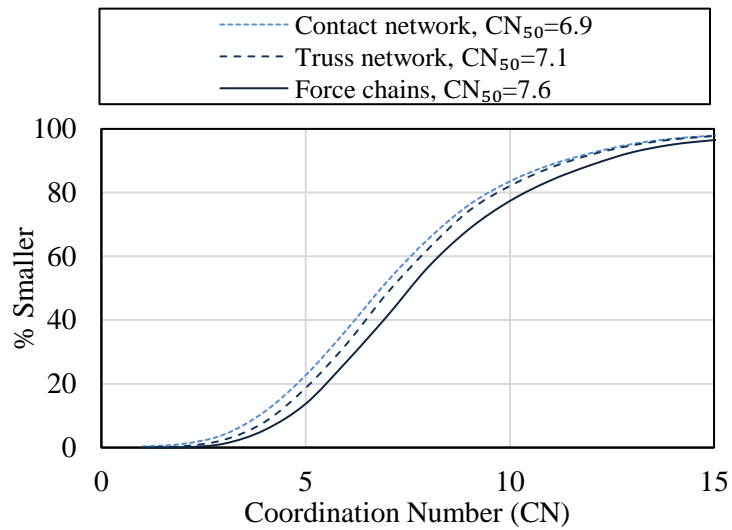


(a)

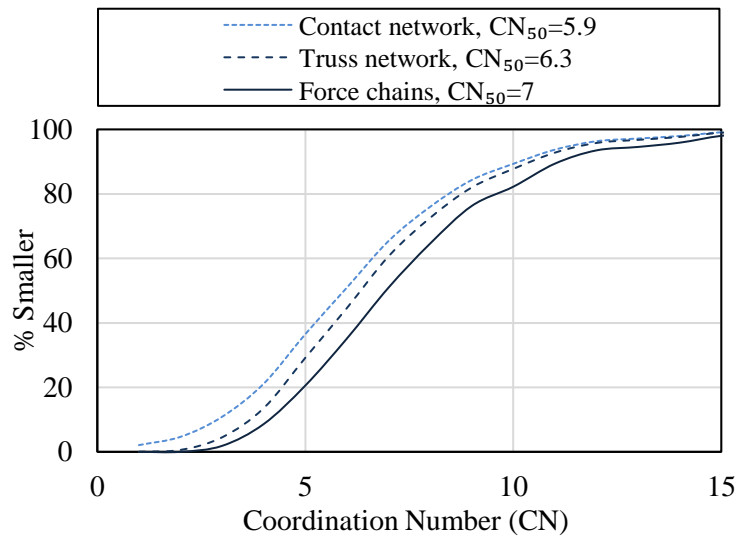


(b)

Fig. 2-14. Comparison of the particle size distribution for the grains composing each of the three networks, respectively: a) for sample Int3 outside the shear band and b) for the sample Int3S containing the shear band



(a)



(b)

Fig. 2-15. Coordination number distribution for the grains composing each of the three networks, respectively: a) for sample Int3 and b) for the sample Int3S

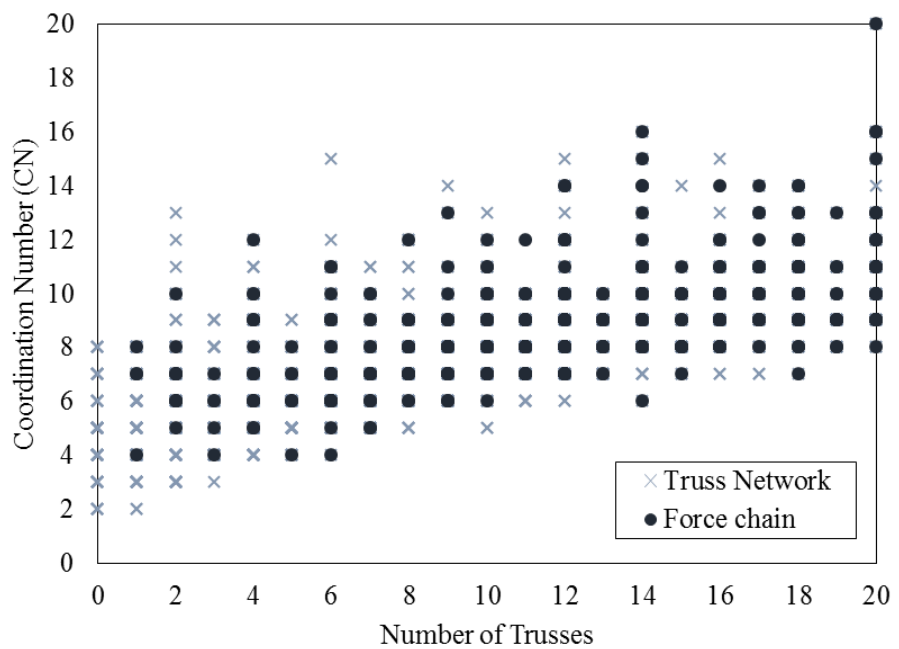
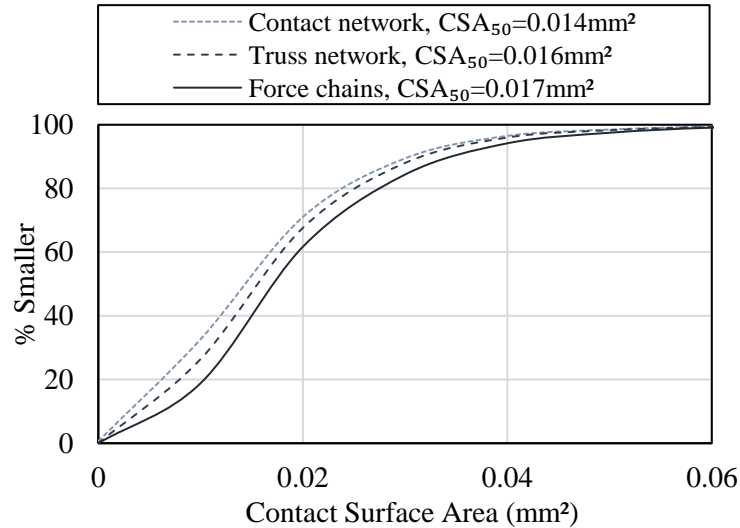
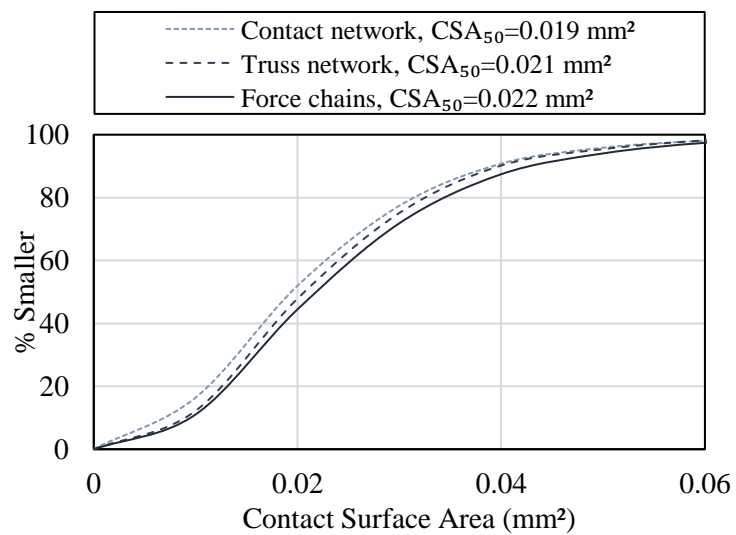


Fig. 2-16. Coordination number versus number of trusses for both the truss network and the force chain for sample Int3

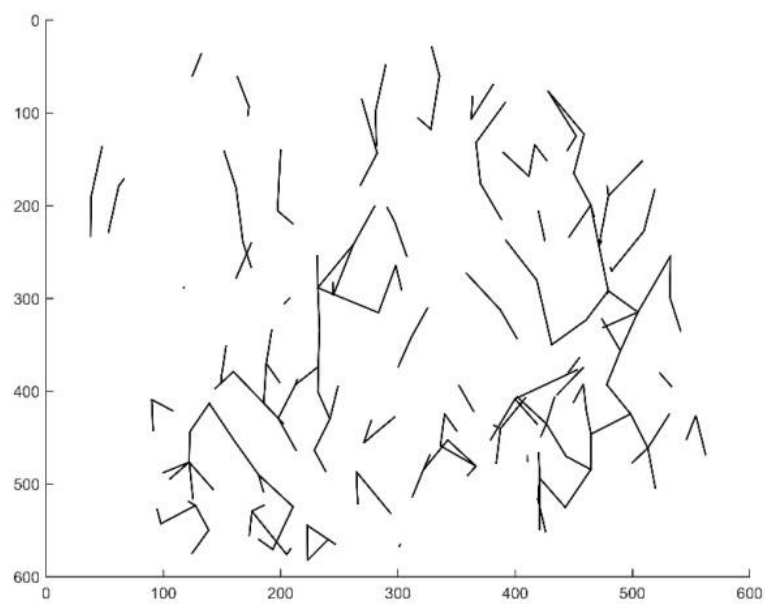


(a)

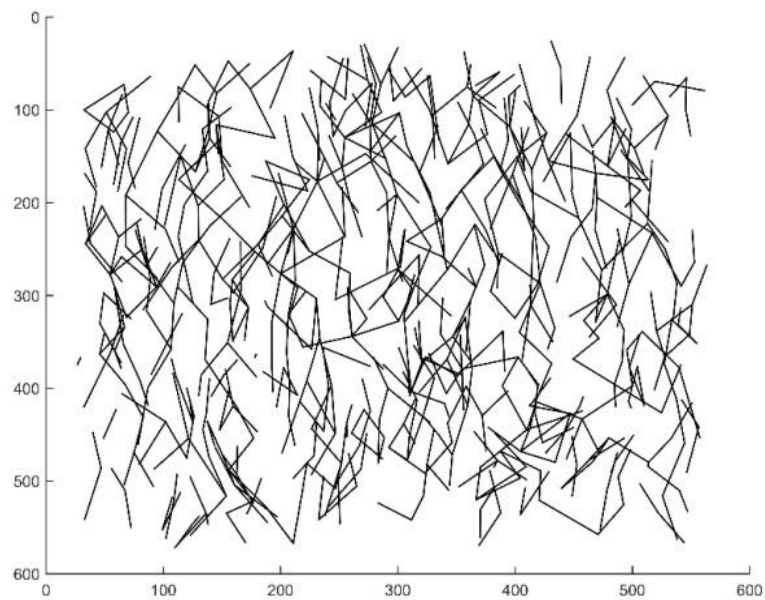


(b)

Fig. 2-17. Contact surface area distribution using all grains in the sample, using the grains that passed the stability criterion and the one that satisfy the load transmission criterion, a) for the intact sample outside the shear band and b) for the intact sample containing the shear band



(a)



(b)

Fig. 2-18. Force chains obtained for sample Int3 for a section of: a) 60 voxels thickness and b) 300 voxels thickness

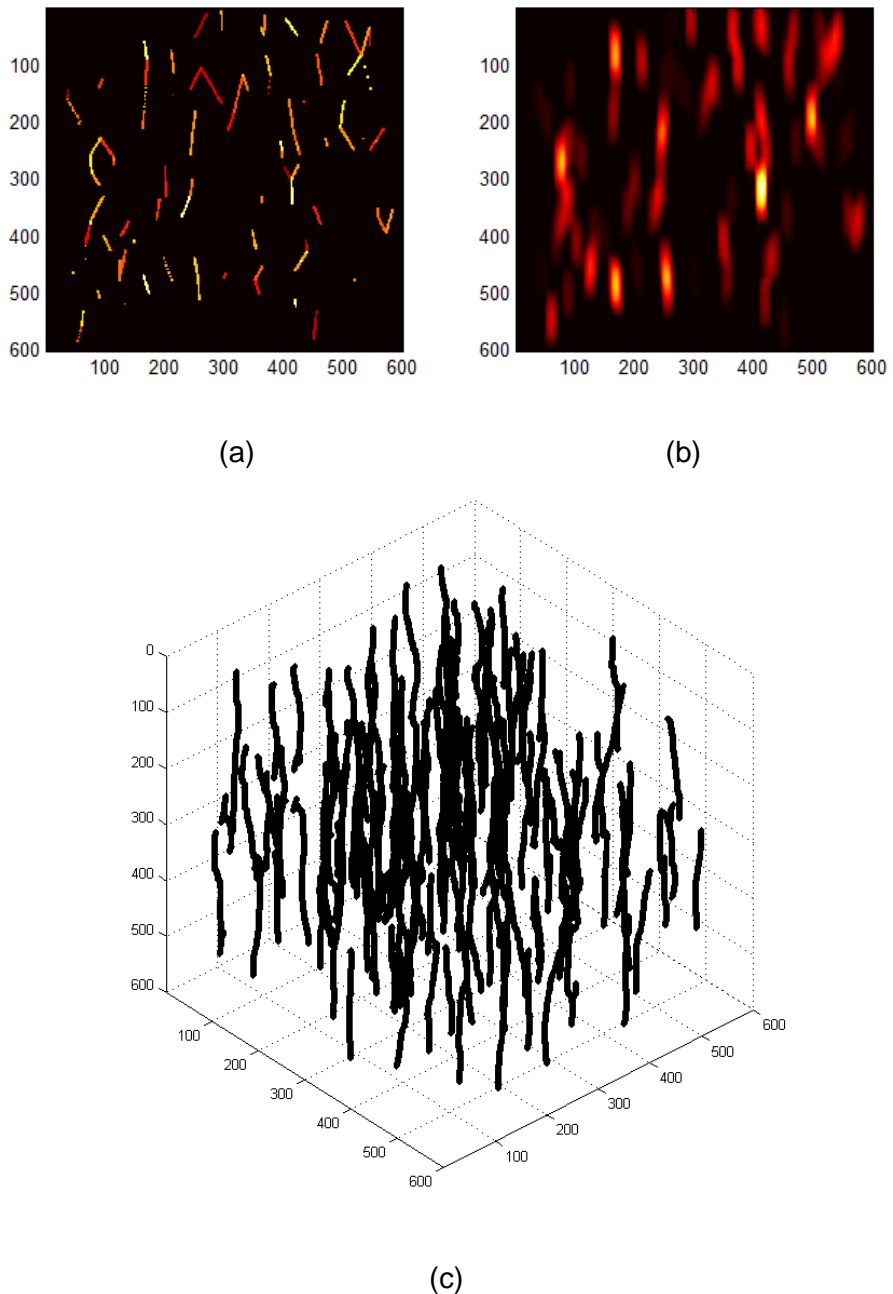


Fig. 2-19. Illustration of the steps to obtain the network of the stress transmitting grains for the sample Int3: a) 3D vectors, represented by the segments connecting the centroids of the grains forming quasi-vertical contact normals, the vectors associated with larger contact surfaces have brighter colours (only a projection is presented), b) 3D vectors following the low pass filter (c) final network

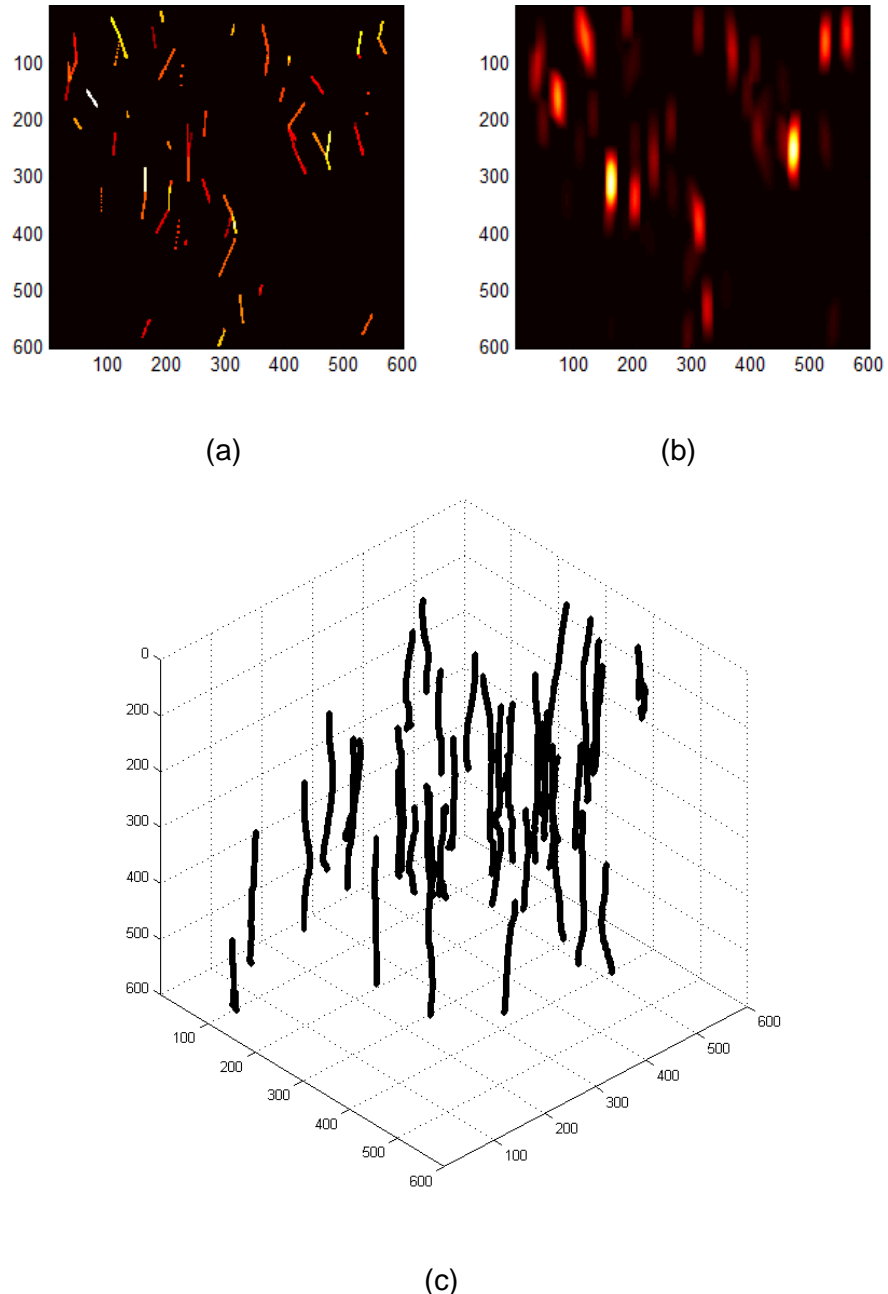


Fig. 2-20. Illustration of the steps to obtain the network of the stress transmitting grains for the sample Int3S: a) 3D vectors, represented by the segments connecting the centroids of the grains forming quasi-vertical contact normals, the vectors associated with larger contact surfaces have brighter colours (only a projection is presented), b) 3D vectors following the low pass filter (c) final network

A MICRO FINITE-ELEMENT MODEL FOR SOIL BEHAVIOUR

Published in: *Géotechnique* 2017; [<http://dx.doi.org/10.1680/jgeot.16.P.147>]

3.1 Introduction

Since first proposed by Cundall & Strack (1979), the discrete element method (DEM) has become a primary tool to model granular behaviour. For the most part, three dimensional (3D) DEM models use spherical particles and, although this idealisation facilitates contact detection and force calculation, it also limits the field of application of the method (Ferrellec & McDowell, 2010). As noted by Cavaretta & O'Sullivan (2012), spherical shapes cannot capture the variation in effective stiffness caused by particle rotation and inter-particle sliding observed in real sand. The effect of particle morphology on the mechanical response of granular material has been repeatedly emphasised in previous numerical and experimental studies (Oda & Iwashita, 1999; Lu & McDowell, 2007; Katagiri *et al.*, 2010; Miskin & Jaeger, 2013; Nguyen *et al.*, 2015). Particle shape alone can affect dilation and, consequently, the shear resistance of the material (Matsushima & Chang, 2011; Azéma & Radjai, 2012). Efforts to overcome this limitation include the use of clusters or agglomerates of spheres/disks (e.g. Lu & McDowell, 2007; Wang *et al.*, 2007; Matsushima *et al.*, 2009; Cil & Alshibli, 2014; Katagiri *et al.*, 2014; Yang *et al.*, 2016). The outcomes from these studies have highlighted the effect of overall particle shape on the rolling resistance mobilized by the multiple contact points between two particles. More advanced DEM studies using μ CT include the use of spherical harmonic-based principal component analysis (Zhou & Wang, 2016) and of non-uniform rational basis-splines and level set methods (Andrade *et al.*, 2012; Kawamoto *et al.*, 2016) to describe the morphological features of sand.

The rigid body conditions and associated contact laws underlying traditional DEM approaches constitute also an important limitation to accurately model granular materials, as discussed in Zheng *et al.* (2012). Conventional contact laws such as Hertz (1882) and Mindlin & Deresiewicz (1953) used for the most part of DEM studies may be of limited use for modelling contact interaction of irregular particles as demonstrated from micro-mechanical tests carried at the grain-to-

grain contact (Cavarretta *et al.*, 2010; Cole *et al.*, 2010; Senetakis *et al.*, 2013). These studies have in particular emphasised the need to include plastic behaviour at the contacts. The DEM models used in geotechnics are still largely limited to elastic behaviour, despite the progress in developing adhesive and plastic contact laws in powder technology (Alonso-Marroquin *et al.*, 2005; Luding & Bauer, 2011; Pasha *et al.*, 2014; Thakur *et al.*, 2014).

The diversity of grain morphologies found in natural sands leads to complex contact topologies which directly affect the stress distribution and the deformation within the granular assembly (e.g. Fonseca *et al.*, 2013a; Druckrey *et al.*, 2016). Contact topologies were reported to be linked to the primary fabric of stress-transmitting particles and to the realignment of the contact normal during loading (Fonseca *et al.*, 2016), thus playing a key role on the mechanical response of the material. It is therefore suggested that a more accurate simulation of granular behaviour should account for particle shape, particle orientation and the associated contact topologies. This paper makes use of the numerically validated model (μ FE) to extend it to the grain morphologies found in natural soil.

The rationale underlying this μ FE model is twofold: a) discrete modelling of granular systems requires a more truthful spatial distribution of the constituent grains and their morphologies, which is now possible to obtain using μ CT, and b) a more realistic representation of the physics of the granular behaviour can be obtained using a finite element (FE) formulation based on deformable bodies. The model presented here makes use of the geometrical grain scale data obtained from μ CT in the framework of combined discrete-finite element method (Munjiza, 2004; Harthong, *et al.*, 2012) to model the individual grains and their interactions under loading. The idea consists of virtualising the soil fabric by meshing the constituent grains and allowing them to interact and deform according to appropriate constitutive model and frictional contact conditions. The contact response results from the deformation of contacting bodies, which accounts for the specificities of each contact surface. This discrete finite-element approach has the potential to elucidate the fundamental parameters that control the micro scale phenomena, thus providing a better link between the micro and macro scales. Moreover, this modelling technique can contribute insights into yield initiation within the grain, thus providing a step change for the understanding of grain breakage (to be developed in future work). The present paper focuses,

first, on the methodology used to obtain the numerical fabric, including acquiring and processing the 3D images and meshing the individual grains. This is followed by a case study on one-dimensional (1D) compression of Reigate sand for which the measured micro scale data are discussed.

3.2 The μ FE Model

One challenge in modelling physical phenomena of real soil is obtaining a detailed numerical representation of the constituent grains to simulate grain interaction. The framework presented here makes use of advanced image processing and mesh generation techniques to obtain an accurate and computationally tractable representation of the complex geometries of real sand grains. This virtual fabric is used to compute the macroscopic global response under externally applied load and, most importantly, to investigate the microscale phenomena that takes place. The flowchart summarising the procedure used to develop the model is presented in Fig. 3-1. The main stages comprise: discretising the individual grains from the tomographic data, generating the finite-element mesh and performing the numerical experiment according to the assigned constitutive behaviour. The details are provided in the three following sections the image acquisition and processing, mesh generation and a case study. The model described here follows an earlier two-dimensional (2D) version described in Nadimi *et al.* (2015). The adaptation to three dimensions is clearly challenging and required the use of more sophisticated algorithms as described herein.

3.2.1 Image acquisition and processing

The internal structure of the soil is obtained from 3D images acquired using x-ray μ CT. The images are maps of x-ray attenuation based on the composition of the material represented by the intensity, or colour, of each voxel (or 3D pixel). The accuracy of this 3D representation depends on the quality and detail of the images. Image quality is to a great extent controlled by the size of the focal spot and the detector pixel size, which determine the number of possible source-detector paths. The loss of definition in an image occurs when the radiation is originated over an area rather than a single point, this is called geometric

unsharpness (more details can be found in Fonseca (2011)). A micro-focus tube scanner, the ‘nanotom’ (phoenix|x-ray, GE), is used here. This lab source has a signal-to-noise ratio comparable to synchrotron sources (Brunke *et al.*, 2008) and produces sharp images so that the boundaries of the grains can be clearly identified. The 3D images acquired have a voxel size of 5 μm , which means that each grain is represented by a large number of voxels (60 voxels across the diameter for a d_{50} of approximately 300 μm) and the overall grain shape can be well captured.

The discretisation of the individual grains consists of extracting the solid phase from the image and subsequently separating the grains touching and categorising the individual grains. This process is documented in previous publications by the authors (Fonseca *et al.*, 2012; Fonseca *et al.*, 2013b) and a summary is provided here for completeness. In order to identify the solid phase, a thresholding technique was employed, which consists of producing a binary image where the voxels representing the solid phase are assigned a value of 1 and the voxels representing the void phase are assigned the value of 0, based on a chosen threshold value. The threshold value was obtained by fitting a Gaussian curve to each of the two peaks of the histogram of intensity values and determining the minimum point between them. This threshold value was confirmed using Otsu’s method (Otsu, 1979) employing the algorithm implemented in Image J (Schindelin *et al.*, 2015). To identify the individual grains within the solid phase a watershed approach was used. Watershed segmentation consists of taking the image as a terrain surface, where the elevations are represented by a distance map, and identifying the single grains as if they were drainage basins (Beucher & Lantuejoul, 1979). The distance map was computed by calculating the number of iterations required to fill every solid region (Atwood *et al.*, 2004). The watershed algorithm employed here is based on the ITK approach (Ibanez *et al.*, 2005) and was applied to the inverse distance map (IDM) or height function. For each basin, it is possible to define the total depth D , which is the minimum of the height function, and a watershed depth D_e , which is the depth of water it can hold without flowing to adjacent basins. Two watershed input parameters are used to alleviate over-segmentation, the threshold (T) and the level (l) parameters. The threshold parameter T is used to remove the small catchment basins with depth less than TD_{\max} , where D_{\max} is the maximum depth of all the catchment basins in the IDM. No watershed lines will be generated on the boundaries of these very small

regions, and, as a result, these regions are attached to adjacent basins. The level parameter I is used to fill all the remaining basins by a flood level ID_{\max} . In this way, the basins of D_e smaller than ID_{\max} will be filled entirely and merged into adjacent basins. The parameters used here were $T=0.04$ and $I=0.2$. The output of the watershed segmentation is an image where each grain is defined as a set of voxels with a unique intensity value, the grain's identification (ID). This ID takes integer values between 1 and the total number of grains, whereas the voxels' ID representing the void space takes a value of 0 throughout.

3.2.2 Mesh generation

The meshing stage is pivotal in this work. Obtaining a mesh that is a good finite-element representation of the material is particularly challenging for complex and irregular shapes as the ones found in real sand. The numerical mesh is therefore expected to be able to provide a good approximation of the object boundaries and, in addition, must fulfil additional constraints over shape, orientation and size of the elements.

A simple way of converting voxel data into a mesh is to use a direct conversion method that transforms each voxel or a cluster of voxels directly into a mesh. In this case, the squared elements of the mesh will result in ‘stepped’, non-smooth boundaries of the objects or grains. Thus, this voxelised mesh has a number of drawbacks that can affect the simulation of the object-to-object interaction. An alternative approach is to use the so-called marching cubes algorithm, first developed by Lorensen & Cline (1987), to extract a polygonal mesh from the voxel elements defining an object. This method computes a local triangulation of constant density within each voxel, resulting in a uniform resolution. The limitation of this method lies on the fact that it does not allow optimisation of the mesh size according to geometrical constraints of the object. In other words, a requirement of a good meshing approach would be to allow the use of small elements for regions of high detail and large elements, for example, on flat regions.

The surface mesh extraction technique used here is a refinement of the constrained Delaunay triangulation (Shewchuk, 2002). Delaunay refinement algorithms are powerful because they exploit several favourable characteristics of Delaunay triangulations, such as preserving boundaries and avoiding ‘skinny’

triangles by maximizing the minimum angle of all the triangles in the triangulation. This is particularly relevant for the numerical simulation as elements with high aspect ratio elements may lead to slow convergence of the finite-element solver and, therefore, avoiding these shapes is critical to reduce the processing time and consequently improve computational efficiency (see Postscript for details). An advanced surface reconstruction algorithm is employed here that uses the open source Computational Geometry Algorithms Library (CGAL, Rineau & Yvinec, 2015).

This technique is implemented using a developed MATLAB (Mathworks, 2015) script to generate the image-based mesh. The process of mesh generation comprises essentially two stages. In the first stage, triangular iso-surfaces are extracted from the 3D segmented image with pre-set values for density and the smallest angle. The density value controls the size and number of triangles representing the surface of each grain and thus, the number of nodes in the numerical analysis. The second stage consists of ‘filling’ the tetrahedral elements for the sub-volumes bounded by the iso-surfaces to obtain the volumetric mesh. Fig. 3-2 shows an example of the generated mesh. A fine mesh is used to describe more angular features of the grains (Fig. 3-2a) while large triangles are used in flat surfaces (Fig. 3-2b). The key advantage of the technique employed here is to preserve the original boundary of the grain with no restrictions for complex topologies.

3.2.3 Numerical fundamentals

The numerical formulations for body deformation and body motion are presented here. In the framework of combined finite-discrete element method, grain deformability can be described by a finite-element formulation, whereas the motion of the individual grains and contact detection are presented using DEM principles. Deformability depends on the straining of the material rather than on its rigid body motion. If there is no strain, the grain will undergo rigid body motion only. The motion of the grains is governed by the internal forces acting on the element nodes. The nodal forces include the contribution from contact interaction, internal deformation of a discrete element and external loads

$$\mathbf{M} \frac{\partial^2 \mathbf{x}}{\partial t^2} + \mathbf{F}_{int} - \mathbf{F}_{ext} - \mathbf{F}_c = 0 \quad \text{Eq. 3-1}$$

where \mathbf{x} is the nodal displacement vector, \mathbf{F}_{int} is the internal resisting forces vector, \mathbf{F}_{ext} is the applied external loads vector and \mathbf{F}_c is the contact forces vector.

The equations of motion for the body are integrated through time (t) using an explicit central difference integration rule

$$\dot{\mathbf{u}}^{(i+1/2)} = \dot{\mathbf{u}}^{(i-1/2)} + \frac{\Delta t^{(i+1)} + \Delta t^{(i)}}{2} \ddot{\mathbf{u}}^{(i)} \quad \text{Eq. 3-2}$$

$$\mathbf{u}^{(i+1)} = \mathbf{u}^{(i)} + \Delta t^{(i+1)} \dot{\mathbf{u}}^{(i+1/2)} \quad \text{Eq. 3-3}$$

where $\dot{\mathbf{u}}$ is velocity, $\ddot{\mathbf{u}}$ is acceleration and i refers to the increment number.

An advantage of using explicit time integration is the possibility of utilizing the diagonal lumped mass matrix. Computational efficiency can be improved by using the inversion of the mass matrix, for which the computation for the accelerations at the beginning of the increment can be reduced to a simple operation (Wu, 2006)

$$\ddot{\mathbf{u}}^{(i)} = \mathbf{M}^{-1} \cdot (\mathbf{F}^{(i)} - \mathbf{F}_I^{(i)}) \quad \text{Eq. 3-4}$$

where \mathbf{M} is the diagonal lumped mass matrix, \mathbf{F} is the applied load vector, and \mathbf{F}_I is the internal force vector. The explicit procedure requires no iterations and no tangent stiffness matrix.

In an explicit scheme, the time step must be small enough to ensure the stability of the integration. Abaqus automatically adjusts the time increment during the analysis based on a global estimation method. The advantages of using a global time increment estimation is the constant update of the maximum frequency of the algorithm leading to a better and more stable simulation. The trial stable time increment is calculated for each element in the mesh as follows

$$\Delta t = \frac{2}{\omega_{max}^{element}} \quad \text{Eq. 3-5}$$

where $\omega_{max}^{element}$ is the maximum eigenvalue of the element (Abaqus Theory Manual in Dassault Systèmes, 2014). A conservative estimation of the stable time increment is given by the minimum value taken over all elements.

The summary of the constitutive contact behaviour for an elastic sphere is provided in Fig. 3-3 by means of non-dimensional quantities. These solutions are reproducible in this numerical framework by considering hard contact in normal direction and Coulomb friction in the tangential direction. The principles of using deformable spheres to simulate contact interaction for normal, tangential, rotational and torsional loading, and the numerical validation of the constitutive contact behaviour against existent theories (including mesh size dependency) will be discussed in more detail in a follow-up publication (Chapter 4 of this thesis; Nadimi & Fonseca, 2017b).

3.3 A Case Study

A case study is presented to demonstrate the ability of the proposed μ FE approach to model a sample of sand. The model runs in Abaqus finite element package (Dassault Systèmes, 2014) and is implemented with an explicit algorithm that uses a dynamic framework. The tetrahedral mesh generated in MATLAB is first imported into the finite-element solver using a text file readable by Abaqus. The *voxel coordinates* in the MATLAB matrix are converted into *object coordinates* using the resolution value of the μ CT images. This Section includes first a brief description of the governing equations and the numerical model. An assessment of the energy quantities is then presented, which enables: a) assessment of the plausibility of the simulation to carry out quasi-static analysis and also b) evolution of the assembly response in terms of plastic and frictional behaviour. This is followed by an investigation into the effect of microscopic yield stress, which will help in understanding grain breakage (to be discussed in future work). Finally, the measurement of the internal stress distribution and four-dimensional (4D) kinematics of the grains are discussed.

3.3.1 The model

An Oedometer test on a sample of a natural sand is used. The input data consists of a high resolution μ CT image of an intact sample of Reigate sand, a quartzitic formation from Southeast England, part of the Lower Greensand formation (Fonseca *et al.*, 2012). The particle size distribution is shown in Fig. 3-4. The sand has a median grain diameter (d_{50}) of 300 μm and is characterized by very high densities and an interlocked fabric, which enables the use of block sampling to collect intact samples (Fig. 3-5a) from an outcrop of this material (details in Fonseca, 2011). A minimal cement content was observed in the samples retrieved. The shapes of the grains in this geologically old, once deep, buried sand vary from near-spherical to highly non-spherical with embayments. The most striking feature of this sand is the predominance of flat, extended contacts (Fig. 3-5b), in contrast to the point contacts found in more recent sand formations or in reconstituted samples of the same sand.

The model consists, in this case, of a small sample represented by an image of $400 \times 400 \times 200$ voxels subjected to 1D compression. Fig. 3-6 shows a 3D view of the sample together with the boundary conditions imposed—namely, fixed lateral boundaries and displacement allowed along the vertical direction only. This is a sub-volume cropped from the larger 3D image, which explains the flat boundaries of the sample. The assembly contains 630 grains and each grain includes on average 1,096 nodes and 3,080 tetrahedral elements. Average values of 100 GPa for Young's modulus and 0.15 for Poisson's ratio (Holtzman *et al.*, 2009) were used, corresponding to a bulk modulus of $K=47.6$ GPa and shear modulus of $G=43.5$ GPa. Plastic behaviour is assumed to initiate at 10 MPa stress using an isotropic hardening model. Subsequently, the material is allowed to harden to 110 MPa at 0.05 strain (hardening modulus, $E_t=2$ GPa), after which it behaves perfectly plastic. In other words, if the contact stress decreases due to grain rearrangement, there is a residual deformation after the yield point. The yield and hardening values were obtained from curve fitting of the normal force versus displacement response, from single grain experiments conducted on silica sand. To account for grain breakage, a more advanced constitutive assumption is required (e.g. Nadimi & Fonseca, 2017e; Appendix C in this thesis). The coefficient of inter-particle friction for the grains was assumed to be 0.23, the

value obtained from experimental grain-scale measurements on silica grains (Senetakis *et al.*, 2013). The 1D compression test was carried out under vertical displacement control, up to a vertical strain of 0.1. The analysis took 13.5hrs (running on DELL Precision T7610). For a full size sample, such as those described in Kawamoto *et al.* (2016) and Fonseca *et al.* (2013c), the simulation is expected to take approximately 6 days.

3.3.2 Assessing energy quantities

When using an explicit dynamics model for a static problem, the quasi-static conditions need to be checked during the simulation. The energy balance for the model, according to the first law of thermodynamics, can be written as follows

$$E_K + E_U = \int_0^t \dot{E}_{WF} dT + \text{constant} \quad \text{Eq. 3-6}$$

or

$$\int_V \frac{1}{2} \rho \mathbf{v} \cdot \mathbf{v} dV + \int_V \rho U dV = \int_0^t \dot{E}_{WF} dT + \text{constant} \quad \text{Eq. 3-7}$$

where E_K is the kinetic energy, E_U is the internal energy and \dot{E}_{WF} is the external work defined as the rate of work done by external forces and contact friction forces between the contact surfaces. In addition, ρ is the density, \mathbf{v} is the velocity field vector and U is the internal energy per unit mass.

The energy quantities used here are the kinetic and internal energies. Fig. 3-7 shows the evolution of the kinetic and internal energies over time for the four simulations reported in this case study. It can be seen that while the internal energy increases, the kinetic energy remains near zero throughout the whole simulation, which confirms the quasi-static nature of the process.

3.3.3 The effect of the yield stress

Given the difficulty in measuring microscopic yield stress and plastic behaviour of sand grains, experimental results are commonly reported in terms of force-

displacement (as contact area evolves during loading). Although for the microscopic yield stress a value of 10 MPa has previously been assigned, interest also lies in investigating the effect of using different values on the macroscopic response of the assembly. To this end, additional yield stresses of 20, 30 and 40 MPa are also used. In order to better understand the effect of yield stress and isolate it from the influence of grain shape and contact topology, the Hertzian response of elastic-plastic spherical grains was investigated with analogous constitutive behaviour, as presented in Fig. 3-8. This plot shows that for a given normal force the grains with lower yield stress exhibit larger displacement and thus softer response. The macro response of the assembly, computed based on reaction force measured at the top platen resulting from the applied displacement, is presented in terms of the stress-strain response (Fig. 3-9) and in terms of force-displacement (Fig. 3-10).

As expected, it can be seen from Fig. 3-10 that higher load is required for higher yield stress. This observation is in agreement with the trend presented in Fig. 3-7 in terms of energy quantities; that is, the internal energy is higher for higher yield stress. Traditionally used stress-strain curves cannot, however, represent this difference as shown in Fig. 3-9. Frictional and plastic energy dissipation for the different yield stress is reported in Figs. 3-11 and 3-12, respectively. It can be observed that the plastic dissipation (Fig. 3-12) is one order of magnitude higher when compared to frictional dissipation (Fig. 3-11). This observation is believed to be related to the microscale mechanisms that take place during 1D compression and does not apply, for example, to triaxial compression.

3.3.4 Grain kinematics and stress distribution inside grains

The micro scale response is investigated in terms of grain kinematics and the mechanisms of stress transmission. In order to infer grain kinematics we need to compute the internal displacement field of each individual grain. The displacement or rearrangement of the grains includes a combination of rotation and translation. The displacement field is obtained from the spatial coordinates of the nodes composing each grain at subsequent time steps during deformation. Similarly, the stress distribution inside the grains is obtained from the stress values measured at each node.

Fig. 3-13 shows a 3D view of the stress distribution in the whole assembly at three stages of loading, initial ($t=0$), intermediate ($t=500$) and final ($t=1000$) using von Mises criterion. It can be seen that, at the initial stage (Fig. 3-13a) the sample is not loaded yet and all grains have a stress field constant and equal to zero. At the intermediate stage (Fig. 3-13b), it can be seen the stress concentration starting at the grain contacts and propagates through the grain before being transmitted to another neighbouring grain, again by way of their contacts. At the final stage (Fig. 3-13c), the assembly has been heavily loaded and this is translated in the large internal stress values exhibited by the grains. These data enable the identification of the stress-transmitting particles and the investigation of the micro-mechanisms that lead to the formation of the heterogeneous networks of force transfer, the so-called ‘force chains’. It is interesting to note that, despite the high levels of stress measured at the individual grains at the final loading stage, there are, however, grains that remain essentially with near zero stress. The presence of these apparently unstressed grains surrounded by highly stressed grains is a clear indication of the heterogeneity of the contact force network that forms in stressed granular media (e.g. Radjai, 2008; Fonseca *et al.*, 2016). When using this stress distribution is important to note that Von Mises yield criterion is independent of the first stress invariant, while the failure condition for soil grains depends on both the first and second invariant of stress.

Fig. 3-14 shows detailed views of the contact areas, the internal stress distribution and displacement field for single grains selected from the assembly, measured at $t=1000$. Four grains are displayed, termed ‘grain 1’, ‘grain 2’, ‘grain 3’ and ‘grain 4’. The contact area was obtained by computing the contact pressure at the surface of each grain (Figs. 3-14a, d, g, j), termed here active contacts. The condition for a node to be part of an active contact is to have a contact pressure greater than zero. While these contact areas are associated with higher stress values, a stress value greater than zero is not necessarily a contact because of the stress propagation within the grain, this can be seen in Figs. 3-14b, e, h, k). It can be observed that for ‘grain 1’ a constant displacement value is exhibited at all points of the grain (displacement map described by a unique colour in Fig. 3-14c) which indicates that this grain undergoes pure translation motion. In contrast, ‘grain 2’, ‘grain 3’ and ‘grain 4’ exhibit both translation and rotation. This is represented by a gradient in the colour representing the displacement field of

each grain, which indicates that different parts of the grain experience different displacement values (Figs. 3-14c, f, i, l).

Two parameters are proposed here for the kinematics analysis: the inertia tensor and the active coordination number. The inertia tensor of each individual grain is a measure of the imbalance in the mass distribution within the grain which is directly related to grain shape. This tensor is particularly useful for irregular shaped grains and can be used to quantify the grain resistance to rotation (Wang *et al.*, 2007). The principal moments of inertia (Eq. 3-8 in Postscript 3.5.2) are the eigenvalues of the inertia tensor and the corresponding eigenvectors give the direction of the principal axes. The major eigenvalue is termed I_1 , the intermediate I_2 and the minor I_3 . The moment of inertia of the grain will be smaller along the longest axis of the grain, which direction is given by the eigenvector of I_3 . This means that the grain is more likely to rotate along this direction. The difference between the magnitude of the three eigenvalues is an indicator of the deviation of the grain shape from a spherical shape ($I_1=I_2=I_3$ in the case of a sphere). In Table 3-1 the inertia tensors and the associated eigenvalues and eigenvectors are presented for the four grains previously discussed. In addition, displacement arrows are used to describe the displacement field in each grain, the magnitude is given by the arrow's size and the direction is given by the vector's direction.

Although the moment of inertia can be directly related to rotational kinematics, in the case of grains belonging to a confined assembly, the resistance to rearrangement is also controlled by the resistance imposed by contacts transmitting stress, the active contacts. In order to better understand the mechanisms that control grain rearrangement within the assembly we relate grain displacement to the inertia tensor and to the number of active contacts (N_{cA}). Referring again to Table 3-1, it can be seen that the kinematic mechanism tends to become more complex for grains with larger number of active contacts – for example, ‘grain 3’ and ‘grain 4’ when compared with the pure translation observed in ‘grain 1’ with only one contact.

While in previous figures we have presented measurements taken at the final stage of deformation, Fig. 3-15 demonstrates the ability of this model to measure truly 4D kinematics (the fourth dimension being deformation). Two different grains are presented to show the evolution of the stress and displacement values measured at a pre-selected point throughout deformation from $t=0$ to $t=1000$. For

the grain shown in Fig. 3-15a it can be seen that, for t values between 400 and 600, while the displacement increases from 0 to approximately 13 μm the stress values are seen to remain relatively unchanged. Moreover, while for t greater than 600 the displacement remains relatively constant, the stress is seen to undergo a steady increase, suggesting the formation of a highly stressed and stable contact. Further insightful observations on the mechanisms of stress transmission can also be obtained from Fig. 3-15b. In this case, as the stress value remains very low and near zero for t values up to 800, it is expected that significant rearrangement occurs during this period. For t greater than 800 the increase in the stress value is accompanied by a significant drop in the increasing rate of displacement and an expected reduction in the rearrangement of this grain.

3.4 Conclusions

The numerical framework presented has an interesting potential to answer long-standing questions on the macro-response of soil triggered at the grain level. A key contribution of this method is to enable inferring the stress transmission mechanisms under various load conditions. To the best of authors' knowledge, the map of internal stresses for real grain morphologies and extended contact surfaces has not been captured previously by any model or experimental analysis. The results presented here demonstrate that heterogeneous force transfer networks can be characterised while accounting for the effect of contact topology, grain morphology and the preferential orientation of the grains. The displacement field obtained for each individual grain allows an accurate characterisation of the grain kinematics based on a truly 4D quantification of fabric evolution throughout deformation. By combining inertia tensor with the distribution of the active contact areas we can improve our understanding of grain kinematics under loading. Although computational expensive, the model is instrumental for clarifying the fundamentals of granular media at the grain-scale that need to be considered when modelling their mechanical behaviour. Future work will include refining this simulation technique through direct comparison with experiments and expanding the model to include grain breakage. Finally, the μFE model presented here can offer significant insight into the micro-phenomena

triggered by the rich topologies found in natural soil, which have been insufficiently represented in traditional numerical simulation approaches.

3.5 Postscript

3.5.1 Delaunay refined algorithm

The efficiency and robustness of Delaunay triangulation makes it the most commonly used unstructured triangulation algorithm (Chen & Xu, 2004). In order to optimise the triangulation, the Delaunay approach gives a set of ‘quality’ triangles to use as polygons presenting the extracted surface (Shewchuk, 2014). The challenge is to find a triangulation that covers the surface of individual objects, in this case the grains, while satisfying shape and size constraints (the angles should not be too small or too large, similarly, the triangles should not be very small or very large). For ease of visualisation, a 2D example is presented here to illustrate the refinement process (Fig. 3-16). For this particular case, the input data is a polygonal region with constraining edges and vertices inside the region. The aim is to generate a triangulation of the region whose edges and vertices cover all input edges and vertices. A triangulation of the input is obtained by taking a subset of triangles. As shown in Fig. 3-16, the input data is represented by solid vertices and edges and the output for this meshing problem represented by hollow vertices and dashed edges. The quality of triangles, in terms of size and shape is commonly controlled by assessing the smallest and largest internal angles and the aspect ratio. Here, we use the threshold approach to generate an output such that its smallest angle is not less than some predefined threshold (Shewchuk, 2002). A practical way to deal with sharp input features is to isolate them during the refining process so they do not reduce the quality of the triangulation. The triangulation output is refined by adding more points to resolve triangles with very small and/or very large angles and cover edges that may not covered. In general, Delaunay algorithms consist of maintaining a constrained Delaunay triangulation, which is refined by inserting carefully placed vertices until the mesh meets the constraints on triangle quality and size.

3.5.2 Inertia tensor

The inertia tensor is defined as follows

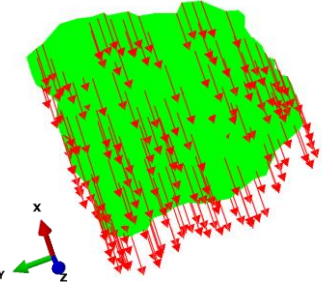
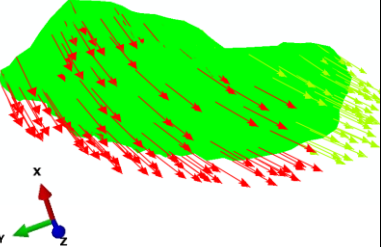
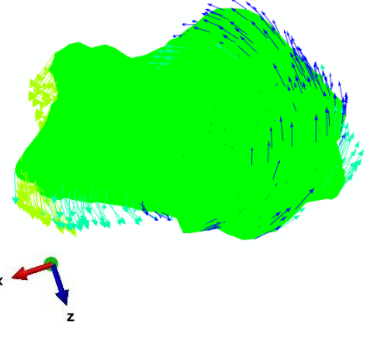
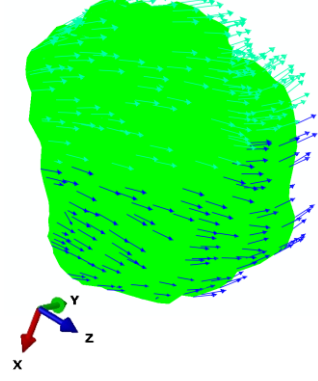
$$I = \begin{bmatrix} I_{xx} & I_{xy} & I_{xz} \\ I_{yx} & I_{yy} & I_{yz} \\ I_{zx} & I_{zy} & I_{zz} \end{bmatrix} \quad \text{Eq. 3-8}$$

$$= \begin{bmatrix} \int (y^2 + z^2) dm & - \int xy dm & - \int xz dm \\ - \int xy dm & \int (x^2 + z^2) dm & - \int yz dm \\ - \int zx dm & - \int zy dm & \int (x^2 + y^2) dm \end{bmatrix}$$

where the quantities I_{xx} , I_{yy} , and I_{zz} are termed moments of inertia and the quantities I_{xy} , I_{xz} , I_{yx} , I_{yz} , I_{zx} and I_{zy} are the products of inertia.

3.6 Tables and Figures

Table 3-1. Analysis of four selected grains in terms of displacement arrows, inertia tensor and the associate eigenvalues and eigenvectors and number of active contacts

ID	Displacement arrows	Inertia tensor	Eigenvalue	Eigenvector	N _{cA}
1		$\begin{bmatrix} 2.964 & -3.942 & -1.649 \\ . & 3.401 & -2.130 \\ . & . & 5.428 \end{bmatrix}$	$\lambda_1=7.304$	$\begin{bmatrix} -0.538 \\ 0.751 \\ -0.380 \end{bmatrix}$	4
			$\lambda_2=6.245$	$\begin{bmatrix} -0.511 \\ 0.067 \\ 0.856 \end{bmatrix}$	
			$\lambda_3=-1.754$	$\begin{bmatrix} 0.669 \\ 0.655 \\ 0.348 \end{bmatrix}$	
2		$\begin{bmatrix} 8.309 & -1.038 & -5.157 \\ . & 5.625 & 2.457 \\ . & . & 3.422 \end{bmatrix}$	$\lambda_1=12.311$	$\begin{bmatrix} 0.778 \\ -0.319 \\ -0.540 \end{bmatrix}$	4
			$\lambda_2=5.308$	$\begin{bmatrix} -0.412 \\ -0.909 \\ -0.056 \end{bmatrix}$	
			$\lambda_3=-0.262$	$\begin{bmatrix} 0.472 \\ -0.267 \\ 0.839 \end{bmatrix}$	
3		$\begin{bmatrix} 4.926 & 1.124 & 1.526 \\ . & 8.213 & 8.668 \\ . & . & 8.005 \end{bmatrix}$	$\lambda_1=17.067$	$\begin{bmatrix} 0.152 \\ 0.701 \\ 0.696 \end{bmatrix}$	16
			$\lambda_2=4.653$	$\begin{bmatrix} 0.986 \\ -0.147 \\ -0.067 \end{bmatrix}$	
			$\lambda_3=-0.576$	$\begin{bmatrix} 0.055 \\ 0.697 \\ -0.714 \end{bmatrix}$	
4		$\begin{bmatrix} 4.269 & 3.648 & 8.891 \\ . & 4.519 & 1.301 \\ . & . & 4.803 \end{bmatrix}$	$\lambda_1=14.642$	$\begin{bmatrix} 0.678 \\ 0.329 \\ 0.656 \end{bmatrix}$	11
			$\lambda_2=3.651$	$\begin{bmatrix} 0.086 \\ -0.923 \\ 0.373 \end{bmatrix}$	
			$\lambda_3=-4.701$	$\begin{bmatrix} 0.729 \\ -0.196 \\ -0.655 \end{bmatrix}$	

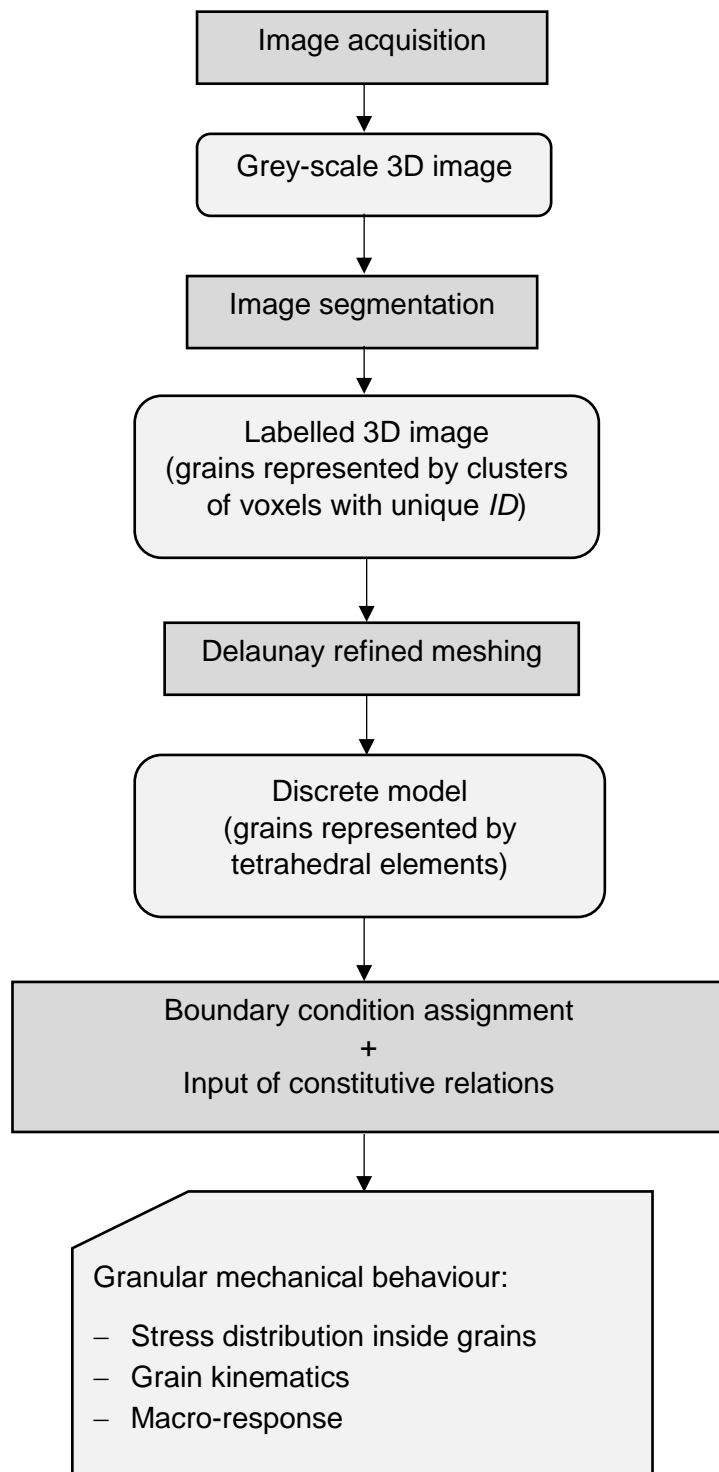


Fig. 3-1. Flowchart illustrating the various processes/tools and outcomes involved in the development of this FE model

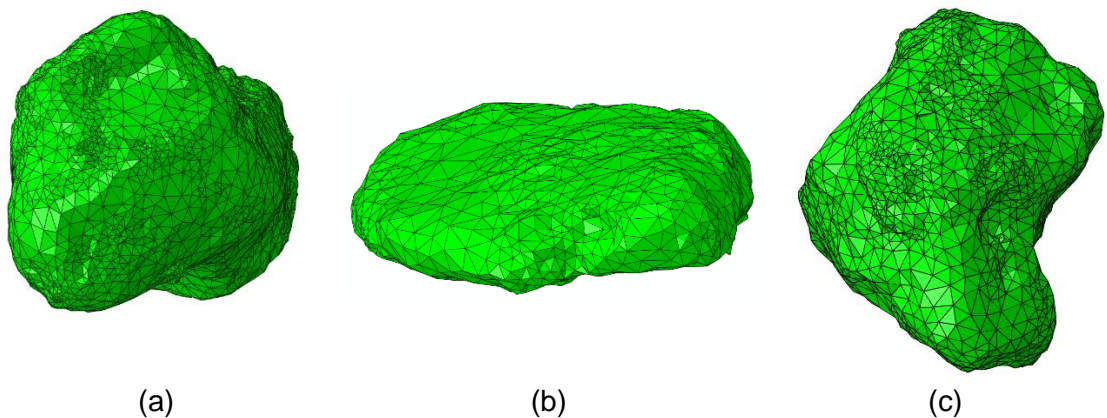


Fig. 3-2. Three examples of meshed grains to illustrate: (a) the finer mesh used to describe angular features of the grain, (b) the large elements used in flat regions, (c) the mesh of a concave grain

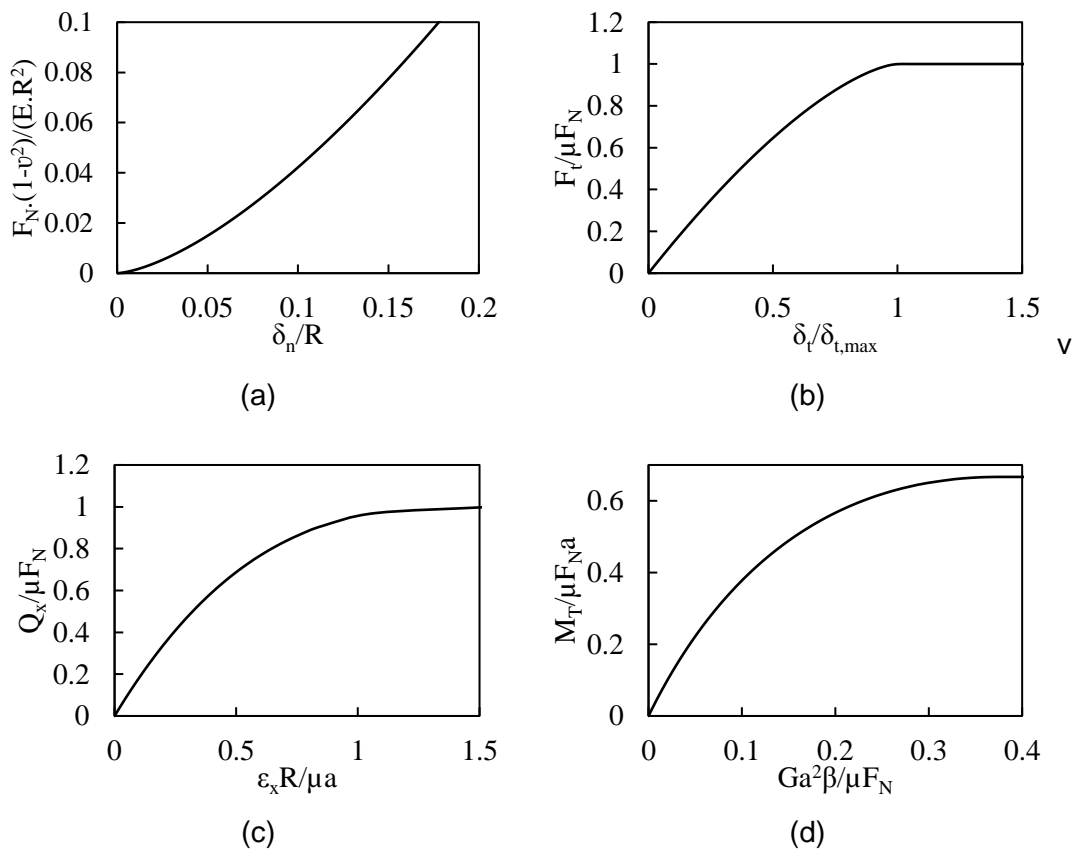


Fig. 3-3. Summary of contact constitutive behaviour for elastic spheres by means of non-dimensional quantities: (a) normal force displacement, (b) tangential force displacement, (c) rolling moment, (d) twisting moment

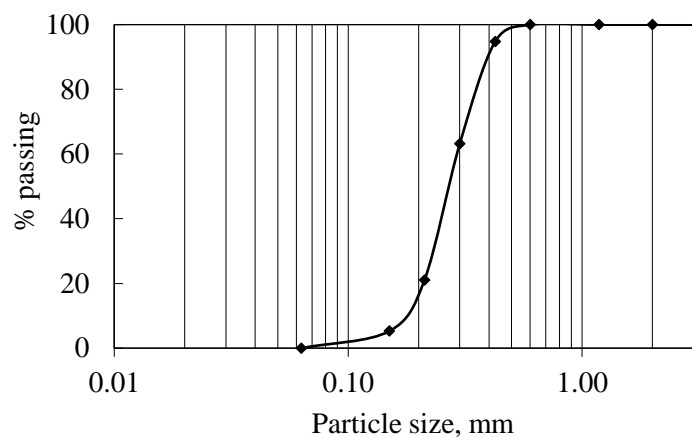


Fig. 3-4. Particle size distribution of Reigate sand obtained from sieving (after Fonseca *et al.*, 2012)

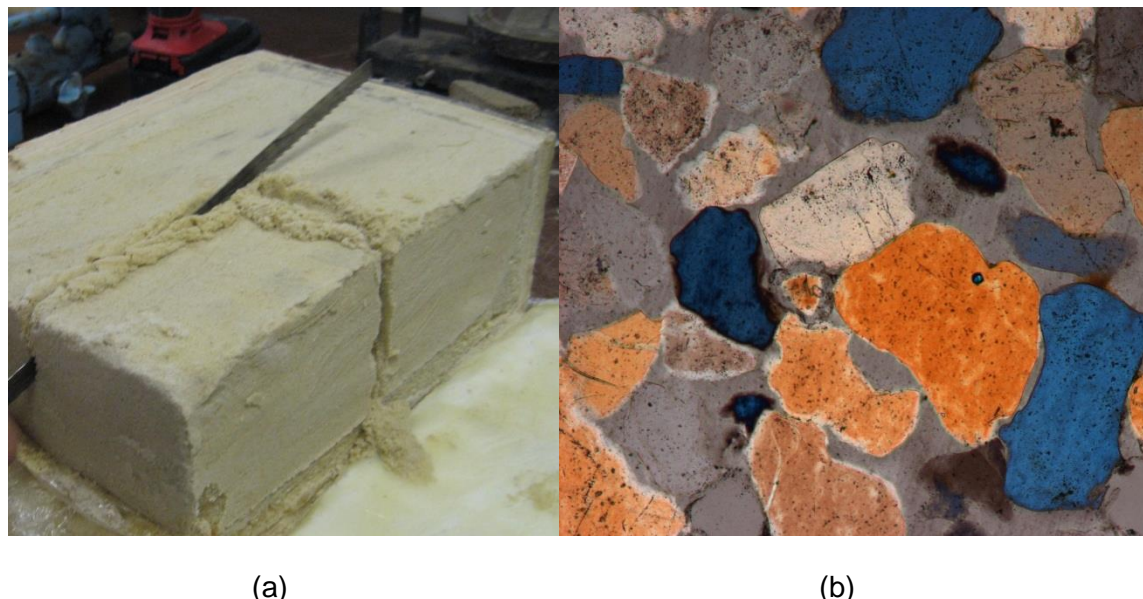


Fig. 3-5. Intact Reigate sand: (a) illustration of the block sample and (b) micrograph of a thin section under cross-polarised light showing the extended flat contacts between the grains (after Fonseca, 2011)

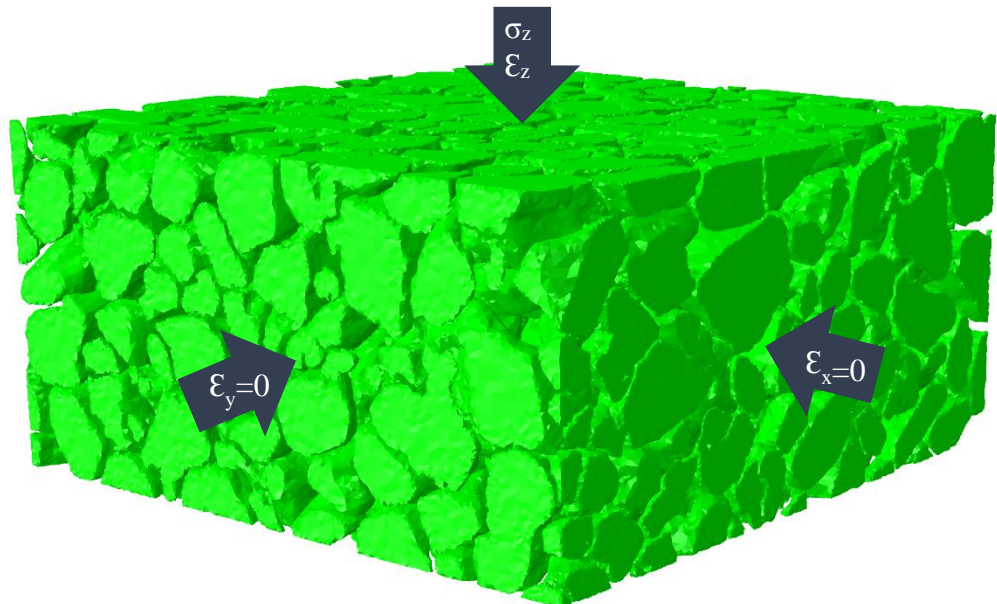


Fig. 3-6. Boundary conditions used for the simulation of the Oedometer compression

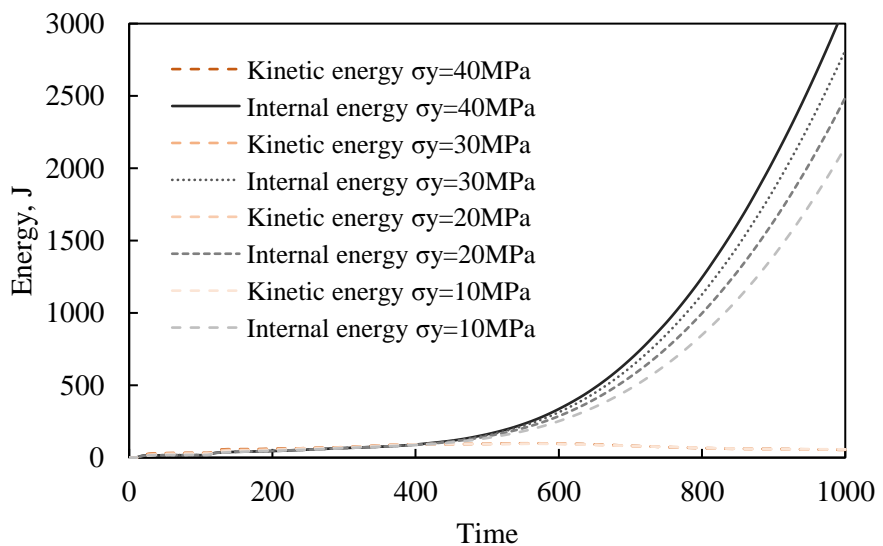


Fig. 3-7. Evolution of the measured kinetic and internal energies for the simulations reported in this study, the near zero values measured for the kinetic energy demonstrates the quasi-static nature of the simulations

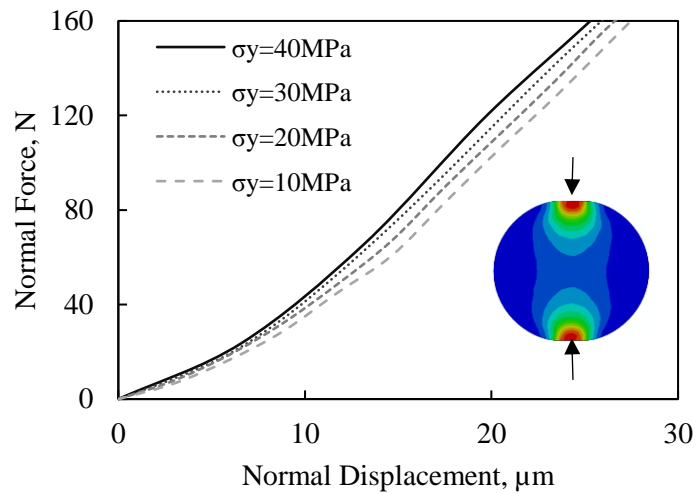


Fig. 3-8. Hertzian response of an elastic-plastic sphere measured for four different yield stresses and the general stress field inside the grain

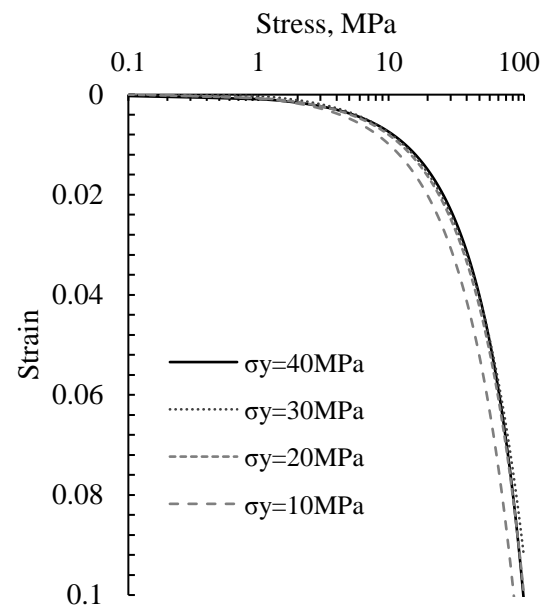


Fig. 3-9. Stress-strain response of the Oedometer compression simulations

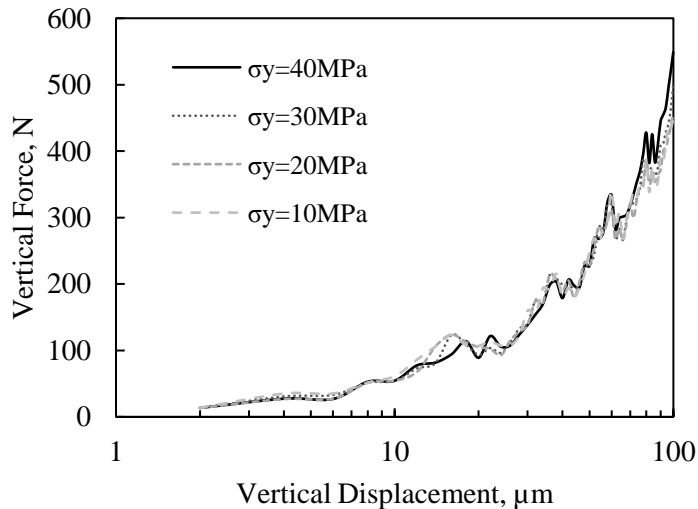


Fig. 3-10. Force-displacement measurements from the Oedometer compression simulations

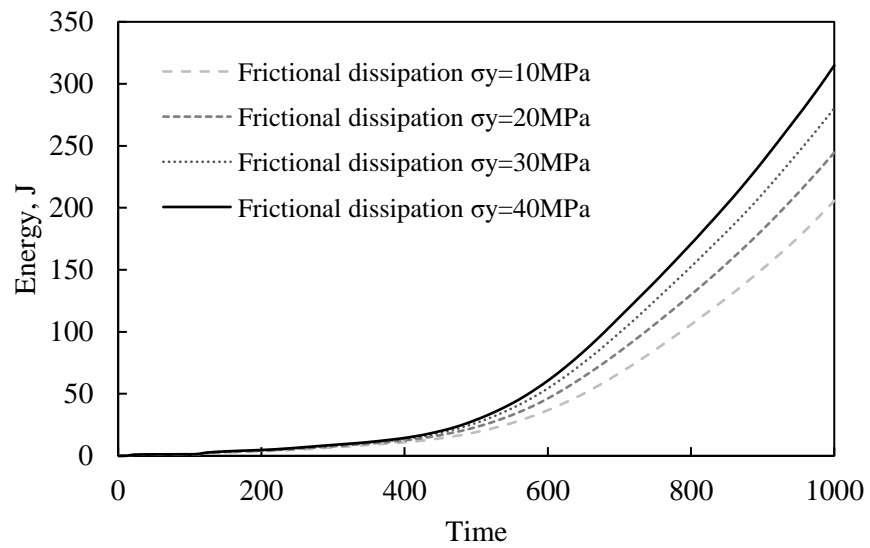


Fig. 3-11. Frictional dissipation measured for the four Oedometer test with different yield stresses

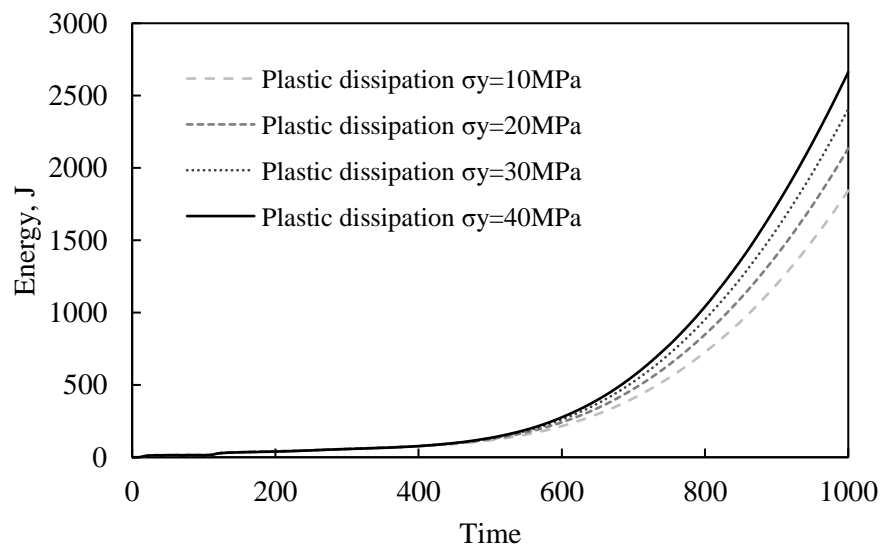


Fig. 3-12. Plastic dissipation measured for the four Oedometer tests with different yield stresses

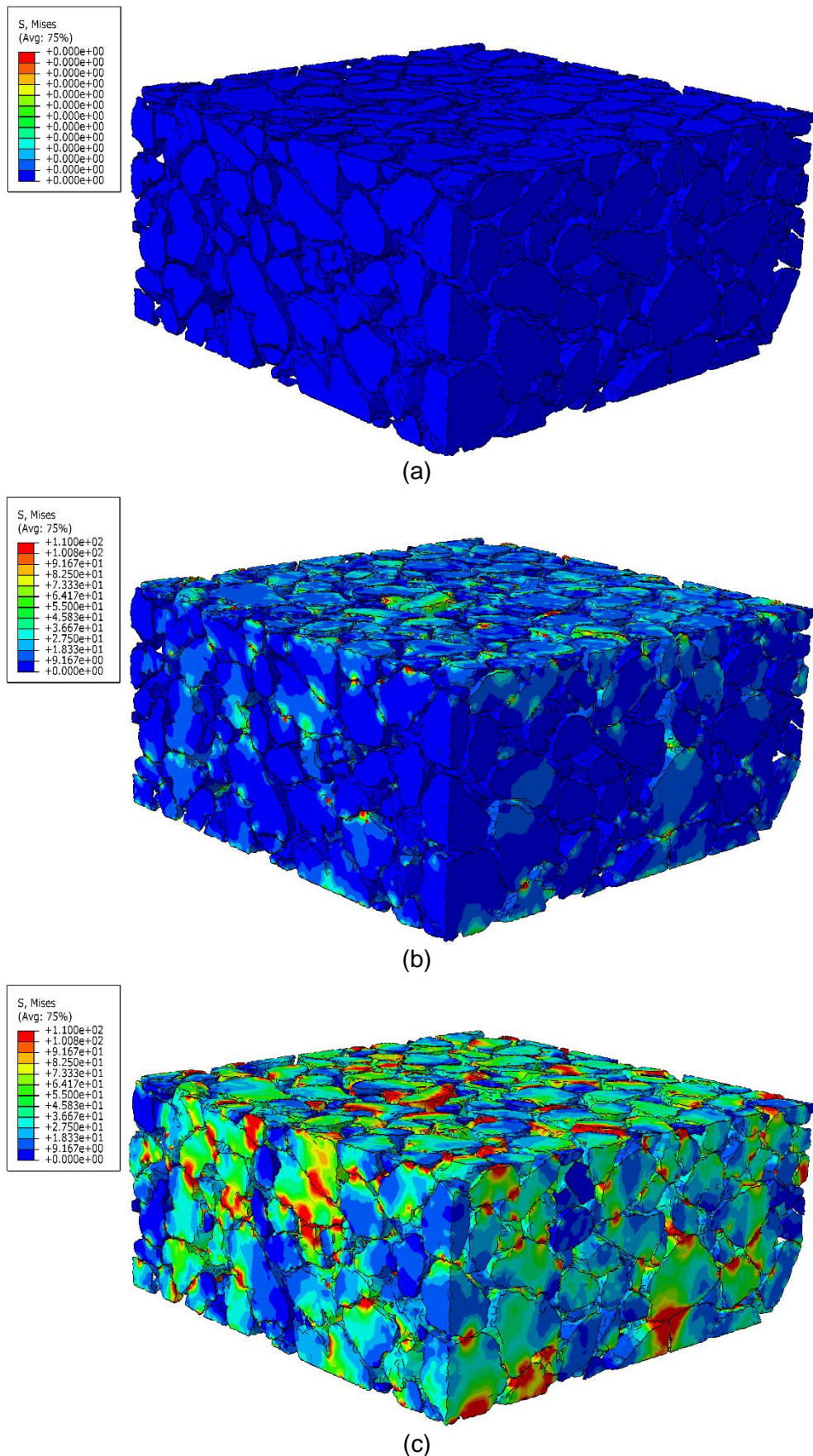


Fig. 3-13. Granular stress field obtained from the Oedometer compression test for the stages: (a) initial ($t=0$), (b) intermediate ($t=500$), (c) final ($t=1000$)

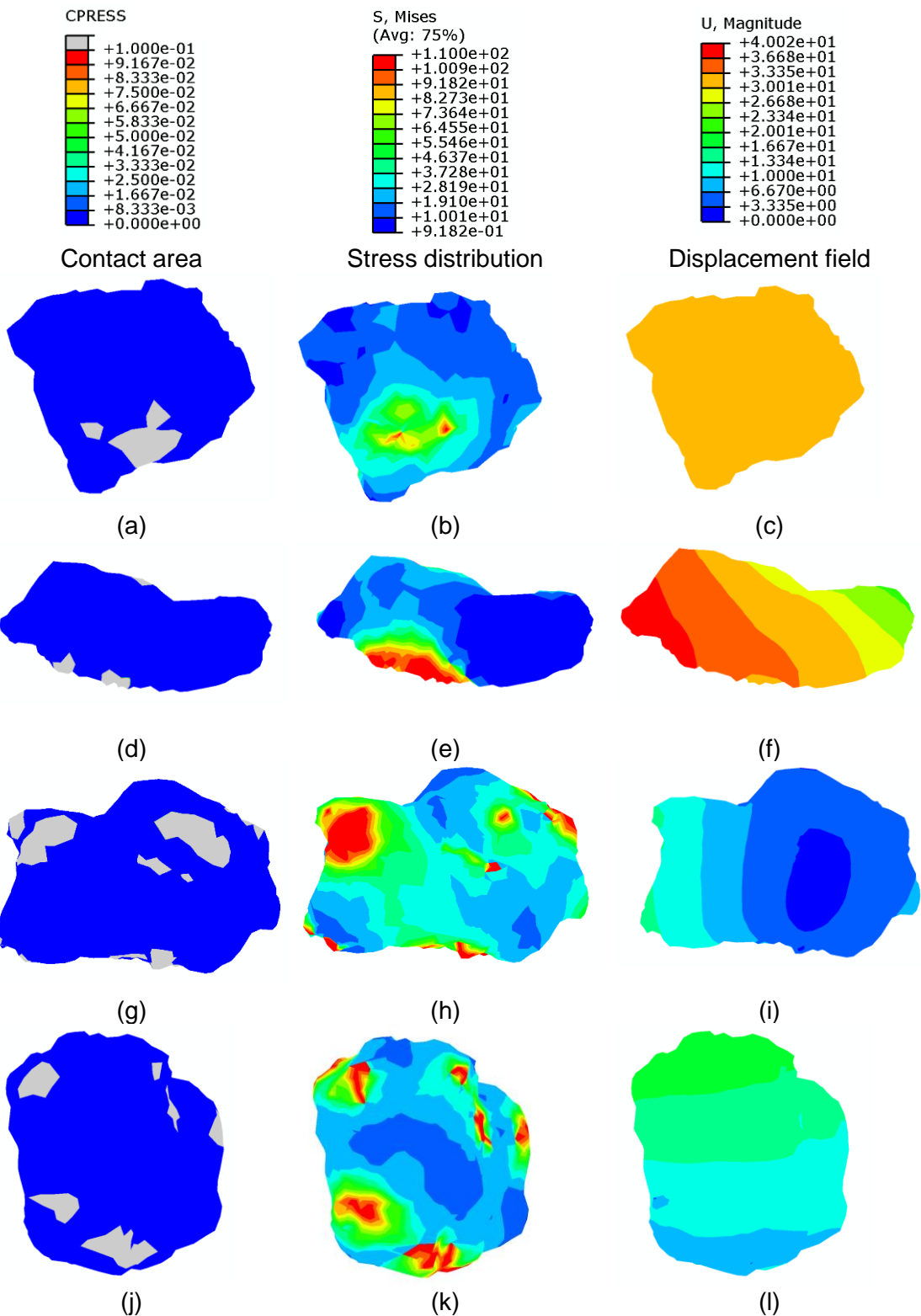


Fig. 3-14. Detailed views of the contact areas (a,d,g,j), the internal stress distribution (b,e,h,k) and displacement field (c,f,i,l) for single grains selected from the assembly, measured at $t=1000$

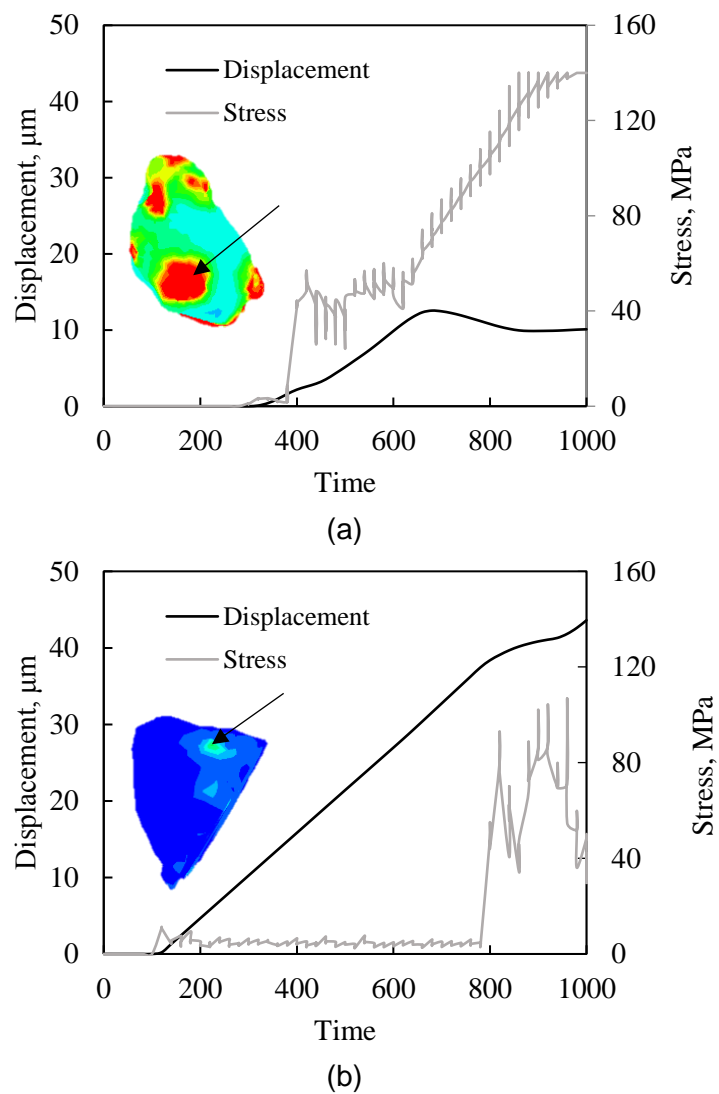


Fig. 3-15. Evolution of point stress and displacement values measured at two selected grains throughout deformation from $t=0$ to $t=1000$

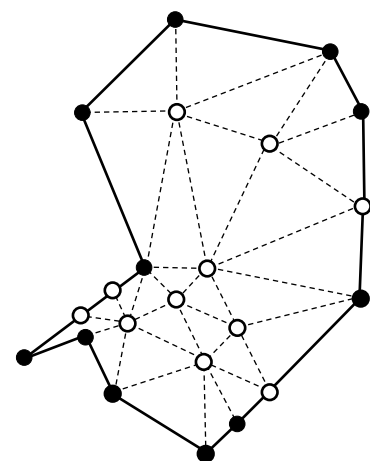


Fig. 3-16. Example of a 2D triangulation problem, the input data is represented by the solid vertices and edges and the obtained triangulation is given by the hollow vertices and dashed edges

A MICRO FINITE-ELEMENT MODEL FOR SOIL BEHAVIOUR: NUMERICAL VALIDATION

Published in: *Géotechnique* 2017; [<http://dx.doi.org/10.1680/jgeot.16.P.163>]

4.1 Introduction

The irregular shape of sand particles originate complex contact topologies (e.g. Fonseca *et al.*, 2013a), which differ significantly from the point contact condition assumed for deriving theoretical contact laws (Thornton, 2015). This implies that the ideal shapes and conventional contact laws used for the most part of Discrete Element Method (DEM) studies may be of limited application to model real sand. According to previous experiments studies (e.g. Cavarretta, 2009; Cavarretta *et al.*, 2010; Cole *et al.*, 2010; Senetakis *et al.*, 2013), contact response depends not only on contact topology, but also on previous loading history and deformation mechanisms the grain undergoes during rearrangement under loading. In addition, particle rearrangements computed based on inter-particle penetration in DEM may lead to the misrepresentation of the kinematics in granular media.

The micro finite-element (μ FE) model (Nadimi & Fonseca, 2017a) was developed with the aim of providing a more realistic representation of the physics of granular behaviour by incorporating the actual particle morphology and contact topology of real soil into deformable numerical grains. One advantage of representing grains as deformable bodies is the possibility of introducing plasticity at the grain-scale. Continuum deformable representation of ideal shapes using finite elements has been considered previously, particularly, in powder technology (e.g. Harthong *et al.*, 2009; Nezamabadi *et al.*, 2015; Rathbone *et al.*, 2015). The use of combined finite-discrete approaches to model systems of spheres is, however, not well established. This paper fills this gap by providing the numerical validation of the μ FE model for an assembly of spheres. Moreover, the finite-element (FE) discretisation is assessed for a single sphere and the elastic-plastic behaviour of a granular system is simulated under triaxial compression.

4.2 Behaviour of a Single Sphere

The problem here consists of modelling the contact between two identical spheres under loading (Fig. 4-1). The material parameters used in the simulation are listed in Table 4-1. An explicit integration scheme was employed so that the same procedure can be used to simulate an assembly of grains (Nadimi & Fonseca, 2017a). The properties of hard contact behaviour- that is, all the force is transmitted through the contact, were defined between the two contacting bodies.

4.2.1 Mesh size effect

The simulation results are mesh size dependent. Although using a very fine mesh will yield more accurate results, the computational cost involved to simulate a large assembly of grains would require optimising the mesh size value. In order to investigate the effect of mesh size and find the optimal value, a range of mesh sizes was examined. The size of the mesh is quantified using the meshing ratio (MR) parameter, defined as follows

$$MR = s/2R$$

Eq. 4-1

where s is the seeding distance and R is the sphere's radius.

An example of a seeding distance of 0.1 on a sphere with a radius of 1.1mm, which leads to 70 seeds along one perimeter, is presented in Fig. 4-2a. Figs. 4-2b, 4-2c and 4-2d show examples of three spheres with different meshing ratio used in this study.

4.2.2 Normal loading

Hertz theory provides a relationship between normal force (F_N) and displacement for two elastic spheres in contact (Hertz, 1882). In this case, F_N can be determined from the following equation

$$F_N = \iint_S \sigma_{zz} ds = F_{Hertz} = \frac{4}{3} E^* \sqrt{R} \delta_n^{\frac{3}{2}} \quad \text{Eq. 4-2}$$

where E^* is the effective contact stiffness given by $E^* = E/(1 - \nu^2)$, R is the sphere's radius, δ_n is the normal displacement, S denotes the contact area, E is the elastic modulus and ν is the Poisson ratio.

The simulation of an elastic sphere under normal loading was conducted using different meshing ratios, as shown in Fig. 4-3. As the mesh becomes more refined for MR increasing values of 0.090, 0.045 and 0.014, no significant difference can be observed in comparison with the reference results. Only for very coarse meshing, that is MR=0.364, is a very dissimilar response observed.

4.2.3 Tangential loading

Mindlin (1949) and Mindlin & Deresiewicz (1953) investigated the elastic deformation of two contacting spheres under tangential loading. Based on their results, the tangential force-displacement can be described as follows

$$F_{M\&D} = \iint_s \sigma_{xy} ds = \mu F_N \left[1 - \left(1 - \frac{\min(|\delta_t|, \delta_{t max})}{\delta_{t max}} \right)^{\frac{3}{2}} \right] \quad \text{Eq. 4-3}$$

where μ is the friction coefficient, $\delta_{t max}$ is the maximum tangential deflection before sliding, $\delta_{t max} = 0.5\mu\delta_n(2 - \nu)/(1 - \nu)$, and when $|\delta_t| \geq \delta_{t max}$ sliding occurs.

Tangential loading was applied to the sphere, under a constant normal load $F_N=5$ N, for MR=0.045 and MR=0.023. Fig. 4-4 shows the tangential force-displacement obtained using the results from the μ FE against Mindlin and Deresiewicz (M&D) theory, in this plot two distinct regions can be identified, the 'stick' region and the 'slip' region. A perfect agreement can be observed for a MR=0.023. The very small discrepancy in the sticking region, in this case of

$MR=0.045$ for a tangential displacement between $0.2 \mu\text{m}$ and $0.4 \mu\text{m}$, is related to mesh size only.

4.2.4 Torsional loading

Torsional loading is defined as the twisting moment (M_T) around the axis of the contact normal. When M_T is applied in combination with normal loading to an elastic sphere, the contact area will undergo rotation (given by the angle β). The frictional forces at the contact will provide some resistance to sliding. The region that meets the Coulomb's friction condition will experience sliding and the rest of the contact area will undergo sticking according to the normal forces distribution (Dintwa *et al.*, 2005). Lubkin (1951) provides the solution to this problem by proposing an equation to determine the shear stress at the contact surface within the stick region, using elliptical integrals (see Appendix B of this thesis for more details). The complexity of Lubkin's solution was simplified by Deresiewicz (1954) by proposing an explicit approximation between a , M_T and β for simple implementation, defined as follows

$$\frac{G a^2 \beta}{\mu F_N} = \frac{1}{8} \left[1 - \sqrt{1 - \frac{3}{2} \frac{M_T}{\mu F_N a}} \right] \times \left[3 - \sqrt{1 - \frac{3}{2} \frac{M_T}{\mu F_N a}} \right] \quad \text{Eq. 4-4}$$

where G is the shear modulus.

The comparison of the μ FE results for different meshing ratio values against Deresiewicz theory are presented in Fig. 4-5. It can be observed that, although for a mesh ratio of 0.045 there is a large discrepancy between the theoretical and the FE model curves, for finer mesh ratios, of 0.014 and 0.023, a good agreement is shown.

4.2.5 Rotational loading

Rolling resistance or friction is related to energy dissipation due to an asymmetric stress distribution at the contact area. When the stress distribution at the front of

the contact region is higher than at the back, this originates a resistance moment, termed rolling resistance. Similar to the case for M_T , the coexistence of slip and stick zones, makes the calculation of the rolling moment less trivial. Considering a very small angle of rotation, Johnson (1985) proposed a creep model to calculate the difference between the tangential strains in both the stick and slip areas. For a circular contact area and under a transmitting traction Q_x , creep is given by

$$\varepsilon_x = -\frac{3\mu F_N(4-3\nu)}{16G a^2} \left\{ 1 - \left(1 - \frac{Q_x}{\mu F_N} \right)^{1/3} \right\} \quad \text{Eq. 4-5}$$

and when under transmitting traction Q_y , creep is obtained as follows

$$\varepsilon_y = -\frac{3\mu F_N(4-\nu)}{16G a^2} \left\{ 1 - \left(1 - \frac{Q_y}{\mu F_N} \right)^{1/3} \right\} \quad \text{Eq. 4-6}$$

The problem of purely rolling for two spheres in contact was simulated in the μ FE model under constant normal loading of 70 N. The results of this simulation were compared with Johnson's theory and depicted in Fig. 4-6. Similarly to the observations for the torsional loading, although some discrepancy can be observed for an MR of 0.045, for MR values of 0.014 and 0.023 a good agreement between the curves is shown. Here, the rolling resistance is derived from the actual rotational moment between two contacting bodies, which differs from the artificial rolling resistance used in previous studies to account for the effect of grain shape (Iwashita & Oda, 1998; Jiang *et al.*, 2005).

4.3 Behaviour of an Assembly of Spheres

This Section investigates the ability of the model to simulate the response of an assembly of spheres subjected to triaxial compression. First, pure elastic behaviour is assigned to the model, which allows comparison with the theoretical response. The response of the assembly is subsequently investigated using an elastic-plastic model.

4.3.1 Model description

A specimen of 2,000 uniform spheres with radius of 1.1 mm and prepared with a face centred cubic (FCC) packing, was generated within the μ FE framework. This FCC packing was chosen so that the analytical failure method proposed by Thornton (1979) for a FCC array of uniform rigid spheres under triaxial compression can be used (e.g. O'Sullivan *et al.*, 2004; Barreto, 2010; Huang, 2014). According to the theoretical solution, σ_1 is calculated from the following equation for an infinite number of spheres

$$\frac{2\sigma_1}{\sigma_2 + \sigma_3} = \frac{2(1+\mu)}{(1-\mu)} \quad \text{Eq. 4-7}$$

Frictionless rigid boundaries were applied to the triaxial sample. A hybrid mesh of fine elements at the surface ($MR=0.045$) and coarser elements inside the sphere was adopted to reduce the computational cost of the simulation without compromising the accuracy of the results. In total, the model contains 16,197,200 elements and 4,099,372 nodes. The loading process comprises isotropic compression at 50 kPa followed by shearing under controlled strain. The full simulation took approximately 24 hrs running on DELL Precision T7610.

4.3.2 Elastic behaviour

The material parameters used in this simulation are indicated in Table 4-1. Under elastic conditions the failure of the system is believed to occur as a result of the formation of a gap between the initially contiguous spheres. According to Thornton's solution this so called 'failure' is expected to occur at $\sigma_1 = 156.4$ kPa for the confining stress $\sigma_2=\sigma_3=50$ kPa and interparticle friction of $\mu=0.22$. In the μ FE it was seen to occur at $\sigma_1 = 162.5$ kPa (Fig. 4-7a). The small difference between these σ_1 values can be attributed to the effect of the rigid boundaries used in the μ FE simulation when compared with the infinite boundaries considered in the theoretical formulation. The simulation was run for four additional coefficient of friction values (0.3, 0.4, 0.5 and 0.6) and the measured stress ratio σ_1/σ_3 was compared with the theoretical results. A very good

agreement can be observed between the response from the μ FE model and Thornton's theory as shown in Fig. 4-7b.

4.3.3 Elastic-plastic behaviour

Energy may be dissipated by plastic deformation of the contacting bodies which leads to residual deformation and significantly affects reloading of that particular contact area. Plastic behaviour is introduced for the assembly using an isotropic hardening model with 100 MPa yield stress applied to all particles, similarly to what has been described previously. Failure was observed to occur at $\sigma_1=158$ kPa, i.e., a slightly lower value when compared with the pure elastic case. The response of the elastic and the elastic-plastic models was compared in terms of energy quantities. The energy balance for the model can be obtained, according to the first law of thermodynamics. Fig. 4-8 shows the evolution of the applied external work with time for both elastic and elastic-plastic models. It can be seen that failure occurs earlier in the elastic-plastic simulation and after failure the external work is also greater for the elastic-plastic case. In order to further investigate the contribution of plasticity, we compared recoverable and internal energy and also plastic dissipation and frictional dissipation for both the elastic and the elastic-plastic models. Fig. 4-9a shows that all the internal strain energy is recoverable for the elastic simulation (as shown by the overlapping of the two curves) while only approximately one third of the energy is recoverable in the plastic simulation. This is an indicator of the significant contribution of plasticity on unloading of the grains under shearing. In the elastic-plastic model presented, the contribution of plastic dissipation is twice the frictional dissipation as depicted in Fig. 4-9b. The plastic dissipation curve in Fig. 4-9b also suggests the creation of a new plastic contact surface between the grains that got detached at failure. These observations emphasise the need to include plasticity for discrete simulation of granular media.

Fig. 4-10 shows the distribution of elastic and plastic energy dissipation for the case of a single grain in Hertzian contact. Based on this, Amini *et al.* (2015) recently proposed a plastic dissipated energy index for a single elastic-plastic particle given by the ratio between plastic and total contact energy (i.e., the sum of elastic and plastic energies). Using the same concept, a friction dissipated energy index is introduced here, defined as the ratio between friction energy and

total energy. The evolution of those two indices is presented in Fig. 4-11. It can be seen that the plastic index shows a high increase during isotropic compression and exhibits only small fluctuation in the shearing stage. The friction index continues to increase at the beginning of shearing and shows a little drop at failure. Overall, the plastic energy contribution is higher than the frictional energy dissipation, for this loading scenario.

4.4 Conclusions

The ability of the μ FE model to simulate contact behaviour for a system of spheres was demonstrated here by comparison with theoretical formulations. Mesh size dependency was investigated and a hybrid mesh is proposed to improve the computation cost of the simulation. Since contact interaction is modelled based on the deformation of the contacting area and an assigned friction coefficient, this avoids the use of complex contact laws and presents a clear improvement for modelling irregular shaped particles with complex contact topology found in real sand. Dissipated energy indices for friction and plastic behaviour are introduced to quantify energy dissipation due to unloading-reloading of contacts during grain rearrangement. For the case of an assembly of regularly packed spheres under triaxial compression, the greater contribution of plasticity was shown in comparison with friction. The results from the simulations here presented illustrate the potential of the μ FE approach to simulate more realistic contact interaction of granular media, including soil.

4.5 Tables and Figures

Table 4-1. Material parameters used in the simulations

Parameter	Symbol	Value	Units
Young's modulus	E	63	GPa
Poisson's ratio	ν	0.22	-
Density	ρ	2.5	t/m ³
Coefficient of friction	μ	0.22	-

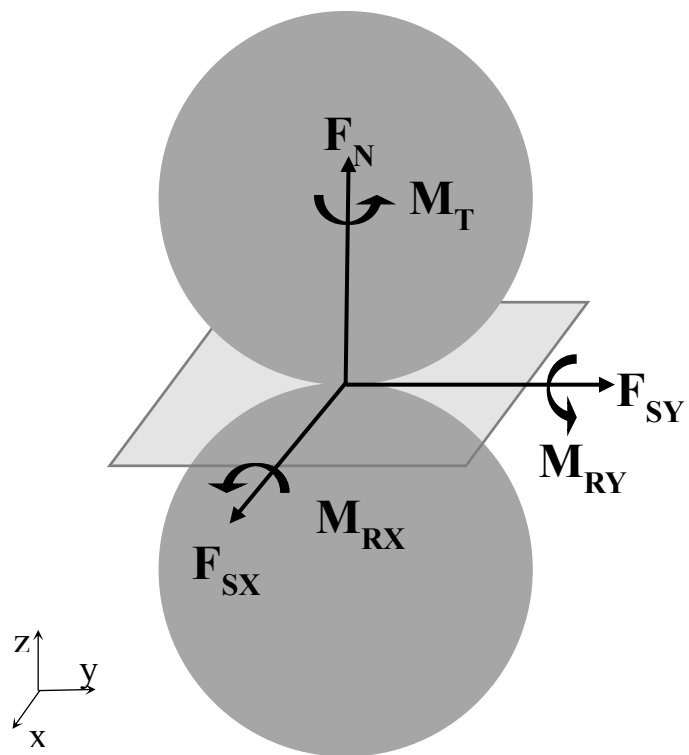


Fig. 4-1. Transmitting forces and moments between two spheres in contact: normal force (F_N), two tangential forces (F_{SX} and F_{SY}), twisting (M_T) and rolling moments (M_{RY} and M_{RX})

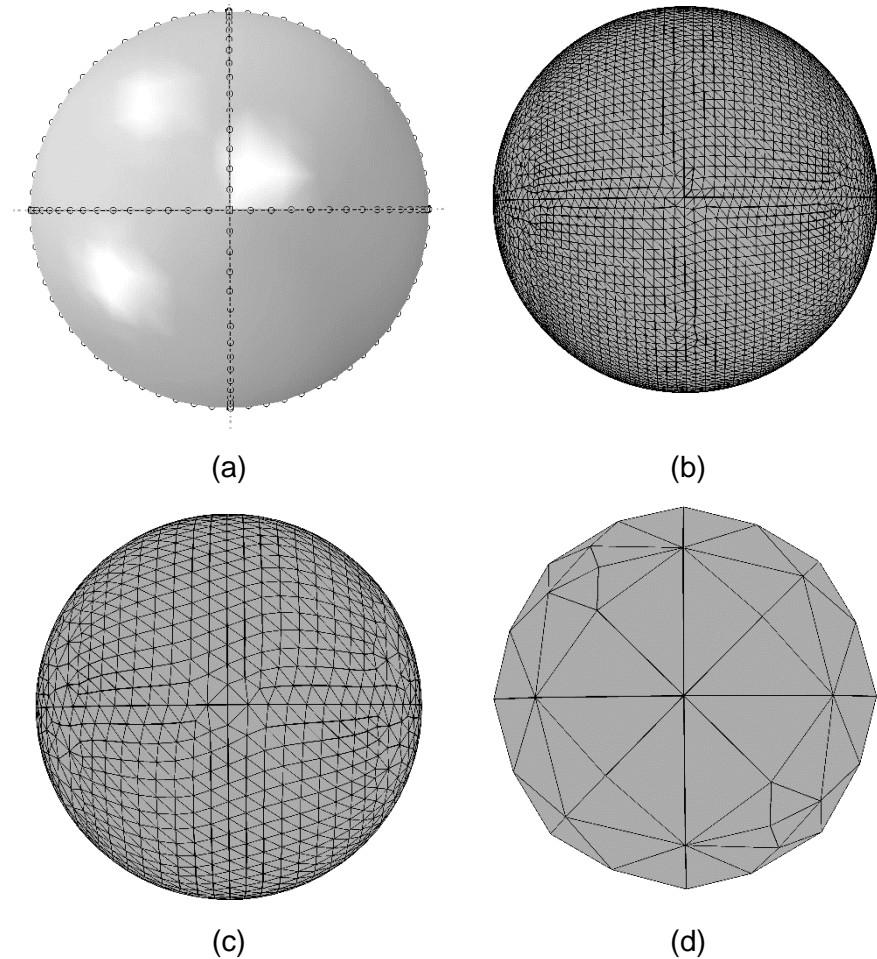


Fig. 4-2. (a) Seeding along three perimetrical edges of a sphere and three examples of different meshing ratios: (b) $MR=0.014$; (c) $MR=0.045$; (d) $MR=0.364$

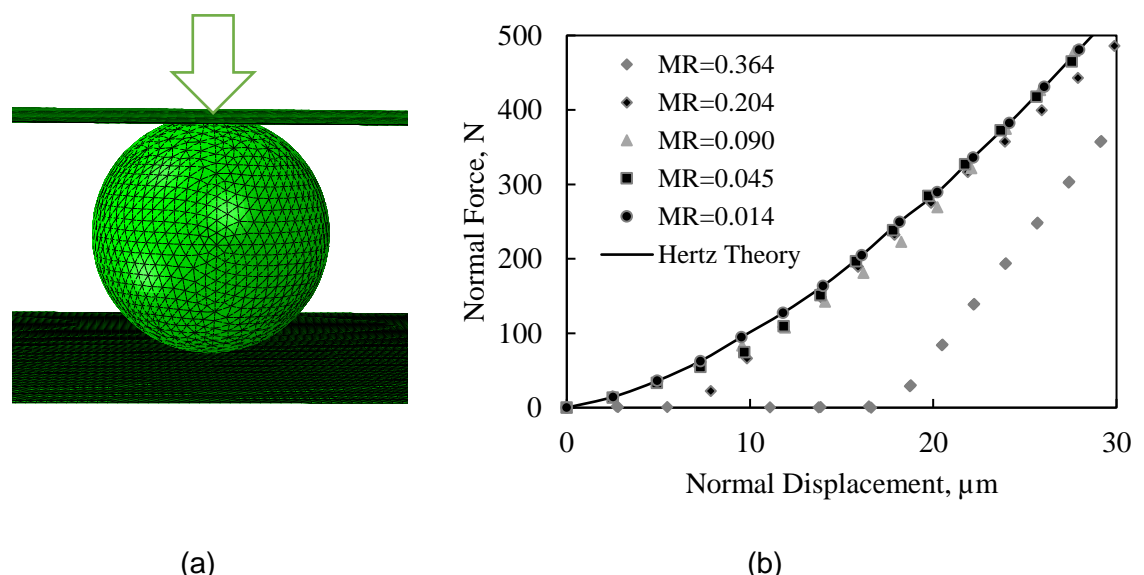


Fig. 4-3. (a) Layout of model for normal loading, (b) effect of the meshing ratio on normal loading of an elastic sphere

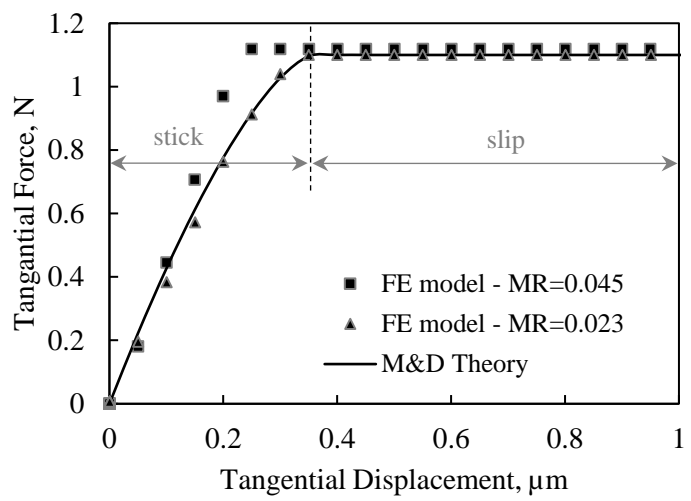


Fig. 4-4. The effect of meshing ratio on the tangential response of a sphere, $F_N=5\text{N}$

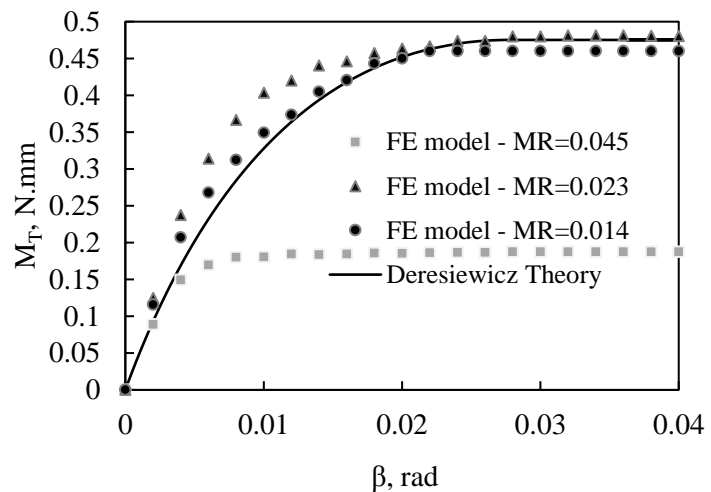


Fig. 4-5. The effect of meshing ratio on the relationship torque versus twisting angle, for an elastic sphere under $F_N=40 \text{ N}$

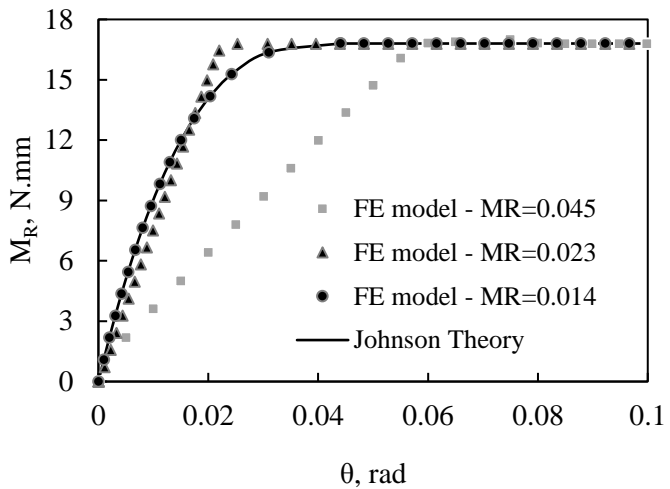


Fig. 4-6. Rolling moment versus rotational angle under constant normal force $F_N=70$ N

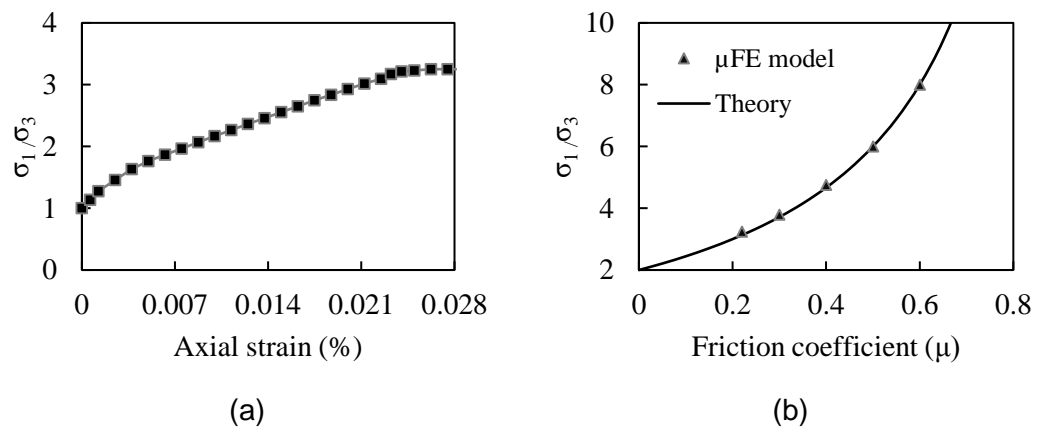


Fig. 4-7. μ FE results for a triaxial test on FCC packed elastic spheres: (a) stress ratio versus axial strain response at $\sigma_3=50$ kPa; (b) comparison with Thornton's theory in terms of stress ratio versus friction coefficient

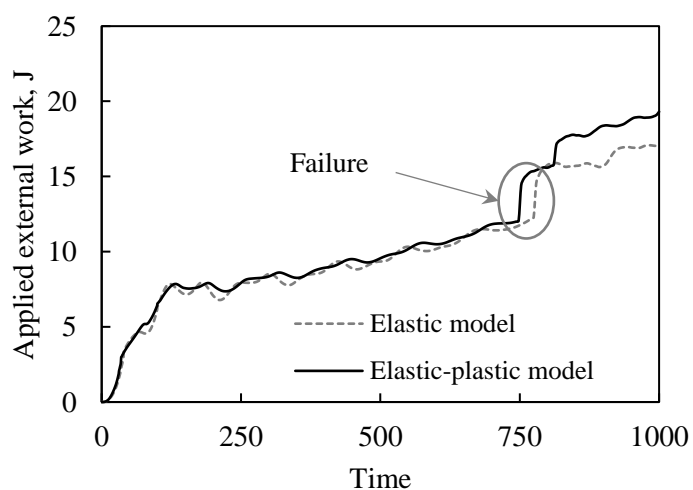
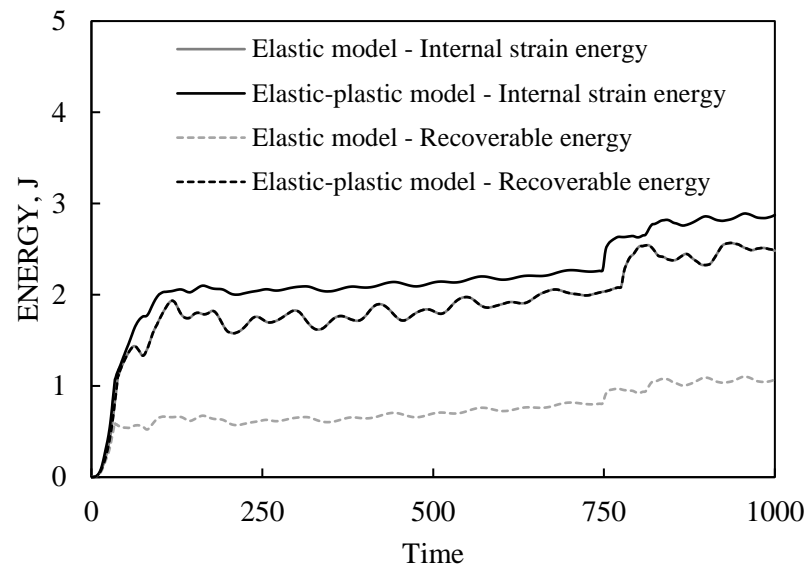
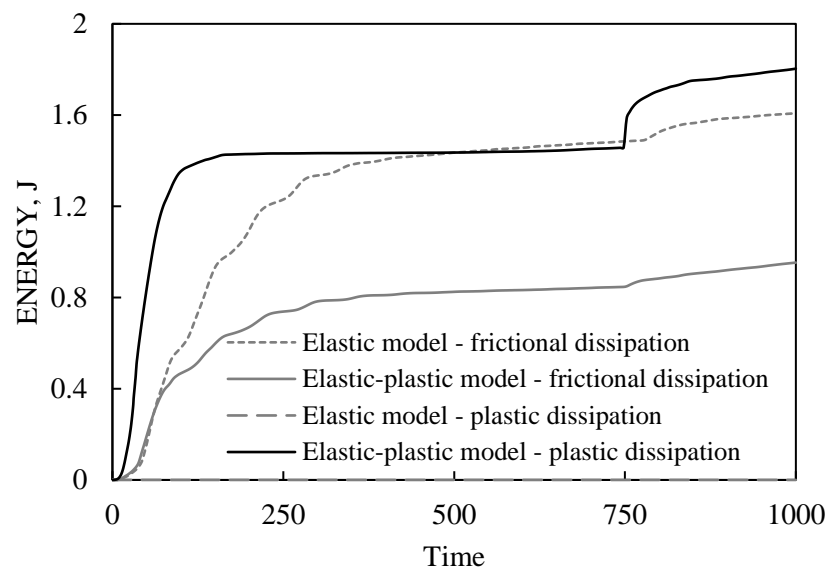


Fig. 4-8. Applied external work versus time for elastic and elastic-plastic models ($\mu=0.22$)



(a)



(b)

Fig. 4-9. (a) Comparison of the internal strain energy with recoverable strain energy for both elastic and elastic-plastic models; (b) Comparison of frictional and plastic energy dissipation ($\mu=0.22$)

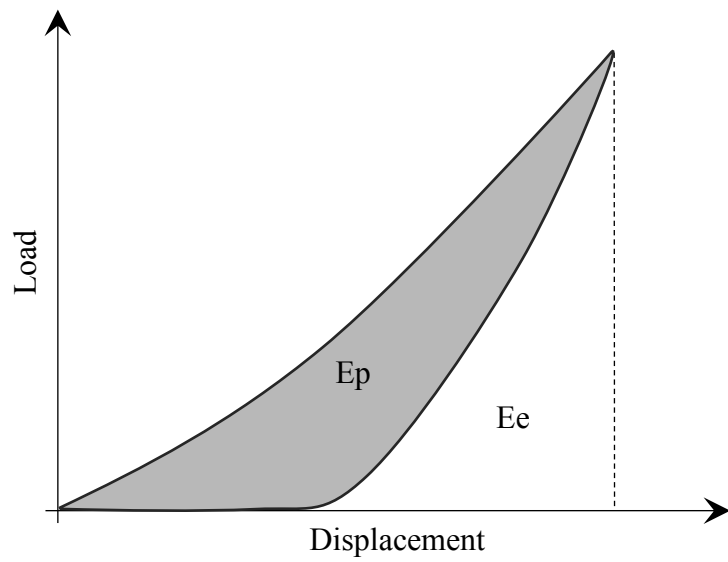


Fig. 4-10. Energy dissipation by plastic yielding during a Hertzian contact cycle, E_e is the elastic energy and E_p is the plastic energy (after Amini *et al.*, 2015)

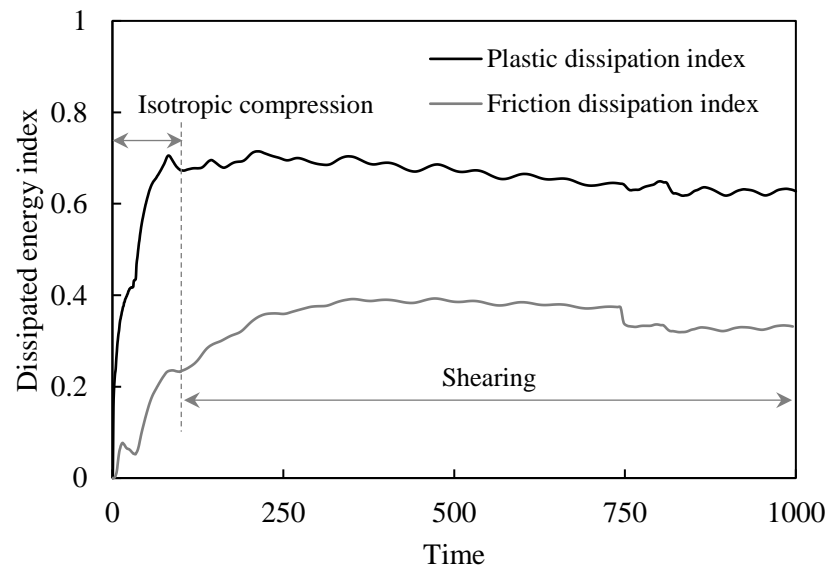


Fig. 4-11. Dissipated energy index for an elastic-plastic assembly of spheres

SINGLE-GRAIN VIRTUALISATION FOR CONTACT BEHAVIOUR ANALYSIS ON SAND

Published in: *Journal of Geotechnical and Geoenvironmental Engineering* 2017;
143 (9): 06017010.

5.1 Introduction

The mechanical behaviour of natural soil results from contact interaction of discrete grains (e.g. O'Sullivan, 2011; Fonseca *et al.*, 2016). The influence of grain morphology, including size and shape, on the overall response of granular materials has been investigated by means of experimental and numerical methods (e.g. Oda & Iwashita, 1999; Lu & McDowell, 2007; Vlahinić *et al.*, 2014; Nguyen, *et al.*, 2015). There are, however, very few studies on the effect of single grain morphology and contact topology on contact interaction (Cavarretta *et al.*, 2010; Wang & Coop, 2016). Previous studies on single grain response have, for the most part, focused on the tensile strength and breakage potential of a single grain at high stress level (McDowell & Bolton, 1998; Nakata *et al.*, 2001; Zhao *et al.*, 2015). Zhao *et al.* (2015) presented single grain compression of a few sand grains using micro-Computed Tomography (μ CT) and noted that grain morphology and initial microstructure are the most important factors for determining the fracture pattern. For idealized particulate systems, Russell & Einav (2013) derived the energy dissipation due to fracturing of a single grain and by load redistribution in the surrounding grains. However, despite the wide range of physical, numerical and analytical studies, single grain response has not been fully characterised. In particular, there is little understanding of the behaviour at low stress level.

It is expected that for irregular shapes under external applied load, disturbance of stress distribution within the grain will occur, which will affect the measured normal force-displacement response. The normal force-displacement relationship is critical for discrete modelling of soils. Hertzian theory provides the relation of normal force-displacement for two contacting spheres (Hertz, 1882), which constitutes a large simplification for representation of soil grains. This

theory was adopted in soil mechanics to model the discrete nature of soil (Cundall & Strack, 1979) and has been widely used since (O'Sullivan, 2011; Thornton, 2015).

For a large part of engineering applications, the maximum value of the contact forces in the assembly is believed to be lower than 10 N (Cavarretta, 2009). At low stress level, it has been observed that the initial contact displacements are the result of damage of asperities (Greenwood & Tripp, 1967; Kendall, 1969). Greenwood & Tripp (1967) have shown that Hertzian response occurs only after a threshold load. Johnson *et al.* (1971) developed a new contact model based on these observations.

Asperities and contact topology are scale dependent parameters. Figs. 5-1a and 5-1b show a detailed contact between two sand grains (Terzaghi *et al.*, 1996) and the multiple-asperities scale (Archard, 1957 cited in Greenwood & Wu, 2001). In soil mechanics, Cavarretta *et al.* (2010) quantified the surface roughness of sand grains and glass beads using an optical interferometer. The authors observed that the initial rotation of the grain together with asperity damage cause the pre-Hertzian response for irregular grains; concluding that although the material response can be slightly dependant on the surface roughness, the influence of grain shape is more significant. Altuhafi *et al.* (2016) concluded that grain shape affects the intercept of the critical state line in the e - $\ln p'$ plane for low stress levels. They also highlighted that shape has a strong effect on many aspects of sand behaviour, whereas the effect of roughness is more subtle.

This paper investigates the effect of grain morphology on single grain response under compression. The methodology consists of capturing the morphology of the grain, from the experimental test, to be used in numerical simulations with the aims of a) calibrating discrete numerical simulations and b) investigating the grain-scale parameters shaping the mechanical response. The outcome can contribute to the development of new contact laws considering the effect of grain morphology and asperities as investigated here. In this way, discrete numerical simulations, which include conventional discrete element methods (DEM) and other approaches using deformable grains (e.g. Gethin *et al.*, 2003; Komodromos & Williams, 2004; Nezamabadi *et al.*, 2015; Nadimi & Fonseca, 2017a), can be enhanced. The morphology of the grain is obtained using a novel technique that uses 2D images of the grain to reconstruct the 3D shape. This technique, largely

inspired from μ CT, has the advantage of only requiring the use of a camera and other simple tools readily available in a geotechnical laboratory. The image acquisition is, however, limited to a grain at a time. In contrast with studies that have considered breakage, this paper focuses on the behaviour of grains under low compression loads.

5.2 Virtualisation of a Single Grain

This section describes the image acquisition system used to obtain the projections of the grain and the algorithm used to reconstruct the 3D images and subsequently generate the numerical mesh. The accuracy of the reconstruction algorithm was examined for artificial projections of a sphere.

5.2.1 Image acquisition system

The setup developed to acquire the incremental rotation included a camera, lens, remote controller, stepper motor (to rotate an object in controllable and precise increments), control kit, power supply, and set background. A schematic of the setup is shown in Fig. 5-2.

The camera used was a digital SLR camera Canon (Tokyo, Japan) EOS 60D 18 MP CMOS with EF-S 18-200 mm lens and 65 mm macro tube. A remote controller was used and shutter sound was muted to minimise any potential vibration. The motor was a hybrid, permanent magnet stepper motor with 0.9° step angle and 0.22 Nm holding torque. The step angle accuracy was $\pm 5\%$. The object to be imaged was mounted on the shaft of the motor using a tube with 0.5 mm diameter and with a pedestal ending shape to make the contact area with the object as small as possible. The grain was glued to the end point of the pedestal. The image resolution is controlled by the distance between the camera lens and the object. The 2D projections of the grain were acquired at various positions by rotating the step motor by an angle θ .

5.2.2 Volume reconstruction & mesh generation

Following image acquisition, the process of conversion of a real sand grain into a numerical grain involved three main steps: image binarisation, volume

reconstruction, and mesh generation, as detailed in the flowchart presented in Fig. 5-3. These operations were implemented using an in-house MATLAB (Mathworks, 2016) script with the rationale as follows. The binarisation process requires the selection of the features of interest in the image, which in this case was the grain. In order to extract the grain from the image, there was need to identify the pixels forming the grain and separate them from the pixels composing the background and the pedestal. The histogram of pixel intensity showed three clear peaks of higher intensities corresponding to the pixels composing the grain, the pedestal and the background, respectively. Using Otsu's method (Otsu, 1979), the threshold value was obtained, below which pixels take value 0 (pedestal and background pixels) and above take value 1 – that is, pixels forming the grain projection (grain area). A total of N binary images, each associated with a unique label i (varying between 1 and N) and a specific θ angle (acquisition angle), were used to reconstruct the 3D grain.

The algorithm for reconstruction consisted, first, of extending (extruding) the grain projection from each binary image along a constant depth to form a cylinder with the cross section defined by the grain projection. For computational reasons the depth was taken as the largest dimension of the grain. The 3D grain was obtained from finding the intersection of all the N cylinders rotated by the cumulative angle of $(i-1)\times\theta$ according with the schematics shown in Fig. 5-4. Fig. 5-5 shows the reconstruction process of a sphere. In this case, it can be observed that with the use of only the intersection of two cylinders (or projections), the overall 3D shape could not be accurately captured (Fig. 5-5b), but as the number of projections increases to 6 (Fig. 5-5c) and subsequently to 30 (Fig. 5-5d), the 3D shape becomes progressively more refined. The optimal angle of rotation (θ) and number of projections needed to accurately capture the 3D outline is investigated later in this Section.

The numerical mesh used consisted of triangular elements at the surface and tetrahedral elements filling the inside of the grain. The surface mesh extraction technique used here is a refinement of the constrained Delaunay triangulation (Shewchuk, 2014). The quality of the mesh is controlled by three input parameters: a) the element size at the surface, b) the angle of the triangles and c) the volume of the tetrahedrals.

5.2.3 Sensitivity analysis of the reconstruction method

The influence of the number of projections on the reconstructed 3D outline was investigated for the case of a standard spherical shape. Two sizes of spheres with 500 μm and 1000 μm diameter were considered, corresponding to the size range of the sand grains used in this study. In both cases, a binary image of a circle with the diameter of the respective sphere was used as the planar projection (Figs. 5-5a and 5-6a). Both images have a resolution of 5 μm , which means that the larger sphere has a more detailed representation (Figs. 5-5e and 5-6e). The analysis was carried out by comparing the real volume of the object (V_R) with the measured volume (V_M). The V_M was obtained by counting the voxels (volume pixels) in MATLAB. The evolution of the V_R/V_M ratio with the number of projections (and associated angle of rotation) is presented in Figs. 5-7a and 5-7b for the small and large spheres, respectively. The reconstructed shapes are also presented for the cases of 2, 6 and 30 projections in Figs. 5-5b-d and Figs. 5-6b-d, again for the small and large spheres, respectively. We can observe that using only two projections results in a very crude representation of the sphere (Fig. 5-6b) but the overall shape was well captured when the number of projections equals four, for which a volume ratio of approximately 0.95 was obtained (Fig. 5-7). The measured volume equals the real volume when the number of projections equals 20 for the large sphere and 25 for the smaller sphere. Thus, 25 projections were used in this study.

The measured volume following meshing was also compared with the real volume for a coarse and a fine mesh (Figs. 5-7a and 5-7b). The V_M of the meshed volumes was measured in ABAQUS finite element package (Dassault Systèmes, 2014) using mass properties. As expected, a better agreement between the reconstructed and the meshed volumes is observed for the fine mesh. Using a coarse mesh seemed, in this case, to underestimate the reconstructed volume for the small grain and overestimate for the larger grain (more detailed image). Nonetheless, it can be said that the effect of meshing in the reconstructed volume was minimal.

5.3 Single Grain Compression Test

This section describes the experimental and numerical single grain tests carried out on glass beads and Leighton Buzzard Sand (LBS). The spherical grains were used in order to compare the results against the well-established Hertz theory and thus validate the numerical and experimental modelling.

The experimental tests were carried out using the strain controlled machine ‘Instron 5969’ (Instron ®), shown in Fig. 5-8. The instrumentation accuracy was measured to be $<1\text{ }\mu\text{m}$ for displacement and $<0.1\text{ N}$ for load. Prior to the experimental test, each grain was virtualised as described in the previous Section. A total of 25 projections, corresponding to an angle of rotation of 7.2° , were acquired for each grain ($N=25$ and $\theta=7.2^\circ$). In other words, each increment of rotation includes eight steps of 0.9 degree. The surface of the grain was cleaned with acetone before testing in order to remove any dust or glue remains.

5.3.1 Single grain tests on spherical beads

The nonlinear elastic relationship between the normal displacement and the normal contact force was computed using the simplified version of Hertz theory (Hertz, 1882; Zheng *et al.*, 2012) for two identical spheres in contact

$$F_N = \iint_S \sigma_{yy} ds = F_{Hertz} = \frac{4}{3} E^* \sqrt{R} \delta_n^{\frac{3}{2}} \quad \text{Eq. 5-1}$$

where E^* = effective contact stiffness given by $E^* = E/(1 - \nu^2)$, R = sphere's radius, δ_n = normal displacement, S = contact area, E = elastic modulus and ν = Poisson ratio.

This problem was reproduced in the framework of combined finite-discrete element model using dynamic explicit formulation by means of an explicit central difference time integration scheme (Munjiza, 2004; Nadimi & Fonseca, 2017a). Due to symmetry, one sphere in contact with a rigid plate was simulated (Fig. 5-9). Physical and mechanical parameters of silica sand were assigned to the model, as listed in Table 5-1. The diameter of the sphere was defined based on the size of one of the LBS grains investigated here. Properties of hard contact

were defined for the normal interaction. Due to deformation of the elastic sphere, the reaction force shows a nonlinear relationship with displacement as proposed by Hertz theory (Fig. 5-10a). A good agreement between the two curves can be observed for displacements lower than 30 μm . Beyond this displacement value, the numerical and theoretical responses start to diverge; because the Hertz solution is applicable only at small normal displacements (Vanimisetti & Narasimhan, 2006; Zheng *et al.*, 2012). At the end of the test, the internal stress field within the spherical grain showed a regular pattern of stress distribution as presented in Fig. 5-10b.

The experimental test was carried out on a single glass bead and the response was again compared with the theory to validate the setup. The physical and mechanical properties of the glass bead used for the analytical solution are listed in Table 5-2. Fig. 5-11 compares the experiment and the theory in terms of normal force and displacement, which showed excellent agreement and slightly stiffer response for displacements larger than 30 μm in line with the numerical simulations presented before.

5.3.2 Single grain tests on sand

Four LBS grains were randomly selected for this study. A view of the 3D outline after meshing, for each grain, are shown in Fig. 5-12. The nodes and elements were generated in MATLAB and imported into ABAQUS using an *.inp file containing the nodal coordinates and properties of all elements forming the mesh. The problem was solved using a dynamic explicit formulation mentioned previously. The diameter (d) of each grain, as presented in Fig. 5-12, was defined here as the distance between the two horizontal platens used in the loading test. The geometrical resolution, or voxel size, used varies between 4 and 5 μm depending on the distance of each grain to the camera. For the experimental test, the grain was placed in the loading system in a stable position which was recorded to better reproduce the grain position in the numerical domain and thus to better replicate the experimental response.

The numerical simulations were carried out for the case of a purely elastic grain and also using an elastic-perfectly plastic constitutive model with a yield stress of 100 MPa. To model these silica sand grains, the elastic modulus was assumed

to be 100 GPa and the Poisson ratio of 0.22. Similarly with the experimental tests, for the numerical simulation, each grain was compressed between two rigid plates. Hard contact was assumed for contact interaction. The experimental results and the numerical response are compared in Fig. 5-13 for the elastic model. Similarly, the results of the experiments and the numerical elastic-plastic response will be discussed later (Fig. 5-15).

5.4 Results and Discussion

Referring to Fig. 5-13, it can be seen that for all cases the experimental results showed an initial pre-Hertzian response, as reported in the literature. A common feature in these four cases was the threshold load value of $F_N=2.0$ N, marking the transition from an initial pre-Hertzian response to a Hertzian response. The corresponding displacement values (δ_i) for this transition point were, however, different for each grain. Displacement values of $\delta_i=16$, 23, 91 and 11 μm , respectively, for Grains LBS1, LBS2, LBS3, and LBS4 were measured. This initial displacement was believed to result from the effect of asperities and grain rotation in the experiments. Since asperity values measured for sand are less than 1.5 μm (Cavarretta *et al.*, 2010; Altuhafi *et al.*, 2016); it could be concluded that contact roughness constitutes only a small contribution to δ_i and the larger effect comes from the initial rotation of the grain (due to the irregular shape of the grain, more precisely the top irregularity and the platen).

When comparing the numerical with the experimental results, and again focusing on the pre-Hertzian part of the curve, very good agreement is observed for Grains LBS1, LBS2 and LBS4. This suggested that the level of detail of the images, which captures the overall form and not the asperities, could still provide a good prediction of the behaviour at very low stress. This again supports the previous hypothesis of the importance of shape over roughness. Grain LBS3 shows exceptionally high experimental initial displacement, $\delta_i= 151$ μm , and although the numerical prediction was also significantly large, $\delta_i= 91$ μm , the agreement was less good (Fig. 5-13c). The explanation offered here is that the shape of this grain did not allow a clear stable position, thus contributing to: a) further grain rotation during testing until two stable and near parallel contacts can be formed with the top and bottom platens, respectively and b) difficulties in reproducing the position of the grain in the numerical simulation and thus in capturing the

experimental behaviour. To support this, the evolution of the stress distribution within the grain was analysed. Fig. 5-14 shows the stress propagation from the top and bottom contact points at various load stages for Grain LBS3 (through a vertical cut). The grain in the initial position, before load was applied, is shown in Fig. 5-14a; after 25 μm displacement we can observe a small stressed area near the top and bottom contacts (Fig. 5-14b). However, as the applied force increased, the contacts were lost because of rotation of the grain, resulting in an absence of stressed areas at this stage (Fig. 5-14c). With further increases in force and displacement, new contacts with new locations started to form, as shown in Fig. 5-14d. These newly formed contacts were shown to be stable active contacts able to transmit forces higher than the threshold value (Figs. 5-14e and 5-14f).

From the normal force-displacement response for the elastic-perfectly plastic grain presented in Fig. 5-15, a softer numerical response when compared with the elastic formulation can be observed and thus better agreement with the experimental results. This was expected because the quartz grains are inelastic. Thus, using this finite-discrete element framework, which allowed introducing plasticity in the grain, presented significant advantages to more accurately capture the physical behaviour of the material. Future work will account for the tensile strength of the material to represent the drop in load using fracture mechanics criteria (e.g. Moes *et al.*, 1999; Borst, *et al.*, 2004). Finally, to illustrate the disturbance in stress caused by the shape of the grain, Fig. 5-16 shows the internal stress distribution within the grain for the final stage of loading.

5.5 Conclusions

A methodology was presented to calibrate contact behaviour to advance the numerical representation of grains in simulations using discrete approaches. The imaging setup is very simple and can be easily implemented in any laboratory, thus presenting some advantages when compared with more sophisticated techniques such x-ray compute tomography. The ability of the acquisition method to capture the irregular 3D outline of a grain also enables it to quantify grain's size and shape (e.g. Fonseca *et al.*, 2012; Sun *et al.*, 2014). The analyses presented here demonstrate the suitability of the method for silica sand grains of approximately 1 mm diameter. Larger and smaller grains can be used, with a

compromise of a lower level of detail; that is, larger grains better definition of the outline. By using virtualised Leighton Buzzard Sand grains in single grain numerical simulations, the significance of the initial arrangement of the grain under normal compression for irregularly shaped grains was demonstrated. The numerical simulations presented here captured almost perfectly the pre-Hertzian response of the grain, which was shown to be highly dependent on the grain's shape and its ability to form stable contacts with the load platens. The evolution of stress distribution within the grain was used throughout loading to demonstrate the role of initial particle rotation on the formation and disappearance of new contacts up to the formation of a stable active contact capable of withstanding the load until crack or breakage. It is therefore suggested that contact roughness, for silica sand, is of little significance when compared with the effect of contact topology in modelling contact behaviour.

5.6 Tables and Figures

Table 5-1. Physical and mechanical properties used in the numerical simulations of silica sand

Properties	Value	Unit
Elastic Modulus	100	GPa
Poisson's ratio	0.22	-
Diameter	0.815	mm

Table 5-2. Physical and mechanical properties used for the analytical solution of glass beads

Properties	Value	Unit
Elastic Modulus	63	GPa
Poisson's ratio	0.22	-
Diameter	2.15	mm

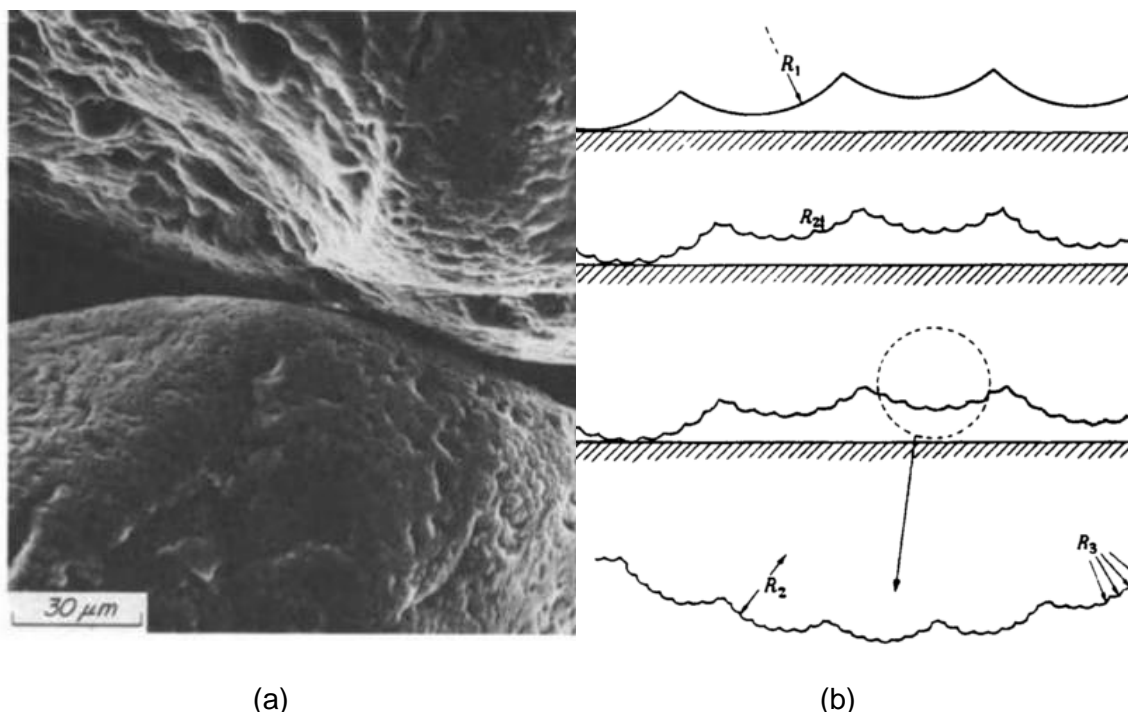


Fig. 5-1. (a) Micrograph of contact between grains of quartz sand (reprinted from Terzaghi et al. 1996, with permission); (b) example of Archard 1957 model of multiple roughness scales (Meccanica, "Surface Roughness and Contact: An Apology," 36, 2001, J.A. Greenwood, © Kluwer Academic Publishers 2001, with permission of Springer)

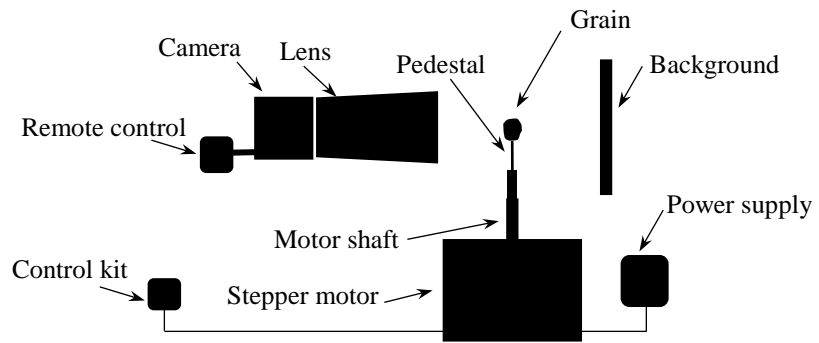


Fig. 5-2. Schematic of setup used for image acquisition

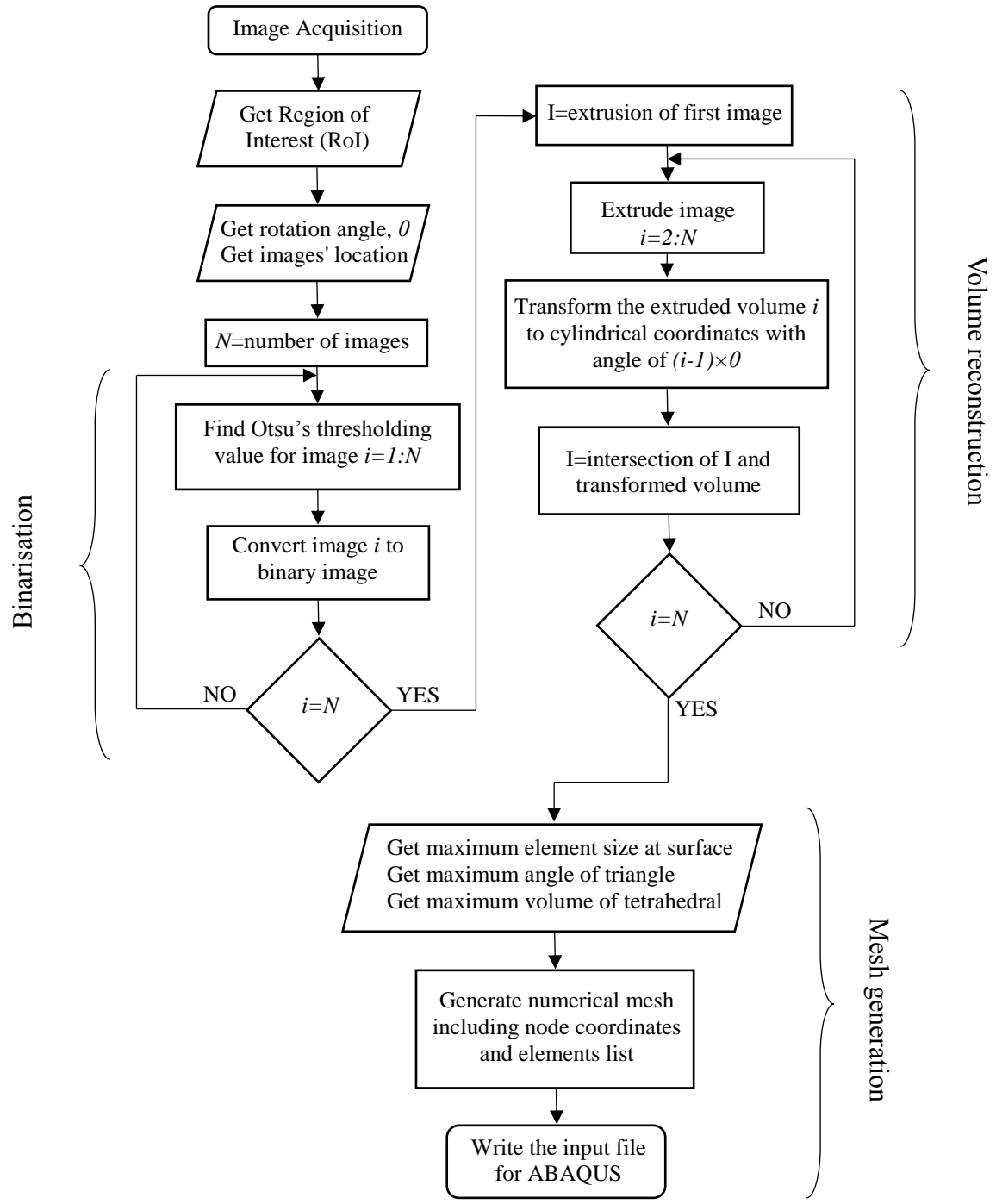


Fig. 5-3. Flowchart of algorithms used for volume reconstruction and meshing

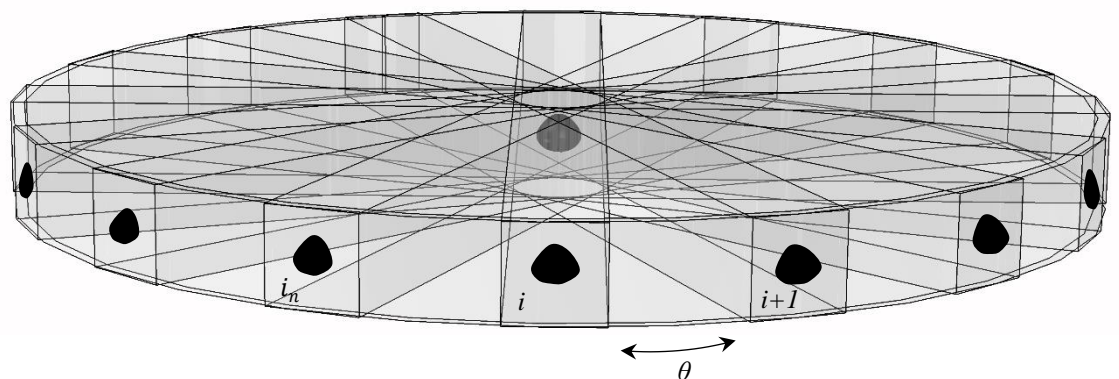


Fig. 5-4. Schematic of the incremental projection method used to reconstruct the 3D volume

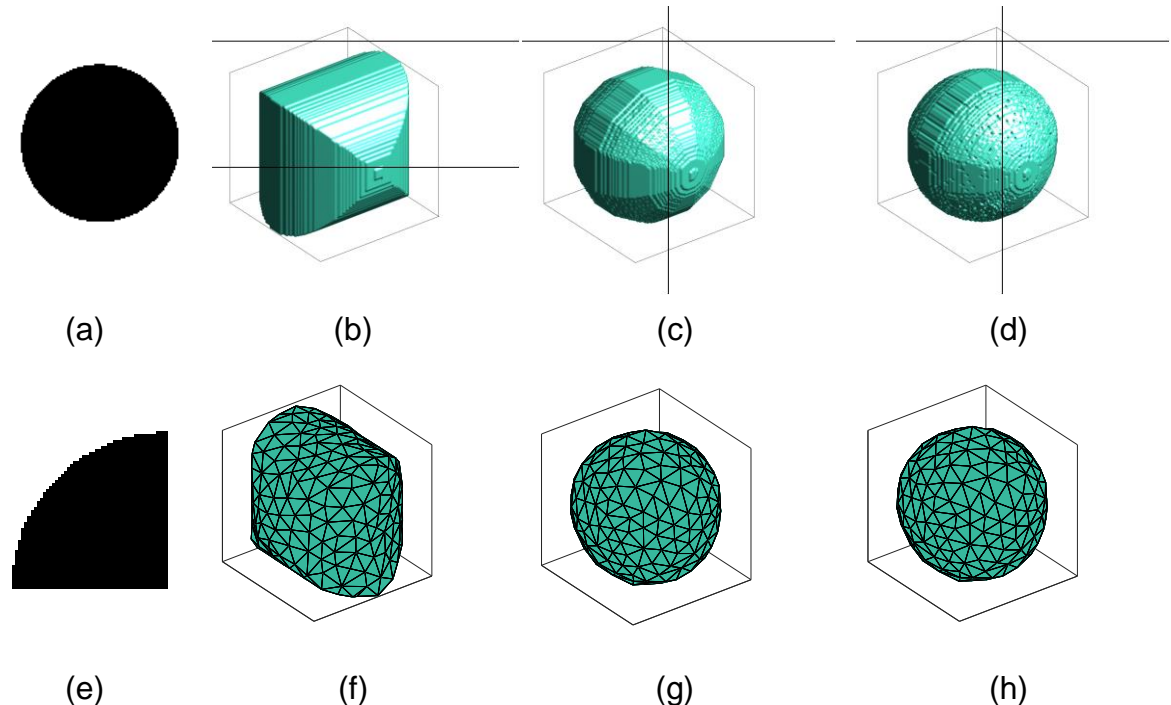


Fig. 5-5. Reconstruction of a sphere with 500 μm diameter (a) planar projection; (b) reconstructed volume (RV) using 2 projections; (c) RV using 6 projections; (d) RV using 30 projections; (e) zoomed view of (a); (f) coarse meshed volume (CMV) of (b); (g) CMV of (c); (h) CMV of (d)

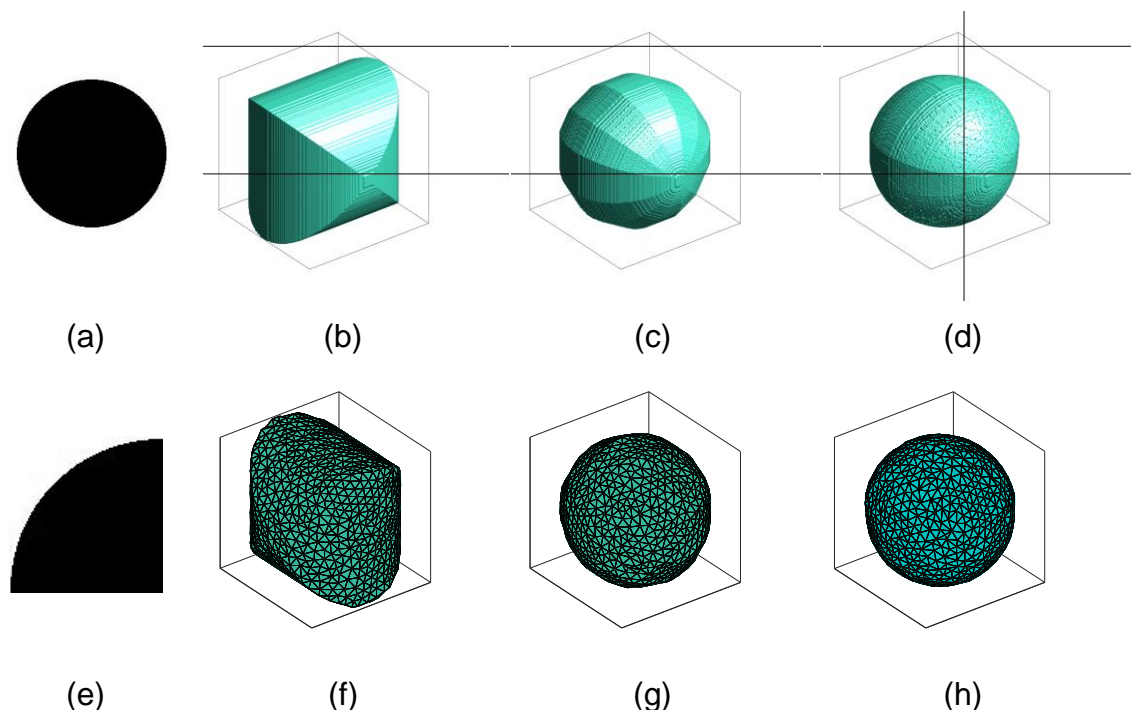
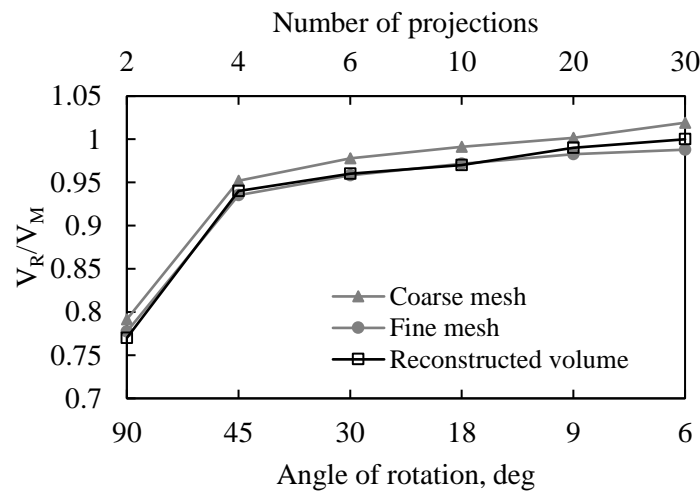
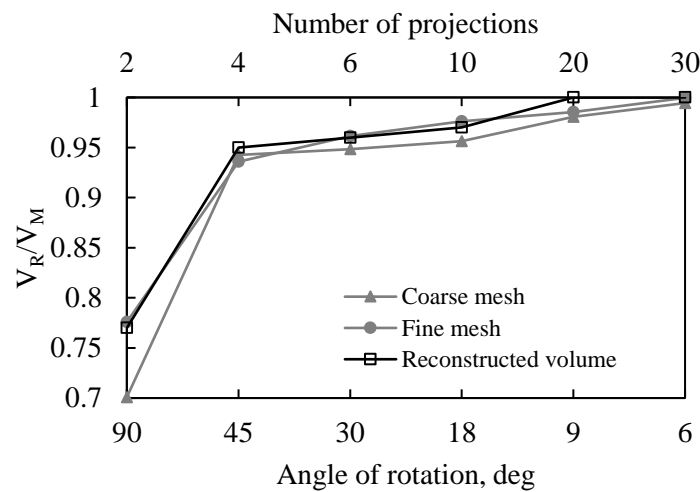


Fig. 5-6. Reconstruction of a sphere with 1000 μm diameter (a) planar projection, (b) reconstructed volume (RV) using 2 projections; (c) RV using 6 projections; (d) RV using 30 projections; (e) zoomed view of (a); (f) coarse meshed volume (CMV) of (b); (g) CMV of (c); (h) CMV of (d)



(a)



(b)

Fig. 5-7. Evolution of the ratio between real volume (V_R) and measured volume (V_M) for a sphere with (a) 500 μm diameter (b) 1000 μm diameter



Fig. 5-8. Setup for the single grain experiments

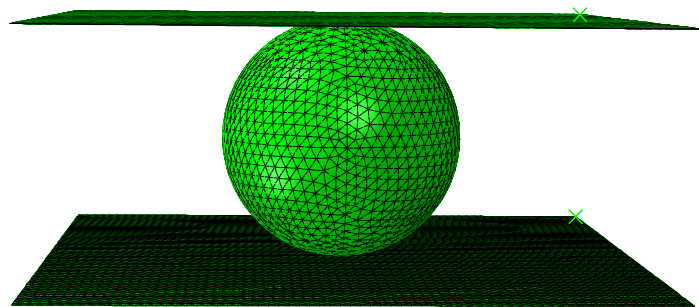


Fig. 5-9. Geometry and mesh of a sphere in contact with two rigid plates

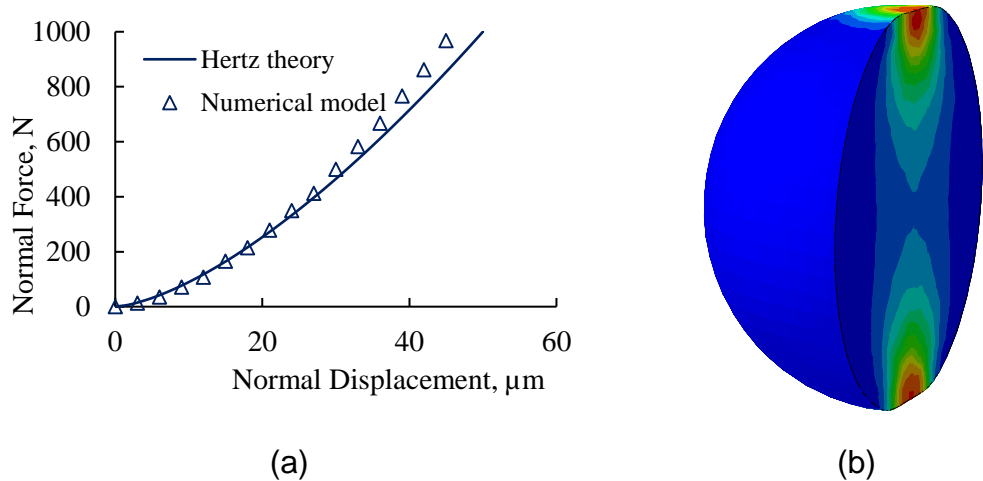


Fig. 5-10. (a) Comparison between numerical modelling and Hertz theory for a single grain under compression; (b) internal stress distribution in a sphere

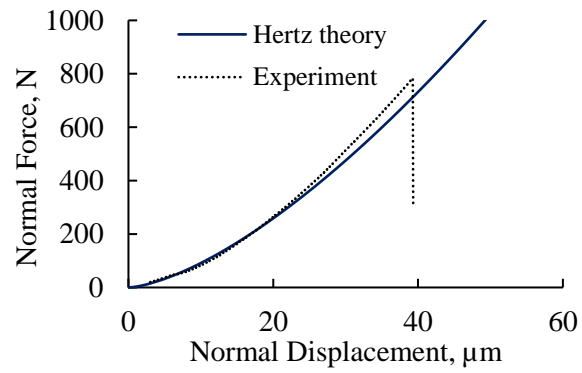


Fig. 5-11. Single grain response of glass beads from Hertz theory and experimental tests

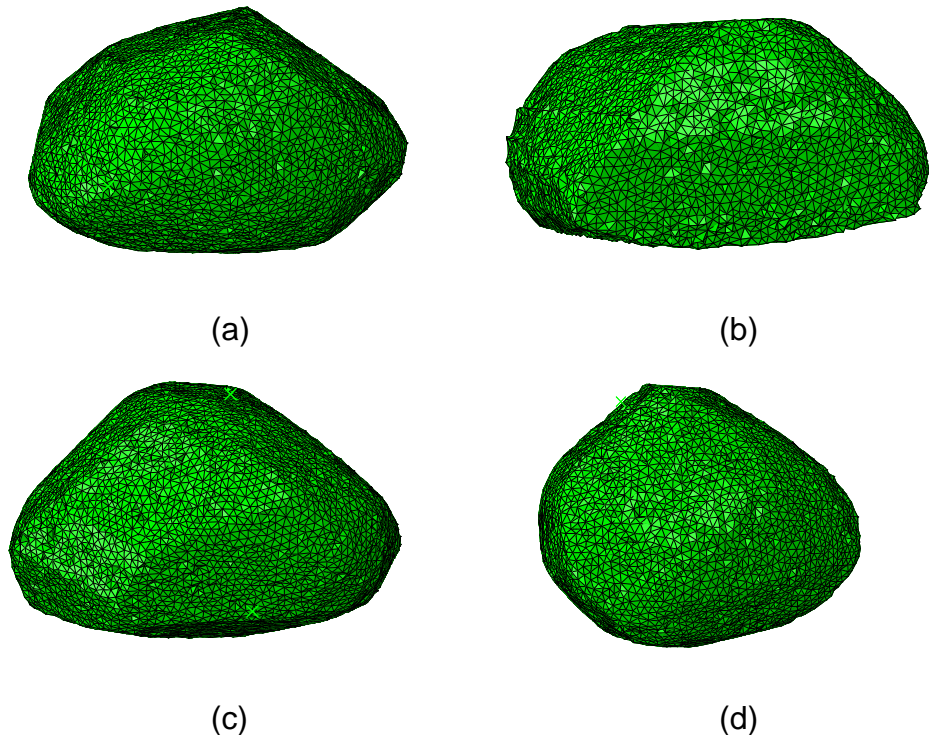


Fig. 5-12. Four grains tested and corresponding measured diameter (d): (a) LBS1, $d=815 \mu\text{m} \approx 200\text{voxel}$; (b) LBS2, $d=1064 \mu\text{m} \approx 226\text{voxel}$; (c) LBS3, $d=1073 \mu\text{m} \approx 253\text{voxel}$; (d) LBS4, $d=1042 \mu\text{m} \approx 254\text{voxel}$

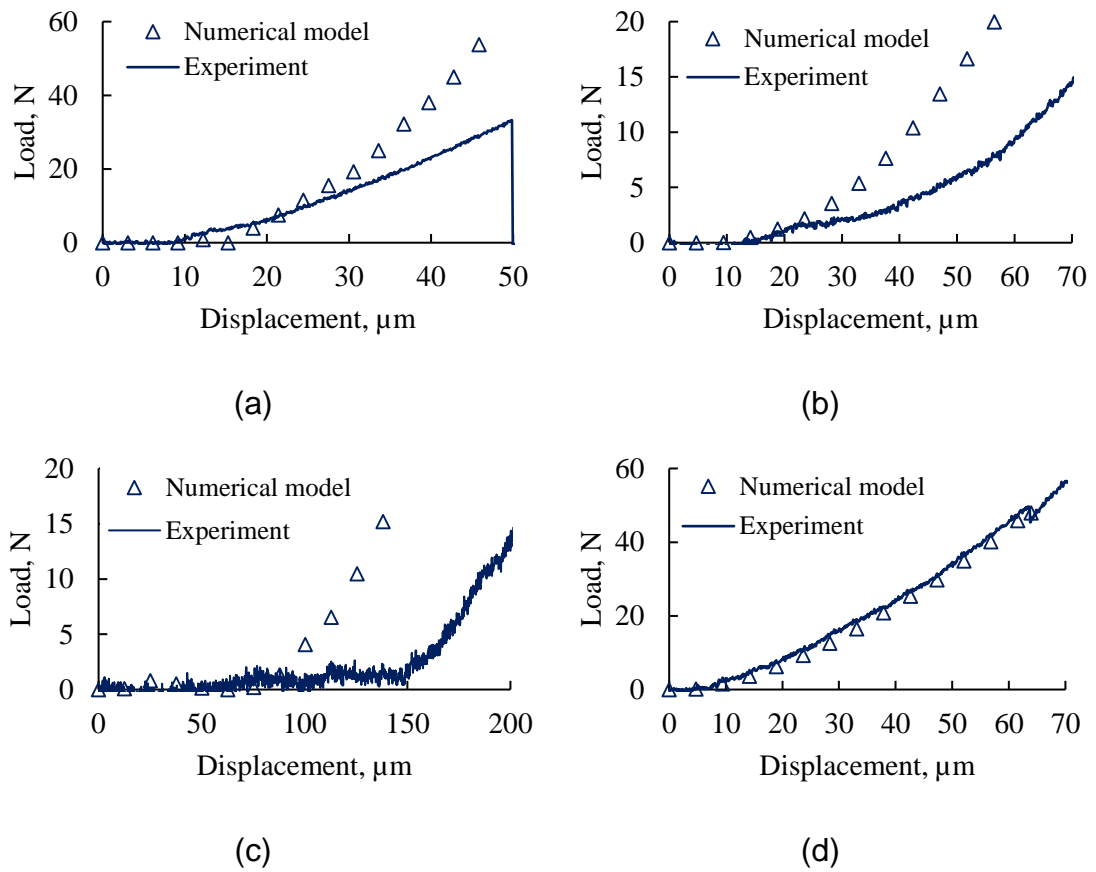


Fig. 5-13. Normal force displacement response from elastic numerical simulations and experimental tests: (a) LBS1; (b) LBS2; (c) LBS3; (d) LBS4

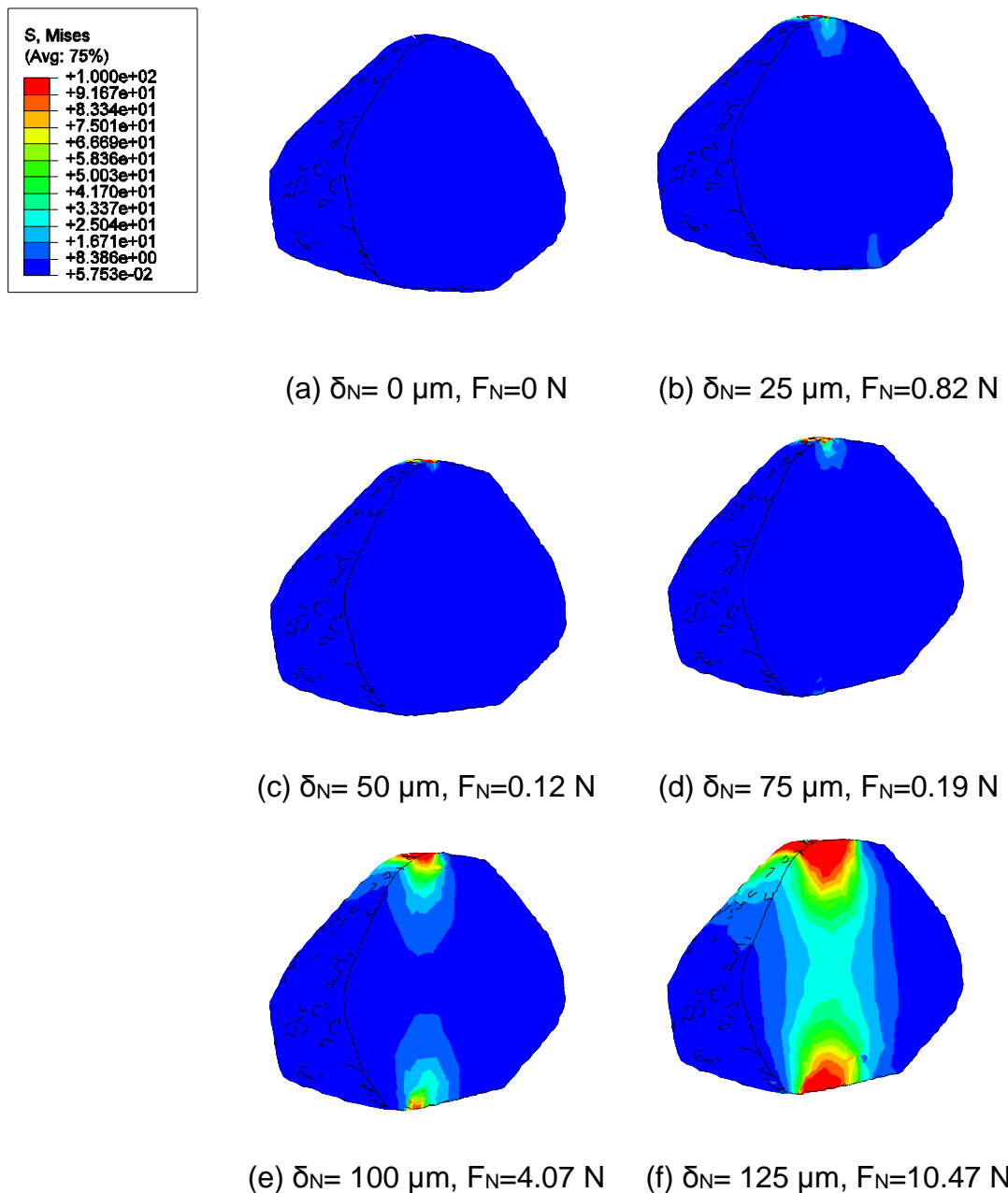


Fig. 5-14. Stress distribution in Grain LBS3 at different loading stages, through a vertical section: (a) displacement = 0 μm , $F_N = 0 \text{ N}$; (b) displacement = 25 μm , $F_N = 0.82 \text{ N}$; (c) displacement = 50 μm , $F_N = 0.12 \text{ N}$; (d) displacement = 75 μm , $F_N = 0.19 \text{ N}$; (e) displacement = 100 μm , $F_N = 4.07 \text{ N}$; (f) displacement = 125 μm , $F_N = 10.47 \text{ N}$

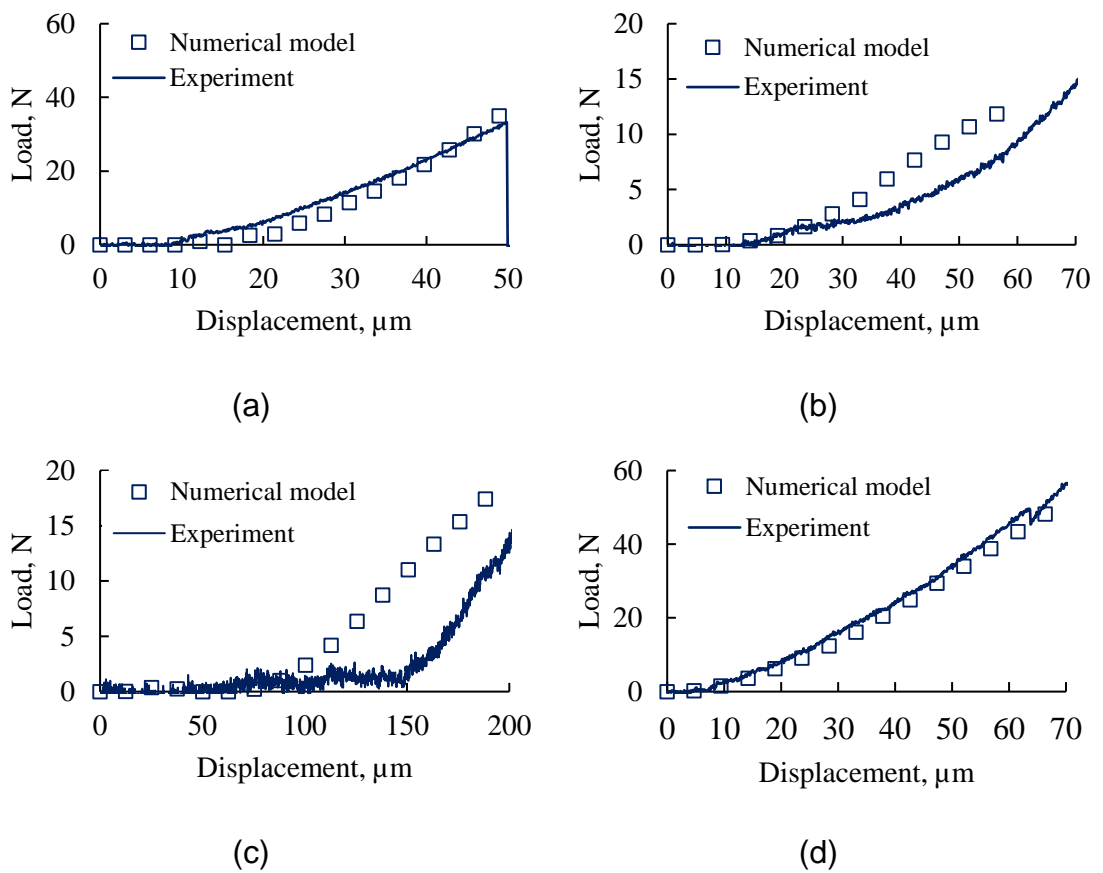


Fig. 5-15. Normal force displacement response from plastic numerical simulations and experimental tests for (a) LBS1; (b) LBS2; (c) LBS3; (d) LBS4

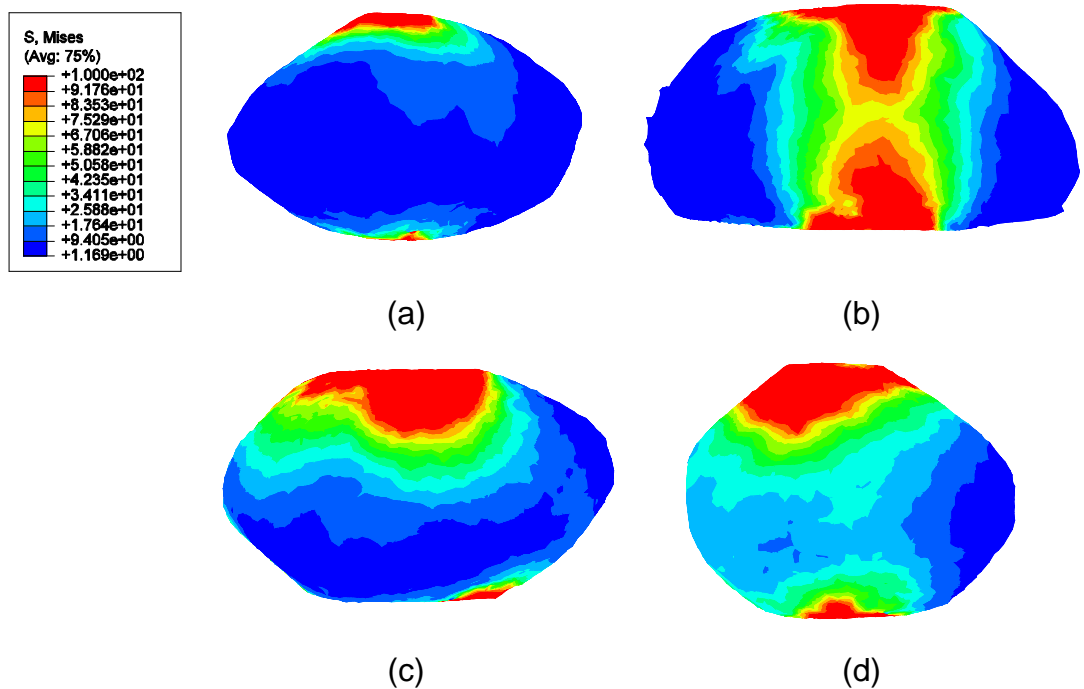


Fig. 5-16. Stress distribution obtained at the end of the elastic-plastic simulation for (a) LBS1; (b) LBS2; (c) LBS3; (d) LBS4

CONTACT BEHAVIOUR OF PARTICLES WITH SURFACE ROUGHNESS

In preparation: *Computers and Geotechnics*.

6.1 Introduction

In recent years, the number of studies that consider the particulate behaviour of soil has significantly expanded in fundamental soil mechanics. One of the requirements in discrete modelling is to define accurate contact constitutive behaviour between grains (O'Sullivan, 2011; Thornton, 2015). Therefore, the relationship between force-displacement of two grains in contact needs to be measured and incorporated in these simulations.

Although previous studies show that grain shape has a predominant influence on contact behaviour, surface roughness also plays a crucial role, in particular for low normal loading (Cavarretta *et al.*, 2010; Senetakis *et al.*, 2013; Nadimi & Fonseca, 2017c). Several studies have emphasised the importance of roughness on macroscopic soil stiffness (e.g. Duffy & Mindlin, 1956; Santamarina & Cascante, 1998; Sharifpour & Dano, 2006), while the microscopic quantification had not been taken into account.

An analytical and numerical studies have been carried out by Yimsiri & Soga (2000) and Otsubo *et al.* (2015), to measure the effect of surface roughness on small strain stiffness. Yimsiri & Soga (2000) assumed that the tangential contact response is not influenced by surface roughness, whereas this assumption was reformed in Otsubo *et al.* (2015) by considering a reduction in both normal and tangential force-displacement relationships of rough particles in contact. In an experimental work on a single grain, Senetakis *et al.* (2013) noted that tangential stiffness might not be significantly affected by surface roughness, while Cavarretta *et al.* (2010) observed a higher friction for rough contacts. However, it is not trivial to systematically control roughness in an experiment to develop new contact models.

The present study provides an alternative approach to previous direct experiments to evaluate and quantify the effect of roughness on contact

behaviour based on a micro finite-element (μ FE) model proposed by Nadimi & Fonseca (2017a), which can improve our understanding and help in estimating empirical parameters for advanced contact laws. The next section describes the numerical model and the effect of surface roughness on the normal and tangential force-displacement relationship. The effect of loading history and contact area on friction are also discussed. Finally, recent analytical work for estimating contact area are compared with numerical approximation.

6.2 Modelling of Surface Roughness

This section firstly provides the optical interferometry measurement and interferometric based mesh generation. Then, the numerical model is defined. The effect of roughness on normal and tangential loading is finally presented with a further discussion on the effect of loading history.

6.2.1 Roughness measurement

The roughness measurements were made with a Fogale Nanotech optical interferometer (Fogale, 2005). The roughness maps of two borosilicate ballotini with 1.2 mm diameter were obtained for a region of interest $106 \mu\text{m} \times 106 \mu\text{m}$, as shown in Fig. 6-1 at correct scale. An artificially rough ballotini was made by milling a smooth ballotini (following Cavaretta *et al.*, 2012). Three-dimensional (3D) views of the measurement are presented in Fig. 6-2a for a rough surface with root mean square (RMS) roughness of $0.767 \mu\text{m}$ and Fig. 6-2b for a semi-smooth surface with RMS roughness of $0.096 \mu\text{m}$.

6.2.2 μ FE mesh generation

The output of the interferometer is a surface made of points with X, Y, and Z coordinates, in which there is an equal spacing in X and Y direction of $0.184 \mu\text{m}$. This data has been converted to a volumetric matrix, of which each cell has a dimension of $0.184 \mu\text{m} \times 0.184 \mu\text{m} \times 0.184 \mu\text{m}$. For the same X and Y coordinates, if the position of a cell is lower than Z, a value of '1' was assigned to the cell. Otherwise, a value of '0' was given for the cells higher than corresponding Z. This algorithm gives us a binary volume with solid and air elements. Then, a refined

Delaunay triangulation algorithm was used to convert the volumetric matrix to a numerical mesh, as described previously by Nadimi & Fonseca (2017a). To improve computational performance a small volume was used instead of the full sphere. A cross-section through this volume of interest (Vol) is shown in Fig. 6-4. The Vol thickness was assumed to be $44+Z$ μm , to assure that the stressed areas are contained in the Vol. In other words, nodes associated to asperities are far enough from boundary nodes.

The nodes and elements were generated in MATLAB (Mathwork, 2016) and imported into Abaqus using an *.inp file containing the nodal coordinates and all elements forming the mesh. In total, 513,357 nodes and 2,814,643 tetrahedral elements formed the rough Vol and 558,165 nodes and 2,927,981 elements created the semi-smooth Vol.

6.2.3 Numerical model description

The problem, as shown in Fig. 6-4, was defined in the framework of the combined finite-discrete element model using a dynamic explicit formulation by means of an explicit central difference time integration scheme (Nadimi & Fonseca, 2017a). Hard contact was assumed for normal contact interaction and the coefficient of friction of 0.2 was set for shearing. The physical and mechanical parameters of the glass ballotini were assigned to the model, as listed in Table 6-1. Normal loading was first applied to the rough and semi-smooth Vols. Then, the Vols were sheared on a rigid platen under different normal loads, as discussed in the next sub-section.

6.2.4 Roughness effect in normal loading

Fig. 6-5 compares the results of simulations under normal loading with Hertzian theory (Hertz, 1884). It can be seen that the semi-smooth case shows an almost similar response to Hertzian theory. However, initial plasticity was induced because of surface roughness, in agreement with literature.

To assess the thickness of Vol chosen in this study, i.e. $44+Z$ μm , the stress propagation has been checked throughout the model. Figs. 6-6a and 6-6b show two cross-sectional views of stress propagation for rough Vol under $F_N=10$ N.

Stress concentration can be seen around the asperities with a maximum value of 130 MPa. At the top of the model, the stress value is zero, which means that the boundary condition did not affect the stress propagation. Therefore, the choice of $44+Z \mu\text{m}$ was reasonable. In the semi-smooth Vol, the condition is less critical with a maximum value of 68 MPa stress concentration (Fig. 6-6c).

6.2.5 Roughness effect in tangential loading

Fig. 6-7a compares the results of simulations of rough Vol under tangential loading for different normal loads $F_N=2, 4, 6$, and 8 N . As a reference, the M&D theory for same physical and mechanical properties are shown in Fig. 6-7b. It can be seen that in all cases the tangential load required for sliding of the rough surface is lower at about 80% of the theoretical expectation. In other words, although the coefficient of friction of 0.2 was specified in the simulation, the tangential load-displacement obtained corresponds to a coefficient of 0.16 due to the effect of the physical roughness. An interesting observation is an early slippage due to complex geometry at $0.1 \mu\text{m}$ displacement for $F_N=6 \text{ N}$ and $F_N=8 \text{ N}$, when compared with the expected response shown by the dash line (Fig. 6-7a). The comparison of M&D theory with the smooth surface is systematically presented in Nadimi & Fonseca (2017b; chapter 4 of this thesis), therefore it is not shown here.

6.2.6 The effect of loading history

It is well known that grains are very dynamic, even at the critical state condition (e.g. Radjai, *et al.*, 2017). Contacts have a short life as new contacts are being created and others destroyed. Therefore, it is important to investigate the effect of loading history on contact behaviour. For this purpose, the elastic numerical simulation is not adequate, as it is essential to consider the deformation of asperities under loading. Thus, it was assumed that plastic behaviour initiates at 10 MPa stress using an isotropic hardening model and the material was allowed to harden up to 110 MPa at 0.05 strain (hardening modulus, $E_t=2 \text{ GPa}$), after which it behaves perfectly plastic (consistent with the plastic assumption in Nadimi & Fonseca, 2017a; chapter 3 of this thesis).

Three simulations were carried out to investigate the effect of loading history on tangential force-displacement. The rough surface has been loaded up to $F_N=2$, 4, and 8 N. Then, the normal load was reduced to the half of initial value, that is $F_N^*=1$, 2, and 4N respectively (superscript * denotes loading history due to reduction in normal loading). Finally, the Vol was sheared under reduced normal loading. Fig. 6-8 shows the result of the simulations under tangential loading. The discussion can benefit from presenting a theory, rough-elastic response, and rough-elastoplastic response with unloading history, under a given normal load, in one diagram (Fig. 6-9). It can be clearly seen that contact with loading history requires higher tangential force to slide than a ‘virgin’ contact. This can be because of larger contact area in rough-elastoplastic model in comparison with a rough-elastic model. Therefore, further study on contact behaviour can be improved by a theoretical method to estimate contact area with surface roughness. In next section, the result of a recently proposed analytical approach is compared with contact area measurement from aforementioned numerical simulations.

6.3 Contact Area Measurement

6.3.1 Theoretical considerations

In 1881, Hertz showed the contact of a smooth sphere with radius R is a circle with radius a_0

$$a_0 = \sqrt[3]{\frac{3F_N R}{4E^*}} \quad \text{Eq. 6-1}$$

where E^* = effective contact stiffness given by $E^* = E/(1-\nu^2)$, E = elastic modulus, ν = Poisson ratio

Greenwood & Williamson (1966) and Greenwood & Tripp (1967) models approximate the rough surface by considering spherical asperities of the identical radius with a Gaussian distribution of heights. The idealisation of Greenwood & Williamson theory, which leads to nearly linear variation of real contact area with F_N , was criticised in Persson, *et al.* (2005) and Campana & Müser (2007).

Subsequently, Pastewka & Robbins (2016) proposed an analytical relationship between the contact area and the normal force

$$A_{PR} = \pi a_0^2 \operatorname{erf}\left(\frac{\kappa F_N}{2\sqrt{\pi E^* g} a_0^2}\right) \quad \text{Eq. 6-2}$$

where κ = constant that typically takes the value of 2 (Müser, 2016), g = root mean square slope of the surface. The definition of parameter g is demonstrated in Fig. 6-10.

Recently, Müser (2016) compared the approximation of Pastewka & Robbins theory with numerical reference data and confirmed that the theory predicts the real contact area with less than 10% error. He improved the original formula by cancelling the mean-field approximation for a better scaling at large loads, where Hertzian theory dominates. In the next subsection, the estimation of A_{PR} is compared with the measurement from the numerical model.

6.3.2 Comparison with numerical measurement of contact area

For the case of a single contact, the actual contact area can be quantified numerically by requesting contact area in Abaqus history outputs. Fig. 6-11a shows the numerical results of a smooth surface in terms of contact force and contact area versus normal displacement. Figs. 6-11b-e give an illustration of contact area at different normal displacement values, $\delta_n = 0.6, 1.2, 1.8$, and $2.4 \mu\text{m}$, respectively (it was assumed that the contact area is formed by the elements with contact pressure higher than zero, for illustration only). Similarly, Fig. 6-12a shows the numerical results of the rough surface in terms of contact force and contact area versus normal displacement. Fig. 6-12b-e present a picture of contact area at different normal displacement, $\delta_n = 0.6, 1.2, 1.8$, and $2.4 \mu\text{m}$, respectively. The differences in contact area caused by physical asperities can be clearly seen by comparing Fig. 6-11 and 6-12.

The Equation 6-2 was plotted for different values of g , as shown in Fig. 6-13. Hertzian response and numerical rough response are illustrated by grey dash line and black bold dash line, respectively. A good agreement can be seen for

numerical simulation and theoretical curve for $g=0.06$. Despite a commendable estimation from the theoretical equation, a contact law based on the reduced contact area of Pastewka & Robbins will be expensive and non-trivial for directly implementation in DEM simulations and still limited to spherical grains.

6.4 Conclusions

A μ FE numerical model was employed to investigate uncertainties in contact behaviour with surface roughness. A reduction of tangential force required for sliding of a rough-smooth contact was seen. This has contributed to clarify some uncertainties regarding the effect of surface roughness on tangential force-displacement. The effect of loading history was also investigated, which shows a slight increase in tangential load due to flattening of asperities.

6.5 Tables and Figures

Table 6-1. Physical and mechanical properties for glass ballotini

Properties	Value	Unit
Elastic Modulus	70	GPa
Poisson ratio	0.2	-
Density	2.5	t/m ³

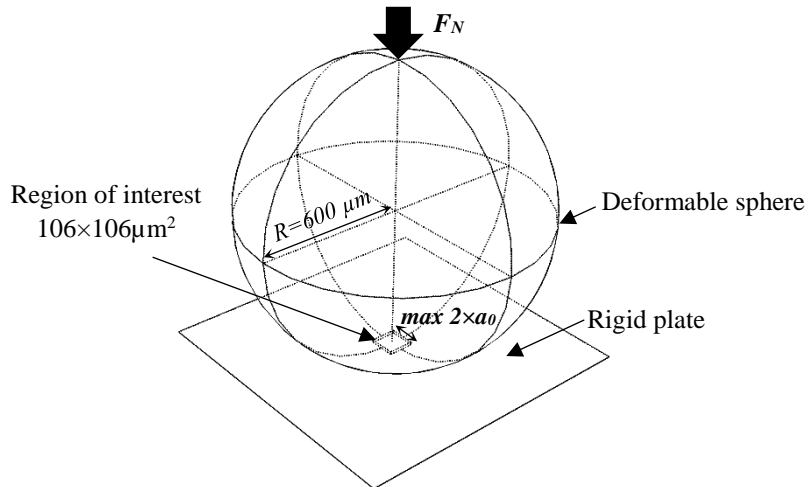
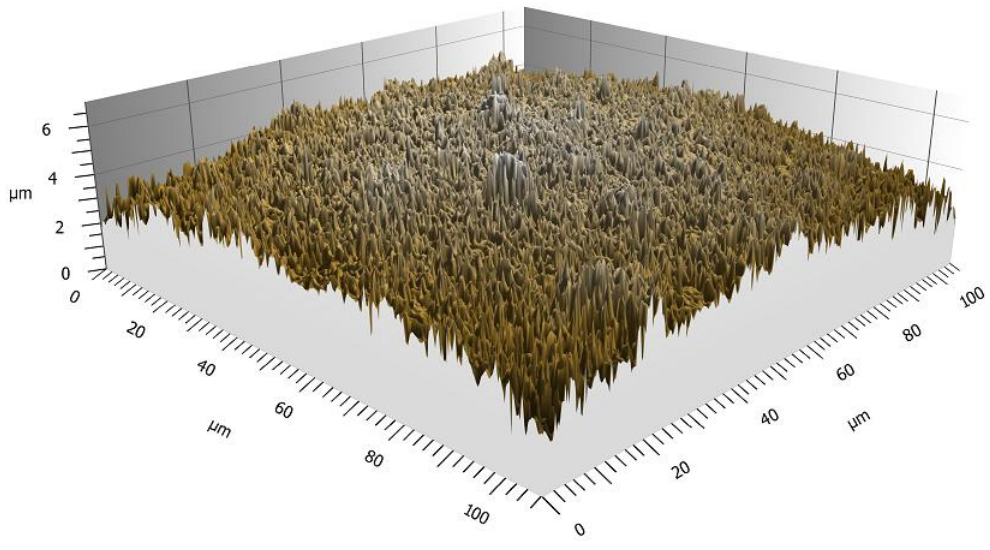
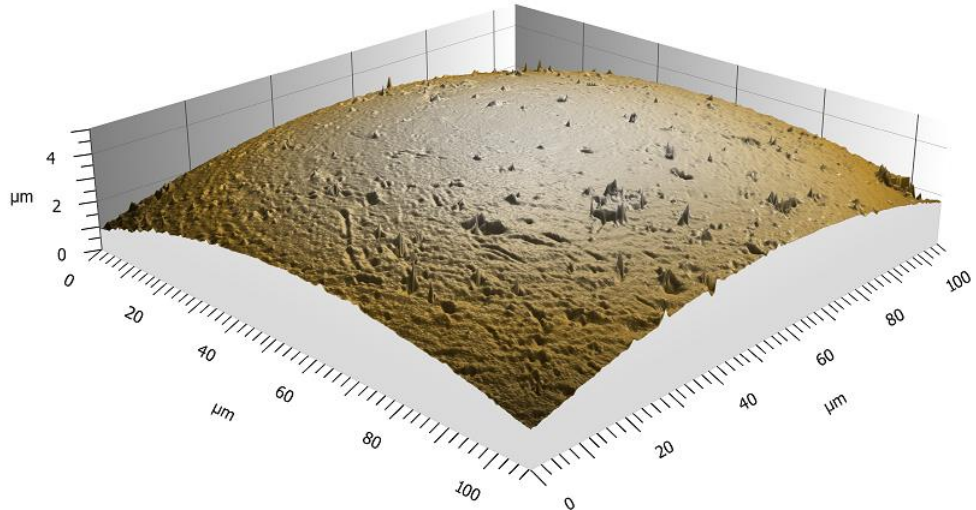


Fig. 6-1. Schematic of a sphere in contact with a plate under normal loading showing the region of interest (correct scale)



(a)



(b)

Fig. 6-2. 3D views of the measured regions of interest for (a) rough surface, (b) semi-smooth surface

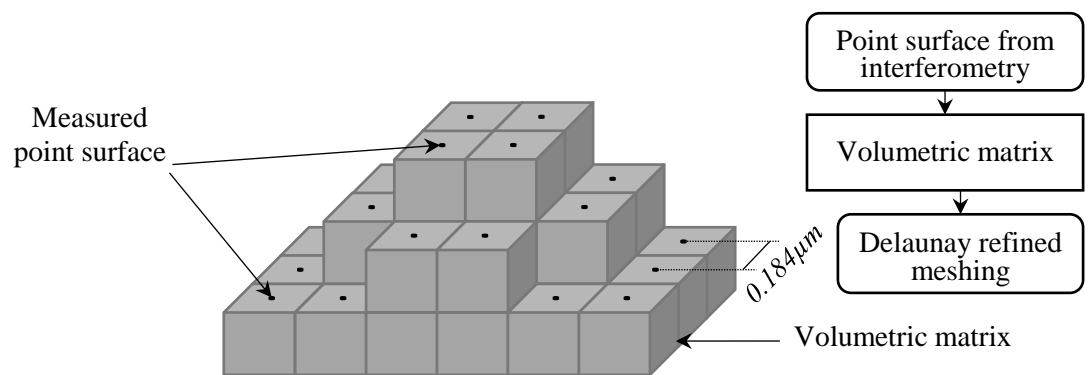


Fig. 6-3. Work flow used to convert the measured roughness map to a numerical mesh

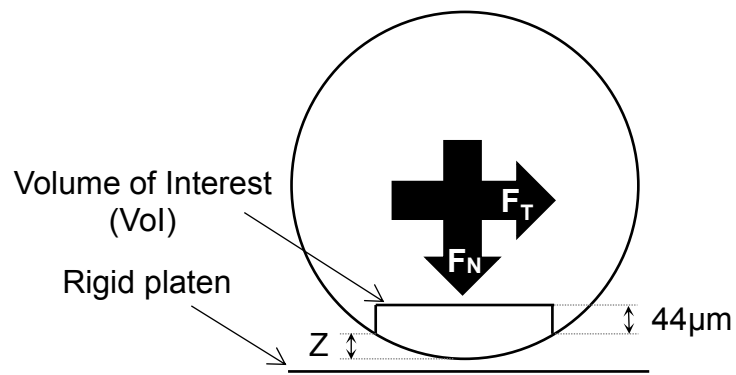


Fig. 6-4. Cross section through a sphere showing the Volume of Interest (Vol)

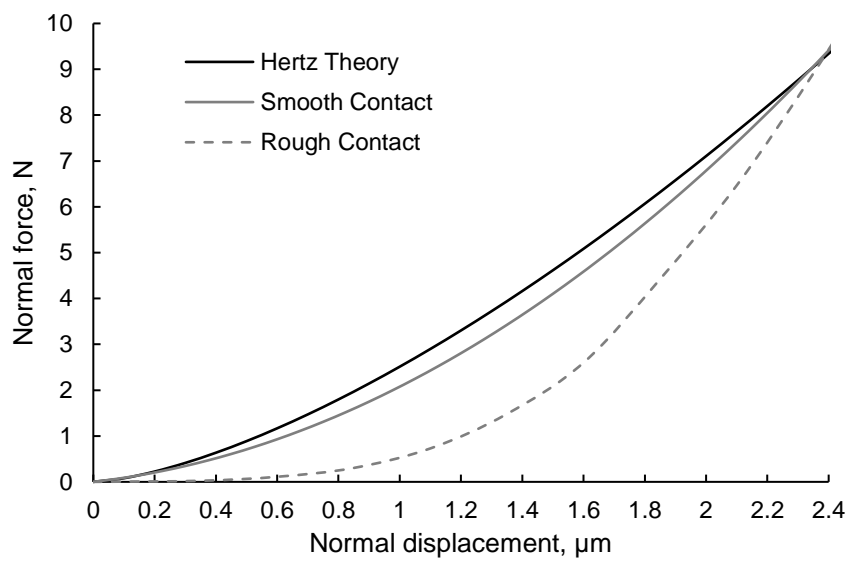


Fig. 6-5. Comparison between theory and numerical simulations for smooth and rough contacts in terms of normal force-displacement

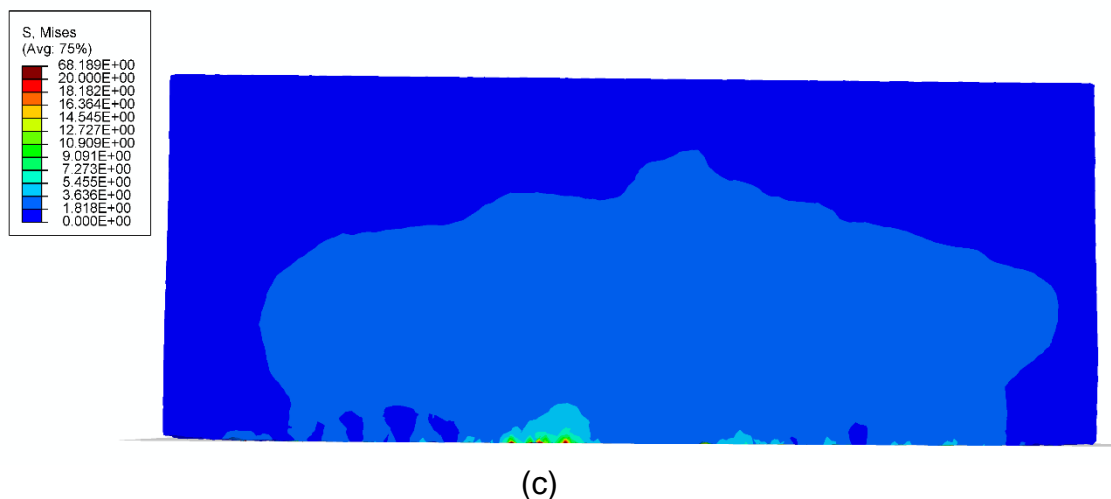
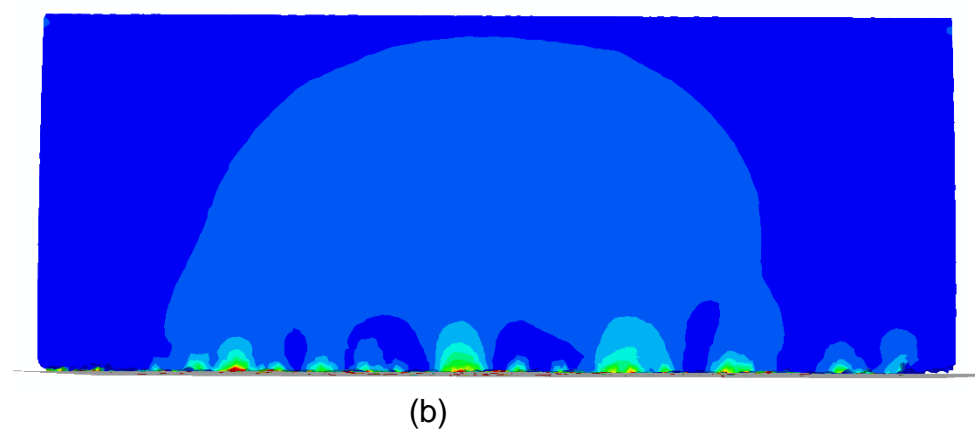
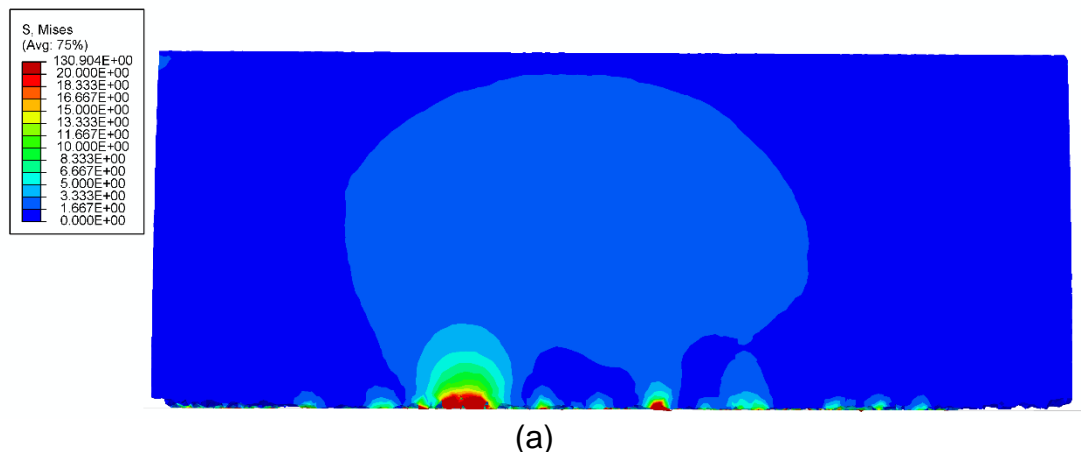
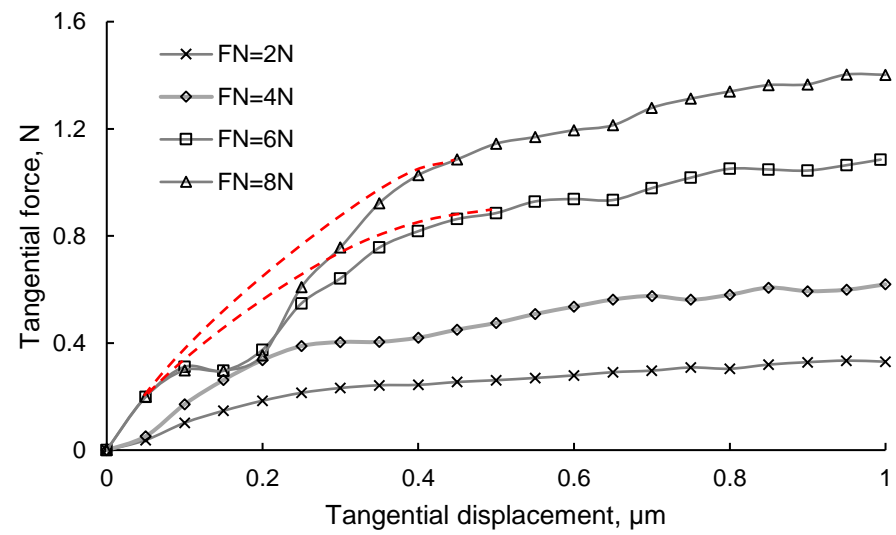
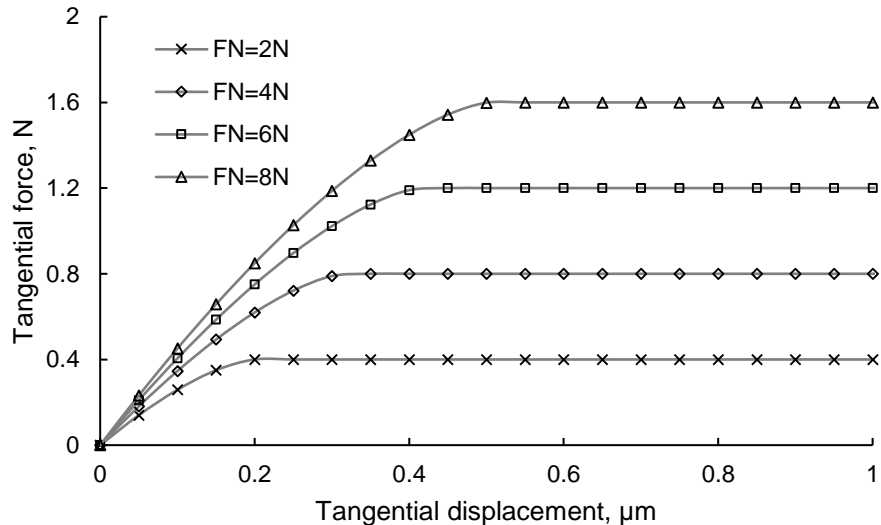


Fig. 6-6. Cross section of stress distribution inside the Vol for (a) rough surface at $X=30 \mu m$, (b) rough surface at $X=70 \mu m$ (c) semi-smooth surface at $X= 70 \mu m$ under $F_N=10 N$



(a)



(b)

Fig. 6-7. Tangential force-displacement obtained from (a) simulation of rough surface, (b) M&D theory

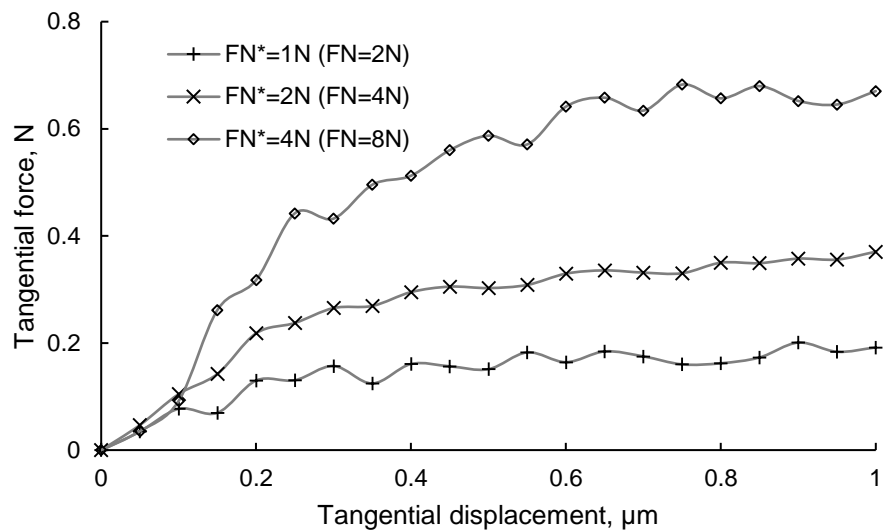


Fig. 6-8. Tangential force-displacement for a rough surface with unloading history

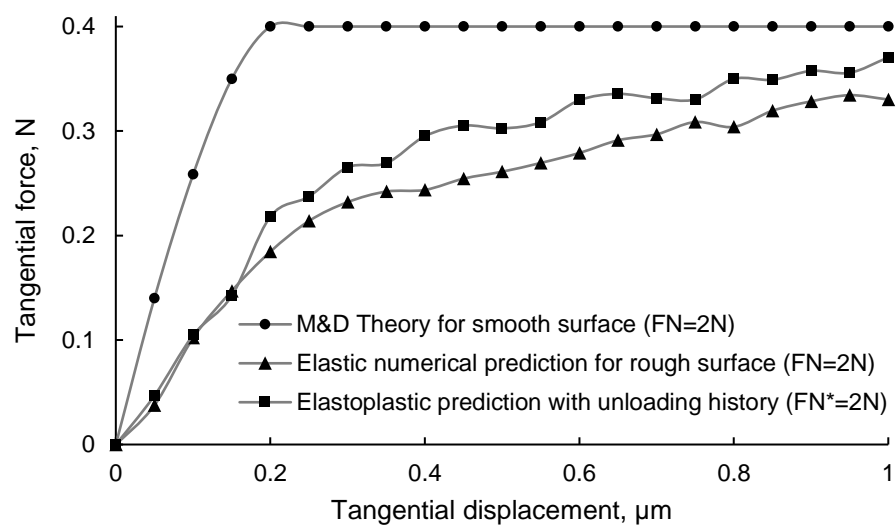


Fig. 6-9. Comparison between M&D theory, rough-elastic numerical simulation, and rough-elastoplastic simulation with unloading history

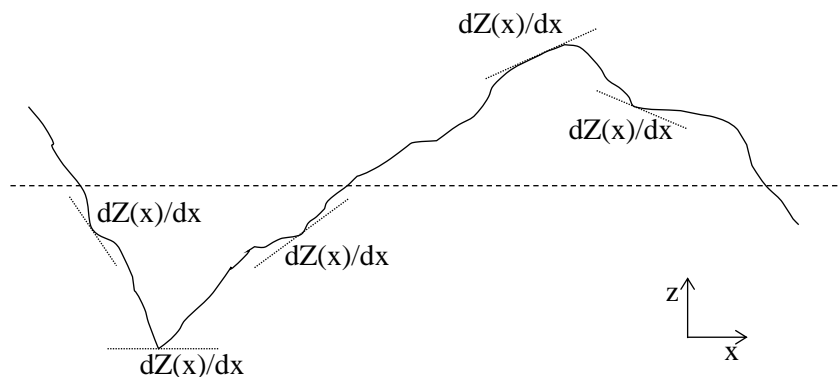


Fig. 6-10. Schematic representation of the root mean square slope (g) within a sampling profile

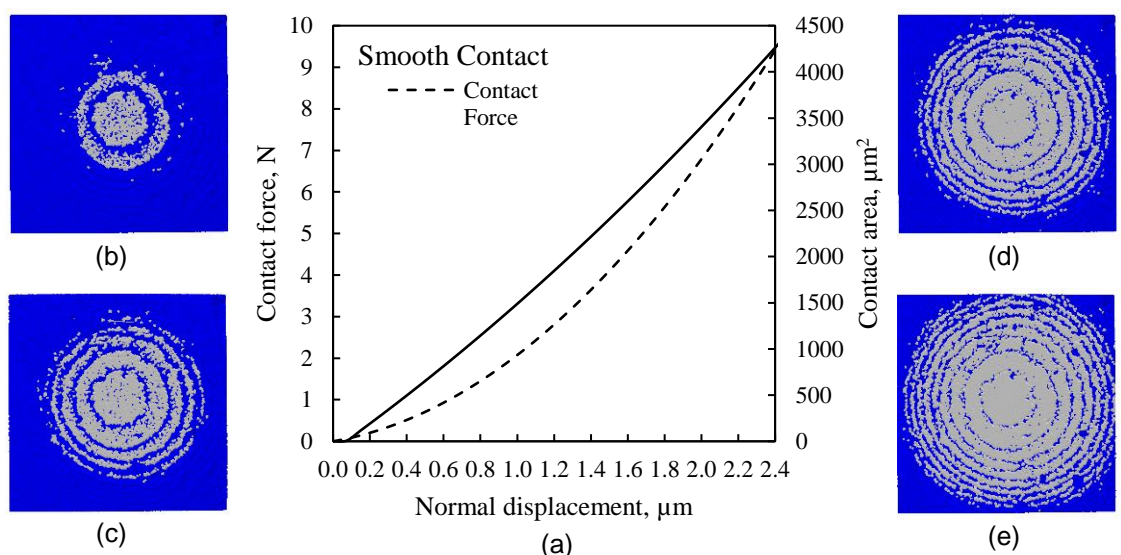


Fig. 6-11. Numerical results of a semi-smooth surface, a) contact force and contact area versus normal displacement; and contact regions (shown in grey) for values of normal displacement of b) $\delta_n=0.6 \mu\text{m}$, c) $\delta_n=1.2 \mu\text{m}$, d) $\delta_n=1.8 \mu\text{m}$, e) $\delta_n=2.4 \mu\text{m}$

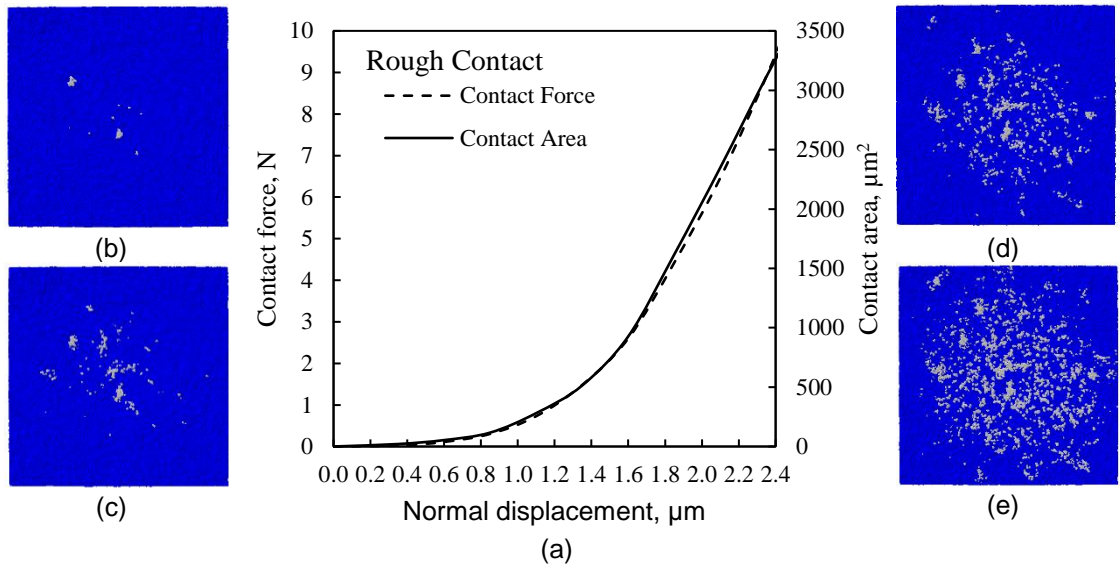


Fig. 6-12. Numerical results of a rough surface, a) contact force and contact area versus normal displacement; and contact regions (shown in grey) for values of normal displacement of b) $\delta_n=0.6 \mu\text{m}$, c) $\delta_n=1.2 \mu\text{m}$, d) $\delta_n=1.8 \mu\text{m}$, e) $\delta_n=2.4 \mu\text{m}$

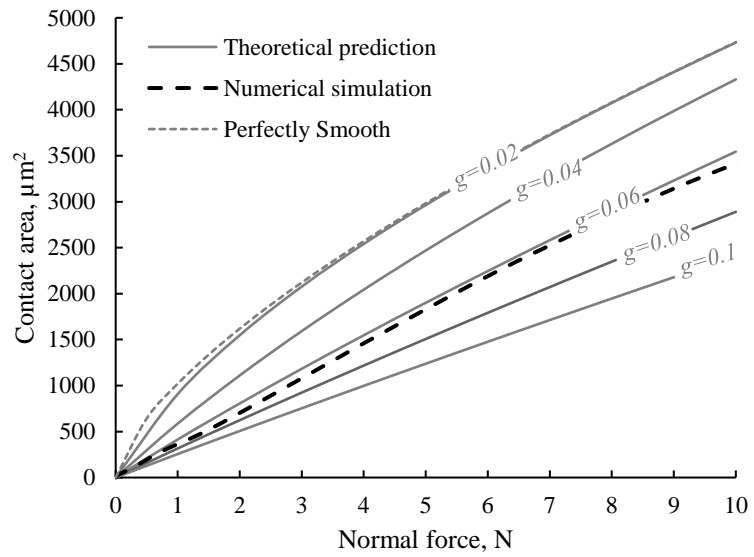


Fig. 6-13. Effect of g on contact area versus normal force

A MICRO FINITE ELEMENT MODEL FOR SOIL BEHAVIOUR:

EXPERIMENTAL EVALUATION

In preparation: *Géotechnique*.

7.1 Introduction

Improving computational modelling towards a more realistic description of granular behaviour is a long standing challenge (e.g. Cundall & Strack, 1979; O'Sullivan, 2011; Andrade, *et al.*, 2012; Kawamoto, *et al.*, 2016). Nadimi & Fonseca (2017a) proposed a μ FE model that virtualises the fabric of a natural sand obtained from μ CT to simulate the mechanical response under loading, in which the grain-to-grain interactions are modelled in a framework of combined discrete-finite element method (Munjiza, 2004).

This μ FE was motivated for two reasons: Firstly, single grain experiments have shown that contact response for natural grains does not follow a Hertzian response (Michalowski, *et al.*, 2017). In fact, contact response has a strong dependency on the grain shape as demonstrated in Nadimi & Fonseca (2017c) for a series of silica and carbonate grains. In the μ FE framework, the contact response originates from the deformation of the grain, which constitutes an important advance when compared with the rigid body assumption and the associated pre-defined contact laws used in most part of discrete element approaches.

Secondly, the effect of fabric on the mechanical response of the granular material is well known (Oda & Iwashita, 1999; Fonseca, *et al.*, 2016). A complete three-dimensional arrangement of the grains and their morphologies can be obtained by using μ CT scanning (Andò, *et al.*, 2013; Fonseca, *et al.*, 2013a; Vlahinić, *et al.*, 2013). Therefore, an image based representation of the internal structure and grain morphology in the numerical domain is a step towards a more complete representation of a granular system.

Here, the μ FE model is evaluated against a triaxial compression experiment. One of the challenges in numerical modelling of a triaxial test is the correct representation of boundary conditions (Cui *et al.*, 2007; Cheung & O'Sullivan,

2008). In triaxial compression, the circumferential boundary should apply the correct confining pressure while allowing for grain rearrangement. De Bono, *et al.* (2012) proposed a cylindrical wall comprised of bonded spheres to represent the membrane. Using bonded spheres, however, has the disadvantage of restraining rolling and translation of grains near the boundary, and grains may penetrate the boundary depending on the size of bounding spheres. In this study, deformable thin-shell elements are used to represent the laboratory membrane.

The term ‘force chains’ is widely used in granular matter to describe filamentary patterns of grains transmitting above average contact forces (e.g. Majmudar & Behringer, 2005; Radjai, *et al.*, 2017). A handful of studies have instead used the terminology ‘stress chain’ (Gerritsen, *et al.*, 2008; Maeda *et al.*; 2010; Blumenfeld & Ma, 2017). When dealing with irregular shaped grains that are prone to form contacts through an area (in some cases, large) rather than a point as for a perfect sphere, the discussion on whether to use force or stress to identify the heavily loaded grains becomes pertinent. The present study investigates, for the first time, the formation of columns of load bearing grains using both force and stress measurements. In addition the evolution of contact forces through deformation is linked to grain kinematics to investigate the role of the force network in the stability of the assembly.

7.2 μ FE Model

The μ FE model combines four techniques: (i) image acquisition using μ CT and image processing; (ii) image-based mesh generation; (iii) finite element solver, and (iv) discrete element solver. Fig. 7-1 shows a schematic of these four techniques.

The first step is image acquisition (Fig. 7-1a). Using X-ray imaging, the internal structure of the specimen is obtained including shape and size of each individual grain. In order to obtain the individual grains, image segmentation approaches are employed (e.g. Kong & Fonseca, 2017). The numerical approximation of the problem starts from discretising an object into a collection of elements and nodes (Fig. 7-1b). A Delaunay refined algorithm is employed to extract a grain iso-surface (Shewchuk, 2014). The grain is then filled with tetrahedral elements for the sub-volumes bounded by the iso-surfaces to obtain the volumetric mesh. The

generated mesh is imported into the finite-discrete numerical domain. More details can be found in Nadimi & Fonseca (2017a); chapter 3 of this thesis.

In this domain, the nodal force includes the contribution from contact forces, internal strain and external loads. A grain can locally deform depending on the current nodal forces. Consequently, the stress field can be computed within each grain (Fig. 7-1c). The motion for the body is calculated using an explicit central difference integration rule (Fig. 7-1d). Currently, the model is implemented in Abaqus explicit which uses a dynamic framework.

7.3 A Case Study

A case study is presented to experimentally evaluate the μ FE approach to model a specimen of Martian regolith-like sand under triaxial compression (Seiferlin *et al.*, 2008; Kawamoto *et al.*, 2016). This section firstly includes a brief description of the experiments. A comparison between experiment and modelling is then presented in terms of axial stress-axial strain and volumetric strain-axial strain relations. This is followed by an investigation into the evolution of contact orientation and forces. Finally, the formation of stress chains in the specimen is studied.

7.3.1 Experiments

The sand specimen with 11 mm diameter and 22 mm height was first compressed isotropically to 100 kPa and subsequently subjected to displacement controlled axial loading with a strain rate of 0.1%/min under constant confining pressure. The test was performed inside a micro-CT scanner to image the internal structure of the specimen (e.g. Andò, *et al.*, 2013). The sample was prepared by air pluviation and a void ratio of 0.56 was measured at onset of axial loading. The three-dimensional (3D) images were acquired at a voxel size of 15.5 μ m, which means that a typical grain with 1.2 mm diameter, is represented by approximately 70 voxels across its diameter. Following image segmentation, 3,158 individual grains were identified in the specimen.

7.3.2 Numerical modelling

The 3D image of the specimen prior to loading was meshed and each voxel in the images was converted to Cartesian coordinates. A total of 10,105,720 elements comprised of 3,503,151 nodes represents the specimen in the numerical domain. The elastic material model was assigned to the grain with Elastic modulus $E=70$ GPa, density $\rho=2,500$ kg/m³ and Poisson's ratio $\nu=0.3$. The coefficient of friction was set to 0.28 (obtained from single grain experiments).

To better simulate the experimental conditions, deformable triangular thin-shell elements with $E=125$ MPa and $\nu=0.49$ were used to represent the membrane. For the top and bottom platens, rigid elements were used. The mesh size of the elements defining the membrane was set to be lower than the elements defining the grains, this is an important aspect for a more accurate modelling at the grain-membrane interface. The numerical sample was axially compressed to 10% strain under the same conditions as the experimental sample.

Fig. 7-2a shows the numerical sample at the start of the test and Fig. 7-2b. shows the sample at the end of the test. At 10% axial strain the specimen shows a slight barrelled shape, also in agreement with experiments. The stress-strain response obtained from the μFE model is compared with the experimental response in Fig. 7-3a. Overall a good agreement can be seen. In particular, both tests show a strain hardening phase up to around 3% axial strain, the numerical simulation being slightly stiffer, followed by a relatively steady state phase. For the relation between volumetric and axial strains presented in Fig. 7-3b, again a very good match between both tests can be observed. Figs. 7-4a and 4b show local views of the flexible membrane at the end of compression.

7.3.3 Evolution of the active contacts

The grain-to-grain contacts were identified based on the principle of active contacts, in other words, the contact region is defined by the surface nodes that have contact force higher than zero. This is illustrated in the schematic presented in Fig. 7-5. Relying on force measurements to identify contacts has the potential to avoid uncertainties related to image segmentation and voxel size issues

commonly found in purely geometric contact identification (e.g. Fonseca *et al.*, 2013a; Viggiani, *et al.*, 2013).

Another advantage of making use of the nodal forces acting at the contacts is that the vector defining the nodal force, which is orthogonal to the contact region at each node, can be used to investigate the evolution of the orientation of the contacts as deformation progresses. Four strain levels (2.5%, 5.5%, 7.5%, and 9.5%) were chosen to investigate the evolution in the number of contact normal vectors and their predominant orientations. Fig. 7-6 shows the evolution of contact normal orientation in XY, XZ and YZ planes (Z being the vertical/ axial direction). Fig. 7-6a shows the distribution in the horizontal XY plane, which exhibits essentially an isotropic distribution as expected for an axisymmetrical loading scenario where no major localisation was observed to form. For the two vertical planes, XZ and YZ (Figs. 7-6b and 6c, respectively) we can see the alignment of the contact normal vectors in the direction of the major principal stress, as shown previously by Fonseca *et al.* (2016). When comparing the four stages, the shape of the distribution is similar and it is the number of nodal vectors that varies mostly. The evolution in the number of vectors for each of the four loading stage is of 105744, 129431, 93160, and 69078, respectively. The number of vectors is in this case proportional to the active contact area and so this suggests that the contact areas engaged in transmitting load decreases for the stages of larger deformation, *i.e.* for axial strain of 9.5% the active contact area is approximately half the value at axial strain of 5.5%.

7.3.4 Force balance condition

In order to gain better insight into nonlinear behaviour of granular materials under complex loading conditions, the normal and shear contact forces at nodes forming the contact areas were plotted versus their displacement magnitude (U). The same four macroscopic axial strain levels were used, which have the particularity of the overall axial stress not changing more than 60 kPa (Fig. 7-7a). The three intervals defined by these strain levels (i_1 , i_2 and i_3) have the common nodes of 27674, 49168 and 34057, respectively. These common nodes were used in the analysis. Figs. 7-7b, 7d and 7f show the change in nodal normal contact forces (ΔF_n) versus the change in displacement magnitude (ΔU) for i_1 , i_2 and i_3 , respectively. In all increments, the changes in the normal forces of the

nodes are mostly within -20 to 20 N (the reason of axis limits). Figs. 7-7c, 7e and 7g present the differences in nodal tangential contact forces (ΔF_t) versus ΔU . In all increments, the majority of tangential forces are within -10 and 10 N.

The distribution of changes in nodal forces allows the dynamic environment within the specimen to be clearly seen (Fig. 7-7b-g), despite the almost steady-state macroscopic response. The nearly symmetrical distribution of forces around $\Delta F_n=0$ and/or $\Delta F_t=0$ suggests a balance for the rates of gain and loss of forces, which may be the reason of the relatively constant stress ratio (Radjai *et al.*, 2012; 2017; Pouragh & Wan, 2016). Regarding displacement, there is no strong axis of symmetry due to non-uniform specimen deformation as a result of local grain rearrangement.

7.3.5 Formation of stress chains

For the case of spherical grains, the initial contact area is always a point, so the debate around whether to use force or stress to identify the load bearing grains is not an issue. For real sand grains, however, the contact topologies arising from the irregular shaped grains, makes this condition not necessarily valid. To demonstrate this, the force chains in the triaxial test were identified using a threshold value of 3 times the mean normal contact force, *i.e.* $3 \times 3.02\text{N}=9.06\text{ N}$. This selection resulted in the identification of approximately 200 grains belonging to the strong force network. Similarly, the 200 grains with the highest internal stresses were also filtered out. The results revealed that only half (*i.e.* 47.8%) of grains were both in the force and stress networks. This suggests that grain breakage may initiate outside of the force chain and change the stability and self-organisation of assembly.

7.4 Concluding Remarks

Simulation of more than 3,000 grains interacting in a finite-discrete element framework has been successfully evaluated against a triaxial experiment.

By assigning only elasticity to individual grains, the non-linear plastic response of the specimen was reproduced based on granular rearrangement and grain deformation.

A novel representation of the laboratory membrane that uses deformable thin-shell elements that allows for more realistic grain rearrangement at the lateral boundaries has been proposed.

A grain-to-grain contact identification technique based on contact forces has been employed as an alternative to current geometrical contact detection approaches. The evolution of orientation of contact normals obtained for the active contact areas was in agreement with previous studies.

The force balance condition was characterised for an assembly of irregular shaped grains in a way that was previously accessible for ideal spheres.

Based on the observation that grains forming a force chain are not necessarily experiencing high stresses, the use of the ‘stress chain’ concept was assessed as an alternative way to consider grain breakage that may initiate on the weak force network and compromise the stability of assembly.

7.5 Tables and Figures

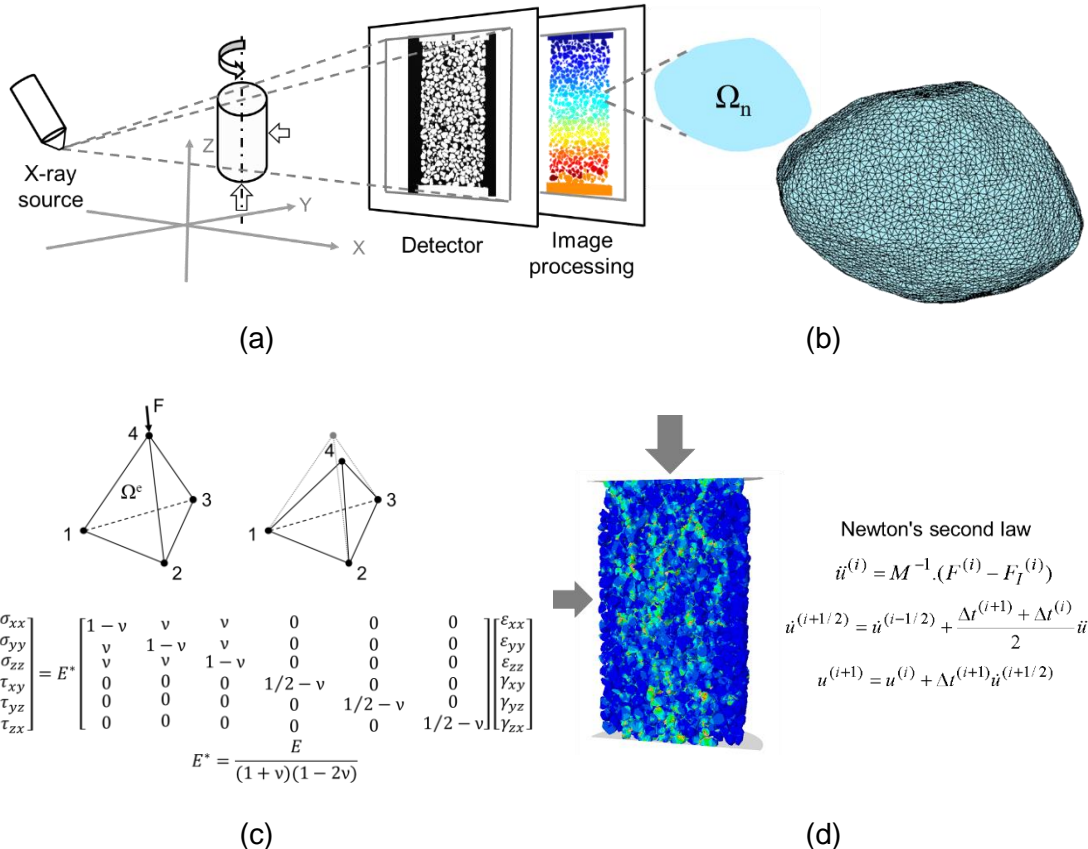


Fig. 7-1. Schematic illustration of the μ FE model (a) image acquisition and processing, (b) the discretization of a grain Ω_n into a collection of elements and nodes, (c) element deformation and stress field computation in finite element context, (d) interaction of grains based on Newton's second law using explicit integration

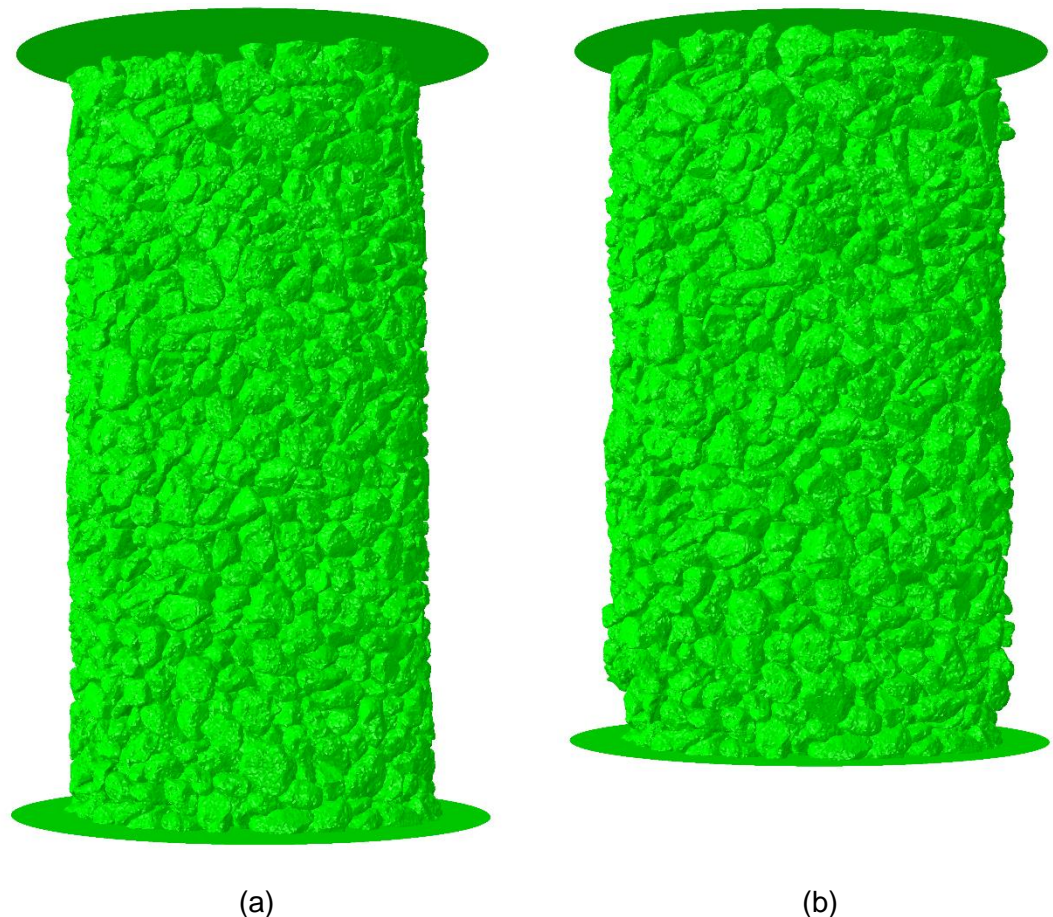
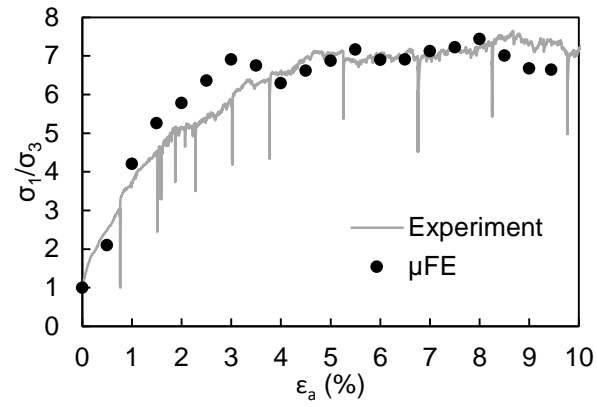
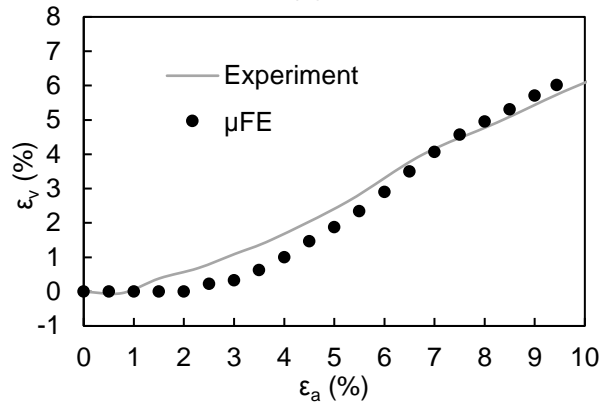


Fig. 7-2. Numerical full specimen, (a) at the beginning of the test and (b) at 10% axial strain

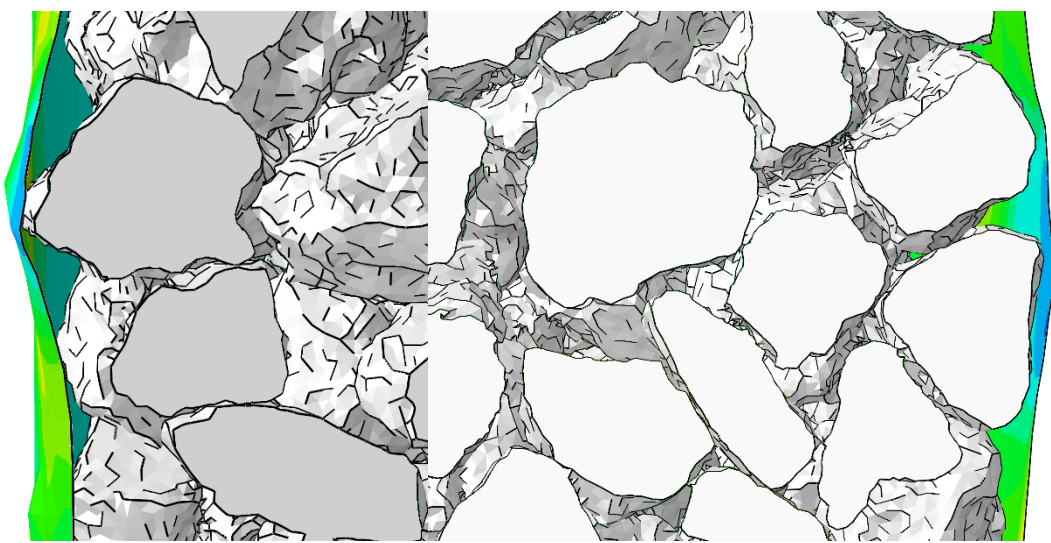


(a)



(b)

Fig. 7-3. Comparison between the μ FE model and experiments, (a) stress-strain response and (b) volume-axial strains relations



(a)

(b)

Fig. 7-4. Two local views of deformation in the membrane

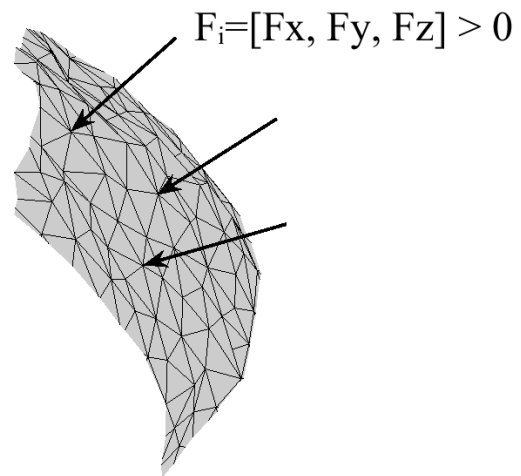


Fig. 7-5. Schematic showing the criterion used to identify a node belonging to an active contact

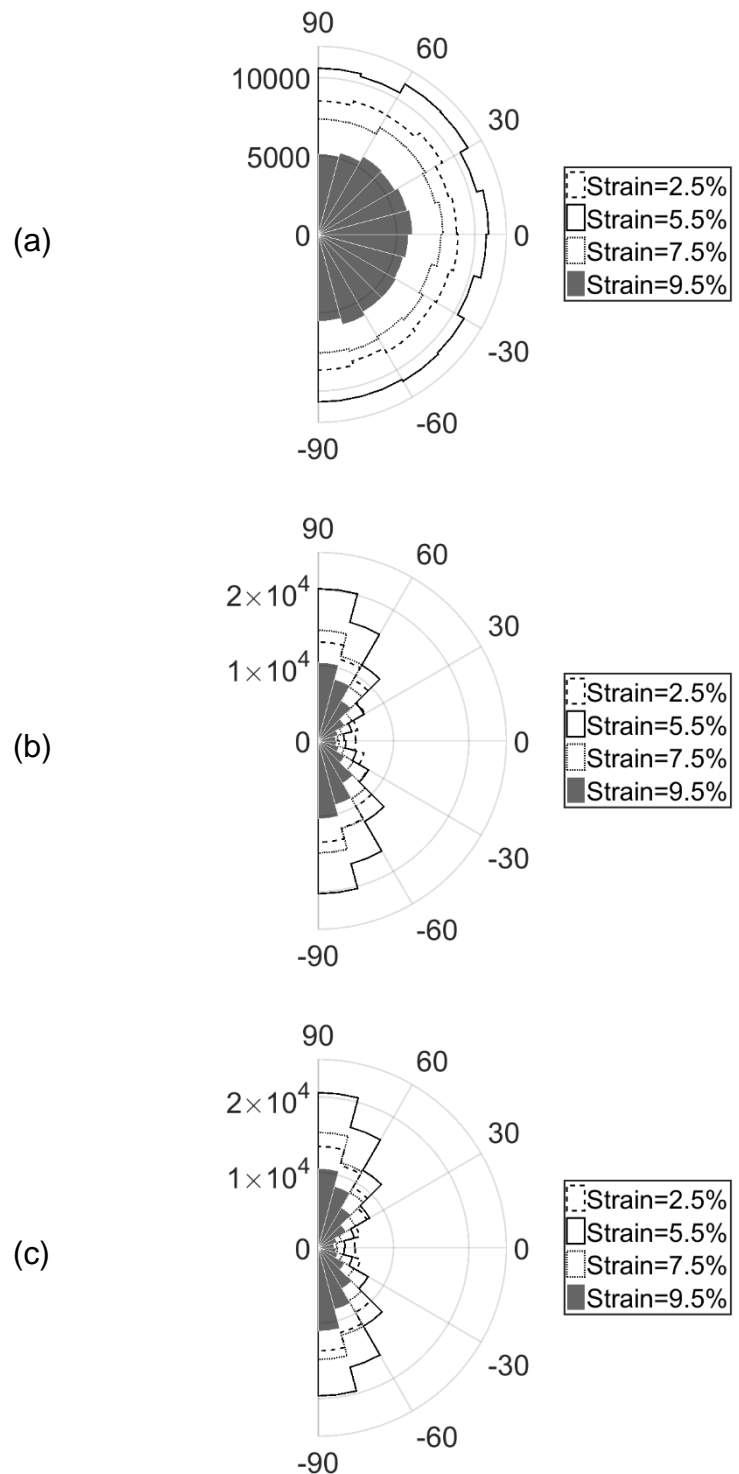


Fig. 7-6. Evolution of contact normal in: (a) XY plane, (b) XZ plane, (c) YZ plane, for the four stages with an axial strain level of 2.5%, 5.5%, 7.5%, and 9.5% and the associated number of vectors of 105744, 129431, 93160, and 69078, respectively

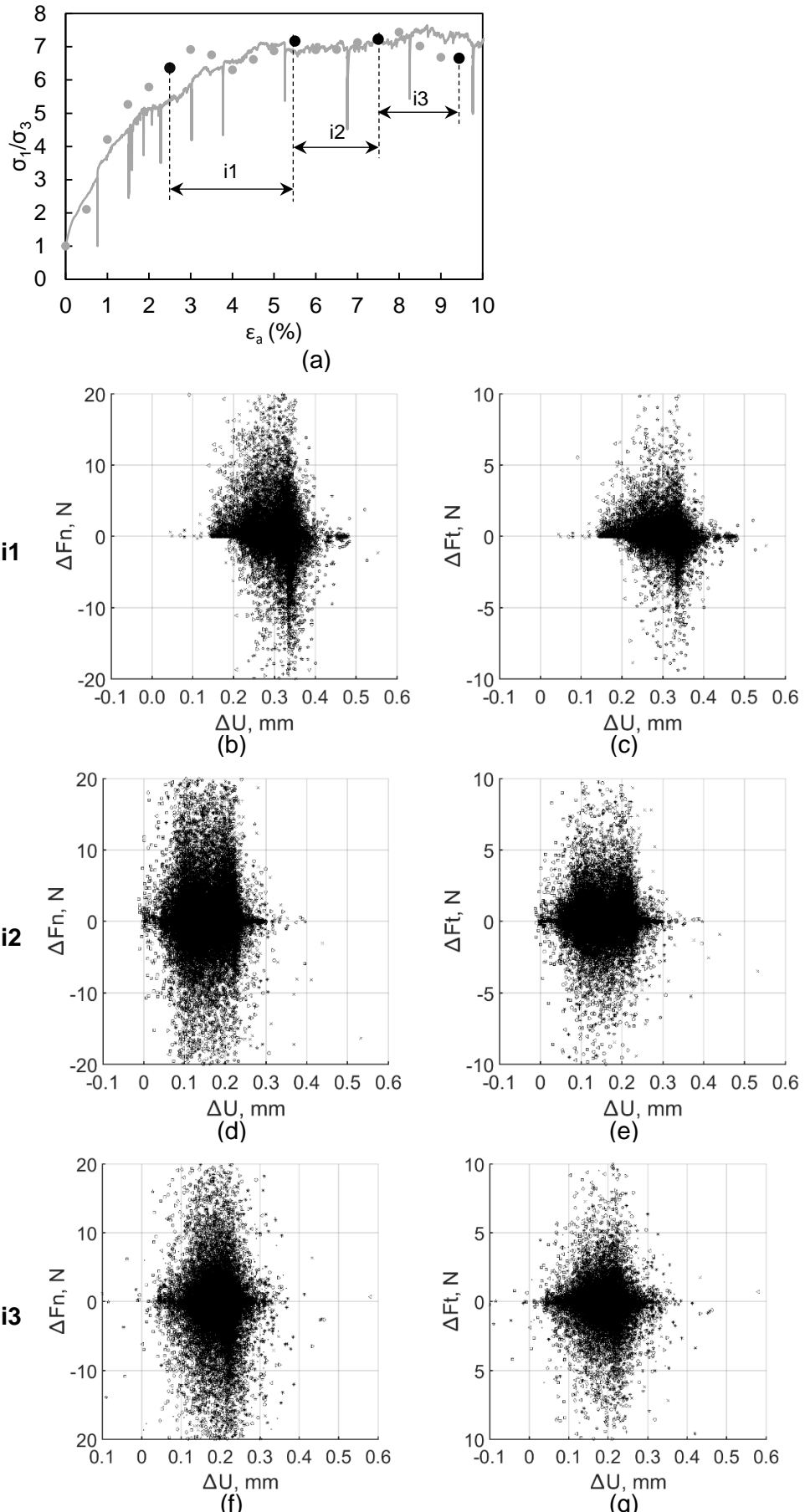


Fig. 7-7. The nodal force-displacement distribution at three strain increments shown in (a); (b, d, f) distribution of normal force-displacement and (c, e, g) distribution of tangential force-displacement for i_1 , i_2 and i_3 , respectively

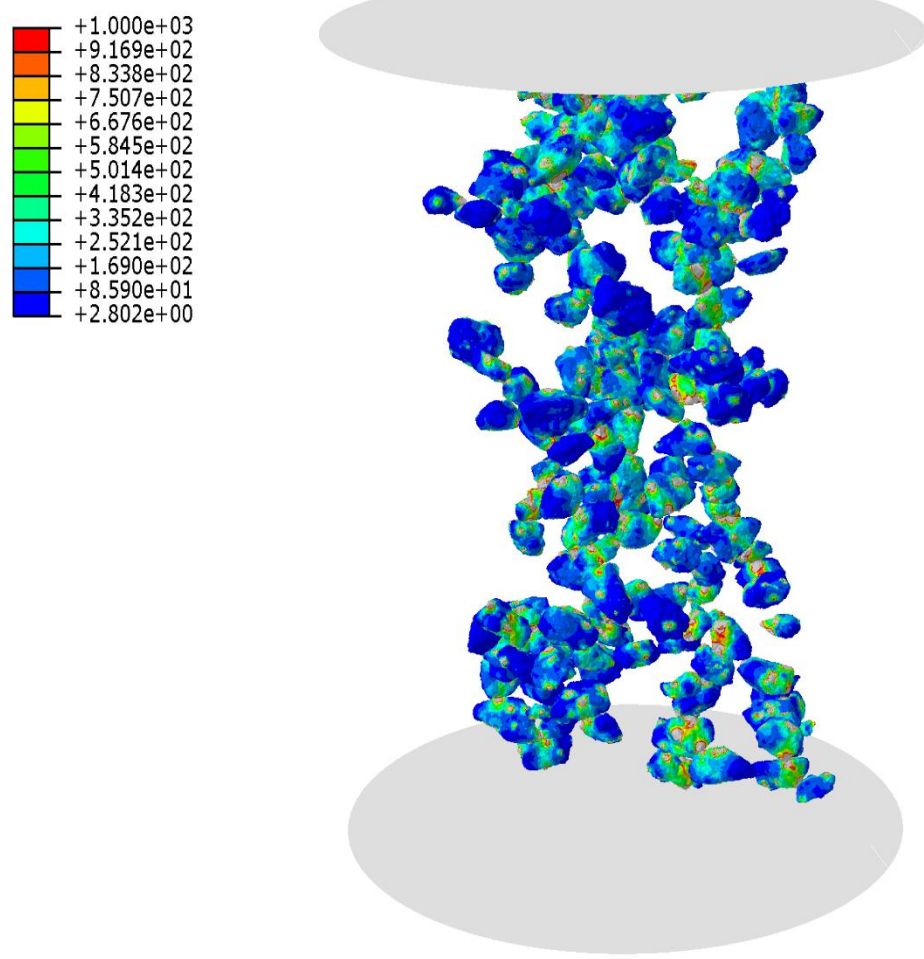


Fig. 7-8. Formation of stress chains at 9.5% strain for the 200 most stressed grains

CONCLUSIONS AND FUTURE WORK

8.1 Summary

The nonlinear mechanical behaviour of soil can be described by investigating inter-particle stress transmission. Although the direct measurement of stress transmission in an assembly of soil grains is a challenging task, this work provided important insights by analysing the mechanisms of stress transmission in a specimen of natural sand using an image-based approach and a numerical approach summarised below.

8.1.1 Image-based investigation

Stress transmitting grains in a sand specimen have been identified by following the evolution of intergranular contacts as the grains rearrange and by considering how these rearrangements enhance the stability of the material. The methodology used geometrical data of the individual grains and their associated contacts from μ CT images to characterise load-bearing sand grains using an algorithm based on a stability criterion (3-cycle contact triangles) and a load transmission criterion (near-to-vertical contact normal vectors). Statistical analysis showed that these columnar structures of stress-transmitting grains were associated with a larger contact area and were forming contacts aligned along the direction of the major principal stress.

Comparing the grain-to-grain contacts in an intact sample with a reconstituted sample in this study, raised the question of how to enhance granular packing and the soil-boundary interface to perform better laboratory investigations. A novel technique that relies on a systematic increase of density induced by thermal cycling was proposed (Appendix A). When the sample is heated the grains and their container undergo thermal expansion and this leads to the settling of the material due to the differential thermal expansion between the grains and the container and the metastable nature of the granular assembly. This change in fabric is not reversible upon cooling down of the sample, so the newly formed

fabric can be used for experimental testing. Moreover, the soil fabric can be incrementally enhanced using successive thermal cycles of heating–cooling.

8.1.2 Numerical investigation

The second research objective has been to advance stress measurement in granular materials by introduction of 3D images of granular fabric in the finite-discrete element framework, termed the μ FE model. Each individual grain was represented with a finite-element mesh and modelled as a continuum body allowed to deform according to a prescribed constitutive model with appropriate friction contact conditions. By incorporating grain deformation into the model, the contact response emerges from the interaction of contacting bodies and each irregular contact area produced a unique response.

A case study of an intact sand subjected to 1D compression was presented to demonstrate the insights that can be gained into the stress transmission mechanisms and yield initiation within the grains. The displacement field, inertia tensor, and active contacts were used to quantify grain kinematics as the sample deforms.

The μ FE model was evaluated against experimental data obtained from an *in situ* triaxial test performed inside a μ CT scanner. The initial fabric of the sample was imported in the numerical domain and material properties, contact properties and boundary conditions were defined according to the experimental test. In the simulation of the triaxial condition, a feature of the model was the use of deformable thin-shell elements to represents circumferential boundary, which allows true failure mode and volumetric deformation. The macroscopic response of the virtualised specimen has been compared with experiments in terms of stress ratio and volumetric strain against axial strain. The grain-to-grain contacts were identified and analysed based on normal contact forces. It was found that the evolution of orientation of contact normals obtained for the active contact areas was in agreement with previous studies. An investigation on force balance condition of the material was achieved that had previously been carried out on ideal particles.

Based on the observation that grains forming a force chain are not necessarily experiencing high stresses, the true ‘stress chain’ concept was assessed as an

alternative way to consider grain breakage that may initiate on the weak force network and compromise the stability of assembly.

8.1.3 Contact mechanics

Contact interaction is of great importance in discrete numerical simulations. The constitutive contact behaviour used in the aforementioned simulations was validated against existent theories for a single sphere and for an assembly of spheres under triaxial loading. Single sphere simulations were performed under normal, tangential, torsional and rotational loading and the finite-element discretisation was also assessed. The applicability of Lubkin's theory for torsional loading of an elastic sphere for elastoplastic sphere was reported in Appendix B.

The influence of grain morphology on stress transmission of sand was investigated. A methodology for virtualising irregular shaped grains was developed. The outline of a soil grain was obtained by reconstructing the planar projections acquired at different angles of rotation using a standard camera. The numerical representation of the real grain was obtained by meshing the 3D volume. Numerical simulations using a μ FE model were carried out to reproduce the experimental data from normal compression single grain tests. The contribution of the initial grain rearrangement on the normal force-displacement response and its strong dependency on the shape of the grain was shown. This study demonstrated that particle shape is a critical parameter for calibration of contact behaviour of sand.

At a smaller scale, literature reports conflicting results concerning the effect of roughness on tangential force-displacement. The issue was investigated by incorporating interferometric measurements of surface roughness in the μ FE model. An interferometric-based mesh generation method was developed for this purpose. A reduction of the coefficient of friction due to surface roughness was shown. The influence of loading history on tangential force-displacement was also demonstrated.

8.2 Ongoing and Future Work

8.2.1 Simulation of grain breakage

The proposed framework for modelling granular materials can be improved by introducing grain breakage using

- a) Constitutive models developed in fracture mechanics that accounts for sudden softening in material strength. Appendix C reported a preliminary investigation employing an elastic-damage constitutive model for spheres in the μ FE framework. The interpretation of results was enriched by considering previous theoretical work regarding the tensile strength of a sphere under compression. In this approach, physical breakage can only be obtained by element deletion.
- b) Cohesive element approach which allows physical separation at element-to-element interface. This approach has been checked in the μ FE framework by collaboration of a master student, Lorenzo Di Pasquale (2016). The limitation is that a crack can only propagate in a specific direction for which the cohesive interface has been defined.
- c) Extended finite-element method (X-FEM) which enables the growth of a crack independent of the mesh and nodes are enriched with the discontinuous function. The current implementation of this method requires definition of crack-tip/front, which is not suitable for multibody simulations. Therefore, an implementation of X-FEM with a criterion for crack initiation using explicit integration is recommended for future work.

8.2.2 Tribological characterisation of contact interaction

In all simulations, an empirical law of Coulomb has been assumed for friction. As shown in Chapter 6, the particle roughness reduces the frictional forces. The future simulation can be advanced by accounting for small-scale surface roughness and loading history in contact laws.

Additionally, to understand the transport of wear particles in a contact, there is a need to study particle-particle friction in complex contact conditions where asperity breakage are occurring. These tribological characterisations have to be also extended from dry-friction to fluid-friction.

8.2.3 Experimental strain measurement in a granular assembly

An extended grain-scale validation of the numerical approach can be obtained by direct comparison of strain concentration in individual grains. By combining x-ray diffraction and x-ray tomography, the *in situ* evolution of grain strain in a granular system can be quantified. The assessment of the model, in particular for breakage simulation can be carried out by considering strain concentration in individual grains.

8.2.4 Blind prediction of stress-strain behaviour

The aim of the work presented in this thesis is to emphasise the importance of contact behaviour arising from irregular grain shape, which controls the macroscopic stress-strain behaviour. By adopting the grain virtualisation method developed in chapter 5, it may be possible to predict the stress-strain behaviour of soil using the μ FE model with access to only a sample of a few grains. Then, a random RVE can numerically be generated by pouring the grains into a container. A laboratory element test can be prepared in the same way and the result can be compared blindly. The work may have high impact in several fields beyond soil mechanics if it demonstrates a close agreement in the outcomes.

REFERENCES

- Alonso-Marroquin, F., Luding, S., Herrmann, H. J. & Vardoulakis,I. (2005). Role of anisotropy in the elastoplastic response of a polygonal packing. *Physical Review E* **71**, No. 5, 051304-(1-18).
- Altuhafi, F.N. & Coop, M.R., (2011). Changes to particle characteristics associated with the compression of sands. *Géotechnique* **61**, No. 6, 459-471.
- Altuhafi, F.N., Coop, M.R., & Georgiannou, V. (2016). Effect of particle shape on the mechanical behaviour of natural sands. *J. Geotech. Geoenviron. Eng.* 04016071.
- Amini, S., Tadayon, M., Idapalapati, S. & Miserez, A. (2015). The role of quasi-plasticity in the extreme contact damage tolerance of the stomatopod dactyl club. *Nature Mater.* **14**, No. 9, 943–950.
- Andrade, J. E., Lim, K. W., Avila, C. F. & Vlahinic', I. (2012). Granular element method for computational particle mechanics. *Comput. Methods Appl. Mech. Eng* **241–244**, 262–274.
- Andò, E., Viggiani, G., Hall, S.A. & Desrues, J. (2013). Experimental micro-mechanics of granular media studied by X-ray tomography: recent results and challenges. *Géotechnique Letters* **3** (3), 142-146.
- Antony, S. J. (2001). Evolution of force distribution in three-dimensional granular media. *Physical Review E* **63**, 011302.
- Archard, J. F. (1957). Elastic deformation and the laws of friction. *Proc. R. Soc. A.*, **243** (1233), 190–205.
- Ardanza-Trevijano, S., Zuriguel, I., Arévalo, R., Maza, D., (2014). Topological analysis of tapped granular media using persistent homology, *Physical Review E* **89**, 052212.
- ASTM (2008). ASTM D696-08e1: Standard test method for coefficient of linear thermal expansion of plastics between -30°C and 30°C with a vitreous silica dilatometer. West Conshohocken, PA, USA: ASTM International.
- ASTM (2016). ASTM D4253-16: Standard test methods for maximum index density and unit weight of soils using a vibratory table. West Conshohocken, PA, USA: ASTM International.
- Atwood, R. C., Jones, J. R., Lee, P. D. & Hench, L. L. (2004) Analysis of pore interconnectivity in bioactive glass foams using X-ray microtomography. *Scripta Materialia* **51**, No. 11, 1029–1033.
- Azéma, E. & Radjai, F. (2012). Force chains and contact network topology in sheared packings of elongated particles. *Physical Review E* **85**, No. 3, 031303.

Barreto, D. (2010). *Numerical and experimental investigation into the behaviour of granular materials under generalised stress states*. PhD thesis, Imperial College London, London, UK.

Barreto D & O'Sullivan C., (2012). The influence of inter-particle friction and the intermediate stress ratio on soil response under generalised stress conditions, *Granular Matter* **14**, 505-521.

Been, K. & Jefferies, M.G., (1985). A state parameter for sands. *Géotechnique* **35**, No. 2, 99-112.

Beucher, S. & Lantuejoul, C. (1979). Use of watersheds in contour detection. In International Workshop on Image Processing: Real-time Edge and Motion Detection/Estimation, Rennes, France.

Blumenfeld, R. & Ma J. (2017). Bending back stress chains and unique behaviour of granular matter in cylindrical geometries. *Granular Matter* 19:29, DOI: 10.1007/s10035-017-0707-8.

Bolton, M.D. (1999). The role of micro-mechanics in soil mechanics. Presented at the international workshop on soil crushability, Yamaguchi University, Japan, July 1999

Borst, R. D., Remmers, J. J. C., Needleman, A., & Abellán, M.-A. (2004). Discrete vs. smeared crack models for concrete fracture: Bridging the gap. *Int. J. Numer. Anal. Methods Geomech.*, **28** (7–8), 583–607.

Bouchaud, J. P., Claudin, P., Levine, D. & Otto, M. (2001). Force chain splitting in granular materials: A mechanism for large-scale pseudo-elastic behaviour. *The European Physical Journal E*, **4** (4), 451-457.

Brunke, O., Brockdorf, S., Drews, K., Muller, B., Donath, T., Herzen, J. & Felix Beckmann, F. (2008). Comparison between X-ray tube based and synchrotron radiation based microCT. In *Developments in X-ray tomography VI* (ed. S. R. Stock), Proceedings of SPIE volume 7078, paper 70780U. Bellingham, WA, USA: SPIE.

Butterfield, R. & Andrawes, K. Z. (1970). An air activated sand spreader for forming uniform sand beds. *Géotechnique* **20**, No. 1, 97–100.

Camenen, J. F., Cavarretta, I., Hamlin, S. & Ibraim, E. (2013). Experimental and numerical assessment of a cubical sample produced by pluviation. *Géotechnique Letters* **3**, No. 2, 44–51.

Campana, C. & Müser, M.H. (2007) Contact mechanics of real vs. randomly rough surfaces: A Green's function molecular dynamics study. *Europhys. Lett.* **77** 38005.

Cates, M. E., Wittmer, J. P., Bouchaud, J. P. & Claudin, P. (1998). Jamming, force chains, and fragile matter. *Phys. Rev. Lett.* **81**, No. 9, 1841.

Cavarretta, I. (2009). *The influence of particle characteristics on the engineering behaviour of granular materials*. PhD thesis, Imperial College London, London, UK.

Cavarretta, I., Coop, M. & O'Sullivan, C. (2010). The influence of particle characteristics on the behaviour of coarse grained soils. *Géotechnique* **60**, No. 6, 413–423.

- Cavarretta, I. & O'Sullivan, C. (2012). The mechanics of rigid irregular particles subject to uniaxial compression. *Géotechnique* **62**, No. 8, 681–692.
- Cavarretta, I., O'Sullivan, C., Ibraim, E., Lings, M., Hamlin, S. & Wood, D.M. (2012). Characterization of artificial spherical particles for DEM validation studies. *Particuology* **10**, No. 2, 209–220.
- Chen, L. & Xu, J. (2004). Optimal Delaunay triangulations. *J. Comput. Math.* **22**, No. 2, 299–308.
- Chen, K., Cole, J., Conger, C., Draskovic, J., Lohr, M., Klein, K., Scheidemantel, T. & Schiffer, P. (2006). Granular materials: packing grains by thermal cycling. *Nature* **442**, No. 7100, 257.
- Cheung, G. & O'Sullivan, C. (2008). Effective simulation of flexible lateral boundaries in two and three-dimensional DEM simulations. *Particuology* **6**, No. 6, 483–500.
- Christensen, R.M. (2000). Yield functions, damage states, and intrinsic strength. *Mathematics and Mechanics of Solids* **5**, No. 3, 285–300.
- Cil, M. B. & Alshibli, K. A. (2014). 3D evolution of sand fracture under 1D compression. *Géotechnique* **64**, No. 5, 351.
- Cole, D. M., Mathisen, L. U., Hopkinks, M. A. & Knapp, B. R. (2010). Normal and sliding contact experiments on gneiss. *Granular Matter* **12**, No. 1, 69–86.
- Cresswell, A. & Powrie, W. (2004). Triaxial tests on an unbonded locked sand. *Géotechnique* **54**, No. 2, 107–115.
- Cuccovillo, T. & Coop, M. R. (1997). Yielding and pre-failure deformation of structured sands. *Géotechnique* **47**, No. 3, 491–508.
- Cui, L., O'Sullivan, C. & O'Neill, S. (2007). An analysis of the triaxial apparatus using a mixed boundary three-dimensional discrete element model. *Géotechnique* **57**, No. 10, 831–844.
- Cundall, P.A. & Strack, O.D.L. (1979). A discrete numerical model for granular assemblies. *Géotechnique* **29**, No. 1, 47–65.
- Dantu, P. (1957). Contribution à l'étude mécanique et géométrique des milieux pulvérulents. *Proc., 4th Int. Conf. on Soil Mechanics and Foundation Engineering*, Butterworth Scientific, London.
- Dassault Systèmes (2014). ABAQUS user's manual 2014 version 6.14. Providence, RI, USA: Dassault Systèmes.
- de Bono, J., McDowell, G. & Wanatowski, D. (2012). Discrete element modelling of a flexible membrane for triaxial testing of granular material at high pressures. *Géotechnique Letters* **2**, No. 4, 199–203.
- Deresiewicz, H. (1954). Contact of elastic spheres under an oscillating torsional couple. *Trans. ASME, J. Appl. Mech.* **21**, No. 1, 52–56.

Di Pasquale, L. (2016). *Particle breakage of granular material in 1D compression*, Master Thesis, Université Grenoble Alpes, France

Dintwa, E., Van Zeebroeck, M., Tijskens, E. & Ramon, H. (2004). Torsional stiffness of viscoelastic spheres in contact. *The European Physical Journal B-Condensed Matter and Complex Systems* **39**, No. 1, 77–85.

Dintwa, E., Zeebroeck, M. V., Tijskens, E. & Ramon, H. (2005). Torsion of viscoelastic spheres in contact. *Granular Matter* **7**, No. 2-3, 169–179.

Druckrey, A. M., Alshibli, K. A. & Al-Raoush, R. I. (2016). 3D characterization of sand particle-to-particle contact and morphology. *Comput. Geotech.* **74**, 26–35.

Duffy, J. & Mindlin, R. (1956). Stress–strain relations and vibrations of a granular medium. *ASME J. Appl. Mech.* **24**, 585–593.

Dusseault, M. B. & Morgenstern, N.R. (1979) Locked sands. *Q. J. Eng Geol.* **12**, 117–131

Ferellec, J. F. & McDowell, G. R. (2010). A method to model realistic particle shape and inertia in DEM. *Granular Matter* **12**, No. 5, 459–467.

Fogale (2005). Fogale nanotech user manual, version 1.5. Nimes, France: Fogale.

Fonseca, J. (2011). *The evolution of morphology and fabric of a sand during shearing*. PhD thesis, Imperial College London, University of London, London, UK.

Fonseca, J., O'Sullivan, C., Coop, M.R. & Lee, P.D. (2012). Non-invasive characterization of particle morphology of natural sands. *Soils Found.* **52**, No. 4, 712–722.

Fonseca, J., O'Sullivan, C., Coop, M. R. & Lee, P.D. (2013a). Quantifying the evolution of soil fabric during shearing using scalar parameters. *Géotechnique* **63**, No. 10, 818–829.

Fonseca, J., O'Sullivan, C., Coop, M. R. & Lee, P.D. (2013b). Quantifying the evolution of soil fabric during shearing using directional parameters. *Géotechnique* **63**, No. 6, 487–499.

Fonseca, J., Bésuelle, P. & Viggiani, G. (2013c). Micromechanisms of inelastic deformation in sandstones: an insight using x-ray micro-tomography. *Géotechnique Letters* **3**, No. 2, 78–83.

Fonseca, J., Reyes-Aldasoro, C.C., O'Sullivan, C. & Coop, M.R. (2014). Experimental investigation into the primary fabric of stress transmitting particles, *Geomechanics from Micro to Macro*, CRS Press, 1019–1024.

Fonseca, J., Reyes-Aldasoro, C.C. & Wils, L. (2015). Three-dimensional quantification of the morphology and intragranular void ratio of a shelly carbonate sand. In *Deformation characteristics of geomaterials: Proceedings of the 6th international symposium on deformation characteristics of geomaterials*, Buenos Aires, Argentina (eds V. A. Rinaldi, M. E. Zeballos and J. J. Clariá), pp. 551–558. Amsterdam, the Netherlands: IOS Press.

- Fonseca, J., Nadimi, S., Reyes-Aldasoro, C.C., O'Sullivan, C. & Coop, M.R. (2016). Image-based investigation into the primary fabric of stress transmitting particles in sand. *Soils Found.* **56**, No. 5, 818–834.
- Gao, Z., Zhao, J., Li, X.-S. & Dafalias, Y. F. (2014). A critical state sand plasticity model accounting for fabric evolution. *Int. J. for Num. and Anal. Meths in Geomechanics*, **38** (4), 370-3.
- Gerritsen, M., Kreiss, G. & Blumenfeld, R. (2008). Stress chain solutions in two-dimensional isostatic granular systems: fabric-dependent paths, leakage, and branching. *Physical Review Letters* **101**, 098001.
- Gethin, D. T., Lewis, R.W., & Ransing, R. S. (2003). A discrete deformable element approach for the compaction of powder systems. *Modell. Simul. Mater. Eng.*, **11** (1), 101–114.
- Goodman, R.E. (1989). *Introduction to rock mechanics* (Vol. 2, p. 576). New York: Wiley.
- Greenwood, J.A. & Williamson, J.B.P. (1966). Contact of Nominally Flat Surfaces. *Proc. R. Soc. Lond. A* **295**: 300-319.
- Greenwood, J. A., & Tripp, J. H. (1967). The elastic contact of rough spheres. *J. Appl. Mech. Trans. Am. Soc. Mech. Eng.*, **34** (1), 153–159.
- Greenwood, J. A., & Wu, J. J. (2001). Surface roughness and contact: An apology. *Meccanica*, **36** (6), 617–630.
- Hanley, K.J., Huang, X., O'Sullivan, C. & Kwok, F.C. (2014). Temporal variation of contact networks in granular materials, *Granular Matter*, **16**, 41-54.
- Hanley K.J., O'Sullivan C., Wadee M.A. & Huang X. (2015). Use of elastic stability analysis to explain the stress-dependent nature of soil strength. *R Soc Open Sci* **2** (4): 150038.
- Harthong, B., Jérier, J. F., Doremus, P., Imbault, D. & Donzé, F. V. (2009). Modelling of high-density compaction of granular materials by the discrete element method. *Int. J. Solids Structs* **46**, No. 18, 3357–3364.
- Harthong, B., Jérier, J., Richefeua, V., Chareyre, B., Dorémus, P., Imbault, D. & Donzé, F. (2012). Contact impingement in packings of elastic–plastic spheres, application to powder compaction. *Int. J. Mech. Sci.* **61**, No. 1, 32–43.
- Hasan, A. & Alshibli, K.A. (2010). Experimental assessment of 3D particle-to-particle interaction within sheared sand using synchrotron microtomography. *Géotechnique* **60** (5), 369-379.
- Hertz, H. (1882). Über die Berührung fester elastischer Körper. *J. für die reine und angewandte Mathematik* **92**, 156–171 (in German).
- Hidnert, P. & Krider, H.S. (1952). Thermal expansion of aluminium and some aluminium alloys. *J. Res. Natn. Bur. Stands* **48**, No. 3, 209–220.

- Holtzman, R., Silin, D. B. & Patzek, T. W. (2009). Mechanical properties of granular materials: a variational approach to grain-scale simulations. *Int. J. Numer. Analyt. Methods Geomech.* **33**, No. 3, 391–404.
- Huang, X. (2014). *Exploring critical-state behaviour using DEM*. PhD thesis, University of Hong Kong and Imperial College London, London, UK.
- Ibanez, L., Schroeder, W., Ng, L. & Cates, J. (2005). *The ITK software guide*. Clifton Park, NY, USA: Kitware Inc.
- Iwashita, K. & Oda, M. (1998). Rolling resistance contacts in simulation of shear band development by DEM. *J. Eng Mech.* **124**, No. 3, 285–292.
- Jiang, M., Yu, H. S. & Harris, D. (2005). A novel discrete model for granular material incorporating rolling resistance. *Comput. Geotech.* **32**, No. 5, 340–357.
- Johnson, K. L., Kendall, K., & Roberts, A. D. (1971). Surface energy and the contact of elastic solids. *Proc. R. Soc. London. Ser. A Math. Phys. Sci.*, **324** (1558), 301–313.
- Johnson, K. L. (1985). *Contact mechanics*. Cambridge, UK: Cambridge University Press.
- Katagiri, J., Matsushima, T. & Yamada, Y. (2010). Simple shear simulation of 3D irregularly-shaped particles by image-based DEM. *Granular Matter* **12**, No. 5, 491–497.
- Katagiri, J., Matsushima, T., Yamada, Y., Tsuchiyama, A., Nakano, T., Uesugi, K., Ohtake, M. & Saiki, K. (2014). Investigation of 3D grain shape characteristics of lunar soil retrieved in Apollo 16 using image based discrete element modeling. *J. Aerospace Eng. ASCE* **28**, No. 4, 04014092.
- Kawamoto, R., Andò, E., Viggiani, G. & Andrade, J. E. (2016). Level set discrete element method for three-dimensional computations with triaxial case study. *J. Mech. Phys. Solids* **91**, 1–13.
- Kendall, K. (1969). *The stiffness of surfaces in static and sliding contact*. Ph.D. thesis, Engineering Dept., Pembroke College, Univ. of Cambridge, Cambridge, U.K.
- Klotz, E.U. & Coop, M.R. (2001). An investigation of the effect of soil state on the capacity of driven piles in sands. *Géotechnique* **51**, No. 9, 733–751.
- Komodromos, P. I., & Williams, J. R. (2004). Dynamic simulation of multiple deformable bodies using combined discrete and finite element methods. *Eng. Comput.*, **21** (2/3/4), 431–448.
- Kong, D. & Fonseca, J. (2017). Quantification of the morphology of shelly carbonate sands using 3D images. *Géotechnique*, DOI: <https://doi.org/10.1680/jgeot.16.P.278>.
- Kuhn, M. R. (1999). Structured deformation in granular materials. *Mech. Mater.* **31**, No. 6, 407–429.
- Kumanr, N., Luding, S. & Magnanimo, V. (2014). Macroscopic model with anisotropy based on micro-macro information. *Acta Mechanica* **225**, 2319–2343.
- Lee, J. & Fenves, G.L. (1998). Plastic-damage model for cyclic loading of concrete structures. *Journal of engineering mechanics* **124**, No. 8, 892–900.

Lin, Q. & Tordesillas, A. (2014). Towards an optimization theory for deforming dense granular materials, *Journal of Industrial and Management Optimization*, **10**, 337–362.

Lorensen, W. & Cline, H. (1987). Marching cubes: a high resolution 3D surface construction algorithm. Computer Graphics. In Proceedings of 14th annual conference on computer graphics and interactive techniques, siggraph '87 (ed. M. C. Stone), pp. 163–169. New York, NY, USA: Association for Computing Machinery (ACM).

Lu, M. & McDowell, G. R. (2007). The importance of modelling ballast particle shape in the discrete element method. *Granular Matter* **9**, No. 1, 69–80.

Lubkin, J. L. (1951). The torsion of elastic spheres in contact. *ASME J. Appl. Mech.* **18**, No. 2, 183–187.

Lubliner, J., Oliver, J., Oller, S. & Onate, E. (1989). A plastic-damage model for concrete. *International Journal of solids and structures* **25**, No. 3, 299–326.

Luding, S. & Bauer, E. (2011). Evolution of swelling pressure of cohesive-frictional, rough and elasto-plastic granulates. In *Geomechanics and geotechnics: from micro to macro* (IS-Shanghai conference proceedings) (eds M. J. Jiang, F. Liu and M. Bolton), pp. 495–499. Rotterdam, the Netherlands: CRC Press/Balkema.

Maeda, K., Sakai, H., Kondo, A., Yamaguchi, T., Fukuma, M. & Nukudani, E. (2010). Stress-chain based micromechanics of sand with grain shape effect. *Granular Matter* **12**: 499–505.

Majmudar, T.S. & Behringer, R.P. (2005). Contact force measurements and stress-induced anisotropy in granular materials, *Nature* **435**, 1079–1082.

Marketos, G. & Bolton, M.D. (2007). Quantifying the extent of crushing in granular materials: a probability-based predictive method. *Journal of the Mechanics and Physics of Solids* **55**, No. 10, 2142–2156.

Marketos, G. & Bolton, M.D. (2010). Flat boundaries and their effect on sand testing. *Int. J. Numer. Analyt. Methods Geomech.* **34**, No. 8, 821–837.

Mathworks (2015). MATLAB release R2015b. Natick, MA, USA: Mathworks, Inc. Matsushima, T. & Chang, C. S. (2011). Quantitative evaluation of the effect of irregularly shaped particles in sheared granular assemblies. *Granular Matter* **13**, No. 3, 269–276.

Matsushima, T., Katagiri, J., Uesugi, K., Tsuchiyama, A. & Nakano, T. (2009). 3D shape characterization and image-based DEM simulation of the lunar soil simulant FJS-1. *J. Aerospace Eng* **22**, No. 1, 15–23.

Makse, H. A. & Johnson, D. L. (2000). Schwartz, L. M. Packing of compressible granular materials. *Physical Review Letters*, **84** (18), 4160.

McDowell, G. R., & Bolton, M. D. (1998). On the micromechanics of crushable aggregates. *Géotechnique* **48** (5), 667–679.

Michałowski, R.L., Wang, Z. & Nadukuru, S.S. (2017). Maturing of contacts and ageing of silica sand. *Géotechnique*, DOI: <http://dx.doi.org/10.1680/jgeot.16.P.321>.

Mindlin, R. D. (1949). Compliance of elastic bodies in contact. *J. Appl. Mech.* **16**, 259–268.

Mindlin, R. D. & Deresiewiez, H. (1953). Elastic spheres in contact under varying oblique forces. *ASME J. Appl. Mech.* **20**, 327–344.

Miskin, M. Z. & Jaeger, H. M. (2013). Adapting granular materials through artificial evolution. *Nature Mater.* **12**, No. 4, 326–331.

Miura, S. & Toki, S. (1982). Sample preparation method and its effect on static and cyclic deformation-strength properties of sand. *Soils Found.* **22**, No. 1, 61–77.

Moes, N., Dolbow, J., & Belytschko, T. (1999). A finite element method for crack growth without remeshing. *Int. J. Numer. Methods Eng.*, **46** (1), 131–150.

Munjiza, A. (2004). *The combined finite-discrete element method*. Chichester, UK: John Wiley & Sons.

Müser, M.H. (2016). On the contact area of nominally flat Hertzian contacts. *Tribology Letter* **64**: 14.

Nadimi, S., Fonseca, J. & Taylor, R. N. (2015). A microstructurebased finite element analysis of the response of sand. In *Deformation characteristics of geomaterials* (eds V. A. Rinaldi, M. E. Zeballos and J. J. Clariá), pp. 816–823. Amsterdam, the Netherlands: IOS Press.

Nadimi, S. & Fonseca, J. (2016). Enhancing soil sample preparation by thermal cycling. *Géotechnique* **66**, No. 11, 953-958. <http://dx.doi.org/10.1680/jgeot.15.T.033>

Nadimi, S. & Fonseca, J. (2017a). A micro finite element model for soil behaviour. *Géotechnique*, <https://doi.org/10.1680/jgeot.16.P.147>

Nadimi, S. & Fonseca, J. (2017b). A micro finite element model for soil behaviour: numerical validation. *Géotechnique*, <http://doi.org/10.1680/jgeot.16.P.163>

Nadimi, S. & Fonseca, J. (2017c). Single grain virtualisation for contact behaviour analysis on sand. *Journal of Geotechnical and Geoenvironmental Engineering* **143** (9) [https://doi.org/10.1061/\(ASCE\)GT.1943-5606.0001740](https://doi.org/10.1061/(ASCE)GT.1943-5606.0001740)

Nadimi, S. & Fonseca, J. (2017d). On the torsional loading of elastoplastic spheres in contact. In Powders and grains 2017 – 8th international conference on micromechanics on granular media (eds F. Radjai, S. Nezamabadi, S. Luding and J. Y. Delenne), *EPJ Web of Conferences* Vol. **140**, paper 05001. Les Ulis, France: EDP Sciences – Web of Conferences.

Nadimi, S. & Fonseca, J. (2017e). On the tensile strength of soil grains in Hertzian response. In Powders and grains 2017 – 8th international conference on micromechanics on granular media (eds F. Radjai, S. Nezamabadi, S. Luding and J. Y. Delenne), *EPJ Web of Conferences* Vol. **140**, paper 07001. Les Ulis, France: EDP Sciences – Web of Conferences.

Nadimi, S., Shire, T. & Fonseca, J. (2017). Comparison between a μ FE model and DEM for an assembly of spheres under triaxial compression. In Powders and grains 2017 – 8th international conference on micromechanics on granular media (eds F. Radjai, S.

Nezamabadi, S. Luding and J. Y. Delenne), *EPJ Web of Conferences* Vol. **140**, paper 15002. Les Ulis, France: EDP Sciences – Web of Conferences.

Nakata, Y., Kato, Y., Hyodo, M., Hyde, A. F. L., & Murata, H. (2001). One-dimensional compression behaviour of uniformly graded sand related to single particle crushing strength. *Soils & Foundations*, **41** (2), 39–51.

Nardelli, V., Coop, M.R., Andrade, J.E. & Paccagnella, F., (2017). An experimental investigation of the micromechanics of Eglin sand. *Powder Technology* **312**, 166-174.

Newman, M.E.J. (2003). The structure and function of complex networks. *SIAM Rev.* **45**, 167.

Nezamabadi, S., Radjai, F., Averseng, J. & Delenne, J. Y. (2015). Implicit frictional-contact model for soft particle systems. *J. Mech. Phys. Solids* **83**, 72–87.

Nguyen, D., Azéma, E., Sornay, P. & Radjai, F. (2015). Effects of shape and size polydispersity on strength properties of granular materials. *Phys. Rev. E* **91**, No. 3, 032203.

Oda, M. (1972). Initial fabrics and their relations to mechanical properties of granular material. *Soils and Foundations* **12** (1), 17-36.

Oda, M., Konishi, J., & Nemat-Nasser, S. (1982). Experimental micromechanical evaluation of strength of granular materials: Effects of particle rolling. *Mech. Mater.* 1, No. 4, 269–283.

Oda, M. & Kazama, H. (1998). Microstructure of shear bands and its relation to the mechanisms of dilatancy and failure of dense granular soils *Géotechnique* **48** (4), 465-481.

Oda, M. & Iwashita, K. (1999). *Mechanics of granular materials, an introduction*. Rotterdam, the Netherlands: CRC Press.

Oda, M., Takemura, T. & Takahashi, M. (2004). Microstructure in shear band observed by microfocus X-ray computed tomography. *Géotechnique* **54** (8), 539-542.

O'Donovan, J., Hamlin, S., Marketos, G., O'Sullivan, C., Ibraim, E., Lings, M. & Wood, D. M. (2015). Micromechanics of seismic wave propagation in granular materials. In *Geomechanics from micro to macro* (eds K. Soga, K. Kumar, G. Biscontin and M. Kuo). London, UK: Taylor & Francis Group.

Ostojic, S., Somfai, E. & Nienhuis, B. (2006). Scale invariance and universality of force networks in static granular matter. *Nature* **439** (7078), 828–830.

O'Sullivan, C., Bray, J. D. & Riener, M. (2004). Examination of the response of regularly packed specimens of spherical particles using physical tests and discrete element simulations. *J. Eng Mech. – ASCE* **130**, No. 10, 1140–1150.

O'Sullivan, C. (2011). *Particulate Discrete Element Modelling: A Geomechanics Perspective*. Spon Press.

Otsu, N. (1979). A threshold selection method from gray-level histograms. *IEEE Trans. Systems, Man and Cybernetics* **9**, No. 1, 62–66.

- Otsubo, M., O'Sullivan, C., Hanley, K.J. & Sim, W.W. (2017). The influence of particle surface roughness on elastic stiffness and dynamic response. *Géotechnique* **67** (5): 452–459.
- Paniagua, P., Fonseca, J., Gylland, A.S. & Nordal, S. (2015). Microstructural study of the deformation zones during cone penetration in silt at variable penetration rates, *Canadian Geotechnical Journal*, 10.1139/cgj-2014-0498.
- Pasha, M., Dogbe, S., Hare, C., Hassanpour, A. & Ghadiri, M. (2014). A new linear contact model for elasto-plastic and adhesive contacts in Distinct Element Method. *Granular Matter* **16**, No. 1, 151–162.
- Pastewka, L. & Robbins, M.O. (2016). Contact area of rough spheres: large scale simulations and simple scaling laws. *Appl. Phys. Lett.* **108**, 221601.
- Percier, B., Divoux, T. & Taberlet, N. (2013). Insights on the local dynamics induced by thermal cycling in granular matter. *Europhys. Lett.* **104**, No. 2, 24001.
- Persson, B.N.J., Albohr, O., Tartaglino, U., Volokitin, A.I. & Tosatti, E. (2005). On the nature of surface roughness with application to contact mechanics, sealing, rubber friction and adhesion. *Journal of Physics: Condensed Matter* **17** (1).
- Peters, J. F., Muthuswamy, M., Wibowo, J. & Tordesillas, A. (2005). Characterization of force chains in granular material, *Physical Review E* **72**, 041307.
- Pouraghah, M. & Wan, R. (2016). Onset of structural evolution in granular materials as a redundancy problem. *Granular Matter* **18**, No. 3, 38.
- Thornton, C. (1979). The conditions of failure of a face-centered cubic array of uniform rigid spheres. *Géotechnique* **29**, No. 4, 441–459.
- Thornton, C. (2015). *Granular dynamics, contact mechanics and particle system simulations*, Springer International, Cham, Switzerland.
- Rad, N. S. & Tumay, M. T. (1987). Factors affecting sand specimen preparation by raining. *Geotech. Testing J.* **10**, No. 1, 31–37.
- Radjai, F., Wolf, D. E., Jean, M. & Moreau, J. J. (1998). Bimodal character of stress transmission in granular packings. *Physical Review Letters*, **80** (1), 61.
- Radjai, F. (2008). Particle-scale origins of shear strength in granular media. Second Euro-Mediterranean symposium on advances in geomaterials and structures (AGS08), Hammamet, Tunisia.
- Radjai, F., Delenne, J. Y., Azema, É., & Roux, S. (2012). Fabric evolution and accessible geometrical states in granular materials. *Granular Matter* **14**, No. 2, 259–264.
- Radjai, F., Roux, J.N. & Daouadji, A. (2017). Modeling Granular Materials: Century-Long Research across Scales. *Journal of Engineering Mechanics*, **143** (4), 04017002.
- Rechenmacher, A., Abedi, S. & Chupin, O. (2010). Evolution of force chains in shear bands in sands. *Géotechnique*, **60** (5), 343–351.

Reyes-Aldasoro, C.C. (2015). *Biomedical Image Analysis Recipes in MATLAB: For Life Scientists and Engineers*, Wiley-Blackwell, London.

Reynolds, O. (1885). LVII. On the dilatancy of media composed of rigid particles in contact. With experimental illustrations. *The London, Edinburgh, and Dublin Philosophical Magazine and Journal of Science* **20**, No. 127, pp.469-481.

Rineau, L. & Yvinec, M. (2017). 3D surface mesh generation. In CGAL user and reference manual, 4.10 edn, chapter 53. Valbonne, France: CGAL Editorial Board, Geometry Factory.

Roscoe, K.H. (1970). The influence of strains in soil mechanics. *Géotechnique* **20**, No. 2, 129-170.

Russell, A.R. & Wood, D.M. (2009). Point load tests and strength measurements for brittle spheres. *International Journal of Rock Mechanics and Mining Sciences* **46**, No. 2, 272-280.

Russell, A. R., & Einav, I. (2013). Energy dissipation from particulate systems undergoing a single particle crushing event. *Granular Matter*, **15** (3), 299–314.

Santamarina, C. & Cascante, G. (1998). Effect of surface roughness on wave propagation parameters. *Géotechnique* **48**, No. 1, 129–136.

Santamarina, C. (2001). Soil behaviour at the microscale: particle forces. *Proc. Symp. Soil Behavior and Soft Ground Construction*, in honor of Charles C. Ladd – MIT.

Satake, M. (1982). Fabric tensor in granular materials. In IUTAM Conference on Deformation and Failure of Granular Materials.

Schindelin, J., Rueden, C. T., Hiner M. C. & Eliceiri K. W. (2015). The ImageJ ecosystem: an open platform for biomedical image analysis. *Molecular Reproduction and Development* **82**, No. 7–8, 518–529.

Schofield, A. & Wroth, P. (1968). *Critical state soil mechanics* (Vol. 310). London: McGraw-Hill.

Seiferlin, K., Ehrenfreund, P., Garry, J., Gunderson, K., Hütter, E., Kargl, G., Maturilli, A. and Merrison, J.P., (2008). Simulating Martian regolith in the laboratory. *Planetary and Space Science* **56** (15), pp.2009-2025.

Senetakis, K., Coop, M. R. & Todisco, M. C. (2013). The inter-particle coefficient of friction at the contacts of Leighton Buzzard sand quartz minerals. *Soils Found.* **53**, No. 5, 746–755.

Sharifipour, M. & Dano, C. (2006). Effect of grains roughness on waves velocities in granular packings. *Proceedings of the 1st Euro Mediterranean conference on advances on geomaterials and structure*. Hammamet, pp. 123–128.

Shewchuk, J. R. (2002). Constrained Delaunay tetrahedralizations and probably good boundary recovery. Proceedings of the 11th international meshing roundtable, Ithaca, NY, USA, pp. 193–204.

- Shewchuk, J. R. (2014). Reprint of: Delaunay refinement algorithms for triangular mesh generation. *Computational Geometry: Theory and Applications* **47**, No. 7, 741–778.
- Silbert, L.E., Grest, G.S. & Landry, J.W. (2002). Statistics of the contact network in frictional and frictionless granular packings. *Physical Review E* **66** (6), 061,303.
- Skinner, B. J. (1966). Thermal expansion. In *Handbook of physical constants*, revised edn (ed. S. P. Clark), Memoir 97, pp. 75–96. Boulder, CO, USA: The Geological Society of America, Inc.
- Sun, Y., Indraratna, B., & Nimbalkar, S. (2014). Three-dimensional characterisation of particle size and shape for ballast. *Géotechnique Lett.*, **4** (3), 197–202.
- Terzaghi, K.V. (1920). Old earth pressure theories and new test results. *Engineering News-Record* **85**, No. 14, pp.632-637.
- Terzaghi, K., Peck, R. B., & Mesri, G. (1996). *Soil mechanics in engineering practice*. 3rd Ed., Wiley, New York.
- Thakur, S. C., Morrissey, J. P., Sun, J., Chen, J. F. & Ooi, J. Y. (2014). Micromechanical analysis of cohesive granular materials using the discrete element method with an adhesive elasto-plastic contact model. *Granular Matter* **16**, No. 3, 383–400.
- Thornton, C. (1993). On the relationship between the modulus of particulate media and the surface energy of the constituent particles. *J. Phys. D: Appl. Phys.* **26** 1587.
- Tordesillas, A. & Muthuswamy, M. (2009). On the modelling of confined buckling of force chains. *J. Mechanics Physics Solids* **57**, 706–727.
- Tordesillas, A., Walker, D. M. & Lin, Q. (2010). Force cycles and force chains. *Physical Review E* **81** (1), 011302.
- Tordesillas, A., Sibille, L., Pucilowski, S., Nicot, F. & Darve, F. (2011). Microstructural evolution in diffuse granular failure: force chains and contact cycles. In *Second International Symposium on Computational Geomechanics* (ComGeo II).
- Tordesillas, A., Tobin, S.T., Cil, M., Alshibli, K. & Behringer, R.P. (2015). Network flow model of force transmission in unbonded and bonded granular media, *Physical Review E*.
- Troadec, H., Radjai, F., Roux, S., & Charmet, J. (2002). Model for granular texture with steric exclusion. *Physical Review E* **66**, No. 4, 041305.
- Vaid, Y. P. & Negussey, D. (1984). Relative density of pluviated sand samples. *Soils Found.* **24**, No. 2, 101–105.
- Vanimisetti, S. K., & Narasimhan, R. (2006). A numerical analysis of spherical indentation response of thin hard films on soft substrates. *Int. J. Solids Struct.*, **43** (20), 6180–6193.
- Viggiani, G., Ando, E., Jaquet, C., & Talbot, H. (2013). Identifying and following particle-to-particle contacts in real granular media: An experimental challenge. *AIP Conference Proceedings* **1542**, 60 DOI: <http://dx.doi.org/10.1063/1.4811868>

- Vlahinić, I., Andò, E., Viggiani, G., & Andrade, J. E. (2014). Towards a more accurate characterization of granular media: Extracting quantitative descriptors from tomographic images. *Granular Matter* **16** (1), 9–21.
- Voivret, C., Radjai, F., Delenne, J. Y. & El Youssoufi, M. S. (2009). Multiscale force networks in highly polydisperse granular media. *Physical review letters* **102** (17), 178001.
- Wang, L., Park, J. Y. & Fu, Y. (2007). Representation of real particles for DEM simulation using X-ray tomography. *Constr. Building Mater.* **21**, No. 2, 338–346.
- Wang, W., & Coop, M. R. (2016). An investigation of breakage behaviour of single sand particles using a high-speed microscope camera. *Géotechnique* **66** (12), 984–998.
- Wils, L., Van Impe, W. F., Haegeman, W. & Van Impe, P. O. (2013). Laboratory testing issues related to crushable sands. *Proceedings of the 18th international conference on soil mechanics and geotechnical engineering*, Paris, France, pp. 275–278.
- Wu, S. R. (2006). Lumped mass matrix in explicit finite element method for transient dynamics of elasticity. *Comput. Methods Appl. Mech. Eng.* **195**, No. 44–47, 5983–5994.
- Yang, Y., Wang, J. F. & Cheng, Y. M. (2016). Quantified evaluation of particle shape effects from micro-to-macro scales for non-convex grains. *Particuology* **25**, 23–35.
- Yimsiri, S. & Soga, K. (2000). Micromechanics-based stress–strain behaviour of soils at small strains. *Géotechnique* **50**, No. 5, 559–571.
- Zhao, B., Wang, J., Coop, M. R., Viggiani, G., & Jiang, M. (2015). An investigation of single sand particle fracture using X-ray microtomography. *Géotechnique* **65**, No. 8, 625–641.
- Zheng, Q. J., Zhu, H. P. & Yu, A. B. (2012). Finite element analysis of the contact forces between a viscoelastic sphere and rigid plane. *Powder Technology* **226**, 130–142.
- Zhou, B. & Wang, J. (2017). Generation of a realistic 3D sand assembly using X-ray micro-computed tomography and spherical harmonic-based principal component analysis. *Int. J. Numer. Analyt. Methods Geomech.* **41**, 93–109.
- Zuriguel, I., Mullin, T. & Rotter, J.M. (2007). Effect of particle shape on the stress dip under a sandpile. *Phys. Rev. Lett.* **98** (2), 028001.

ENHANCING SOIL SAMPLE PREPARATION BY THERMAL CYCLING

Published in: *Géotechnique* 2016; 66 (11): 953–958.

A.1 Introduction

For the most part, the behaviour of soil has been investigated using laboratory-prepared samples. Depending on the mode of deposition and the grain morphology, different topological configurations in terms of grain rearrangements and void geometries may emerge, and this has a fundamental role in determining the properties of the material being measured (Butterfield & Andrawes, 1970; Miura & Toki, 1982; Rad & Tumay, 1987; Fonseca *et al.*, 2013a). While the uniformity of the sample is a matter of concern, there is limited control on the local void ratio variations and the contact topologies obtained using either gravity-induced deposition or mechanical-energy-based methods.

For samples produced by different air pluviation configuration, density within the granular medium appear to be non-uniform (Vaid & Negussey, 1984). In fact, higher densities are often attained in the central part of the sample and lower densities at the boundaries (e.g. Camenen *et al.*, 2013). Marketos & Bolton (2010) have pointed out that not only the lower void ratio attained at the boundary of the sample, but also the low number of contacts in the soil-boundary interface affects the soil behaviour measured from laboratory testing.

A key aspect in sample preparation is to mimic *in situ* characteristics such as relative density and soil fabric as closely as possible. Intact sand, in particular older formations possess mature fabrics that have developed during geological history, which can hardly be reproduced using conventional laboratory techniques. Cuccovillo & Coop (1997) have shown that the low void ratio values found on intact samples of Greensand could not be attained in the laboratory by loading the sample to values closer to the overburden stresses experienced by the intact material. Fonseca *et al.* (2012) have used a combination of pouring and tamping to prepare reconstituted samples with densities close to the intact values. However, these mechanical processes have led to the disintegration of pre-

cracked grains and thus, have produced samples with distinct fabric, grading and contact topologies and consequently distinct mechanical response when compared to the intact sand.

Increasing computational power has enabled numerical simulations to model the discrete nature of soil, and validation of the numerical results require better and more controllable physical samples. Difficulties in obtaining the same void ratio values for laboratory samples and DEM specimens obtained using an analogous process have been highlighted previously (e.g. O'Donovan *et al.*, 2015). It is clear from previous studies that laboratory characterisation of soil response requires enhanced sample fabrication able to provide more uniform specimens with more stable and controllable fabric and those are the key aspects that the technique presented here aims to advance.

A.2 Experimental Method

The technique presented here consists of making use of thermal energy to enhance the granular packing of sand for laboratory testing. This work draws upon previous studies on the dynamics induced by thermal cycling on granular media (Chen *et al.*, 2006; Percier *et al.*, 2013). The rise in temperature results in a thermal expansion of the grains and the container, which causes the granular assembly to settle and densify. The change in the density of the sample is a function of the differential thermal expansion between the grains and the container. Bringing the sample back to room temperature does not alter the newly formed fabric, so the sample can be used for laboratory and physical testing. The packing of the grains can incrementally be enhanced using successive thermal cycles of heating-cooling; termed thermal cycling herein. Fig. A.1 shows a schematic of how thermal cycling acts in producing a more compacted fabric.

A.2.1 Materials

The materials used in the experiments were: a fine graded Dogs Bay carbonate sand from the Republic of Ireland (Klotz and Coop, 2001), a coarse graded carbonate sand from the Persian Gulf (Fonseca *et al.*, 2015); a silica Leighton Buzzard sand; and glass ballotini. The material properties are presented in Table A.1 and the particle size distributions (PSDs) of all four materials are shown in

Fig. A. 2. The sands had been chosen for their diverse properties, that is, particle mineralogy and morphology, and their extensive use in previous research. The carbonate sands are made from the remains of marine organisms, such as shells and skeletal materials. These shelly grains are angular and tend to form loose fabrics. Moreover, the relative softness of the grains makes them more susceptible to crushing under relatively small loads. Leighton Buzzard sand is part of the Lower Greensand formation from the UK, it comprises angular to sub-angular particles, free of silt or clay (Klotz and Coop, 2001).

Cylindrical containers made of poly (methyl methacrylate) PMMA and aluminium, with the dimensions as specified in Fig. A-3, were used. This is believed to be representative of the vessels commonly found in soil mechanics laboratories.

A.2.2 Sample preparation and void ratio measurements

The samples were prepared using the air pluviation method as described by Cavarretta (2009). This technique consists of filling the throat of the funnel at each deposition step while keeping it in contact with the top surface of the soil. The throat is then raised and the soil is deposited without excessive impact or agitation. Tapping on the sides of the container was applied to produce the denser samples and a slight tapping was also used at the end of the pluviation process in order to create a flat surface; this is particularly important for the accuracy of the void ratio measurements. A height over diameter ratio (H/D) of approximately 1.2 was used for all samples.

For the measurement of the global void ratio, the height of the sample was obtained by averaging four equally spaced reading points on the sample's top surface using a depth gauge (precision of 0.01 mm) and the mass of soil was measured with a precision of 0.01g. The specific gravity values provided in Table A.1 were used.

A.2.3 Experimental set-up

A piston was placed on top of the sample and a small dead weight of approximately 0.7 kPa was applied; a schematic diagram of the set-up is shown in Fig. A-3. The temperature was increased from a room temperature of

approximately 25 to 85°C, in other words, $\Delta T = 60^\circ\text{C}$. The sample was kept in the oven for 9 h to ensure that the same temperature was reached throughout the granular system. Subsequently, the sample was cooled down to the initial room temperature and the void ratio measurements were taken after 15 h. Each cycle took 24 h. In total, 15 tests were carried out, of which nine were stopped after five cycles and only six were stopped after 20 thermal cycles (Table A-2).

A.3 Results and Discussion

The void ratio values at the end of each cycle were measured in terms of the change in height of the sample or settlement of the piston. The top surface of the sample was found to be fairly levelled after thermal cycling, which is in part related to the effect of the dead weight, but also suggests that packing densification is a bulk effect rather than a boundary effect; this has also been observed by Chen *et al.* (2006). The densification was assessed in terms of relative density, $D_r = (e_{max} - e)/(e_{max} - e_{min}) \times 100$.

A.3.1 Effect of container and initial density

The most significant change in density was obtained using a PMMA container; that is, ΔD_r values of 25% for the silica sand and 13% for the fine carbonate sand were measured at the end of 20 thermal cycles, compared with much lower values of 4.2 and 2% for the aluminium container. The incremental changes throughout the 20 thermal cycles are presented in Fig. A-4a for the silica sand and Fig. A-4b for the fine carbonate sand. For both sands the PMMA container exhibits, clearly, a more marked relaxation.

The experiments carried out on glass ballotini also confirmed a significant densification using the PMMA container, with a final void ratio of 0.57 (very close to e_{min}) attained at the end of 20 cycles (Fig. A-5a). In this case, however, the ΔD_r values measured for the PMMA and aluminium containers were similar, namely, 14 and 13.2%, respectively. This can be related to the distinct initial void ratio of the two samples; thus, the results were plotted using a normalised void ratio, which again shows better results using the PMMA container (Fig. A-5b).

The greater densification obtained using a PMMA container can, in part, be explained based on the expected linear expansion of the grains and the container presented in Table A-3, for a ΔT of 60°C. A linear expansion of 0.46% of the total diameter is expected for the PMMA container and only 0.14% for the aluminium container, therefore explaining the lower efficiency of the latter. The expected expansion of the grains is lower for the carbonate sand (0.04% of the mean diameter) and larger for the silica (0.10%), with the glass ballotini in between (0.05%). Since the H/D ratio of the sample is kept constant, the effect of increasing the sample diameter on the diametrical expansion is compensated by the reduction of the height so the overall volumetric or bulk expansion is not expected to be affected.

A.3.2 *Effect of grain morphology and packing*

As shown in Fig. A-4 and Fig. A-5, when subjected to multiple successive thermal cycles, the density of the granular system continues to increase, while the increment after each cycle tends to become progressively smaller. In fact, after five thermal cycles and for the PMMA container, the void ratio reduction measured for the silica and the fine carbonate sands was more than 50% of the value attained at the end of 20 cycles and after ten cycles the values were as high as 86 and 75%, respectively. The Δe values measured for the glass ballotini were much lower compared with the sands and the reduction was seen to be more gradual throughout the 20 cycles. The lower susceptibility of the glass ballotini to compact under thermal cycling can be attributed to the limited packing configurations that mono-sized spheres exhibit and the more stable fabric when compared with the packing of irregular shaped sand grains.

The ability of thermal cycling to densify samples of the three sands with different initial densities is demonstrated in Fig. A-6a for the coarse carbonate, Fig. A-6b for silica sand and Fig. A-6c for the fine carbonate sand. In addition, when comparing the change in relative density for each specimen, as presented in Table A-4, it can be seen that greater values were measured for the samples with lower initial density, with particularly high values for the silica sand.

Although for the two carbonate sands the final relative densities attained were lower than the silica sand, the results are very satisfactory given the difficulties in

obtaining D_r values greater than 60% without breakage of the grains. In fact, Wils *et al.* (2013) report on the limitations of using standard densification techniques, such as described in ASTM (2016) for carbonate sands, and they cause grain crushing which alters the e_{min} value and the upper limit of D_r .

A.3.3 *Thermally induced grain rearrangement*

Granular systems form contact networks of stress transmitting grains able to resist external loads and other mechanical perturbations, and this increases the resilience of the material to changes in fabric under static loading (Fig. A-7a). It is suggested here that the small disturbance induced by thermal variations causes breakage of force chains, as discussed in Cates *et al.* (1998), which in turn leads to grain rearrangement and the formation of a new contact network (Fig. A-7b). The unlocking of the initial fabric creates additional degrees of freedom, leading to a temporary loss of contacts and consequently to the filling of the large voids (void collapse) in a less invasive way when compared to compaction. In fact, densification using mechanical-energy-based methods requires overcoming friction at the contacts, which in some cases may involve abrasion at the contacts and further grain damage and breakage. These phenomena are particularly relevant for carbonate sands, for which the highly angular grains tend to form large voids randomly distributed, as illustrated in Fig. A-8 and, in addition, the softness of the grains makes them more prone to damage and breakage.

A.4 Conclusions

This paper explores new mechanisms of thermally induced grain dynamics to enhance sample preparation for laboratory experiments. The experimental observations seem to suggest that the densification of the specimen when submitted to thermal cycling is the result of grain rearrangement due to the additional degrees of freedom created by the expansion of the system. In this way, the density of the sample is increased in a systematic and controllable way without resorting to mechanical energy, which makes this technique less invasive when compared, for example, with compaction techniques. It is shown that sands are more susceptible to densification through thermal cycling when compared

with a sample of mono-sized spheres, and this is attributed to the complex morphologies and the metastable fabrics found in natural sands. Future work will investigate the additional potential of thermally induced deformation to produce samples with more uniform densities and more stable/mature fabrics.

A.5 Tables and Figures

Table A-1. Physical properties of granular materials used

	d_{50} (μm)	G_s	e_{\min}	e_{\max}	$C_u(d_{60}/d_{10})$
Fine carbonate sand	240	2.71	0.98	1.87	2.0
Coarse carbonate sand	570	2.82	0.83	2.38	2.8
Silica sand	900	2.65	0.51	1.01	1.5
Glass ballotini	180	2.50	0.50	0.75	1.1

Table A-2. Summary of results obtained from thermal cycling experiments

Test ID*	H	H/D	Cycle	e_i	e_f	Δe	$D_{ri} \%$	$D_{rf} \%$	$\Delta D_r \%$
GB-P32a	37.86	1.18	5	0.642	0.631	0.011	43.2	47.6	4.4
			20		0.570	0.035		72.0	14.0
GB-P32b	36.60	1.14	5	0.605	0.594	0.011	58.0	62.4	4.4
			20		0.574	0.125		87.2	25.0
SS-P32a	39.00	1.22	5	0.699	0.627	0.072	62.2	76.6	14.4
SS-P32b	38.28	1.20	5	0.658	0.626	0.032	70.4	76.8	6.4
SS-P32c	37.78	1.18	5	0.621	0.599	0.022	77.8	82.2	4.4
FCS-P32a	41.90	1.31	5	1.465	1.394	0.071	45.5	53.5	8.0
FCS-P32b	39.98	1.25	20	1.395	1.279	0.116	53.4	66.4	13.0
			5		1.333	0.062		60.3	6.9
FCS-P32c	39.72	1.24	5	1.320	1.273	0.047	61.8	67.1	5.3
CCS-P32a	40.47	1.26	5	1.533	1.430	0.103	29.7	40.0	10.3
CCS-P32b	41.18	1.29	5	1.377	1.322	0.055	45.3	50.8	5.5
CCS-P32c	39.91	1.25	5	1.165	1.111	0.054	66.5	71.9	5.4
GB-P140	142.58	1.02	5	0.623	0.610	0.013	50.8	56.0	5.2
GB-A140	176.95	1.26	20	0.732	0.699	0.033	7.2	20.4	13.2
SS-A140	177.19	1.27	20	0.717	0.696	0.021	58.6	62.8	4.2
FCS-A140	177.40	1.27	20	1.467	1.449	0.018	45.3	47.3	2.0

*Test ID includes granular material abbreviation (GB, glass ballotini; SS, silica sand; FCS, fine carbonate sand; CCS, coarse carbonate sand), material of container (P, PMMA; A, aluminium) and container's internal diameter.

Table A-3. Coefficient of thermal expansion of materials used in experiments and expected expansion

	Coefficients of linear thermal expansion	Expected expansion
Granular media		
Glass ballotini (soda lime)	$9 \times 10^{-6} \text{ K}^{-1}$ (Chen, 2006)	0.10 μm (0.05% of d_{50})
Calcite (CaCo_3)	$6.7 \times 10^{-6} \text{ K}^{-1}$ (Skinner, 1966)	0.23 μm (0.04% of d_{50})
		0.10 μm (0.04% of d_{50})
Quartz (SiO_2)	$16.6 \times 10^{-6} \text{ K}^{-1}$ (Skinner, 1966)	0.89 μm (0.10% of d_{50})
Container		
Perspex (Acrylic)	$77 \times 10^{-6} \text{ K}^{-1}$ (ASTM D696)	148 μm (0.46% of 32 mm container)
Aluminium	$23.5 \times 10^{-6} \text{ K}^{-1}$ (Hidnert & Krider, 1952)	197 μm (0.14% of 140 mm container)

Table A-4. Change in void ratio at end of five thermal cycles for the three sands using the PMMA container

Initial density	$\Delta D_r(a) \%$ Loose	$\Delta D_r(b) \%$ Medium dense	$\Delta D_r(c) \%$ Dense
FCSP-32	8.0	6.9	5.3
CCS-P32	10.3	5.5	5.4
SS-P32	14.4	6.4	4.4

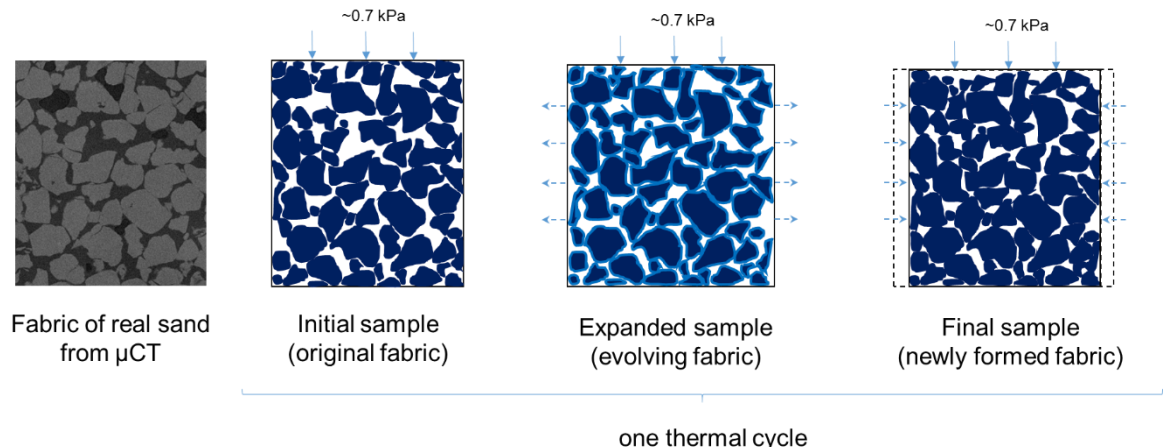


Fig. A-1. Schematic diagram illustrating the evolution of the internal fabric of a natural sand under thermal cycling; initial fabric taken from a tomography image (μ CT)

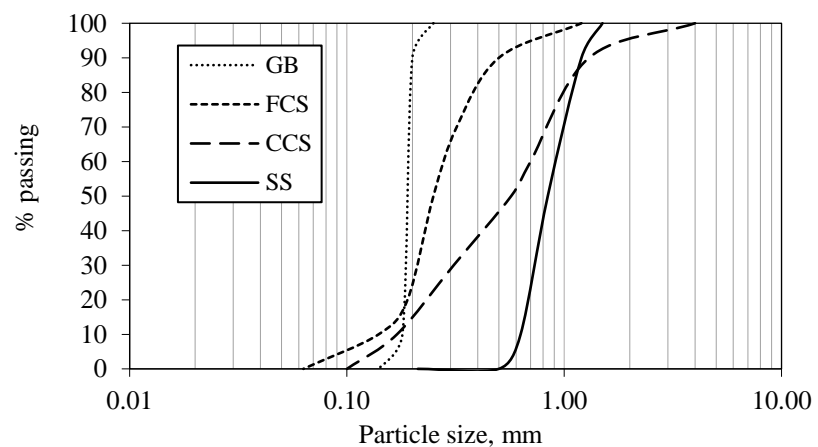


Fig. A-2. Particle size distributions for the four materials: glass ballotini (GB), fine carbonate sand (FCS), coarse carbonate sand (CCS) and silica sand (SS)

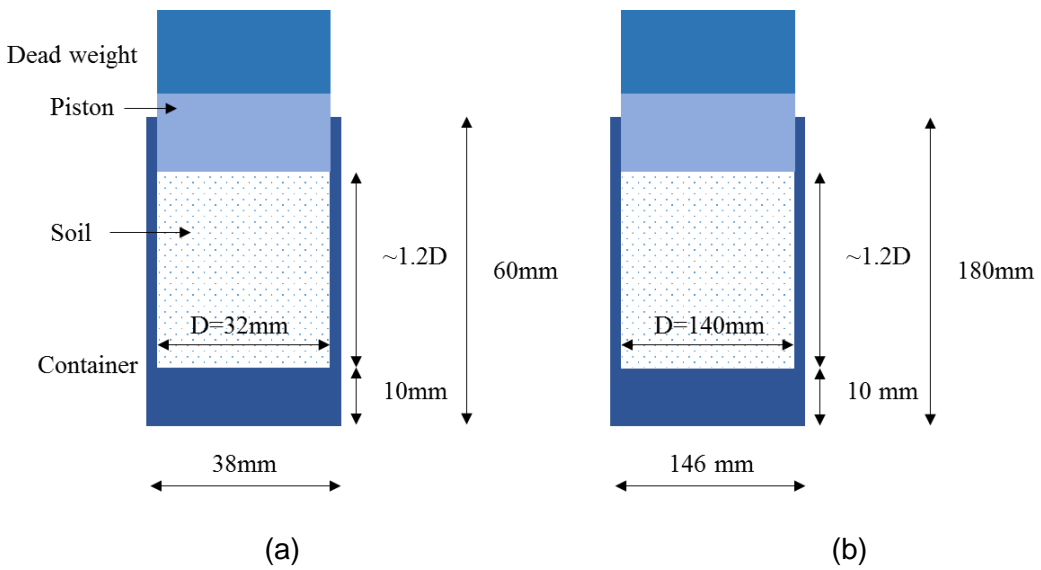
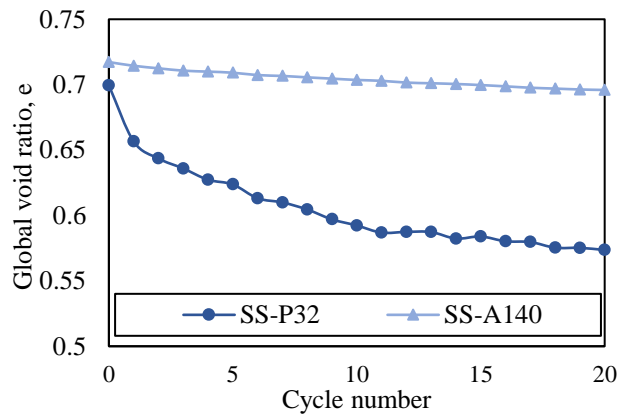
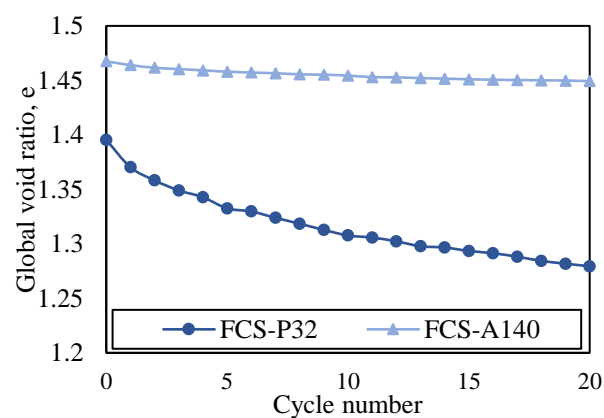


Fig. A-3. Schematic diagram of set-up used in experiments, including details of sample and container sizes (H being the initial height of the sample and D the internal diameter of the container): (a) PMMA container; (b) aluminium container

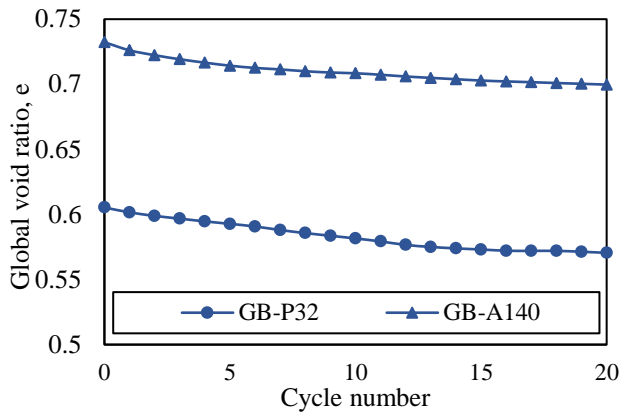


(a)

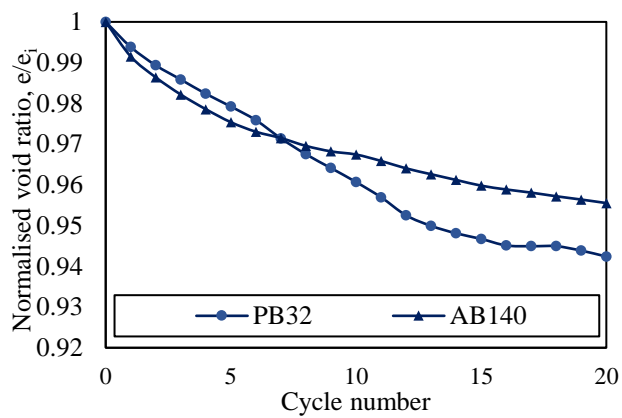


(b)

Fig. A-4. Void ratio evolution for 20 thermal cycles for: (a) silica sand (SS); (b) fine carbonate sand (FCS), for a PMMA container (P32) and an aluminium container (A140)

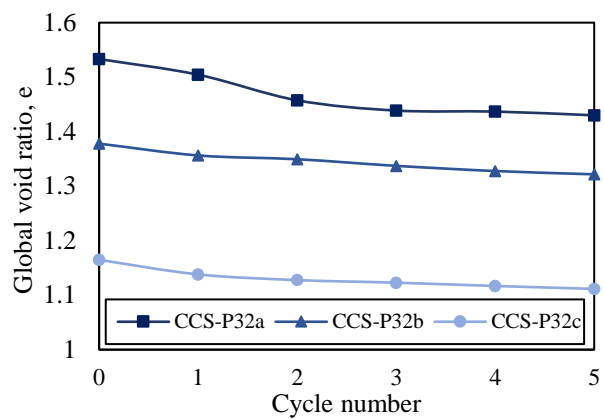


(a)

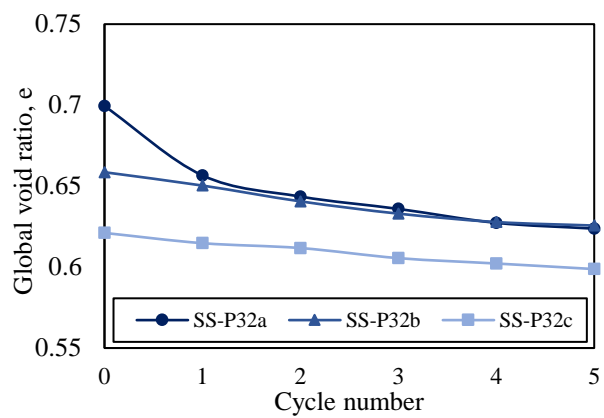


(b)

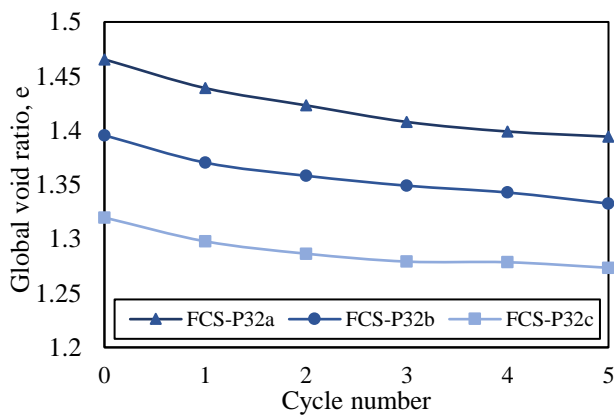
Fig. A-5. Void ratio evolution for 20 cycles of a sample of glass ballotini (GB) for a PMMA container (P32) and an aluminium container (A140): (a) using the global void ratio; (b) using the global void ratio normalised by the initial void ratio



(a)



(b)



(c)

Fig. A-6. Void ratio evolution for five thermal cycles using a PMMA container (P32) for:
(a) coarse carbonate sand (CCS); (b) silica sand (SS); (c) fine carbonate sand (FCS)

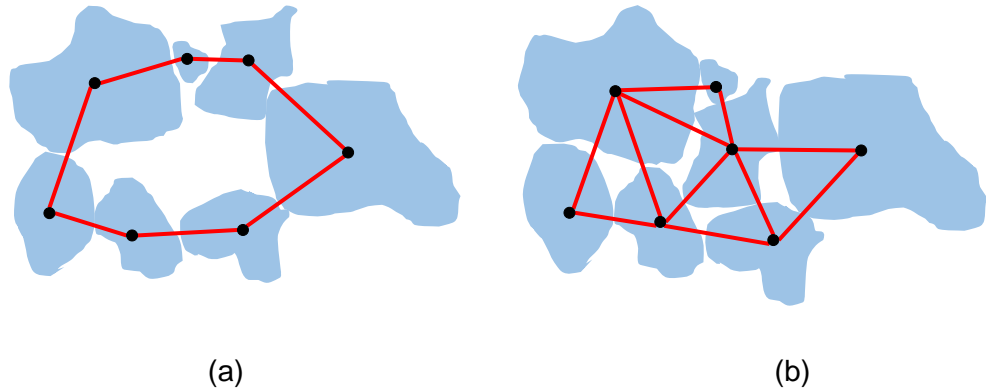


Fig. A-7. Schematic diagram illustrating the grain arrangement due to thermal cycling leading to a more compacted fabric (filling of large void) and formation of a new contact network: (a) contact network before thermal cycling; (b) contact network after thermal cycling



Fig. A-8. Tomographic image of coarse carbonate sand, taken before thermal cycling, showing the presence of large voids within the material

ON THE TORSIONAL LOADING OF ELASTOPLASTIC SPHERES IN CONTACT

Published in: *EPJ Web of Conferences: Powders and Grains 2017; 140, 05001.*

B.1 Background

Mathematical models have been incorporated into discrete modelling of granular system describing the force-displacement relationship between two contacting rigid bodies. This has proven the reliability in simulating granular materials such as soil (O'Sullivan, 2011; Thornton, 2015). The interaction includes normal contact with relative contact area motions such as sliding, rolling or spinning. The spinning around the axis of the contact normal creates a twisting moment (M_T). When M_T in combination with normal loading is applied to two grains in contact, the contact area will undergo some angular displacement (β). The shear forces at the contact will provide some resistance to sliding. Depending on the distribution of normal forces, the region that meets the Coulomb friction condition will experience sliding and the rest of the contact area will undergo sticking (Dintwa, *et al.*, 2005; Nadimi & Fonseca, 2017b). The schematic of this mixed boundary problem for two identical spheres in contact where stick and slip regions coexist is shown in Fig. B-1.

The relationship between the applied moment and the radius of stick region can be written as follows

$$M_T = 2\pi \int_0^a q(r)r^2 dr \quad \text{Eq. B-1}$$

where $q(r)$ is torsional shear traction that is a function of r , the radial position from centre of the contact area. If $c \leq r \leq a$, the traction is limited to $q(r) = \mu F_N(r)$.

Lubkin (1951) delivers the solution to this problem by proposing an equation to define the shear stress at the contact surface within the stick region (Lubkin, 1951). By combining Lubkin's solution with normal force distribution, the twisting moment can be obtained from the following expression (Lubkin, 1951)

$$M_T = \frac{\mu F_N a}{4\pi} \times \left\{ \begin{array}{l} \frac{3\pi^2}{4} + k'^2 \left[6K(k) + (4k'^2 - 3)D \right] - 3kK(k) \sin^{-1} k' - 3k^2 \\ \left[K(k) \int_0^{\pi/2} \frac{\sin^{-1}(k' \sin \alpha) d\alpha}{(1 - k'^2 \sin^2 \alpha)^{3/2}} - D(k) \int_0^{\pi/2} \frac{\sin^{-1}(k' \sin \alpha) d\alpha}{(1 - k'^2 \sin^2 \alpha)^{1/2}} \right] \end{array} \right\} \quad \text{Eq. B-2}$$

where $k = \sqrt{1 - (c/a)^2}$, $k' = \frac{c}{a}$ and $\sin \alpha = r/c$. $D(k)$ is the complete elliptical integral with modulus K , given by $D(k) = (K-E)/k^2$ with K and E being the complete elliptical integrals of the first and second type, respectively.

Given the complexity of Eq. B-1, a simplified solution was proposed by Deresiewicz (1954) between a , M_T and β based on an explicit approximation for numerical modelling which is defined as follows

$$\frac{Ga^2 \beta}{\mu F_N} = \frac{1}{8} \left[1 - \sqrt{1 - \frac{3}{2} \frac{M_T}{\mu F_N a}} \right] \times \left[3 - \sqrt{1 - \frac{3}{2} \frac{M_T}{\mu F_N a}} \right] \quad \text{Eq. B-3}$$

where G is the shear modulus. Therefore, the torsional stiffness can be specified as

$$k_t = \frac{dM_T}{d\beta} = \frac{16Ga^3}{3} \left[2 \left(1 - \frac{3}{2} \frac{M_T}{\mu F_N a} \right)^{-1/2} - 1 \right]^{-1} \quad \text{Eq. B-4}$$

It is important to note that the Eqs. B-3 and B-4 are only applicable for small values of twisting moment where $M_T/\mu F_N a \ll 1$ (Dintwa, et al., 2005). Fig. B-2 shows a non-dimensional moment-twist profile derived from Eq. B-3.

Despite the development of this theoretical approach for the elastic interaction of spheres in the fifties, the elastoplastic interaction under torsion has not been verified yet, as discussed in Thornton (2015).

In this paper, the problem is replicated in the framework of a finite-discrete element method (Munjiza, 2004). In this framework, a continuum body can deform using finite element formulation and can interact with other objects (rigid

and deformable) based on the law of motion, i.e. Newton's second law, used in discrete element modelling. Firstly, the elastic behaviour of a sphere in contact is verified against theoretical equations. Then, the elastoplastic behaviour is presented. The aim of this study is to investigate the applicability of Deresiewicz's solution for elastoplastic grains in contact under twisting moment. The results have implications for describing a granular system with elastoplastic grains.

B.2 Elastic Interaction

The interaction of two identical spheres in contact is simplified, due to symmetry, by the interaction of a sphere in contact with a rigid plate. In order to apply pure torsion to a deformable sphere, a rigid core was generated inside the sphere and was tied to the sphere (Fig. B-3). Fig. B-4 shows the numerical mesh of the problem in Abaqus software package. The sphere has a diameter of 2.2 mm and is represented by a mesh formed by 60,743 elements and 18,112 nodes. The mesh at the contact area was refined for a more accurate presentation of the problem. The material parameters used in the simulation are listed in Table B-1. Explicit time discretization was employed to allow for future work on a large number of grains, since the implicit time discretization is computationally very expensive. The property of hard contact was defined between the sphere and the plate. Using 'hard contact' behaviour means that all the force is transmitted through the contact. Due to body deformability, the relation of normal force versus normal displacement with hard contact assumption follows exactly Hertzian theory (Nadimi & Fonseca, 2017b).

The simulation includes two steps: normal loading and torsional loading. In step one, controlled displacement of 10 μm was applied to the sphere in the normal direction, which corresponds to 95 N normal loading for this problem. In the second step, the sphere was purely rotated around the contact normal using controlled angular displacement of 0.04 rad.

The comparison between Deresiewicz theory and the numerical simulation is presented in Fig. B-5. The plot shows a good agreement between the numerical model and theory. As can be seen in Fig. B-5, there is a small discrepancy in the angular displacement (β) corresponding to the occurrence of pure slipping.

B.3 Elastoplastic Interaction

The torsional interaction becomes plastic when the yield strength is reached in normal loading. This is particularly important for soil grains due to initial contact plasticity (Thornton, 2015; Nadimi *et al.*, 2015). The contact area would be larger for elastoplastic interaction in comparison with elastic interaction for a given normal load. Therefore, pure shear force shows higher tangential stiffness (Thornton, 2015). It is also expected to observe higher stiffness (k_t) due to the larger radius of contact area (a) in torsional loading.

To incorporate the plastic behaviour in numerical modelling, isotropic hardening constitutive laws were assigned to the sphere. It is assumed that the material yields at 100 MPa and then hardens with hardening modulus of 20 GPa (Table B-2). The stress-strain relation assigned to the material is shown in Fig. B-6.

The simulation steps were exactly the same as for the elastic model. In order to keep the normal load of 95 N, a 47 μm controlled displacement was applied in the normal direction which changes the ‘ a ’ value from 149 μm (for elastic) to 319 μm for plastic interaction. This was obtained by trial and error. In the second step, controlled angular displacement of 0.04 rad was applied to the sphere around the contact normal.

Fig. B-7 shows the comparison of the numerical simulations for elastic and elastoplastic interaction in terms of twisting moment and angular displacement. It can be seen that the value of plastic twisting moment is 2.5 times the elastic twisting moment for a constant normal loading, while the contact area was nearly doubled. The normalised twisting moment, presenting in Fig. B-8, shows that the plastic interaction is stiffer than the elastic interaction and pure slipping occurs at smaller values of angular displacement. Finally, the comparison of the theoretical, elastic and plastic models for normalised twisting moment versus normalised angular displacement are presented in Fig. B-9. The good agreement observed, suggests the applicability of Deresiewicz solution for elastoplastic interaction.

B.4 Closing Remarks

This study makes use of the general contact model for two identical spherical grains twisted around their contact normal as proposed by Lubkin and later

simplified by Deresiewicz. The formulations proposed were verified for elastic and more importantly for elastoplastic interactions by means of a finite-discrete element method. It was shown that the plastic torsional interaction is much stiffer than the elastic interaction. This is due to the larger contact area for plastic interaction under a given normal force. It was also presented that pure slipping occurs at smaller values of angular displacement for plastic interaction. The data presented here confirm the applicability of Deresiewicz's solution for elastoplastic torsional interaction.

B.5 Tables and Figures

Table B-1. Physical and mechanical parameters of the spheres

Elastic modulus	E (GPa)	63
Poisson ratio	ν (-)	0.3
Density	ρ (gr/mm ³)	2.5
Friction coefficient	μ (-)	0.22
Diameter	D (mm)	2.2

Table B-2. Isotropic hardening parameters

Yield strength	Y (MPa)	100
Hardening modulus	E_t (GPa)	20

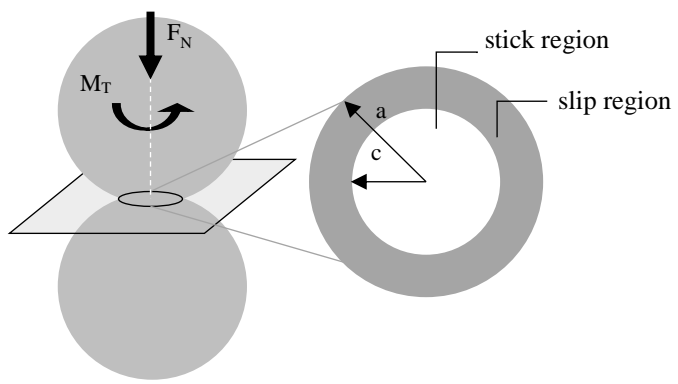


Fig. B-1. Contact area including stick and slip regions for two identical spheres subjected to torsional moment and normal loading

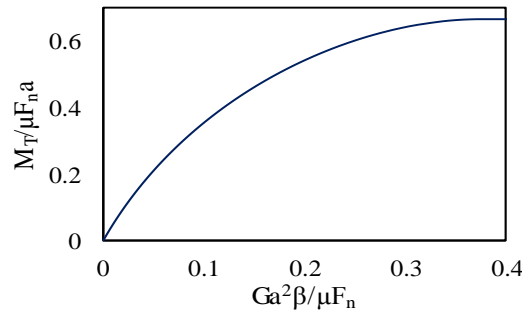


Fig. B-2. Non-dimensional relationship between torque and twisting angle for spherical grains

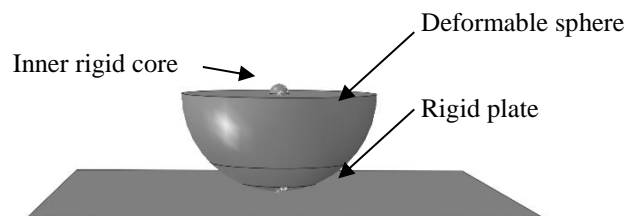


Fig. B-3. Schematic showing the inner core and cut section of the deformable sphere

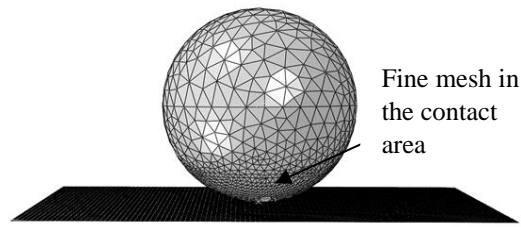


Fig. B-4. Meshed sphere in contact with the rigid plate; mesh defined by smaller elements in the contact area

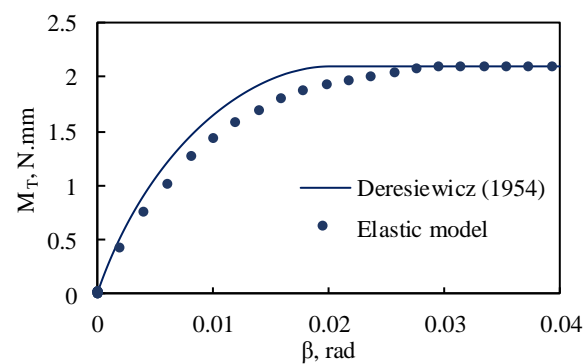


Fig. B-5. Comparison between theory and numerical modelling for elastic interaction of two identical elastic spheres

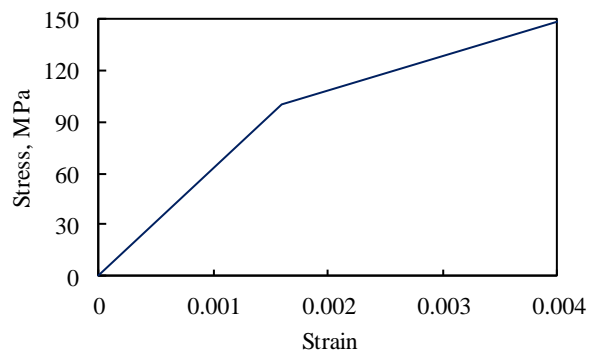


Fig. B-6. Stress-strain for isotropic hardening material used in the simulation

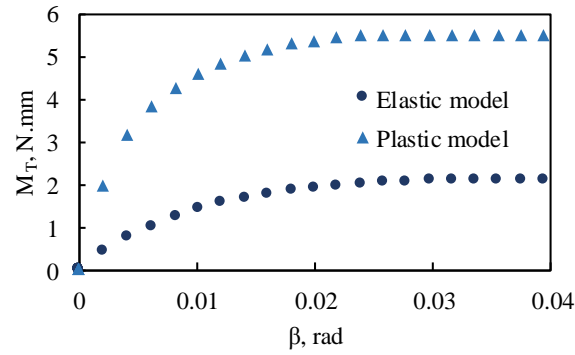


Fig. B-7. Comparison between the numerical modelling of elastic and plastic interaction of two identical spheres under torsion and constant normal loading

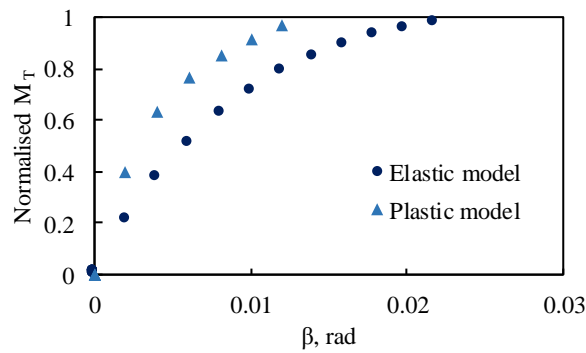


Fig. B-8. Comparison between the normalised twisting moments derived from numerical modelling of elastic and plastic interaction of two identical spheres under torsion and constant normal loading

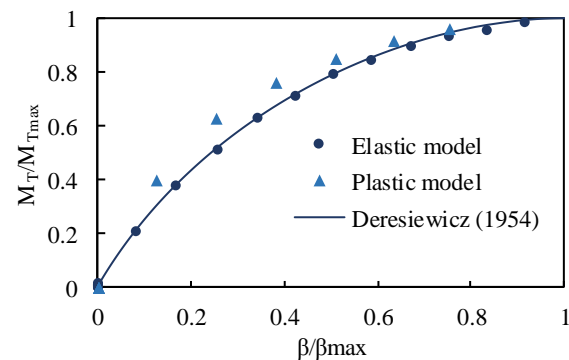


Fig. B-9. Comparison between the numerical modelling of elastic and plastic interaction and Deresiewicz's solution of two identical spheres under torsion and constant normal loading

ON THE TENSILE STRENGTH OF SOIL GRAINS IN HERTZIAN RESPONSE

Published in: *EPJ Web of Conferences*: Powders and Grains 2017; 140, 07001.

C.1 Introduction

C.1.1 Single grain breakage

The importance of grain breakage in granular assemblies has been well documented (McDowell & Bolton, 1998; Nakata, *et al.*, 1999; Marketos & Bolton, 2007; Altuhafi & Coop, 2011). This is of interest to geotechnical, mineral, chemical, food and transportation industries. Recent research advances have been obtained by focusing on the response of a single grain (Zhao, *et al.* 2015; Wang & Coop, 2016). The elastic normal force-displacement response of a grain under compression is called Hertzian response due to pioneering work by German physicist, Hertz (1882). Soil grains are brittle material and break under loading. They will ideally follow a Hertzian response up to the grain strength has been reached. The breakage of a grain is believed to be a tensile phenomenon (cracking) rather than be related to compressive strength (crushing) of the material.

Russell & Muir Wood (2009) proposed an approximate expression for compressive and tensile strength of an ideal grain (sphere) under diametrically-compression. They adopted Christensen (2000) multiaxial failure criterion which has two parameters for brittle materials: (1) intrinsic strength, κ and (2) microstructure factor, χ . The latter parameter (χ) which was described as the microstructural deviations from the ideal is further investigated in this paper by means of numerical and experimental investigation. The theoretical model is presented in the first part of the paper. This is followed by a numerical investigation presented in the second part and finally the experiment is described in part three and compared with the numerical investigation.

C.1.2 Theoretical consideration

The internal stress field propagation in a single spherical grain subjected to the contact forces was presented in Russell & Muir Wood (2009). This has been linked to failure criterion of Christensen which states a material is not at failure as long as the following condition is compiled

$$\frac{\chi\kappa}{\sqrt{3}} I_1 + (1+\chi)^2 J_2 < \frac{\kappa^2}{1+\chi} \quad \text{Eq. C-1}$$

$$J_2 = \left(\frac{I_1^2}{3} - I_2 \right) \quad \text{Eq. C-2}$$

where I_1 and I_2 are the first and second invariants of stress tensor. J_2 is the second invariant of the deviatoric stress tensor. Here, for unconfined compression, $I_1=\sigma_c$, $I_2=0$, $J_2=(\sigma_c)^2/3$ and σ_c is the uniaxial compressive strength.

The intrinsic strength, κ and the microstructure factor, χ are defined as follows

$$\chi = \frac{|\sigma_c|}{\sigma_t} - 1 \quad \text{and} \quad \kappa = \frac{1+\chi}{\sqrt{3}} |\sigma_c| \quad \text{Eq. C-3}$$

where σ_t is the tensile strength.

According to Christensen (2000), κ is the strength of the material with no microstructural damage and is associated to atomic scale properties. The unconfined compressive and tensile strengths of the material are

$$\sigma_c = -\frac{\sqrt{3}\kappa}{1+\chi} \quad \text{and} \quad \sigma_t = -\frac{\sqrt{3}\kappa}{(1+\chi)^2} \quad \text{Eq. C-4}$$

The approximate expressions for compressive and tensile strength of an elastic sphere under compression are (Russell & Muir Wood, 2009)

$$\sigma_c = \frac{aF}{\pi R^2 \sin^2 \theta} \quad \text{and} \quad \sigma_t = \frac{-aF}{\chi \pi R^2 \sin^2 \theta} \quad \text{Eq. C-5}$$

where R is radius, F is the contact force at failure, θ is the contact area in degrees and a is defined as

$$a = \frac{3 \left(\frac{3}{32} + \frac{\sqrt{2}}{24} + \left(\frac{\sqrt{2}}{12} - \frac{1}{4} \right) \mu + \left(\frac{1}{2} - \frac{\sqrt{2}}{3} \right) \mu^2 \right)}{(2 - \sqrt{2})(1 + \mu)} \quad \text{Eq. C-6}$$

where μ is the coefficient of friction.

In Eq. C-5, the contact area θ can be derived by considering the Hertz solution

$$F_n = \frac{4}{3} \frac{E}{1-\nu^2} \sqrt{R\delta_n^{3/2}} \quad \text{Eq. C-7}$$

where F_n is the normal force, E is the elastic modulus, ν is the Poisson ratio and δ_n is the normal displacement. Therefore, θ can be computed using Eq. C-8

$$\theta = 2 \cos^{-1} \left(1 - \left(\frac{3F(1-\nu^2)}{4ER} \right)^{2/3} \right) \quad \text{Eq. C-8}$$

To the best knowledge of the authors, the microstructural origin of κ and χ has not been supported by any atomic scale studies. In approximate solution for strength of sphere, σ_c is unaffected by the value of χ (Eq. C-5). According to literature, the parameter χ varies from 10 to 170 for a range of rock types (Goodman, 1989; Russell & Muir Wood, 2009). Russell & Muir Wood considered four values for $\chi = 19, 49, 99, 199$ in their parametric study. In this paper, the effect of χ on the normal force-displacement behaviour of a sphere under compression is presented.

C.2 Numerical Investigation

The problem is investigated in the framework of combined finite-discrete element framework (Munjiza, 2004; Nadimi & Fonseca, 2017a). The interaction of two contacting spheres is simplified to interaction of a sphere with rigid plate, due to symmetry. The effect of χ on the normal force-displacement is investigated by means of an elastic-damage constitutive model. This model uses isotropic damage elasticity in combination with isotropic tensile and compressive plasticity. The constitutive model, numerical model and results are presented in this section.

C.2.1 Constitutive model

The response of the material is modelled using damage plasticity based on two failure mechanisms: (1) tensile cracking and (2) compressive crushing (Lubliner, et al., 1989; Lee & Fenves, 1998). Damage states are characterised by two hardening parameters: the equivalent plastic strain in tension, ϵ_t^{pl} , and in

compression, ε_c^{pl} . The stress-strain relation is governed by scalar damage elasticity as defined as follows

$$\sigma = (1-d)D_0^{el} : (\varepsilon - \varepsilon^{pl}) = D^{el} : (\varepsilon - \varepsilon^{pl}) \quad \text{Eq. C-9}$$

where d is a scalar describing the amount of isotropic damage. D_0^{el} is the initial elastic stiffness, D^{el} is the damaged elastic stiffness, ε is the total strain ε^{pl} is the plastic strain.

The states of failure and damage are determined using a yield surface in the effective stress space. The yield condition proposed by Lubliner *et al.* (1989) and modified by Lee & Fenves (1998) has been incorporated to model both tensile and compressive behaviour. The flow potential surfaces are not described here, as it is out of scope of this paper. The typical uniaxial tensile stress strain is shown in Fig. C-1a. The degradation of stress depends on the formulation of d . Similarly, for the compressive stress-strain curve, the degradation is controlled by the value of d after the ultimate compressive strength (Fig. C-1b). The material hardens from yield compressive strength to the ultimate strength and then softens.

This constitutive model is attractive, as it can represent a different failure mechanism for cracking and for crushing. Thus, enabling investigating the effect of χ by changing σ_t for constant σ_c .

C.2.2 Numerical model

The model sphere has a diameter of 2.2 mm and is represented by a mesh formed by 60,743 elements and 18,112 nodes. The material parameters used in the simulation are listed in Table C-1. Explicit time discretization was employed. The property of hard contact was defined between the sphere and the plate. Using ‘hard contact’ behaviour means that all the force is transmitted through the contact. The relation of normal force-displacement with hard contact assumption follows exactly the Hertzian theory for pure elasticity, due to the deformability of bodies (Nadimi & Fonseca, 2017b). A series of six simulations were conducted. Different values of χ were considered which is listed in Table C-2 with corresponding tensile and compressive strengths.

C.2.3 Results

Fig. C-2 shows the results of the simulations. The pure elastic model is also presented to observe the deviation of the elastic-damage simulations from pure elasticity. The increase in the value of χ shows the decrease in the normal force which corresponds to the onset of breakage. The exact value of the normal force, F_N , for different χ values is listed in the last column of Table C-2.

C.3 Experimental Investigation

Single grain experiments are presented in this section on the three type of grains, including glass bead, silica sand and carbonate sand. The schematic of the set-up is shown in Fig. C-3. A strain controlled machine ‘Instron 5969’ was used over a range of force applications up to 2 kN. The instrumentation accuracy was $<1\mu\text{m}$ for displacement and $<0.1\text{ N}$ for load measurements.

C.3.1 Glass beads

Forty single grain tests were carried out on glass beads. They are commercially supplied by Sigmund Lindner GmbH as type S beads with specific gravity of 2.57. Three range of diameters were chosen, including 1.1 to 1.4 mm, 2.0 to 2.4 mm, and 3.6 to 4.1 mm. In previous experimental work, the tensile strength of a grain has been defined as the maximum normal force over the squared grain diameter (McDowell & Bolton, 1998). In order to show the variation of tensile strength, the histograms of maximum normal loads applied on the grains are presented. Figs C-4a, 4b and 4c show the variation of the maximum normal force applied to the glass beads with the different diameters mentioned above. The Standard Deviation (SD) and median values (Med) are also presented in Fig. C-4 caption. McDowell & Bolton proposed a relationship between tensile strength and grain diameter as follows

$$\sigma_t \propto D^{-3/m} \quad \text{Eq. C-10}$$

They reported the value of m is in the range of 5-10 for silica sand, and limestone aggregates. Here, the value of m was obtained from power regression to be 2.89 ($R^2=0.75$) for glass beads. This will be further discussed in the next Section. According to Fig C-3b and numerical simulation, a low value of χ (approximately

9) is expected for glass beads. Fig. C-4d shows the comparison of a typical experimental response observed with the Hertzian response.

C.3.2 Silica sand

Forty grains of Leighton Buzzard sand, from England, with median diameter of 0.84 mm were randomly picked. Fig C-5a and b show the typical response of silica sand grain under compression. It comprises an initial plateau associated with grain rotation and asperity damage, followed by inelastic Hertzian type of hardening and finally breakage. Fig. C-6a shows the variation of maximum normal force for silica grains with a standard deviation of 6.1 N and a median value of 15.5 N, excluding 8 grains with capacity from 40 N to 80 N, for better visualisation. Despite the similarity in mineralogy and elastic modulus between glass beads and silica sand, the tensile strength is significantly different which suggests different value for χ .

C.3.3 Carbonate sand

Forty grains of a shelly carbonate sand from the Persian Gulf with median diameter of 2 mm were randomly picked. Fig. C-6b shows the histogram of maximum normal load carried by carbonated sand grains with a standard deviation of 7.9 N and a median value of 9.2 N, excluding 10 grains with very wide capacity from 40 N to 384 N, for better visualisation. Although the majority of grains can bear less than 10 N, this diversity in response can be attributed to the various shape found in this bioclastic material (Fonseca, *et al.*, 2015)

C.4 Closing Remarks

The numerical and experimental tests presented here show that the failure of a single grain under compression is a tensile (cracking) phenomenon. We can observe that the lower the tensile capacity, the softer the Hertzian response. The low value of χ for glass beads in comparison with the high value for silica grains can be related to geological history and weathering of the sand grains. There might be a direct relation between the parameter m in McDowell & Bolton (1998) and χ in Russell & Muir Wood (2009), which needs further investigation.

Carbonate sand bearing capacity can be categorised by considering grain morphology and intergranular void ratio.

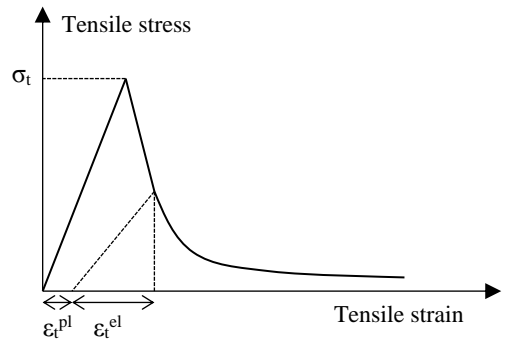
C.5 Tables and Figures

Table C-1. Physical and mechanical parameters

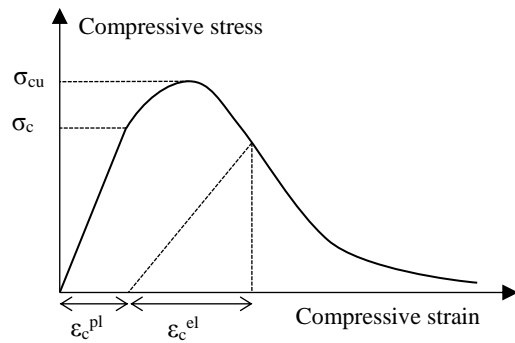
Elastic modulus	E (GPa)	63
Poisson ratio	ν (-)	0.3
Density	ρ (gr/mm ³)	2.5
Diameter	D (mm)	2.2

Table C-2. Compressive and tensile strengths for different value of parameter χ and the maximum normal force obtained corresponds to the onset of breakage

χ	σ_c (MPa)	σ_t (MPa)	F_N (N)
9	2000	200	942
19	2000	100	589
49	2000	40	263
99	2000	20	138
199	2000	10	65



(a)



(b)

Fig. C-1. Response of the material under uniaxial loading (a) in tension and (b) in compression

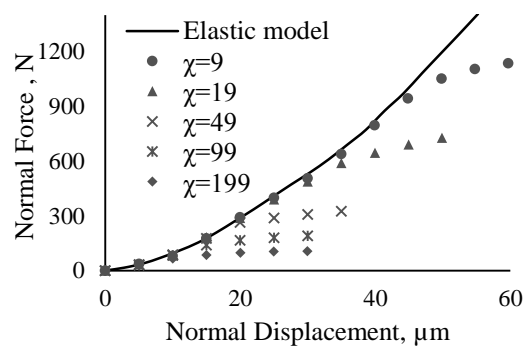


Fig. C-2. Response of a spherical grain under compression for different tensile strengths

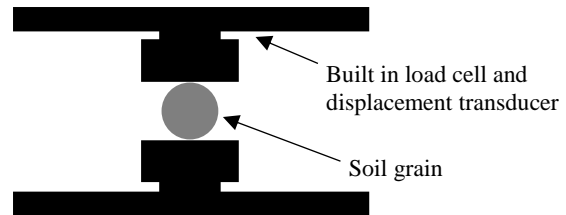


Fig. C-3. Schematic of the single grain test under normal load

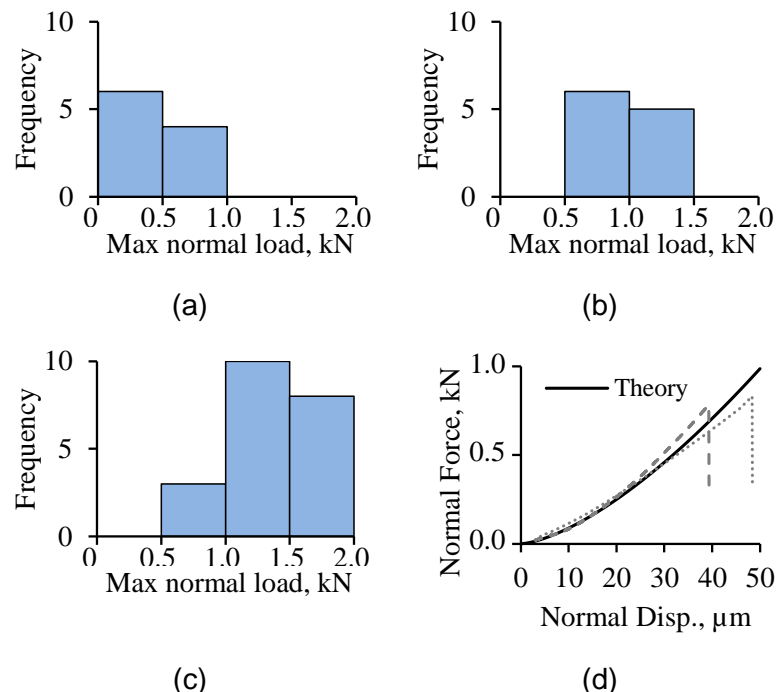


Fig. C-4. Distribution of the maximum normal load applied on the glass beads of a) 1.1-1.4mm ($SD=123$, $Med=459$), b) 2.0-2.4mm ($SD=136$, $Med=979$), c) 3.6-4.0mm diameter ($SD=357$, $Med=1290$); d) comparison between the typical normal force-displacement response of glass beads and Hertzian theory

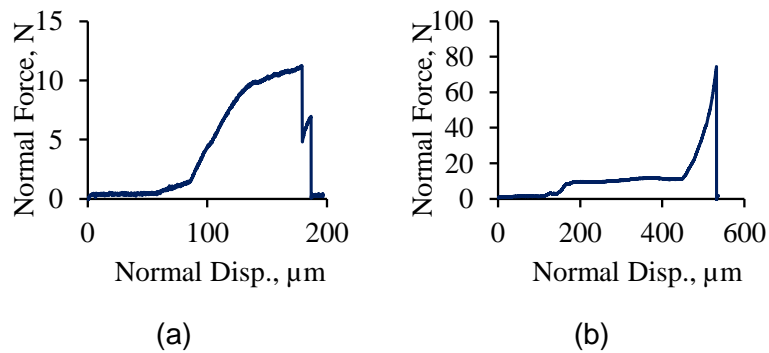


Fig. C-5. Typical normal force-displacement response of silica sand

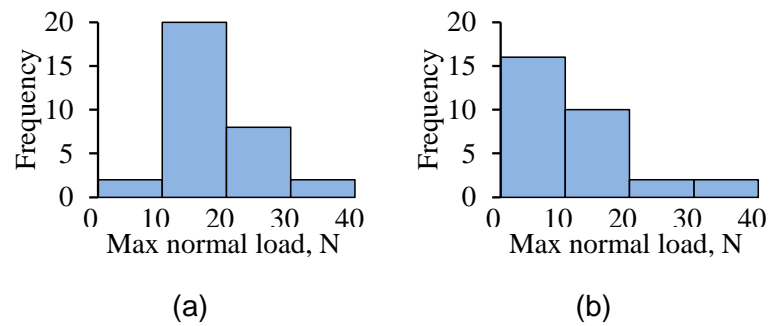


Fig. C-6. Distribution of maximum normal load applied on the grains of, a) silica sand, b) carbonate sand